



**HAL**  
open science

# Study of light-induced dipolar interactions in cold atoms assemblies

Ludovic Brossard

► **To cite this version:**

Ludovic Brossard. Study of light-induced dipolar interactions in cold atoms assemblies. Optics [physics.optics]. Université Paris-Saclay, 2020. English. NNT : 2020UPASO002 . tel-02880041

**HAL Id: tel-02880041**

**<https://pastel.hal.science/tel-02880041>**

Submitted on 24 Jun 2020

**HAL** is a multi-disciplinary open access archive for the deposit and dissemination of scientific research documents, whether they are published or not. The documents may come from teaching and research institutions in France or abroad, or from public or private research centers.

L'archive ouverte pluridisciplinaire **HAL**, est destinée au dépôt et à la diffusion de documents scientifiques de niveau recherche, publiés ou non, émanant des établissements d'enseignement et de recherche français ou étrangers, des laboratoires publics ou privés.

# Study of light-induced dipolar interactions in cold atoms assemblies

**Thèse de doctorat de l'université Paris-Saclay**

École doctorale n° 572, Ondes et Matières (EDOM)

Spécialité de doctorat : Physique

Unité de recherche : Université Paris-Saclay, Institut d'Optique Graduate School, CNRS, Laboratoire Charles Fabry, 91127, Palaiseau, France

Référent : Institut d'Optique

**Thèse présentée et soutenue à Palaiseau, le 26/02/2020, par**

**Ludovic BROSSARD**

## Composition du Jury

**Éric CHARRON**

Professeur des Universités, UPS - ISMO

Président

**Mathilde FOUCHE**

Chargée de Recherche, CNRS - INPHYNI

Rapporteur & Examinatrice

**Athanasios LALIOTIS**

Chargé de Recherche, CNRS - LPL

Rapporteur & Examineur

**Franck PEREIRA**

Directeur de Recherche, SYRTE

Examineur

**Antoine BROWAEYS**

Directeur de Recherche, CNRS - LCF

Directeur de thèse

**Yvan SORTAIS**

Maître de Conférences, UPS - LCF

Co-Directeur de thèse

**Igor FERRIER-BARBUT**

Chargé de Recherche, CNRS - LCF

Invité



# ACKNOWLEDGMENTS

---

Ce manuscrit conclue les trois années et demie de thèse qui se sont déroulées à l'Institut d'Optique. Les travaux qui y sont présentés n'auraient pas été possibles sans la présence et l'accompagnement de nombreuses personnes que je tiens à remercier chaleureusement.

Je commence par la personne qui à mes yeux mérite le plus ces remerciements. En effet, si tu m'as permis de faire cette thèse comme tu en donnerais la chance à bien d'autres, tu as été bien plus qu'un simple directeur de thèse pour moi. Avoir pu bénéficier de tes enseignements et de ton encadrement a été un véritable honneur. Et si tes qualités scientifiques sont indéniables, tes qualités humaines le sont tout autant. Tu as toujours fait preuve d'une extrême gentillesse et d'une patience infinie à mon égard, et tu as aussi su être là quand j'étais au plus bas. Je ne serais jamais allé au bout de cette thèse sans toi Antoine, alors pour cela aussi merci. J'espère ne pas m'être montré trop indigne de la chance incroyable que tu m'as offerte. J'espère également avoir un jour l'occasion de te prouver ma reconnaissance. Je pourrais remplir des pages entières d'éloges et d'anecdotes à ton sujet mais le fond resterait le même. Je ferai donc plus concis et direct: un grand merci à toi!

Merci également à toi Yvan de m'avoir donné ma chance, et pour avoir passé bien des heures à jouer, dans le noir, avec des petits trous... Ou encore pour m'avoir aidé à vider le réservoir de ma voiture, tombée en panne sur une aire de repos en plein soleil! J'ai pu bénéficier des tes enseignements, bien évidemment, mais je crois avoir surtout gagné un peu de la rigueur et du soin qui te caractérisent. Tu as toujours fait preuve de beaucoup de patience avec moi, pour m'expliquer les choses comme pour essayer de comprendre mes questions. Si j'ai été un peu plus distant la dernière année, crois bien que je le regrette. J'espère néanmoins que tu conserveras un souvenir positif cette collaboration et qu'on sera amené à se revoir.

Je tiens aussi à remercier toutes les personnes avec qui j'ai eu la chance, ou plutôt le privilège de travailler. No one said it would be easy, and you were absolutely right dear Daniel. It was an honour to meet you, on a professional level and also on a personal one. I will always remember the time spent in the lab with you, sometimes very late at night, the frustration and above all the fun that we had together. The magic around your personality will always remain in my memory. I wish you, and to your family, all the best for the future. And good luck with your life! Merci Toni pour le temps que

## Acknowledgments

---

j'ai passé avec toi dans le labo. Travailler avec toi n'a été qu'une partie de plaisir. Ça a dû être bien différent pour toi qui a dû supporter mes déprimés passagères, désolé... J'espère néanmoins que tu en garderas un bon souvenir. De toute façon, on a surtout traversé des problèmes techniques, et les problèmes techniques, ça se retrouve en annexe! Je te souhaite de t'amuser sur l'expérience et j'espère que tu obtiendras plein de jolis résultats. Igor, je n'ai malheureusement pas pu travailler avec toi dans le labo, mais je suis sûr que ça aurait été une expérience très enrichissante. Je te souhaite beaucoup de succès pour la suite. Bon courage à toi! Nikola, it was a great pleasure to work with you. Thank you very much to have spent the needed time to explain to me the numerical models, the physical concepts and basically everything. I wish you all the best for the future. Un grand merci à toi Florence. Sans ton travail, je n'aurais pas pu m'amuser à modifier le système expérimental, et donc j'aurais inévitablement appris beaucoup moins de choses. Merci également d'avoir passé du temps avec moi dans le labo pour me remonter le moral. Je ne t'ai peut-être jamais remerciée officiellement alors je profite de cette occasion pour réparer ce tort.

L'ambiance du groupe d'Optique Quantique ne serait pas la même sans les joyeux délurés de Chadoq, dont la pristinitude n'a d'égale que leur bienveillance et leur sympathie. Merci à toi Thierry, pour avoir répondu à toutes mes questions avec beaucoup de pédagogie. Véritable incollable sur l'électronique, la thermodynamique, la mécanique, la physique atomique... enfin bref, toute la physique quoi, avoir pu bénéficier de tes connaissances aussi bien théoriques que pratiques a été un véritable privilège. Je ne suis pas malade en voiture, mais quand je suis content comme ça je vomi! Juste une petite dernière pour la route, la conductivité électrique du Gallium? Un grand merci au trio de choc: Sylvain, Vincent et Pascal! J'ai apprécié passer du temps avec vous et je ne peux que regretter de ne pas en avoir passer plus. Sylvain, bonne continuation au Japon. J'espère que t'éclates dans tout ce que tu fais et que tu obtiendras des résultats spectaculaires. Cela ne fait aucun doute. Vincent, j'espère que tu retrouveras bientôt ta deuxième oreille! Si tu veux chanter des chansons françaises jusqu'à tard dans la nuit au Hurling ou dans n'importe quel bar de ton choix, c'est tout de même mieux d'avoir le stéréo. Je te souhaite beaucoup de joie dans la suite de ton parcours, quel qu'il soit. J'espère vraiment avoir l'opportunité de croiser ton chemin à l'avenir. Pascal, je n'ai pas eu l'occasion de passer beaucoup de temps avec toi et c'est bien dommage. Bonne continuation sur la manip. Je sais que tu sauras t'inscrire dans le fructueux chemin de tes prédécesseurs. Bon courage également aux autres membres de cette équipe, Kai et Hannah. Je sais déjà qu'aussi bien entouré, rien de bien malheureux ne peut vous arriver. Il ne faut évidemment pas oublier les petits chatons! Martin, j'ai apprécié ta bonne humeur et ton rire très communicatif, même à travers l'épais mur en béton qui séparait nos labos. T'avoir dans les environs apportait un peu de lumière, surtout dans nos labos sans fenêtre. Benjamin, je crois t'avoir plus souvent vu dans mon labo que dans le tien, mais c'est probablement une impression. C'était sympa de t'avoir dans les

---

environs. Bon courage pour la rédaction, à toi et à Clémence.

Il aurait été aussi beaucoup plus difficile de traverser ces trois années et demie sans la présence de quelques amis. Merci à Alexandre et Marine. Quand on est parfois un peu fébrile, c'est super de pouvoir compter sur des amis aussi fidèles. Merci également à Arnaud et Rachel, qui malgré l'éloignement, m'ont toujours accueilli à bras ouverts. Merci à vous Tom et Morgane, vous retrouver a toujours été un plaisir et je souhaiterais que ce soit le cas plus souvent. Tom, je passe l'éponge concernant la planche à découper! Merci à toi Ludivine, une amie avec une telle gentillesse c'est plutôt rare et donc précieux. Merci Aliénor. Nous avons eu un parcours un peu chahuté, et si tu en as souffert je te prie de m'en excuser. Je ne mérite certainement pas une amie comme toi. Un grand merci à toi Nico, et à Minou aussi évidemment! Merci d'avoir *réguler mes repas*, ce qui m'a permis de ne pas perdre les quelques kilos qui me restaient. Nos retrouvailles hebdomadaires étaient une véritable bouffée d'air frais où je pouvais oublier un peu tout mon quotidien et apprécier des discussions aussi variées qu'intéressantes sur les sciences, l'économie, le travail du bois et du métal, la linguistique et j'en passe. Bon, je suis toujours imbattable à Mario Party 5, mais pour tout le reste je ne t'arrive pas à la cheville mon cher Nico. J'espère de tout cœur que cette amitié ne s'arrêtera pas de sitôt et qu'on se verra tous les trois régulièrement avec toujours autant d'enthousiasme. Il ne faut pas que j'oublie aussi mon cher Babou, qui en plus de m'avoir logé (en garde partagée avec les derniers cités) a aussi été très présent pour moi. Que ce soit pour regarder des films débiles à une heure du matin, parce qu'une heure du matin c'est pas si tard déjà, ou bien pour boire un ou deux verres, mais en même temps ce serait dommage d'en laisser dans la bouteille, ou encore pour voyager à l'autre bout du monde et atterrir dans un hôtel de passe dans un quartier *muy peligroso*. C'est dommage quand même, la seule chose que j'avais réservé du voyage. Promis, la prochaine fois je m'occupe vraiment de rien, en espérant qu'il y aura une prochaine fois très bientôt: l'épisode 1 des Branleurs en Colombie appelle forcément une suite!

Et je termine cette liste, qui commence à être bien longue à présent, en remerciant ma famille, notamment mes parents. Merci beaucoup de m'avoir toujours soutenu et accompagné, dans les périodes difficiles tout particulièrement. Je vous aime.

# CONTENTS

---

## ACKNOWLEDGMENTS

INTRODUCTION	1
1. PRODUCTION OF A DENSE CLOUD OF COLD ATOMS	7
1.1. General background on atom-light interactions	8
1.1.1. Trapping potential	8
Resonant approximation - Case of $^{87}\text{Rb}$	9
Full expression - Case of $^{87}\text{Rb}$	10
1.1.2. Scattering rate	11
Rayleigh scattering and Raman scattering	11
1.1.3. Cloud extensions and oscillation frequencies	12
1.2. Preparation of a dense cloud of cold atoms	13
1.3. Experimental measurements of relevant quantities	16
1.3.1. The oscillation frequencies	16
1.3.2. The temperature	17
Time-of-flight measurement principle	17
Comments on the time-of-flight imaging	19
1.3.3. The number of atoms	19
1.3.4. Conclusion	21
2. NEAR-RESONANT LIGHT TRANSMISSION THROUGH A DENSE CLOUD OF TWO-LEVEL ATOMS	23
2.1. Light scattering	24
2.1.1. Interaction between light and an ensemble of atoms	25
2.1.2. The Incoherent and Coherent fields	28
Experimental quantities measured	29
Coherent transfer function	32
Incoherent transfer function	33
2.2. Previous results	33
2.2.1. Incoherent scattering	33
2.2.2. Coherent scattering	35
2.2.3. Conclusion	44

2.3.	Transmission through a dense cloud of cold two-levels atoms . . . . .	45
2.3.1.	Polarization of the sample: towards two-level atoms . . . . .	45
	Choice of the value of $\mathbf{B}$ field . . . . .	46
	Interaction with a static magnetic field . . . . .	47
2.3.2.	Experimental sequence . . . . .	49
2.3.3.	Experimental results . . . . .	50
	Temporal measurement . . . . .	50
	Steady-state regime . . . . .	51
	Conclusion . . . . .	52
2.4.	Comparison between theory and experiment . . . . .	53
2.4.1.	The coupled-dipoles model . . . . .	53
	As a function of the number of atoms . . . . .	54
	As a function of the temperature of the cloud . . . . .	55
	As a function of the trap volume . . . . .	56
	Conclusion . . . . .	57
2.4.2.	Coupled-dipoles model with atomic motion . . . . .	57
	Including motion into the coupled-dipoles model . . . . .	57
	Simulation procedure . . . . .	59
	Simulations results . . . . .	60
	Conclusion . . . . .	60
2.4.3.	A new model to tackle the high intensity regime . . . . .	61
	Maxwell-Bloch equations in the low intensity regime . . . . .	61
	Connection with the experimental measurement . . . . .	62
	Steady-state solution . . . . .	63
	Maxwell-Bloch equations in the high intensity regime . . . . .	64
2.5.	Conclusion . . . . .	65
3.	<b>A NEW APPARATUS TO STUDY DIPOLE-DIPOLE INTERACTIONS</b> . . . . .	67
3.1.	Design of the new apparatus . . . . .	69
3.1.1.	New vacuum chamber . . . . .	69
3.1.2.	MOT coils . . . . .	70
3.1.3.	Microwave antenna . . . . .	74
3.1.4.	Vacuum . . . . .	74
3.1.5.	Other modifications . . . . .	74
	Computer Control . . . . .	74
	New CCD camera . . . . .	75
3.2.	Alignment of the aspheric lenses . . . . .	76
3.2.1.	Relevant optical quantities . . . . .	76
3.2.2.	The aspheric lenses . . . . .	78
	Choice of a given conjugation . . . . .	78
	Alignment procedure . . . . .	81
	Understanding the distribution of intensity . . . . .	84

3.3.	Characterization of performance . . . . .	86
3.3.1.	Single atom regime . . . . .	87
3.3.2.	Trapping frequencies . . . . .	88
	Aspheric lens A . . . . .	88
	Aspheric lens B . . . . .	92
3.3.3.	Lifetime measurement . . . . .	93
3.4.	Limitation of the performance - The viewports and the spherical aberration	95
3.5.	The future tools . . . . .	98
3.5.1.	Optical tweezer of variable size . . . . .	99
3.5.2.	Accordion lattice . . . . .	101
4.	TOWARDS LIGHT SCATTERING BY 1D CHAIN OF ATOMS	103
4.1.	Light scattering in a 1D chain . . . . .	104
4.1.1.	Growth of the excitation probability along the chain . . . . .	106
	General case: $\mathbf{a} \neq j\frac{\lambda}{2}, j \in \mathbb{N}$ . . . . .	107
	Special case: $\mathbf{a} = j\frac{\lambda}{2}, j \in \mathbb{N}$ . . . . .	109
4.1.2.	Robustness of the system with experimental imperfections . . . . .	110
	Perfect system . . . . .	112
	With defects . . . . .	113
	With disorder . . . . .	114
	With disorder and defects . . . . .	116
4.1.3.	Investigation of the effect of the temperature . . . . .	117
4.1.4.	Investigation of the effect of a Gaussian beam in the excitation probability . . . . .	117
4.1.5.	Conclusion . . . . .	118
4.2.	Super Imaging of the 1D chain of atoms . . . . .	119
4.2.1.	Creation of the picture . . . . .	119
4.2.2.	Algorithm . . . . .	121
4.2.3.	Performance evaluation of the algorithm . . . . .	123
4.2.4.	Conclusion . . . . .	124
	CONCLUSION	127
	A. ELECTRIC FIELD PRODUCED BY A DIPOLE	131
	B. CLEBSH-GORDAN COEFFICIENTS OF $^{87}\text{Rb}$ D1 & D2 LINE - $\pi$ TRANSITIONS	137
	C. MAXWELL-BLOCH EQUATIONS FOR COHERENT LIGHT SCATTERING	139
	RÉSUMÉ	147
	REFERENCES	151



# INTRODUCTION

---

The interaction between light and a collection of particles (atoms or molecules) forming the matter has been, and still is, an attractive field in research. The concept of refractive index for instance, a bulk property of dielectrics, can be tracked back to the 11th century [Rashed, 1990]. A variety of everyday life scenarios can be explained by the scattering of light from polarizable object: from the color of the sky to the opacity of the milk. The advent of quantum theory in the 20th century, and more precisely the discovery of the internal structure of atoms [Foot, 2005], has induced a renewed of interest for the study of light-matter interactions. The theoretical description of single atom and dilute samples of atoms achieved an absolutely remarkable accuracy [Huntemann et al., 2016]. However, increasing the number of atoms in a given volume add a new ingredient to the behavior of the system [Anderson, 1972]. The emitters can start interacting with each others via dipole-dipole interactions and then they respond collectively rather than just individually. In its full generality, the problem of near resonant light interacting with atoms has all the complexity of a many body problem, the system being quantum, open, and driven by light. In this introduction, we try to explain why the study of dipole-dipole interactions in dense ensemble may be important for a wide variety of technological applications in a not so distant future, and also that if properly tailored, these interactions can be a key to some interesting light-matter interfaces devices. Then, we briefly summarize the work performed at the Institut d’Optique, in the group of Antoine Browaeys, related to dipole-dipole interactions.

## LIGHT-MATTER INTERACTIONS: MOTIVATIONS

The accurate description of the behavior of dense sample is not only interesting from the fundamental aspect but also for a wide range of technological applications. In nanophotonics, the light interacts with emitters that are confined in volume of the order of  $\lambda^3$ , hence an accurate comprehension of the system response with density may be of crucial importance in order to circumvent a possible departure from their expected behavior. In fact, it has been shown that the emissivity of a system composed of many antennas placed in a small volume can be altered by dipole-dipole interactions [Huang et al., 2010].

Another field that might soon benefit from a fine understanding of the interaction between light and a dense sample is the one of atomic clocks, the new generation of

which being optical. Initially, with the consideration of black body radiation, special and general relativity, standard atomic clocks achieved an uncertainty as low as  $1 \times 10^{-16}$ . Their successive development, making them all optical, enable them to achieve nowadays an absolute frequency uncertainty of  $2.5 \times 10^{-19}$  [Marti et al., 2018], which means the clock will deviates by less than one second in 15 billion years, more than the age of the universe. With such a high resolution, the clock has potential applications that are beyond simply marking time. Using light to probe the resonance of the atoms, the clock could therefore be used as an altimeter by detecting slight changes in the gravity, or explore quantum correlations between atoms, and constantly pushing back the validity boundary of the equivalence principle of Einstein's general relativity theory.

It has been recognized recently that light scattering from atom-based sensors can introduce unwanted energy level shifts ([Chang et al., 2004],[Campbell et al., 2017]). These shifts can generate biases in the reference frequency frame of the clock that reach the same order of magnitude than their actual relative precision. Not understanding quantitatively the way light interacts with matter in dense regime might be one of the limitations that would prevent us from further improving optical atomic clocks.

Not only being a limitation, the dipole-dipole interactions can be an asset if manipulated correctly. Several works suggest ways to use these interactions to create light-matter interfaces: [Bettles et al., 2015a], [Shahmoon et al., 2017a], [Perczel et al., 2017]. By placing the atoms in specific lattice configurations, the field radiated by all the emitters can interact destructively, leading to absolutely no transmission of light for instance. We would therefore create a perfect mirror made of a single 2D layer of atoms.

## **DIPOLE-DIPOLE INTERACTIONS AT LABORATOIRE CHARLES FABRY: A BRIEF HISTORY**

The study of light interacting with dense laser cooled sample of atoms has been initiated around 2012 in the Quantum Optics group at Laboratoire Charles Fabry. To study atom-light interaction in a pristine setting, two requirements are necessary. First, to isolate the effect of the interactions from other environments effects and, second, to be able to change the amount of matter into a constant size volume. Cold atoms fulfilled both requirements and thus provides an ideal platform to tackle light-matter interactions problems. In fact, they have already shown their outstanding performance in many experiments related to this field (a none exhaustive list of works includes [Chalony et al., 2011], [Kwong et al., 2014], [Bourgain et al., 2013], [Bender et al., 2010], [Bienaimé et al., 2010], [Chabé et al., 2014], [Aljunid et al., 2009]). For the dipole-dipole interactions to start modifying the response of the system with

---

respect to the non interacting case, one possibility is to reach  $n/k^3 \approx 1$ , with  $k = 2\pi/\lambda$  the wavevector, or similarly the average distance between atoms in the trap to be on the order of  $\lambda$ , the wavelength associated with the addressed transition. Given the typical temperature of our atoms, the trap characteristics and the fact that we probe the D2 line of  $^{87}\text{Rb}$ ,  $\lambda = 780$  nm, the density associated with a mean distance between atoms of  $\lambda$  is  $\sim 10^{14}$  cm $^{-3}$ . They have designed a system where atoms are trapped in free space thanks to high numerical aperture aspheric lens inside a vacuum chamber. The aspheric lens is tightly focusing a far-off resonance, red-detuned laser beam which forms a conservative potential in which atoms with a thermal energy lower than the potential barrier can be trapped. This apparatus is both suitable for single atom manipulation [Sortais et al., 2007] and for cloud containing  $\sim 100$  atoms. Once the atoms are trapped, the basic idea consists in shining onto the cloud near resonant light and measure the amount of scattered light in a given direction.

It must be pointed out that the approach chosen in our group, small and dense cloud of atoms, is different from other group studying the effect of the density on the way a sample of atoms scatters light.

- For instance, the groups of Havey [Roof et al., 2016], Kaiser [Araújo et al., 2016] and Wilkowski [Kwong et al., 2015] also use cold atoms but with dilute samples. The low density  $n/k^3 \ll 1$  is compensated by a large optical thickness OD, the transmission  $T$  being related to it through the relation  $T = e^{-\text{OD}}$ . In such a case, the optical thickness is shown to govern most properties of the system.
- Another approach, used in the group of Charles Adams [Keaveney et al., 2012], consists in studying hot gaseous vapours with very large densities  $n/k^3 \gg 1$  but low optical thickness. This approach has been fruitful recently with a collaboration between our group and the one of Charles Adams: [Peyrot et al., 2018], [Peyrot et al., 2019a], [Peyrot et al., 2019b], [Peyrot et al., 2019c].

The theoretical description available to model our systems are based on two different point of view. The first one is a macroscopic approach describing the full sample by a single quantity, the refractive index. It is the approach used in the group of Charles Adams in [Keaveney et al., 2012] where they measured a strong shift of the resonance when density is increased, compatible with the so-called *Lorentz-Lorenz* formula found in various textbook theory of refractive indices as [Feynman et al., 1965]. The second description is a microscopic view in which all characteristics of the sample constituents, including their interactions, have to be known. In our case, assuming frozen distribution, this reduces to the individual position of each atoms. Our group have measured the scattered light emitted by the cloud at  $90^\circ$  from the propagation direction of the probe [Pellegrino et al., 2014], but the measured shifts were not significant in comparison with the ones measured in the group of Charles Adams. In order to understand this puzzling fact, they also measured the emitted light in the propagation

axis of the probe [Jennewein et al., 2016]. For this second measurement, they tried a macroscopic and a microscopic approach to try to better understand the results but they only obtained qualitative agreements. To reconcile theory with experimental data, they wanted to address the validity of the underlying hypothesis of the theoretical descriptions. This was the status when I arrived in the group in 2016.

## OUTLINE OF THE THESIS

The manuscript presented here is organized as follows:

- The first chapter 1 is a brief overview of some general light-matter interactions backgrounds. It is the opportunity to introduce the experimental measurement of some basic quantities relevant for the study of dipole-dipole interactions.
- In chapter 2, I will remind the previous results of our group concerning the measurement of scattered light by a cigar shaped cloud of cold  $^{87}\text{Rb}$  atoms probed near resonance. Then I will present the latest result obtained at the very beginning of my PhD: the coherent transmission of light through a cold sample of *two-level* atoms. The goal of this measurement was to get rid of the complex internal structure of the atoms and see if a better agreement with theory can be achieved in this situation. The slight improvement obtained motivates us to investigate others hypothesis, as for instance the role of the atomic motion in the way the cloud scatters light. The end of the chapter is dedicated to the introduction of a new model, based on optical Bloch equations, to study dipole-dipole interactions but not restricted to the weak driving limit, opening the road for a future experiment in this regime.
- After these conclusions, our group has decided to modify the experimental apparatus, both to solve some experimental problems that were present in the previous version and to add a new rather unique ingredient: a second high resolution optical axis. The second axis, not only being able to measure directly parameters of the cloud that were so far deduce from other quantities, will provide us the possibility to explore new regime of densities and new geometries. In chapter 3, I will present the challenging alignment of two confocal axes composed of high numerical aperture aspheric lenses. I will also present the characterization tests that have been performed and we will try to understand them. At the end of the chapter, I will show the new tools that are, or will soon be, implemented on the apparatus.
- The last chapter 4 starts with the theoretical investigation of the propagation of an excitation along a 1D chain of atoms. As our system is able to produce and observe 1D chain thanks to the second axis of aspheric lenses, we want to make

---

sure that the effect presented in [Sutherland and Robicheaux, 2016], namely the enhancement of dipole-dipole interactions through the constructive interference of the fields radiated by the atoms in a one dimensional structure, is robust with respect to experimental imperfections before demonstrating it experimentally. This study is followed by a second one where I have tried to implement an algorithm that would infer the position of the atoms along the chain based on their fluorescence image. Even though the approach is not new, the idea was to investigate the feasibility of such a task given our experimental parameters.

In conclusion, I summarize the whole thesis and try to give a taste of the possible future experiments.



# CHAPTER 1

## PRODUCTION OF A DENSE CLOUD OF COLD ATOMS

---

### Contents

---

<b>1.1. General background on atom-light interactions . . . . .</b>	<b>8</b>
1.1.1. Trapping potential . . . . .	8
Resonant approximation - Case of $^{87}\text{Rb}$ . . . . .	9
Full expression - Case of $^{87}\text{Rb}$ . . . . .	10
1.1.2. Scattering rate . . . . .	11
Rayleigh scattering and Raman scattering . . . . .	11
1.1.3. Cloud extensions and oscillation frequencies . . . . .	12
<b>1.2. Preparation of a dense cloud of cold atoms . . . . .</b>	<b>13</b>
<b>1.3. Experimental measurements of relevant quantities . . . . .</b>	<b>16</b>
1.3.1. The oscillation frequencies . . . . .	16
1.3.2. The temperature . . . . .	17
Time-of-flight measurement principle . . . . .	17
Comments on the time-of-flight imaging . . . . .	19
1.3.3. The number of atoms . . . . .	19
1.3.4. Conclusion . . . . .	21

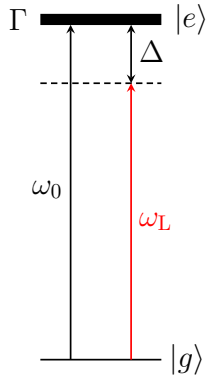
---

In this chapter, after a brief overview of the main theoretical backgrounds on light-matter interaction, I will present how we prepare a dense cloud of cold atoms and how we experimentally measure the relevant quantities that we need to describe it.

## 1.1 GENERAL BACKGROUND ON ATOM-LIGHT INTERACTIONS

We start this section by recalling the expression of some of the standard physical quantities used when dealing with light-matter interaction. All the results of this subsection are standard textbook results. The references that have been particularly used here are: [Dalibard, 2013] and [Grynberg et al., 2010]. Then, I will present how we experimentally prepare a dense cloud of cold Rubidium 87 atoms in a tightly focused optical dipole trap from a Magneto-Optical Trap (MOT). Finally, the experimental measurement of the relevant physical quantities used to characterize our system will be detailed.

### 1.1.1 Trapping potential



Let us consider a two-level system, with the two states denoted respectively  $|g\rangle$  for ground and  $|e\rangle$  for excited state. The energy of the excited state is  $\hbar\omega_0$  (we have chosen the energy of the ground state to be 0) and we note  $\Gamma$  its natural linewidth. The interaction of this system with an electromagnetic field, in the dipolar approximation, is described by the Hamiltonian

$$H_I = -\mathbf{D} \cdot \mathbf{E}_L,$$

where  $\mathbf{D} = \mathbf{d} |e\rangle \langle g| + \mathbf{d} |g\rangle \langle e|$  is the dipole operator,  $\mathbf{d}$  is the dipole moment of the atom, assumed to be real here, and  $\mathbf{E}_L$  is the laser field expressed by

$$\mathbf{E}_L = \mathcal{E}_0 \cos(\omega_L t + \mathbf{k} \cdot \mathbf{r}) \hat{\mathbf{e}}_L.$$

The detuning of the laser with respect to the atomic transition is denoted  $\Delta = \omega_L - \omega_0$ . The interaction of a polarizable system with an electromagnetic field is composed of two parts: a radiative pressure force, responsible for the cooling of the atom, and a trapping force. This force derives from a potential  $U_{\text{dip}}$  which, under the rotating wave approximation which implies that the frequency of the electromagnetic wave is tuned close to an atomic resonance,  $\Delta \ll \omega_0$ , and considering that the spontaneous emission is the only relaxation process in the system, is expressed as

$$U_{\text{dip}} = \frac{\hbar\Delta}{2} \ln(1 + s), \quad (1.1)$$

where we have introduced the saturation parameter  $s$  defined by

$$s = \frac{\Omega^2/2}{\Delta^2 + \Gamma^2/4},$$

and the Rabi frequency

$$\Omega = -\frac{(\mathbf{d} \cdot \hat{\mathbf{e}}_L)\mathcal{E}_0}{\hbar}.$$

In the limit of low saturation  $s \ll 1$ , we expand the logarithm and get

$$U_{\text{dip}} \approx \frac{\hbar\Delta}{2}s = \frac{\hbar\Delta}{2} \frac{\Omega^2/2}{\Delta^2 + \Gamma^2/4}. \quad (1.2)$$

If we suppose that the linewidth is small compared to the detuning, which is the case in our experiment because  $\Gamma = 2\pi \times 6$  MHz for  $^{87}\text{Rb}$  and  $\Delta = 2\pi \times 65$  THz for a trapping wavelength around 940 nm, we obtain

$$U_{\text{dip}} = \frac{\hbar\Omega^2}{4\Delta}. \quad (1.3)$$

### Resonant approximation - Case of $^{87}\text{Rb}$

In the previous section, we have recalled the expression of the trapping potential in the case of a two-level system under several assumptions. Here, we will give the same expression but considering the multi-level structure of Rubidium, restraining our analysis to the D1 and D2 lines.

Let us consider an atomic structure with one ground state  $|g\rangle$  and  $N_e$  excited states denoted  $|e_1\rangle, |e_2\rangle, \dots, |e_j\rangle, \dots, |e_{N_e}\rangle$ . The expression of the trapping potential in this multi-level atomic structure is simply a sum over each one of these excited states

$$U_{\text{dip}} = \sum_{j=1}^{N_e} \frac{\hbar\Omega_{ge_j}^2}{4\Delta_{ge_j}}. \quad (1.4)$$

where  $\Delta_{ge_j} = \omega_L - \omega_{ge_j}$  is the detuning of the laser with respect to the transition  $|g\rangle \rightarrow |e_j\rangle$ . Using the Wigner-Eckart theorem and the relation between  $d_{ge_j}$  and  $\Gamma_{JJ'}$ , (1.4) becomes

$$U_{\text{dip}} = \sum_{j=\{J',F',m_{F'}\}}^{N_e} \frac{\hbar\Gamma_{JJ'}^2}{8} \frac{I}{I_{\text{sat}}^{JJ'}} \frac{2J'+1}{2J+1} \frac{|C_{F,m_F,F',m_{F'}}^{J,J'}|^2}{\Delta_{ge_j}}, \quad (1.5)$$

where  $C_{F,m_F,F',m_{F'}}^{J,J'}$  is the Clebsh-Gordan coefficient associated with the transition  $|J, F, m_F\rangle \rightarrow |J', F', m_{F'}\rangle$  and  $I_{\text{sat}}^{JJ'} = \frac{2\pi^2\hbar c\Gamma}{3\lambda_{JJ'}^3}$  is the saturation intensity. We are only summing over  $J', F'$  and  $m_{F'}$  as we are considering the case of a single ground state  $|g\rangle$ , so  $J, F$  and  $m_F$  are fixed.

Let us now focus on the  $^{87}\text{Rb}$  case. We are considering only the D1 and D2 lines contributions. For that matter, we split the sum into two components: the one corresponding to transitions on the D1 line and the second for the D2 line. We take the approximation a step further noticing that for  $^{87}\text{Rb}$ ,  $\Gamma_{\text{D1}} = 2\pi \times 5.7$  MHz is close to  $\Gamma_{\text{D2}} = 2\pi \times 6.0$  MHz. It is also true for  $I_{\text{sat}}^{\text{D1}}$  and  $I_{\text{sat}}^{\text{D2}}$ . Moreover, the detuning between the laser and one of the hyperfine excited state is similar to the one between the laser and the fine structure of this state (because the hyperfine splitting of the D1 and D2 lines is small compared to the fine splitting). We then rename  $\Delta_{ge_j} = \Delta_1$  for all the excited states in  $5P_{1/2}$  and  $\Delta_{ge_k} = \Delta_2$  for all the excited states in  $5P_{3/2}$ .

For a  $\pi$  polarized laser electric field, the Clebsch Gordan coefficients associated with the transition  $|5S_{1/2}, F=2, m_F\rangle$  to  $(5P_{1/2})$  or  $(5P_{3/2})$  are listed in Appendix B. Replacing those coefficients in (1.5) gives the trap depth seen by a  $^{87}\text{Rb}$  in state  $|g\rangle = |5S_{1/2}, F=2, m_F\rangle$  when a  $\pi$  polarized laser beam is shined onto it (1.6). Remarkably, the light-shift is independent of the  $m_F$  state when the trapping beam is  $\pi$  polarized. That is the reason why we have used a  $\pi$  polarized laser beam for the trapping potential in our experiment.

$$U_{\text{dip}} = \frac{\hbar\Gamma^2}{8} \frac{I}{I_{\text{sat}}} \left( \frac{1}{3\Delta_1} + \frac{2}{3\Delta_2} \right). \quad (1.6)$$

For a more detailed investigation of the light shift experienced by a  $^{87}\text{Rb}$  atom considering all the possible polarizations of the trapping light, see [Darquié, 2005].

### Full expression - Case of $^{87}\text{Rb}$

Expression (1.6) has been obtained under the rotating wave approximation. Indeed, it is derived from the stationary solutions of the optical Bloch equations that has been obtained within this approximation. The expression of the trapping potential in presence of anti-resonant terms is

$$U_{\text{dip}} = \sum_{j=1}^{N_e} \frac{\hbar\Omega_{ge_j}^2}{4\Delta_{ge_j}^-} - \sum_{j=1}^{N_e} \frac{\hbar\Omega_{ge_j}^2}{4\Delta_{ge_j}^+}, \quad (1.7)$$

which, for  $^{87}\text{Rb}$  is specifically

$$U_{\text{dip}} = \frac{\hbar\Gamma^2}{8} \frac{I}{I_{\text{sat}}} \left( \frac{1}{3\Delta_1^-} - \frac{1}{3\Delta_1^+} + \frac{2}{3\Delta_2^-} - \frac{2}{3\Delta_2^+} \right). \quad (1.8)$$

In expression (1.8),  $\Delta_1^- = \omega_L - \omega_1$  is the *resonant* detuning between the laser and the D1 transition, whereas  $\Delta_1^+ = \omega_L + \omega_1$  is its *anti-resonant* counterpart. The same definitions hold for  $\Delta_2^-$  and  $\Delta_2^+$  on the D2 line. This precision may seem of minor importance, and in practice it is for most applications, but it worth mentioning it because the anti-resonant

terms are of non negligible importance for our system. In fact, for a trapping wavelength of 940 nm and a transition wavelength of 780 nm, the anti-resonant terms represent a correction close to 10% with respect to the result provided by the expression without anti-resonant terms. It is the expression that we will consider throughout the manuscript to compute the trap depth seen by the atoms, either experimentally or theoretically.

### 1.1.2 Scattering rate

Another useful quantity when dealing with atoms inside a dipole trap is the scattering rate. It corresponds to the number of photons that the atom is emitting per second due to the absorption of the ones of the trapping light. The scattering rate induced by the trapping light  $R$ , applied to the structure of  $^{87}\text{Rb}$ , is

$$R = \frac{\Gamma^3}{8} \frac{I}{I_{\text{sat}}} \left| \frac{1}{3\Delta_1^2} + \frac{2}{3\Delta_2^2} \right|. \quad (1.9)$$

Once again, (1.9) is valid for an atom in any  $m_F$  state of  $(5S_{1/2}, F = 2)$  manifold and for a  $\pi$  polarized trapping light. The expression only accounts for resonant terms and assumes the detuning to be large compared to the natural linewidth  $\Gamma$  and  $\frac{\Delta}{\Gamma} \gg \frac{I}{I_{\text{sat}}}$ .

#### Rayleigh scattering and Raman scattering

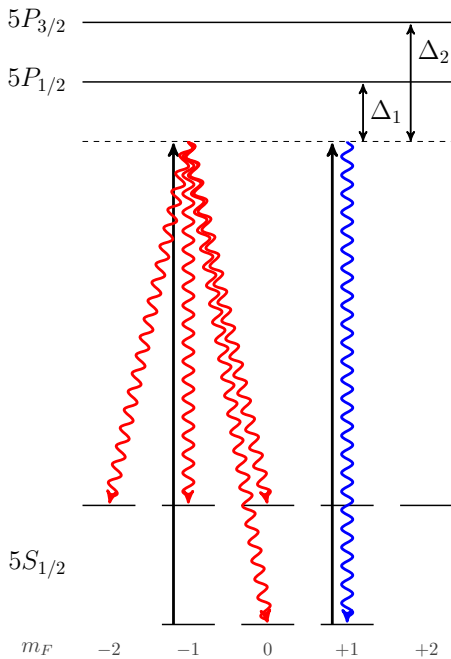


**Figure 1.1.:** Raman and Rayleigh scattering examples for, respectively, an atom initially in  $|5S_{1/2}, F = 1, m_F = -1\rangle$  (red) and in  $|5S_{1/2}, F = 1, m_F = +1\rangle$  (blue).

The scattering rate is the sum of two contributions: the Rayleigh scattering, denoted  $R_{\text{Rayleigh}}$ , for which an atom does not change its internal state, and the Raman scattering, denoted  $R_{\text{Raman}}$ , for which the atom will change its internal state, as represented in Figure 1.1. One can derive the expression of those two contributions and will get [Ozeri et al., 2005]

$$R_{\text{Rayleigh}} = \frac{\Gamma^3 I}{8 I_{\text{sat}}} \times \frac{1}{9} \left| \frac{\Delta_2 + 2\Delta_1}{\Delta_1 \Delta_2} \right|^2,$$

and

$$R_{\text{Raman}} = \frac{\Gamma^3 I}{8 I_{\text{sat}}} \times \frac{2}{9} \left| \frac{\Delta_2 - \Delta_1}{\Delta_1 \Delta_2} \right|^2.$$

This two expressions sum to the total scattering rate (1.9)

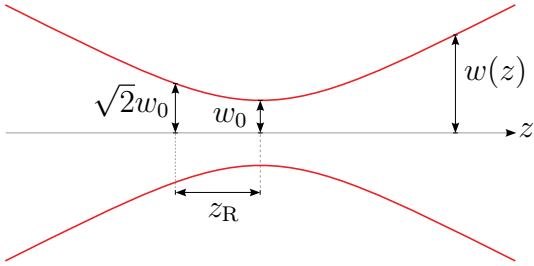
$$R = R_{\text{Rayleigh}} + R_{\text{Raman}}.$$

Our trapping wavelength, initially at 850 nm, has been changed to 940 nm in order to minimize Raman scattering. In fact, if we want to prepare our sample in a specific  $m_F$  state of the ( $5S_{1/2}$ ) with optical pumping, we do not want the Raman scattering induced by the dipole trap to destroy our preparation. A numerical application shows that the ratio of the Raman scattering between 850 and 940 nm is

$$\frac{R_{\text{Raman}}(\lambda = 850 \text{ nm})}{R_{\text{Raman}}(\lambda = 940 \text{ nm})} \approx 24,$$

thus killing drastically Raman scattering. In principle, one could minimize scattering processes even more but would need a lot of laser power to trap an atom as the trap depth scale as  $I/\Delta$ . For a waist of the trap beam around  $1.2 \mu\text{m}$  and a power of 12 mW, at 940 nm, the Raman scattering rate is around  $4.5 \times 10^{-2} \text{ ph.s}^{-1}$ , which is sufficiently low to be neglected. As a comparison, for the same trap depth at 850 nm,  $U = 1.0 \text{ mK}$ ,  $P = 5.2 \text{ mW}$ , the Raman scattering rate is  $4.7 \times 10^{-1} \text{ ph.s}^{-1}$ , more than 10 times bigger.

### 1.1.3 Cloud extensions and oscillation frequencies



In this work, we describe the trapping beam and the probing beam, respectively at 940 nm and 780 nm, by Gaussian beams. The Gaussian beam is a transverse electric mode (TEM) whose electric field amplitude is a solution of the paraxial Helmholtz equation. Assuming a polarization in the  $x$ -direction and a propagation along the  $z$ -direction, the expression of the field, under

the paraxial approximation, is

$$\mathbf{E}(\mathbf{r}, z) = E_0 \frac{w_0}{w(z)} \exp\left(\frac{-r^2}{w(z)^2}\right) \exp\left(-ikz - ik\frac{r^2}{2R(z)} + i\psi(z)\right) \hat{\mathbf{e}}_x, \quad (1.10)$$

where  $r$  is the radial distance from the center axis of the beam,  $z$  is the axial distance from the beam's focus,  $k = 2\pi/\lambda$ ,  $E_0$  is the electric field amplitude at the origin. The waist  $w$ , the wavefront radius of curvature  $R$  and the Gouy phase  $\psi$  are respectively defined by

$$w(z) = w_0 \sqrt{1 + \left(\frac{z}{z_R}\right)^2}, \quad R(z) = z \left[1 + \left(\frac{z_R}{z}\right)^2\right], \quad \psi(z) = \arctan\left(\frac{z}{z_R}\right),$$

where  $w_0$  is the radius of the beam at the origin,  $z_R = \pi w_0^2/\lambda$  is called the Rayleigh range and corresponds to the distance from the focus point where the beam is  $\sqrt{2}$  larger than at the focus.

Using the Gaussian expression for the trapping beam enables us to easily extract a confinement potential of the light on the atoms, used in the coupled-dipoles simulations to draw a random initial configuration of the atoms in the cloud. Indeed, by expanding the Gaussian beam intensity up to second order in coordinates variables, one extracts the oscillations frequencies of the atoms inside the trapping potential. First, let us compute the intensity of the Gaussian beam

$$I(r, z) = \frac{I_0}{1 + (z/z_R)^2} \exp\left(-\frac{2r^2}{w(z)^2}\right), \quad (1.11)$$

where we have used the relations (1.10),  $I_0 = \frac{1}{2}\epsilon_0 c |E|^2$  and  $\epsilon_0 \mu_0 c^2 = 1$ . The quantity  $I_0$  is related to the power of the beam  $P$  through the expression  $I_0 = \frac{2P}{\pi w_0^2}$ . The trapping potential  $U$  follows the distribution of intensity

$$U(r, z) = -\frac{U_0}{1 + (z/z_R)^2} \exp\left(-\frac{2r^2}{w(z)^2}\right), \quad (1.12)$$

where we choose  $U_0 > 0$ . Expanding (1.12) to second order in coordinates and identifying terms with the ones in the expression of the harmonic potential, we obtain the expressions of the transverse and longitudinal oscillations frequencies of a particle of mass  $m$  in the trap

$$\omega_r = \sqrt{\frac{4U_0}{mw_0^2}} \quad \omega_z = \sqrt{\frac{2U_0}{mz_R^2}}. \quad (1.13)$$

Once the oscillations frequencies obtained, the equipartition theorem enables to link the spatial extension of the cloud in the trap with the temperature. Finally, one gets

$$\sigma_r = \sqrt{\frac{k_B T}{m\omega_r^2}} \quad \sigma_z = \sqrt{\frac{k_B T}{m\omega_z^2}},$$

and then, with (1.13)

$$\sigma_r = w_0 \sqrt{\frac{k_B T}{4U_0}} \quad \sigma_z = z_R \sqrt{\frac{k_B T}{2U_0}}. \quad (1.14)$$

## 1.2 PREPARATION OF A DENSE CLOUD OF COLD ATOMS

The experimental apparatus has already been presented in Stephan Jennewein's PHD thesis [Jennewein, 2017] and, in a very detailed way, in the one of Andreas Fuhrmanek [Fuhrmanek, 2011]. The goal here is to sum up the most important parts of the experimental setup.

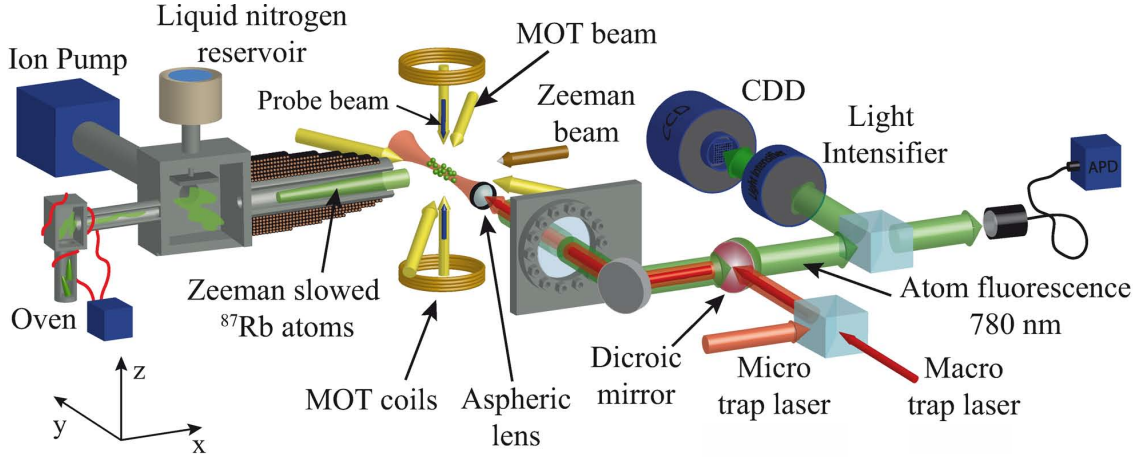


**Figure 1.2.:** Sketch of the experimental setup extracted from [Fuhrmanek, 2011]. A vapor of <sup>87</sup>Rb atoms, initially in solid form in the oven, are slowed down from  $\sim 300 \text{ m.s}^{-1}$  to  $\sim 16 \text{ m.s}^{-1}$  in a Zeeman slower. The atoms are further cooled to  $\sim 0.1 \text{ m.s}^{-1}$  in a magneto-optical trap (MOT). Two red-detuned, far-off resonance from the D2 line of Rubidium 87, laser beams are focused by an aspheric lens into the atomic cloud. The same aspheric lens is used to collect the fluorescence emitted by the atoms that is imaged onto an intensified CCD camera and an avalanche photodiode (APD).

In order to be able to study the influence of dipole-dipole interactions, we need to create atomic samples with a high density. The solution that has been implemented here is to use tightly focused optical dipole traps and try to load as much atoms as possible inside it. In our experiment, we use standard cooling and trapping mechanisms to load a magneto-optical-trap (MOT) of <sup>87</sup>Rb from a solid piece of Rubidium placed in an oven. Depending on the temperature of the oven  $T_{\text{oven}}$ , a certain quantity of Rubidium evaporates and fills the first chamber through a small tube. This first chamber is connected to an ion pump to keep the residual pressure at typically  $10^{-10}$  mbar. Additionally, a finger with a copper surface, cooled down via thermal contact with a reservoir of liquid nitrogen at 77 K, is placed inside this chamber. It absorbs some of the Rubidium atoms in the vapor and probably helps to avoid a rapid saturation of the ion pump. The first part is separated from the main science chamber by a Zeeman tube of length  $\sim 70$  cm and diameter of 15 mm. The velocity distribution of the atomic beam after the oven is given by

$$f(v) = \frac{m^2}{2(k_B T_{\text{oven}})^2} v^3 \exp\left(-\frac{mv^2}{2k_B T_{\text{oven}}}\right).$$

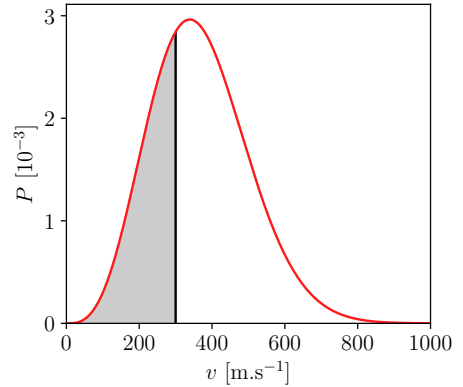


**Figure 1.4.:** Velocity distribution of an atomic beam with  $T_{\text{oven}} = 400 \text{ K}$ .

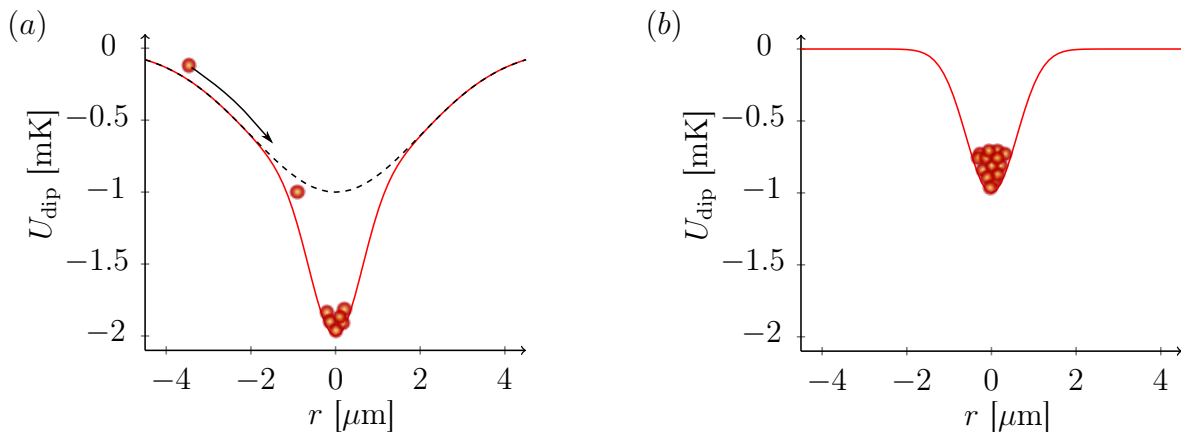


**Figure 1.3.:** Sketch of the micro-trap loading. (a): Trap-depth profile of both the macro-trap and the micro-trap (red solid line). The profile of the macro-trap alone is represented in dark dashed line. This macro-trap enables to increase the capture volume of the micro-trap, as its waist at  $1/e^2$  is about  $4 \mu\text{m}$ , compared to the waist of the micro-trap which is only  $1.2 \mu\text{m}$ . The cooling processes induced by the MOT beams trap the atoms at the bottom of this intensity profile. (b): Micro-trap intensity profile alone, filled with atoms.

For a typical temperature of the oven  $T_{\text{oven}} \approx 400 \text{ K}$ , the average velocity of the atoms in the beam is  $368 \text{ m.s}^{-1}$ . Because the capture range of standard MOT is around  $1 \text{ K}$ ,  $\approx 17 \text{ m.s}^{-1}$ , only a tiny fraction of the original distribution will be captured ( $\sim 10^{-5}$ ). To increase the number of captured atoms, a Zeeman slower ([Phillips and Metcalf, 1982]) is used. It has been designed to slow down atoms with a typical speed of  $300 \text{ m.s}^{-1}$  to  $5 \text{ m.s}^{-1}$ . Doing so, 33% of the initial velocity can now be captured by the MOT.

In the second vacuum chamber, the science chamber, the background pressure is very low ( $\sim 10^{-11} \text{ mbar}$ ) thanks to the Zeeman tube. In this second chamber, two high numerical aperture ( $\text{NA} = 0.5$ ) aspherical lenses are used to both trap the atoms and collect their fluorescence light [Sortais et al., 2007]. Two almost collimated laser beams are focused by the aspherical lens. One of them has a waist at  $1/e^2$  of  $4 \mu\text{m}$ , called macro-trap, while the other one has a waist at  $1/e^2$  of  $1.2 \mu\text{m}$ , which we will call micro-trap. We manage to load around 2000 atoms in the macro-trap. The micro-trap is filled with atoms originally trapped in the macro-trap and we manage to put up to 200 atoms ( $\sim 10\%$  of the number of atoms in the macro-trap), which corresponds to a peak density of approximately  $10^{14} \text{ at.cm}^{-3}$  (see Figure 1.3). The two trapping beams are red-detuned from the D2 line of Rubidium in order to trap atoms in region where the intensity is maximum. Moreover, the traps are orthogonally polarized to avoid any interference effects. They are operated with approximately the same trap depth  $U_0 \approx k_B \times 1 \text{ mK} \approx h \times 21 \text{ MHz}$ .

Finally, once the atoms are loaded in the micro-trap, we start the experiment and we

collect the light emitted through the aspherical lens onto a CCD camera combined with an intensifier. Due to the fact that the system is diffraction limited, we have access to the smallest resolution possible,  $\sim 1 \mu\text{m}$ , in the plane of the atoms [Sortais et al., 2007]. The light emitted by the atoms and collected by the aspherical lens is also coupled to a single-mode fiber connected to an avalanche photodiode in single photon counting mode, followed by a counting card. This second path is time-resolved and thus gives access to the dynamic of the optical response of the cloud. For any particular detail on the experimental setup, see Andreas Fuhrmanek's PHD thesis [Fuhrmanek, 2011].

### 1.3 EXPERIMENTAL MEASUREMENTS OF RELEVANT QUANTITIES

In order to understand our measurements and to be able to compare them with theoretical models, we need to experimentally measure some parameters. In fact, we have to know as precisely as possible the volume of the cloud, *i.e.* the trapping volume of our beam, how many atoms it contains and what is their temperature. The following sections describe experimental measurement of these relevant quantities.

#### 1.3.1 The oscillation frequencies

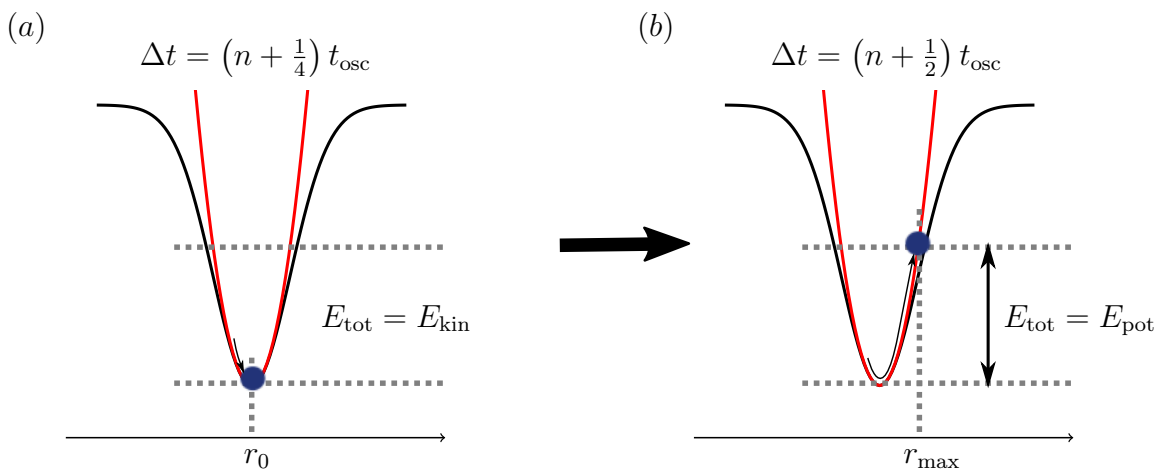


**Figure 1.5.:** (a): The atom is at the bottom of the potential, all its energy is in form of kinetic energy. It happens one fourth of oscillation period  $t_{\text{osc}}$  from its highest point in the trapping potential. (b): The atom's total energy is in form of potential energy.

The measurement of oscillations frequencies of a single atom in an optical dipole trap gives estimations of the waist  $w$  and the Rayleigh range  $z_{\text{R}}$  of the focused Gaussian beam. In other terms, we use the atom to probe the curvature of the trapping potential at its center. Several techniques enable to extract this information. The first technique

used consists in switching off the trap at specific times and measuring the recapture probability of the atom. This idea [Engler et al., 2000] is illustrated in Figure 1.5. In the classical picture, we understand this procedure by considering an atom as a classical particle that oscillates at the bottom of the harmonic potential. When the atom is at the bottom of the potential  $r_0$ , all its energy is in the form of kinetic energy. Therefore, if we switch off the trap at this time  $\Delta t = (n + \frac{1}{4}) t_{\text{osc}}$  or  $\Delta t = (n + \frac{3}{4}) t_{\text{osc}}$ , with  $n = 0, 1, 2, \dots$ , the probability to recapture the atom is small because it will fly away from this position with its highest velocity. On the contrary, when the atom reaches its highest point in the trap  $\pm r_{\text{max}}$ , all its kinetic energy is converted into potential one. In this case, if we switch off the trap at  $\Delta t = nt_{\text{osc}}$  (atom at  $-r_{\text{max}}$ ) or  $\Delta t = (n + \frac{1}{2}) t_{\text{osc}}$  (atom at  $+r_{\text{max}}$ ), it is very likely for the atom to be recaptured as its velocity is zero. The recapture probability as a function of the switching time should be an oscillation at a frequency  $f$ , related to the trapping frequency through the relation  $\omega_r = 2\pi \times (f/2)$ . This first method is not appropriate for the measurement of the axial frequency  $\omega_z$  due to dephasing and atom loss at longer times.

The second technique that we used is called parametric heating. In this one, the trap is not switched off but modulated in amplitude. If the trap amplitude is modulated at twice the oscillation frequency of the atom, the breathing mode, it will gain energy. Above this frequency, the atom will not respond. Classically, we draw an analogy by considering the atom as a particle sitting on a swing and oscillating at its specific frequency. If one gives a kick to the atom when it reaches its highest position on the trajectory, the atom and the swing will get a higher position at the next oscillation. Repeating this kick twice per oscillation, the atom will gain enough energy to finally leave the trapping potential. Thus, measuring the survival probability of the atom in the trap as a function of the modulation frequency of the trap will give the same information as the first technique. This second one has also the advantage to allow observing both the radial and the axial oscillation frequencies.

We will see examples of both methods in chapter 3 where we characterize the optical performances of the aspheric lenses with a single atom in an optical dipole trap.

### 1.3.2 The temperature

The temperature of the cloud can be extracted by time-of-flight imaging as it provides a direct measurement of the momentum distribution of the atoms ([Lett et al., 1988]).

#### Time-of-flight measurement principle

The principle is to measure the position of the atoms after a period of free expansion. The positions of the atoms are obtained by sending a resonant laser beam and collecting

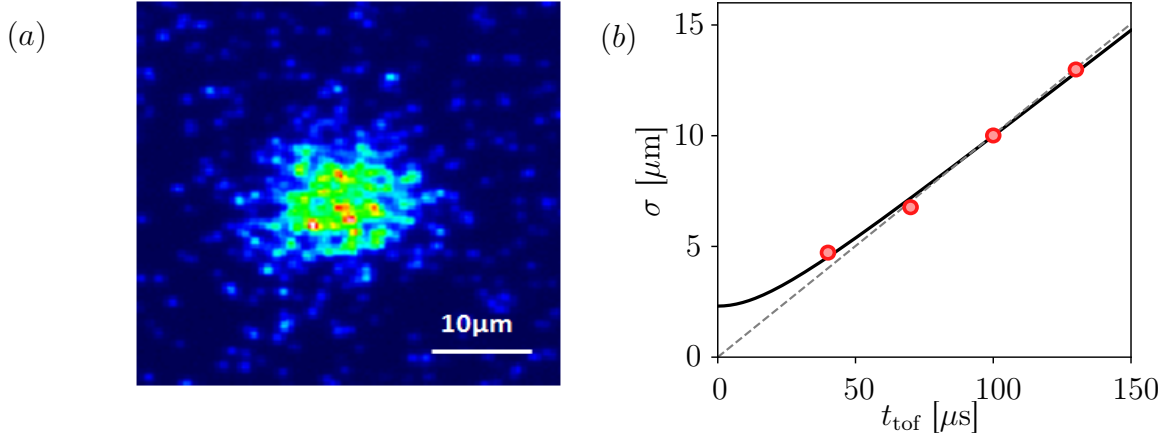


**Figure 1.6.:** (a): Typical fluorescence image of the cloud obtained on the intensified CCD camera after a time of flight of  $70 \mu\text{s}$  (100 repetitions). (b): Measurement of the cloud extension  $\sigma$  as a function of the time of flight  $t_{\text{tof}}$ . The black solid line is a fit from which we extract the *initial cloud size*,  $2.3 \pm 0.5 \mu\text{m}$ , and the extension speed, equals to  $0.10 \text{ m}\cdot\text{s}^{-1}$ . The later corresponds to a temperature of the cloud of  $T = 100 \mu\text{K}$ . The dashed line is a linear fit of the same data, accurate only for long times-of-flight.

their fluorescence on a CCD camera. We measure the size of the cloud  $\sigma$  based on the size of its fluorescence image on the camera (Figure 1.6 (a)) for various released time  $t_{\text{tof}}$ . When the trap light is turned off, the atoms fly apart from each other with a typical speed  $\sigma_v$  that is directly related to their temperature  $T$  through the relation

$$\sigma_v = \sqrt{\frac{k_{\text{B}}T}{m}},$$

with  $m$  the atomic mass of Rubidium.  $\sigma_0$  being the initial size of the cloud, the size of the cloud  $\sigma$  after a time-of-flight of  $t_{\text{tof}}$  is given by

$$\sigma^2(t_{\text{tof}}) = \sigma_0^2 + \sigma_v^2 t_{\text{tof}}^2.$$

When the time-of-flight duration is sufficient to neglect the initial size of the cloud,  $\sigma_v^2 t_{\text{tof}}^2 \gg \sigma_0^2$ , we extract the temperature with the relation

$$\sigma(t_{\text{tof}}) = \sqrt{\frac{k_{\text{B}}T}{m}} t_{\text{tof}}.$$

The temperature of the cloud is thus related to the slope of the asymptote of the curve  $\sigma(t)$  at infinitely long time. To derive these relations, one must assume that the cloud density follows a Gaussian distribution and that interactions between atoms are negligible. These assumptions are verified in our experiments.

### Comments on the time-of-flight imaging

In this section, we will comment on a particular requirement concerning the probe duration when using time-of-flight imaging technique. We also take the opportunity to have a critical look at the initial cloud size value  $\sigma_0$  extracted from the fitting procedure.

**Probe duration** Because we want to measure the position of the atoms, the later has to be changed by less than the resolution of our imaging system during the light pulse. This gives an upper limit on the duration of our probe pulse. Assuming that the resolution of our optical system is around  $1 \mu\text{m}$  and that the temperature of the Rubidium atoms is given by the Doppler temperature  $T_{\text{Doppler}} \approx 150 \mu\text{K}$  which corresponds to an average speed of the atoms of  $0.19 \text{ m}\cdot\text{s}^{-1}$ , the probe pulse needs to be as short as  $8 \mu\text{s}$ . Given the collection efficiency of our imaging system,  $\sim 1\%$ , and a scattering rate  $R \approx \Gamma/2 \approx 2 \times 10^7 \text{ s}^{-1}$ , the number of detected photons per pixels is around 1.5 in single shot, which is less than the read out noise of our CCD camera (around  $3.6 \text{ e}^-/\text{pixel}$ ). The issue has been overcome by inserting an intensifier in front of the CCD camera. For more information about the light-intensified imaging system, see Andreas Fuhrmanek's PHD thesis [Fuhrmanek, 2011].

**The initial cloud size** The value of the initial cloud size given by the fit (Figure 1.6 (b)) is an order of magnitude higher than the expected radial size of a cloud of non interacting atoms in equilibrium and trapped in an harmonic potential. Indeed, for a trap depth of  $1 \text{ mK}$ , a transverse size of the beam of  $1.2 \mu\text{m}$  and a temperature of the cloud of  $100 \mu\text{K}$ , the radial extension is given by (1.14):  $0.2 \mu\text{m}$ . This value is below the diffraction limit of our optical system ( $0.5 \mu\text{m}$ ), thus one would expect a convolution of those two values and an initial size around  $0.6 \mu\text{m}$ . It is nonetheless below the extracted value by a factor  $\sim 3-4$ . The reason is that various elements spread the response of each single atom on our CCD camera, the first one being the intensifier. Other experimental imperfections can play a role, like the depth of focus for instance. By convolution, all those different elements lead to a highly overestimated initial size of our cloud.

**Conclusion** The estimation of the temperature remains nonetheless accurate as one mainly looks at long time-of-flights, where the relation between the size of the cloud and the temperature of the atoms is independent of the initial cloud size.

#### 1.3.3 The number of atoms

Another important quantity that we measure is the number of atoms in the trap. This quantity is of crucial importance when one wants to determine the density of the cloud. The estimation of the number of atoms is based on a calibration measurement with a single atom. When the loss rate compensates the loading rate in the dipole trap, we enter the single atom regime. In this regime, there exists an effect called the collisional

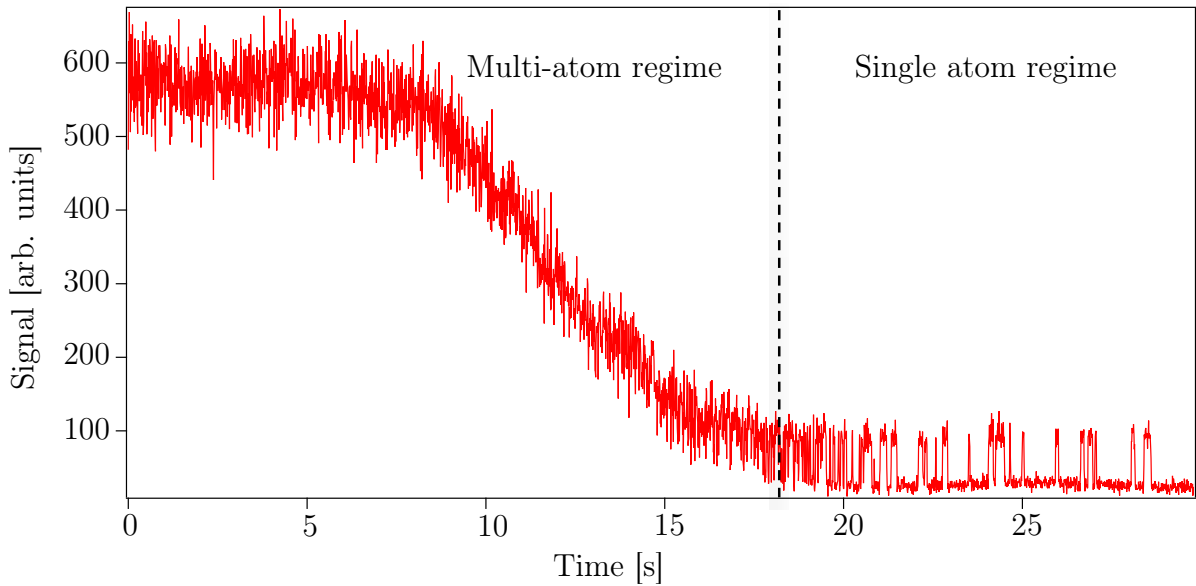


**Figure 1.7.:** Measurement of the fluorescence light scattered by the trapped atoms. The scattered light is collected into an avalanche photodiode connected to a photon counting module. At  $t = 0$  s, the atomic density in the MOT is such that the loading rate  $R$  is bigger than the two-body loss rate: it is the multi-atom regime. At  $t = 7.5$  s, the current in the MOT coils is ramped down. The atomic density in the MOT starts to decrease. Less and less atoms are trapped in the optical tweezer, then the fluorescence signal decreases as well. At  $t = 19$  s, the signal is alternating between two discrete values: low when no atoms are present, high when a single atom is trapped in the optical tweezer. This signal is an experimental signature that the single atom regime has been reached. Figure extracted from [Béguin, 2013].

blockade [Schlosser et al., 2002] that prevents a second atom to enter the trap. If such an event occurs, both atoms, the one initially present in the trap and the incoming one, are expelled from the trap. Therefore, we only have one or zero atom in the trap. Experimentally, we have a signature of this regime by measuring the temporal fluorescence signal that will display a *step*-signal alternating between two values, low for no atom and high when one is present (see Figure 1.7), or, equivalently, by measuring the counting events histogram on the CCD camera. When no atom is in the trap, we only collect background events on the CCD chip. When an atom is present, it scatters photons due to the MOT beams and thus the mean value of the distribution on the camera increases. The distribution of detected events when an atom is in the trap is a Poisson distribution. We then extract a mean number of photons scattered by a single atom when a resonant probe of duration  $\Delta t$  is shined onto it. This calibrated value is then used when the averaged number of atoms is unknown.

When several atoms are in the trap, we switched off the trap to let the cloud expand and then we send the probe beam of duration  $\Delta t$  and we collect the scattered photons on

the CCD camera. The time-of-flight introduced before the probe beam is to ensure that no interaction is present between the atoms, that would modify their fluorescence rate, thus that we can sum their individual fluorescence. Assuring ourselves of the linearity of the counting device, we measure directly the number of atoms in the trap by computing the ratio of the number of collected photons in this measurement with the one collected when only a single atom was present in the trap.

### **1.3.4 Conclusion**

We have presented here some basic techniques that we will use and illustrate by examples from the experiment in the rest of the manuscript.



# CHAPTER 2

## NEAR-RESONANT LIGHT TRANSMISSION THROUGH A DENSE CLOUD OF TWO-LEVEL ATOMS

---

### Contents

---

<b>2.1. Light scattering</b> . . . . .	<b>24</b>
2.1.1. Interaction between light and an ensemble of atoms . . . . .	25
2.1.2. The Incoherent and Coherent fields . . . . .	28
Experimental quantities measured . . . . .	29
Coherent transfer function . . . . .	32
Incoherent transfer function . . . . .	33
<b>2.2. Previous results</b> . . . . .	<b>33</b>
2.2.1. Incoherent scattering . . . . .	33
2.2.2. Coherent scattering . . . . .	35
2.2.3. Conclusion . . . . .	44
<b>2.3. Transmission through a dense cloud of cold two-levels atoms</b>	<b>45</b>
2.3.1. Polarization of the sample: towards two-level atoms . . . . .	45
Choice of the value of $\mathbf{B}$ field . . . . .	46
Interaction with a static magnetic field . . . . .	47
2.3.2. Experimental sequence . . . . .	49
2.3.3. Experimental results . . . . .	50
Temporal measurement . . . . .	50
Steady-state regime . . . . .	51
Conclusion . . . . .	52

<b>2.4. Comparison between theory and experiment . . . . .</b>	<b>53</b>
2.4.1. The coupled-dipoles model . . . . .	53
As a function of the number of atoms . . . . .	54
As a function of the temperature of the cloud . . . . .	55
As a function of the trap volume . . . . .	56
Conclusion . . . . .	57
2.4.2. Coupled-dipoles model with atomic motion . . . . .	57
Including motion into the coupled-dipoles model . . . . .	57
Simulation procedure . . . . .	59
Simulations results . . . . .	60
Conclusion . . . . .	60
2.4.3. A new model to tackle the high intensity regime . . . . .	61
Maxwell-Bloch equations in the low intensity regime . . . . .	61
Connection with the experimental measurement . . . . .	62
Steady-state solution . . . . .	63
Maxwell-Bloch equations in the high intensity regime . . . . .	64
<b>2.5. Conclusion . . . . .</b>	<b>65</b>

---

In this second chapter, I will present several measurements performed in our group and related to the diffusion of light by a cigar-shaped cloud of cold Rubidium atoms. Then, I will present the latest results we obtained: the transmission of light through a dense cloud of cold *two-level* atoms. The end of the chapter is dedicated to simulations. It will be the opportunity to present an attempt to understand the remaining discrepancies between the coupled-dipoles theory and our experimental results by addressing the role of the atomic motion, and to introduce a new model, developed by Pierre Pillet, to describe dipole-dipole interactions but not restricted to the weak driving limit. The goal of the chapter is to point out the difficulty to understand quantitatively the behavior of an apparently as simple system as the one we are studying in our experiment, even though we carefully prepared it in its closest form to the theoretical description.

## 2.1 LIGHT SCATTERING

Before presenting our previous and our latest results, we have to define some concepts concerning light scattering by an ensemble of atoms.

### 2.1.1 Interaction between light and an ensemble of atoms

**One atom** First of all, what happens when we shine light onto *one* atom? A very fruitful description of the atom as a classical damped harmonic oscillator enables to determine how light is scattered. We consider an atom of mass  $m$  as a system composed of a nucleus and a single electron of charge  $q$ , the electron being attached to the nucleus with an harmonic potential. If we shine an electromagnetic field  $E(r, \omega_L)$  onto it, the equation of motion of the electron in the referential frame of the nucleus is

$$m\ddot{x} = qE(r, \omega_L) - m\Gamma\dot{x} - m\omega_0^2x,$$

where  $x$  denotes the relative distance between the electron and the nucleus,  $\Gamma$  is a dissipation term responsible for the damping and  $\omega_0$  is the resonant frequency of the system. In the near resonant limit,  $\omega_L \sim \omega_0$ , the dipole moment  $d(t) = qx(t)$  has a stationary expression given by

$$d_{\text{st}} = -i \frac{qE_0}{2m\omega_0} \frac{1}{i\Delta - \Gamma/2},$$

where  $\Delta = \omega_L - \omega_0$ . This expression can be derived quantum mechanically and we would have obtained

$$d_{\text{st}} = \epsilon_0 \alpha(\omega) E_0,$$

with the atomic polarizability  $\alpha$  given by

$$\alpha(\omega) = \frac{6\pi i}{k^3} \frac{1}{1 - \frac{2i\Delta}{\Gamma}}. \quad (2.1)$$

This expression, valid in the weak-driving limit, is telling us that the induced dipole is proportional to the driving field, its response having a Lorentzian shape centered on  $\omega_0$  with a width  $\Gamma$ . Note that a two-level atom has a classical equivalent: it can be described by the relation

$$\mathbf{d} = \epsilon_0 [\alpha] \mathbf{E},$$

with an anisotropic polarization tensor  $[\alpha]$  given by

$$[\alpha] = \begin{bmatrix} \alpha(\omega) & 0 & 0 \\ 0 & 0 & 0 \\ 0 & 0 & 0 \end{bmatrix}.$$

**Two atoms** Now consider two atoms. The previous classical picture can still be applied if we consider these two atoms as two coupled harmonic oscillators. The interaction between the induced dipoles is called the dipole-dipole interaction. To be more precise, we consider here the *resonant* dipole-dipole interaction where the interaction between atoms is mediated by the dipole field. We do not consider here the

*non-resonant* dipole-dipole interaction, also called the van der Waals interaction, where two atoms in the same state can interact. The description of the later usually introduce the exchange of virtual photons with the vacuum field and does not have a classical analog ([Cohen-Tannoudji et al., 2018]). If we consider a dipole  $\mathbf{d}_1 = d_1 \hat{\mathbf{e}}$  located in  $\mathbf{r}_1$ , it will emit a field at position  $r = |\mathbf{r}|$  given by [Jackson, 1999]

$$\mathbf{E}_1(r) = \frac{k^3 d_1}{4\pi\epsilon_0} \frac{e^{ikR}}{(kR)^3} [(3(\hat{\mathbf{u}} \cdot \hat{\mathbf{e}})\hat{\mathbf{u}} - \hat{\mathbf{e}})(1 - ikR) + (\hat{\mathbf{u}} \times \hat{\mathbf{e}}) \times \hat{\mathbf{u}}(kR)^2], \quad (2.2)$$

where  $\hat{\mathbf{u}}$  is the unit vector in the direction of  $\mathbf{r} - \mathbf{r}_1$ ,  $\hat{\mathbf{e}}$  is the polarization vector of the dipole and  $R = |\mathbf{r} - \mathbf{r}_1|$ . A detailed derivation of (2.2) can be found in Appendix A. Another dipole  $\mathbf{d}_2$  located at  $\mathbf{r}_2$  will feel the sum of the external field  $\mathbf{E}_L$  and the field radiated by the first dipole  $\mathbf{E}_1(r_2)$ . The two dipoles being coupled together, their resonant frequencies and decay rates are modified. In the weak driving limit and in the rotating wave approximation, the coupled system governing the two dipoles is

$$\begin{cases} \dot{\mathbf{d}}_1 = (i\Delta - \Gamma/2)\mathbf{d}_1 + i\frac{3\pi\epsilon_0\Gamma}{k^3}[\mathbf{E}_L(r_1) + \mathbf{E}_2(r_1)], \\ \dot{\mathbf{d}}_2 = (i\Delta - \Gamma/2)\mathbf{d}_2 + i\frac{3\pi\epsilon_0\Gamma}{k^3}[\mathbf{E}_L(r_2) + \mathbf{E}_1(r_2)]. \end{cases}$$

By projecting this set of coupled equations onto the complex conjugate of the polarization vector of the dipoles  $\hat{\mathbf{e}}^*$  we obtain

$$\begin{cases} \dot{d}_1 = (i\Delta - \Gamma/2)d_1 + i\frac{3\pi\epsilon_0\Gamma}{k^3}\mathbf{E}_L(r_1) \cdot \hat{\mathbf{e}}^* - \frac{i}{\hbar}V_{21}d_2, \\ \dot{d}_2 = (i\Delta - \Gamma/2)d_2 + i\frac{3\pi\epsilon_0\Gamma}{k^3}\mathbf{E}_L(r_2) \cdot \hat{\mathbf{e}}^* - \frac{i}{\hbar}V_{12}d_1, \end{cases}$$

with  $V_{12} = V_{21} = V$  the dipole-dipole interaction term between the two atoms. Its expression, in this particular case, is given by

$$V = -\frac{3}{4} \frac{\hbar\Gamma}{(kR_{12})^3} [(3|\hat{\mathbf{r}}_{12} \cdot \hat{\mathbf{e}}|^2 - 1)(1 - ikR_{12}) + (1 - |\hat{\mathbf{r}}_{12} \cdot \hat{\mathbf{e}}|^2)(kR_{12})^2] \exp(ikR_{12}), \quad (2.3)$$

where  $\hat{\mathbf{r}}_{12}$  is the unit vector in the direction of  $\mathbf{r}_2 - \mathbf{r}_1$  and  $R_{12}$  its norm. We solve the set of these two coupled equations in the coupling basis  $d_{\pm} = (d_1 \pm d_2)/\sqrt{2}$ . Summing the two previous equations, one obtains

$$\dot{d}_{\pm} = (i\Delta - \Gamma/2)d_{\pm} + i\frac{3\pi\epsilon_0\Gamma}{k^3} \frac{[\mathbf{E}_L(r_1) \pm \mathbf{E}_L(r_2)] \cdot \hat{\mathbf{e}}^*}{\sqrt{2}} \mp \frac{i}{\hbar}Vd_{\pm}.$$

Finally, splitting the real part and the imaginary part of the interaction potential, one gets

$$\dot{d}_{\pm} = \left[ i(\Delta - \omega_{\pm}) - \left( \frac{\Gamma}{2} - \Gamma_{\pm} \right) \right] d_{\pm} + i\frac{3\pi\epsilon_0\Gamma}{k^3} \frac{[\mathbf{E}_L(r_1) \pm \mathbf{E}_L(r_2)] \cdot \hat{\mathbf{e}}^*}{\sqrt{2}},$$

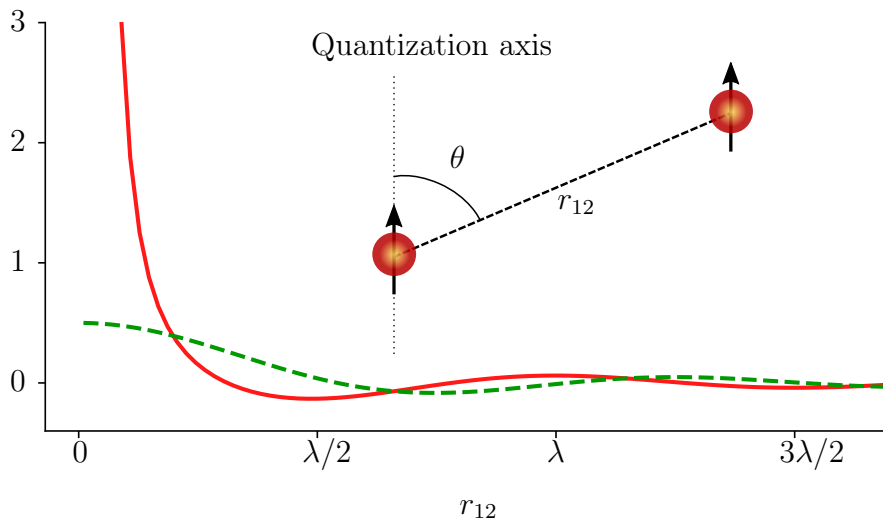


**Figure 2.1.:** Calculation of the frequency shift  $\omega_+$  (red solid line) and the decay rate modification  $\Gamma_+$  (green dotted line) in unit of  $\Gamma$  for two atoms, linearly polarized along the quantization axis with  $\theta = 20^\circ$  (arbitrary case).

where

$$\omega_{\pm} = \pm \frac{\text{Re}\{V\}}{\hbar},$$

$$\Gamma_{\pm} = \pm \frac{\text{Im}\{V\}}{\hbar}.$$

We show that the coupled dipoles solutions  $d_{\pm}$  resonant frequencies are shifted by a quantity  $\omega_{\pm}$  and their decay rates are modified by a quantity  $\Gamma_{\pm}$  (see Figure 2.1 for instance) that depends respectively on the strength of the real and imaginary parts of the dipole-dipole interaction potential.  $d_{\pm}$  are called the eigenstates of the system, characterized by their eigenvalues, the resonant frequency and the decay rate.

**Ensemble of atoms** The study can be extended to an ensemble of atoms. Considering the system as an ensemble of coupled radiators ([Javanainen et al., 1999]), this approach gives a set of closed equations describing the total external field driving each atom. Basically, each dipole  $\mathbf{d}_j$  located at  $\mathbf{r}_j$ , feels the external driving field  $\mathbf{E}_L$  and the sum of all the fields emitted by all the others dipoles  $\sum_{l \neq j} \mathbf{E}_l(\mathbf{r}_j)$

$$\mathbf{E}(\mathbf{r}_j) = \mathbf{E}_L(\mathbf{r}_j) + \sum_{l \neq j} \mathbf{E}_l(\mathbf{r}_j),$$

with  $\mathbf{E}_l(\mathbf{r}_j)$  given by (2.2). In the following, we will note  $\mathbf{E}_{l \rightarrow j}$  the field emitted by dipole  $l$  at the location of dipole  $j$ . We then compute the amplitude of each dipole  $j$  which in

steady-state is equal to

$$\mathbf{d}_j = \epsilon_0 \alpha(\omega) \left[ \mathbf{E}_L + \sum_{l \neq j} \mathbf{E}_{l \rightarrow j} \right], \quad (2.4)$$

where we have assigned a polarizability  $\alpha(\omega)$  to each atom (cf. (2.1)).

The complex amplitude  $d_j = |\mathbf{d}_j| = \mathbf{d}_j \cdot \hat{\mathbf{e}}^*$  of the dipoles, with  $\hat{\mathbf{e}}^*$  the complex conjugate of the polarization vector  $\mathbf{e}$ , are solutions of the following set of coupled equations, obtained by inserting (2.1) into (2.4)

$$\left( i\Delta - \frac{\Gamma}{2} \right) d_j = -i \frac{3\pi\epsilon_0\Gamma}{k^3} \mathbf{E}_L \cdot \hat{\mathbf{e}}^* + i \sum_{l \neq j}^N \frac{V_{jl}}{\hbar} d_l, \quad (2.5)$$

with  $V_{jl}$  the dipole-dipole interaction term. Its expression depends on the polarization of the dipoles and is given by (2.3), replacing 1 and 2 by  $j$  and  $l$ . The coupled system can be solved numerically, that is what we called the coupled-dipoles simulations. The result gives access to the field everywhere in space thanks to the superposition principle

$$\mathbf{E}(\mathbf{r}) = \mathbf{E}_L(\mathbf{r}) + \sum_j \mathbf{E}_j(\mathbf{r}) = \mathbf{E}_L(\mathbf{r}) + \mathbf{E}_{\text{sc}}(\mathbf{r}).$$

In practice, in our experiment, we consider the scattered field  $\mathbf{E}_{\text{sc}}$  in the plane of the aspheric lens, used to both trap and image the atoms. The focal length of our aspherical lens being 8 mm (working distance of  $\sim 5.7$  mm), the distance between the cloud and the lens is 10000 times bigger than the transition wavelength of the D2 line of  $^{87}\text{Rb}$ . Therefore, the scattered field is calculated in the far-field

$$\mathbf{E}_{\text{sc}} \approx \frac{k^2}{4\pi\epsilon_0} \sum_{j=1}^N [(\hat{\mathbf{u}}_j \times \hat{\mathbf{e}}) \times \hat{\mathbf{u}}_j] \frac{d_j}{R_j} e^{ikR_j}, \quad (2.6)$$

where  $\mathbf{R}_j = R_j \hat{\mathbf{u}}_j$  is the vector between atom  $j$  and the position of observation in the plane of the aspheric lens.

### 2.1.2 The Incoherent and Coherent fields

In our experiment, the total field emitted by the cloud is focused by our high-NA aspheric lens onto a single-mode fiber connected to an avalanche photodiode. Therefore, the quantity that we measure is the overlap of the total field  $\mathbf{E}$  with the mode of the fiber  $\mathbf{g}$ , integrated over the lens area (the lens only capture a fraction of the total solid

angle). Depending on whether the driving field is collected by our aspherical lens or not, we have access to two different parts of the scattered field: the *incoherent* or the *coherent* scattering.

When the cloud is defined as a homogeneous medium described by a susceptibility  $\chi$ , the scattered field can be decomposed into two parts:

- the *coherent* part, denoted  $\langle \mathbf{E}_{\text{sc}} \rangle$ , is governed by macroscopic Maxwell's equations and corresponds to the value of the scattered field averaged over many spatial configurations of the atoms in the cloud,
- the *incoherent* part,  $\delta \mathbf{E}_{\text{sc}}$ , corresponds to fluctuations of the scattered field around its mean value. This quantity is not governed by macroscopic Maxwell's equations [Durant et al., 2007] and could therefore not be compared to mean field predictions.

Let us first focus on the measurement of the *coherent* part of the scattered field.

### Experimental quantities measured

In order to be able to measure the *coherent* part of the scattered field, we measure the interference of the laser field and the field scattered by the cloud in the direction of propagation of the excitation laser

$$\begin{aligned} \mathbf{E} &= \mathbf{E}_{\text{L}} + \mathbf{E}_{\text{sc}} \\ &= \mathbf{E}_{\text{L}} + \langle \mathbf{E}_{\text{sc}} \rangle + \delta \mathbf{E}_{\text{sc}}. \end{aligned} \quad (2.7)$$

To be more precise, the actual field measured is the overlap of the field  $\mathbf{E}$  with the mode  $\mathbf{g}$  of the single-mode fiber into which the light is coupled. We note this quantity  $\mathcal{E}$  defined as

$$\mathcal{E}(\omega) = \int \mathbf{E}(\mathbf{r}, \omega) \cdot \mathbf{g}^*(\mathbf{r}) \, dS, \quad (2.8)$$

where  $dS$  is a differential area surface orthogonal to the optical axis, the propagation axis of the laser beam. The mode of the single-mode fiber is a  $\text{TEM}_{00}$  and we make the incoming beam  $\mathbf{E}_{\text{L}}$  mode matched the one of the fiber so that the quantity  $\mathcal{E}$  can be written as

$$\mathcal{E}(\omega) = \int \mathbf{E}(\mathbf{r}, \omega) \cdot \mathbf{E}_{\text{L}}^*(\mathbf{r}) \, dS. \quad (2.9)$$

We now insert (2.7) into (2.9) to obtain

$$\mathcal{E}(\omega) = \int (\mathbf{E}_{\text{L}} + \langle \mathbf{E}_{\text{sc}} \rangle) \cdot \mathbf{E}_{\text{L}}^* \, dS + \int \delta \mathbf{E}_{\text{sc}} \cdot \mathbf{E}_{\text{L}}^* \, dS. \quad (2.10)$$

The experimental quantity is a configuration average of the modulus square of (2.10)

$$\begin{aligned}
 \langle |\mathcal{E}(\omega)|^2 \rangle &\propto \left\langle \left| \int (\mathbf{E}_L + \langle \mathbf{E}_{sc} \rangle) \cdot \mathbf{E}_L^* dS \right|^2 \right\rangle + \left\langle \left| \int \delta \mathbf{E}_{sc} \cdot \mathbf{E}_L^* dS \right|^2 \right\rangle \\
 &+ \left\langle \int (\mathbf{E}_L + \langle \mathbf{E}_{sc} \rangle)^* \cdot \mathbf{E}_L dS \int \delta \mathbf{E}_{sc} \cdot \mathbf{E}_L^* dS \right\rangle \\
 &+ \left\langle \int (\mathbf{E}_L + \langle \mathbf{E}_{sc} \rangle) \cdot \mathbf{E}_L^* dS \int \delta \mathbf{E}_{sc}^* \cdot \mathbf{E}_L dS \right\rangle. \tag{2.11}
 \end{aligned}$$

In (2.11) the first term of the right-hand-side (RHS) does not depend on the spatial configuration of the atoms in the cloud, therefore the  $\langle \cdot \rangle$  can be omitted. In the same way, the third and fourth term (which is only the complex conjugate of the third one) can be simplified since the first integral is independent of the spatial configuration. For instance, with the third term, it gives

$$\begin{aligned}
 &\left\langle \int (\mathbf{E}_L + \langle \mathbf{E}_{sc} \rangle)^* \cdot \mathbf{E}_L dS \int \delta \mathbf{E}_{sc} \cdot \mathbf{E}_L^* dS \right\rangle, \\
 &= \int (\mathbf{E}_L + \langle \mathbf{E}_{sc} \rangle)^* \cdot \mathbf{E}_L dS \left\langle \int \delta \mathbf{E}_{sc} \cdot \mathbf{E}_L^* dS \right\rangle \\
 &= \int (\mathbf{E}_L + \langle \mathbf{E}_{sc} \rangle)^* \cdot \mathbf{E}_L dS \int \langle \delta \mathbf{E}_{sc} \cdot \mathbf{E}_L^* \rangle dS,
 \end{aligned}$$

and since  $\delta \mathbf{E}_{sc}$  and  $\mathbf{E}_L^*$  are independent and  $\langle \delta \mathbf{E}_{sc} \rangle = 0$  by definition,

$$\begin{aligned}
 &= \int (\mathbf{E}_L + \langle \mathbf{E}_{sc} \rangle)^* \cdot \mathbf{E}_L dS \int \langle \delta \mathbf{E}_{sc} \rangle \cdot \langle \mathbf{E}_L^* \rangle dS, \\
 &= 0.
 \end{aligned}$$

Therefore (2.11) simplifies to

$$\langle |\mathcal{E}(\omega)|^2 \rangle \propto \underbrace{\left| \int (\mathbf{E}_L + \langle \mathbf{E}_{sc} \rangle) \cdot \mathbf{E}_L^* dS \right|^2}_{|\mathcal{E}_{coh}(\omega)|^2} + \underbrace{\left\langle \left| \int \delta \mathbf{E}_{sc} \cdot \mathbf{E}_L^* dS \right|^2 \right\rangle}_{\langle |\mathcal{E}_{incoh}(\omega)|^2 \rangle} \tag{2.12}$$

As mentioned in (2.12), we denote the coherent intensity  $|\mathcal{E}_{coh}(\omega)|^2$  and the incoherent intensity (configuration averaged)  $\langle |\mathcal{E}_{incoh}(\omega)|^2 \rangle$ .

Now we will focus on how we can measure each part of the  $\langle |\mathcal{E}(\omega)|^2 \rangle$  quantity. For our particular system, it turns out that  $|\mathcal{E}_{coh}(\omega)|^2 \gg \langle |\mathcal{E}_{incoh}(\omega)|^2 \rangle$  in the direction of propagation of the laser (see the numerical simulations presented in Figure 2.2). To

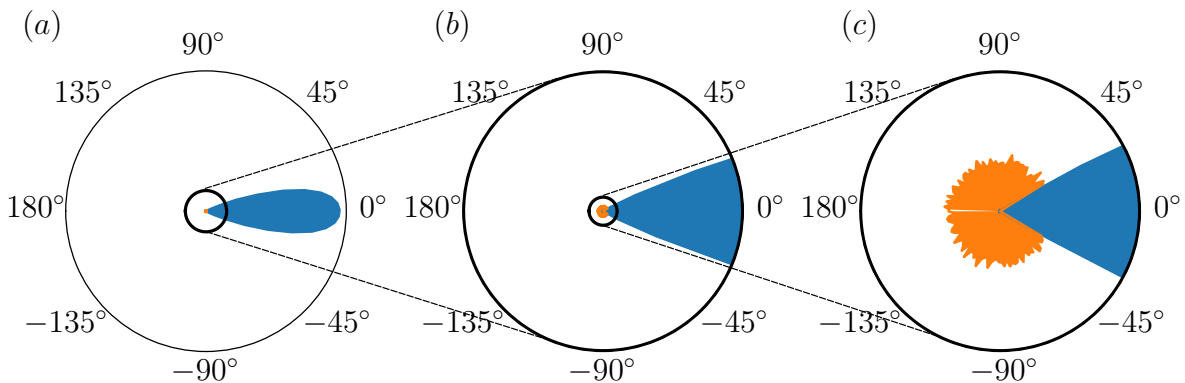


**Figure 2.2.:** Numerical simulations of the coherent (in blue) and incoherent intensity (in orange) emission pattern in polar coordinates. The simulations are performed with a cloud of 180 atoms, at  $100 \mu\text{K}$ , in a Gaussian trap of waist  $1.6 \mu\text{m}$  and  $1.0 \text{mK}$  trap depth. They are repeated 200 times to average the atomic distribution. As explained in the text, the coherent response dominates in the forward direction (a). (b): zoom ( $\times 6$ ) on the pattern emission (a). (c): zoom ( $\times 10$ ) on the pattern emission (b).

understand this result we introduce the form factor  $F$  of the cloud which characterizes the coherent response. It is defined by

$$F(\mathbf{q}) = \frac{1}{N} \int_{\mathcal{V}} n(\mathbf{r}') \exp(-i\mathbf{q} \cdot \mathbf{r}') d^3\mathbf{r}', \quad (2.13)$$

where  $N$  is the number of atoms,  $\mathbf{q} = \mathbf{k} - \mathbf{k}_L$  with  $\mathbf{k}$  the wavevector of emission and  $\mathbf{k}_L$  the wavevector of the laser beam, and  $n$  the density of the cloud, the integration being performed on the cloud volume  $\mathcal{V}$ . Using cylindrical coordinates and assuming that the cloud density follows a Gaussian distribution with a transverse width  $\sigma_{\perp}$  and a longitudinal width  $\sigma_z$ , the integral (2.13) is equal to

$$F(\Psi) = \exp\left(-\frac{1}{2}\sigma_{\perp}^2 k^2 \sin^2 \Psi\right) \times \exp\left(-\frac{1}{2}\sigma_z^2 k^2 (\cos \Psi - 1)^2\right), \quad (2.14)$$

where we have introduced  $\Psi$ , the angle between the direction of emission of the light with respect to the direction of propagation of the laser beam, and used  $\|\mathbf{k}_L\| = \|\mathbf{k}\| = k$ . For a typical temperature of our atoms around  $150 \mu\text{K}$ , (2.14) gives  $\sigma_{\perp} \approx 0.3\lambda$  and  $\sigma_z \approx 1.7\lambda$ . As  $\sigma_z$  is almost a factor 6 bigger than  $\sigma_{\perp}$ , (2.14) is telling us that  $F$ , and thus the coherent response, is peaked in the direction where  $(\cos \Psi - 1)^2 = 0$ , which is  $\Psi = 0$ , the direction of propagation of the laser. Contrarily, the incoherent response would be scattered isotropically. Therefore,  $|\mathcal{E}_{\text{coh}}(\omega)|^2 / \langle |\mathcal{E}_{\text{incoh}}(\omega)|^2 \rangle \gg 1$  in the forward direction.

### Coherent transfer function

The total transfer function, denoted  $S_{\text{tot}}(\omega)$ , is defined as the ratio between  $\mathcal{E}(\omega)$  in presence of atoms with the same quantity without atoms. In absence of atoms, the total field  $\mathbf{E}$  is simply the laser field  $\mathbf{E}_L$  and we note this quantity  $\mathcal{E}_L$ . Explicitly, the total transfer function is equal to

$$S_{\text{tot}} = \frac{\mathcal{E}(\omega)}{\mathcal{E}_L} = \frac{\int \mathbf{E}(\mathbf{r}, \omega) \cdot \mathbf{E}_L^*(\mathbf{r}) dS}{\int |\mathbf{E}_L(\mathbf{r})|^2 dS}. \quad (2.15)$$

We also introduce the coherent transfer function  $S(\omega)$ , given by the average of  $S_{\text{tot}}(\omega)$  over many realizations of the spatial configuration of the atoms in the cloud

$$S(\omega) = \frac{\langle \mathcal{E}(\omega) \rangle}{\mathcal{E}_L} = \frac{\int (\mathbf{E}_L + \langle \mathbf{E}_{\text{sc}} \rangle) \cdot \mathbf{E}_L^* dS}{\int |\mathbf{E}_L|^2 dS} = 1 + \frac{\int \langle \mathbf{E}_{\text{sc}} \rangle \cdot \mathbf{E}_L^* dS}{\int |\mathbf{E}_L|^2 dS}, \quad (2.16)$$

where we have omitted the dependence in  $\mathbf{r}$  and  $\omega$  for clarity. This quantity is called the *coherent* transfer function because  $|S(\omega)|^2 \propto |\mathcal{E}_{\text{coh}}(\omega)|^2$ , as defined in (2.12).

### Difference between the coherent transfer function and the usual transmission

Here, we would like to point out a subtle difference between the quantity that we have defined, the coherent optical transfer function  $S(\omega)$ , and the transmission, denoted  $T(\omega)$  in this section. Generally speaking, the transmission of the cloud is defined as

$$T(\omega) = \frac{\langle \int |\mathbf{E}(\mathbf{r}, \omega)|^2 dS \rangle}{\int |\mathbf{E}_L(\mathbf{r})|^2 dS}. \quad (2.17)$$

If the solid angle of collection of the lens is very small, the transmission  $T(\omega)$  coincide with  $|S_{\text{tot}}|^2$ . Otherwise, you can link  $T(\omega)$  with the coherent transfer function by decomposing the total field  $\mathbf{E} = \mathbf{E}_L + \langle \mathbf{E}_{\text{sc}} \rangle + \delta \mathbf{E}_{\text{sc}}$  and you will get

$$T(\omega) = |S(\omega)|^2 - \left| \frac{\int \langle \mathbf{E}_{\text{sc}} \rangle \cdot \mathbf{E}_L^* dS}{\int |\mathbf{E}_L|^2 dS} \right|^2 + \frac{\int |\langle \mathbf{E}_{\text{sc}} \rangle|^2 dS}{\int |\mathbf{E}_L|^2 dS} + \frac{\int \langle |\delta \mathbf{E}_{\text{sc}}|^2 \rangle dS}{\int |\mathbf{E}_L|^2 dS}.$$

Using Cauchy-Schwarz inequality

$$\left| \int \langle \mathbf{E}_{\text{sc}} \rangle \cdot \mathbf{E}_L^* dS \right|^2 \leq \int |\langle \mathbf{E}_{\text{sc}} \rangle|^2 dS \int |\mathbf{E}_L|^2 dS,$$

it yields to

$$|S(\omega)|^2 \leq T(\omega).$$

The coherent transfer function is the quantity that our group has measured and which is used in subsection 2.2.2 and subsection 2.3.3.

### Incoherent transfer function

Now, if we are not measuring directly in the direction of propagation of the laser but orthogonality to its wavevector direction, then the coherent part  $|\mathcal{E}_{\text{coh}}(\omega)|^2$  is no longer dominant and we are mainly sensitive to the incoherent part  $\langle |\mathcal{E}_{\text{incoh}}(\omega)|^2 \rangle$  (see (2.12)). No normalization is needed since that in the absence of atoms, no light should be collected by the aspherical lens. The incoherent scattering of a dense cloud of cold atoms has been measured by our group and is discussed in subsection 2.2.1. Although, it has been measured not through the overlap of the scattered field with the mode of a single-mode fiber but by collection on a intensified CCD-camera, i.e., without being able to resolve the dynamics of the optical response.

## 2.2 PREVIOUS RESULTS

The experimental study of dipole-dipole interactions in dense ensemble of cold atoms started a few years ago in our group. It was known theoretically that when a collection of emitters are confined inside a volume smaller than  $\lambda^3 = (\lambda/2\pi)^3$ , with  $\lambda$  the transition wavelength, they are coupled via dipole-dipole interaction and their response to a near-resonant light is collective ([Dicke, 1954], [Li et al., 2013], [Scully, 2009]). This effect originates from the excitation of collective eigenstates of the system. Thus, the response of the system differs from the case of non-interacting emitters. Our group decided to show experimentally the influence of these interactions on the optical response of a cloud of cold atoms. However, no quantitative agreement between theory and experiment has been observed yet in the dense regime. The purpose of this section is to remind the experimental results obtained previously in our group as well as the theoretical models that have been used to try to explain them.

### 2.2.1 Incoherent scattering

The information of this section can be found in [Pellegrino et al., 2014]. Let us first remind quickly the experimental procedure. Starting from a MOT, we loaded between 1 and  $\sim 450$  cold  $^{87}\text{Rb}$  atoms in a single-beam optical dipole trap of waist  $1.6 \mu\text{m}$ , wavelength  $957 \text{ nm}$  and trap depth equals to  $1 \text{ mK}$ . Initially prepared in the  $(5S_{1/2}, F = 2)$  manifold, the trap is switched off and a low-intensity ( $I/I_{\text{sat}} = 0.1$ ), near-resonant with the D2 line transition,  $\sigma_+$ -polarized excitation laser is sent *orthogonally* to the trapping axis. We alternate excitation pulses of  $125 \text{ ns}$  with recapture periods in the dipole trap of  $1 \mu\text{s}$ . This sequence is repeated 200 times with the same cloud, and averaged over 100 different cloud configurations. The temperature of the cloud (initially  $\sim 100 \mu\text{K}$ ) remained unchanged within 5% over the entire procedure. Moreover, less than 5% of the atoms initially in the trap were depumped in the  $(5S_{1/2}, F = 1)$  hyperfine level during the excitation. The last two points are important as they could have resulted in a decrease of the density. Finally, the photons scattered by the cloud are collected by

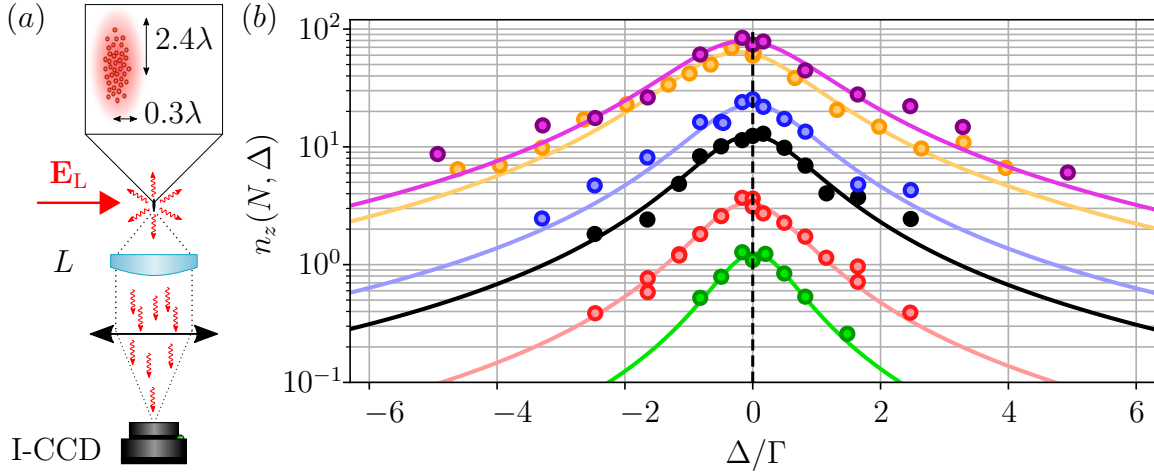


**Figure 2.3.:** (a): Experimental setup. The atoms are initially confined inside an optical dipole trap (not shown) of waist  $1.6 \mu\text{m}$  ( $\lambda = 957 \text{ nm}$ , trap-depth  $1 \text{ mK}$ ). The excitation laser  $\mathbf{E}_L$  propagates along the quantization axis  $x$  defined by a small magnetic field  $B \sim 1 \text{ G}$ . The scattered light emitted along the  $z$  axis is collected by a high-NA aspheric lens  $L$  before being recorded on an intensified CCD camera (I-CCD). (b): Scattered light detected  $n_z(N, \Delta)$  versus detuning  $\Delta$  of the excitation light for various numbers of atoms  $N = 1, 5, 20, 50, 325, 450$  (from bottom to top). The amplitudes of the curves are normalized to the amount of light detected at resonance for the single atom case  $n_z(N = 1, \Delta = 0)$ . The solid lines are Lorentzian fit of the data. Typical uncertainties are 10% vertically and 20% horizontally. The figure is extracted from [Pellegrino et al., 2014].

the aspherical lens (NA= 0.5) that has been used to focused to optical dipole trap and are measured by an intensified CCD camera.

Starting from a single atom case, we observe a broadening of the line when the number of atoms increases, as well as a small red shift with respect to the non-interacting case. The broadening of the line can be understood qualitatively by considering that the more atoms there are in the dipole trap, the smaller the distance between them, thus the stronger the dipole-dipole interactions. We also notice on Figure 2.3 that the amount of scattered light does not scale linearly with the number of atoms, as it would be expected for a non-interacting sample of atoms. These observations can be reproduced by a simple functional form

$$n_z(N, \Delta) \propto \frac{N}{\Gamma_c(N)^2 + 4[\Delta - \delta\omega_c(N)]^2}.$$

This Lorentzian function, with  $\Gamma_c$  the FWHM and  $\delta\omega_c$  the shift of resonance, reproduces very well the experimental data.

Numerical simulations has been performed in order to understand this set of data (see [Pellegrino et al., 2014]). The simulations were based on coupled-dipoles model, assuming a frozen distribution of the atoms and taking into account the Zeeman level structure of  $^{87}\text{Rb}$ . Simulations predict that the spectra  $n_z(N, \Delta)$  should present an increasing broadening, and asymmetry, a negligible shift, as well as a saturation of the scattered light when the number of atoms increases. This features are reproduced in this experiment when the number of atoms is below  $\sim 100$ . For  $N > 100$ , the agreement tends to be only qualitative as the effects are found to be less pronounced experimentally. Two possible explanations can be considered.

- A first possible explanation could be that forces induced by dipole-dipole interactions may expel atom pairs with shortest interatomic distances. This would break down the assumption considering the frozen positions of the atoms during the excitation pulse and would also decreases the density as the average distance between atoms would increase. Unfortunately, this point is hard to check experimentally as the sample has a size smaller than our diffraction limit.
- Another explanation could be related to the initial Zeeman state population distribution taken in the model. In fact, for large numbers of atoms, the optical pumping during the excitation pulse could change dramatically the distribution of atoms in each Zeeman level, a process not taken into account in the model.

Despite of the lack of quantitative agreement between our simulations and the experimental measurements, our group has shown that dipole-dipole interactions do impact the optical response of the cloud to a near resonant light. It was a motivation to further investigate the influence of these interactions in various scenarios, one of them being discussed in the next section.

### 2.2.2 Coherent scattering

In contrast with the last section where we measured the *incoherent* scattering, this section is dedicated to the measurement of the *coherent* scattering of a dense cloud of cold atoms (cf. subsection 2.1.2). The results of this section can be found in [Jennewein et al., 2016].

To measure  $|\mathcal{S}(\omega)|^2$  in steady-state, the experimental procedure is quite similar to the one described in subsection 2.2.1. After preparing the atoms in  $(5S_{1/2}, F = 2)$ , we switch off the dipole trap light during 500 ns and send a 300 ns probe pulse with a temporal top hat profile (rise time of 2 ns). We then recapture the cloud in the trap for 500 ns and repeat this release-probe-recapture 1000 times using the same atomic cloud. This procedure is repeated with 200 different clouds to average the spatial configurations of the atoms. The signal measured (see Figure 2.4 (b)) reaches a steady-state after  $\sim 26$  ns, close to the lifetime  $1/\Gamma$  of the excited state, during which the sample gets polarized. We average the signal over a time interval of 120 ns and we normalize it with respect to

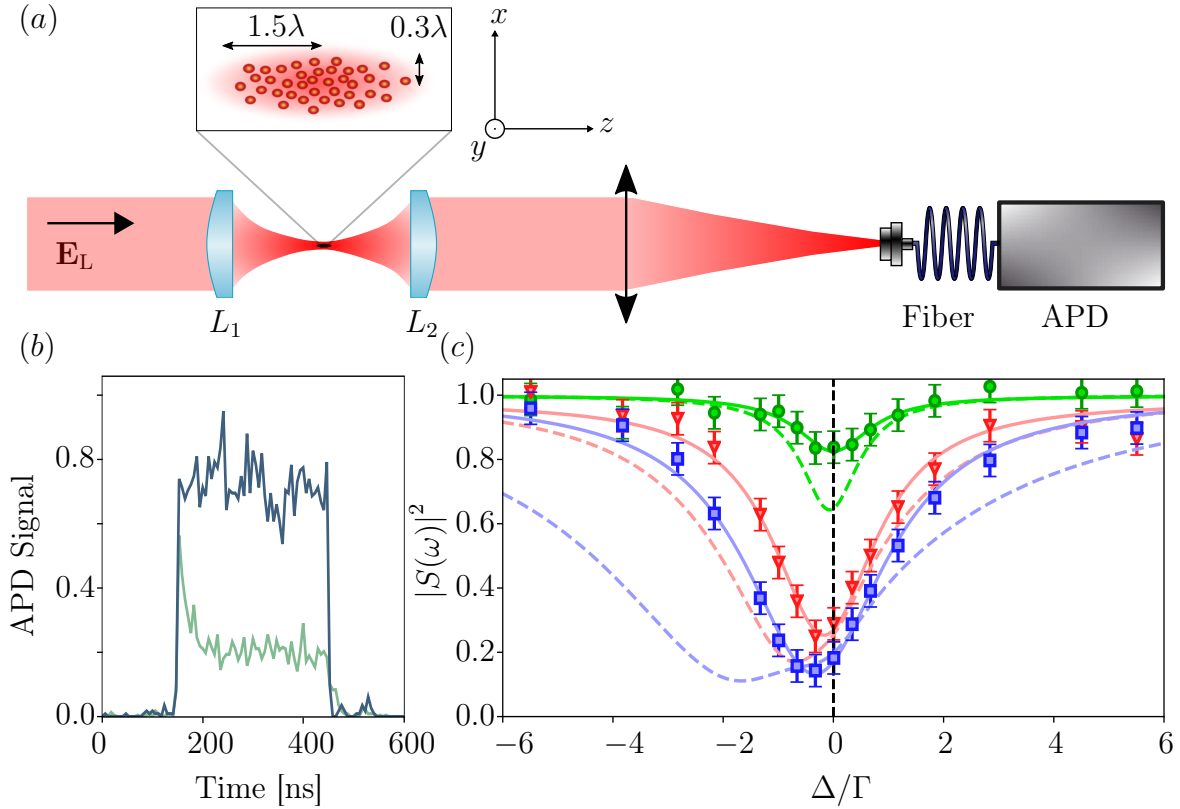


**Figure 2.4.:** (a): Sketch of the experimental setup. A probe laser  $\mathbf{E}_L$  is shinned onto the first aspherical lens and focused on the cloud of cold atoms. The probe laser and the light scattered by the cloud are collected by the second aspherical lens before being coupled into a single-mode fiber connected to an avalanche photodiode (APD). (b): Typical temporal signal recorded by the APD. The blue solid line represents the signal in absence of atoms, the green solid one with atoms. The ratio of the two signals in a region we choose to define the steady-state regime gives one data point in (c) (a specific number of atoms and a specific detuning). (c): Measured transfer function of the cloud of atoms versus detuning  $\Delta$  for  $N = (10, 83, 180)$  (green circles, red triangles and blue squares respectively). Error bars are fixed to the maximal standard deviation obtained for this set of data. The solid lines represent Lorentzian fit of the data. The dotted lines correspond to coupled-dipoles simulation including the 12-level structure of the  $(5S_{1/2}, F = 2)$  to  $(5P_{3/2}, F' = 3)$  transition. The data presented here are extracted from [Jennewein et al., 2016].

the case without atoms. The experiment is performed for various probe detuning  $\Delta$  and for various atom number  $N$  (see Figure 2.4 (c)).

Similarly to the *incoherent* scattering measurement, we understand qualitatively the *coherent* scattering. We observe a broadening of the line, a red-shift, and a suppression of the measured light in the forward direction when the number of atoms increases. The fact that light can be almost completely suppressed by an atom or a cloud of atoms whose

size is smaller than the waist of the incoming beam can be explained by the expression of the on resonance scattering cross section of a single two-level atom [Steck, 2015]

$$\sigma_0 = \frac{\hbar\omega\Gamma}{2I_{\text{sat}}} = \frac{3\lambda^2}{2\pi}.$$

For a single  $^{87}\text{Rb}$  atom,  $\sigma_0 = 0.29 \mu\text{m}^2$  which is, although smaller, not negligible compared to the probe beam cross section given by  $\sim \pi w^2/2 = 2.3 \mu\text{m}^2$ . The experimental features are reproduced by the coupled-dipoles simulations, assuming a frozen distribution of the atoms during the excitation pulse and taking into account the multi-level structure of the atoms, but are less pronounced than the theory.

**Derivation of a functional form** The derivation of a functional form of the  $|S(\omega)|^2$  measured quantity is difficult for a dense cloud of atoms. However, we proposed, as an ansatz, such a form assuming that our cloud behaves as a small dielectric sphere of polarizability  $\alpha_c$  with a size small compared to  $1/k$ . To derive such an expression, we will follow the work presented in [Aljunid et al., 2009] and, in a very detailed way in [Tey et al., 2009]. For that matter, we need first to derive some expressions listed below:

- the expression of the Gaussian field at the focus of the first lens, in the strong focusing regime,
- the expression of the field scattered by the dielectric particle acting as a dipole induced by the excitation beam,
- the laser field at the position of the second lens,
- the overlap between the scattered field and the mode of the fiber taken equal to the one of the laser field, at the position of the second lens.

**Gaussian field in the strong focusing regime** Let us first derive the expression of the electric field at the position of the atoms  $z = 0$ , i.e., in the focal plane of L1. Considering a Gaussian beam of waist  $w_L$  and polarized along the  $x$  axis, the expression of the field just before the lens is

$$\mathbf{E}_{\text{in}}(\rho, z = -f) = E_0 \exp\left(-\frac{\rho^2}{w_L^2}\right) \hat{\mathbf{e}}_x, \quad (2.18)$$

with  $\rho$  the distance from the optical axis. An ideal converging lens transforms a beam with a plane wavefront into one with a spherical wavefront which converges towards the focal point ( $\rho = 0, z = 0$ ). It can then be modeled as a phase plate introducing a radially dependent phase factor  $t(\rho)$  which expression is

$$t(\rho) = \exp\left(-ik\sqrt{\rho^2 + f^2}\right), \quad (2.19)$$

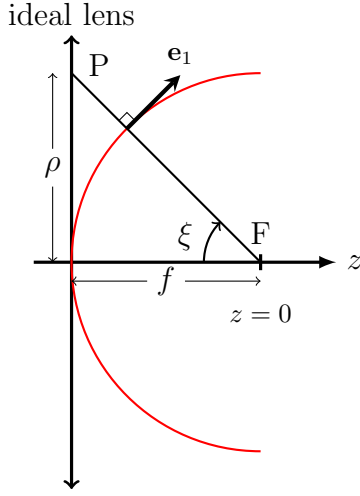


**Figure 2.5.:** Sketch of the ideal lens focusing a spherical wavefront.

with  $f$  the focal length of lens L1. Note that we do not consider here a parabolic wavefront  $\exp(-ik\rho^2/2f)$ , a convenient approximation that is often used, and only valid in paraxial optics. Moreover, simply multiplying the phase introduced by the lens with the input field would give a field incompatible with Maxwell's equations. To make the field compatible with them, we have to modify the local polarization vector keeping in mind three requirements:

1. a lens with rotational symmetry keeps the local azimuthal component unchanged but tilts the local radial component towards the axis,
2. the local polarization vector is orthogonal to the local wavevector,
3. the power before and after any arbitrary small area of the thin ideal lens should be equal.

In the cylindrical basis  $(\hat{\mathbf{e}}_\rho, \hat{\mathbf{e}}_\varphi)$ , in the plane of L1, we have

$$\hat{\mathbf{e}}_x = \cos \varphi \hat{\mathbf{e}}_\rho - \sin \varphi \hat{\mathbf{e}}_\varphi. \quad (2.20)$$

Then, to fulfill requirements 1 and 2, the local polarization vector  $\hat{\mathbf{e}}_1$  just after the first lens is given by

$$\hat{\mathbf{e}}_1 = (\cos \xi \cos \varphi \hat{\mathbf{e}}_\rho + \sin \xi \cos \varphi \hat{\mathbf{e}}_z) - \sin \varphi \hat{\mathbf{e}}_\varphi, \quad (2.21)$$

with  $\xi = \arctan(\rho/f)$ . (2.21) can be expressed in the  $(\hat{\mathbf{e}}_x, \hat{\mathbf{e}}_y, \hat{\mathbf{e}}_z)$  stationary basis and one would get

$$\hat{\mathbf{e}}_1 = \begin{pmatrix} \cos \xi + (1 - \cos \xi) \sin^2 \varphi \\ (\cos \xi - 1) \cos \varphi \sin \varphi \\ \sin \xi \cos \varphi \end{pmatrix}. \quad (2.22)$$

The expression of the laser field, compatible with Maxwell's equations, just after the lens is then given by

$$\mathbf{E}_L(\rho, \varphi, z = -f) = \frac{E_0}{\sqrt{\cos \xi}} \exp\left(-ik\sqrt{\rho^2 + f^2}\right) \exp(-\rho^2/w_L^2) \hat{\mathbf{e}}_1, \quad (2.23)$$

where the  $1/\sqrt{\cos \xi}$  is introduced to meet requirement 3.

Then, various methods exist to propagate this field from lens L1 to the focus. Here, we will use Green theorem that states

$$\mathbf{E}(\mathbf{r}) = \oint_{S'} \{ikc[\hat{\mathbf{n}}' \times \mathbf{B}(\mathbf{r}')]G(\mathbf{r}, \mathbf{r}') + [\hat{\mathbf{n}}' \times \mathbf{E}(\mathbf{r}')] \times \nabla' G(\mathbf{r}, \mathbf{r}') + [\hat{\mathbf{n}}' \cdot \mathbf{E}(\mathbf{r}')] \nabla' G(\mathbf{r}, \mathbf{r}')\} dS', \quad (2.24)$$

where  $S'$  being a closed surface around  $\mathbf{r}$ ,  $\hat{\mathbf{n}}'$  a normal unit vector pointing inside  $S'$  and  $G(\mathbf{r}, \mathbf{r}')$  the Green tensor given by

$$G(\mathbf{r}, \mathbf{r}') = \frac{\exp(ik|\mathbf{r} - \mathbf{r}'|)}{4\pi|\mathbf{r} - \mathbf{r}'|}. \quad (2.25)$$

We are interested in the field near the focus  $\mathbf{r} \approx \mathbf{r}_{\text{focus}}$ . In the far field limit  $|\mathbf{r} - \mathbf{r}'| \gg \lambda$ , the expression of  $\mathbf{B}$  and  $\nabla'G$  can be simplified to

$$\mathbf{B}(\mathbf{r}') \approx \frac{\mathbf{k}'}{ck} \times \mathbf{E}(\mathbf{r}') \quad (2.26a) \quad \begin{aligned} \nabla'G &\approx -i\mathbf{k}'G \text{ before the focus} \\ \nabla'G &\approx +i\mathbf{k}'G \text{ after the focus} \end{aligned} \quad (2.26b)$$

By splitting  $S'$  into two half-spheres,  $S'_{\text{bf}}$  before the focus and  $S'_{\text{af}}$  after the focus, the field expression near the focus and in the far-field limit reduces to

$$\mathbf{E}(\mathbf{r} \approx \mathbf{r}_{\text{focus}}) = -2i \int_{S'_{\text{bf}}} [\hat{\mathbf{n}}' \cdot \mathbf{k}'] \mathbf{E}(\mathbf{r}') G(\mathbf{r}, \mathbf{r}') dS' + 2i \int_{S'_{\text{af}}} [\hat{\mathbf{n}}' \cdot \mathbf{E}(\mathbf{r}')] \mathbf{k}' G(\mathbf{r}, \mathbf{r}') dS'. \quad (2.27)$$

The second term in (2.27) is equal to zero when we choose  $S'_{\text{af}}$  to be an infinitely large half sphere centered at  $\mathbf{r}_{\text{focus}}$  because then  $\hat{\mathbf{n}}'$  is orthogonal to  $\mathbf{E}(\mathbf{r}')$  at all positions  $\mathbf{r}'$ . For  $S'_{\text{bf}}$ , we choose an infinitely large sphere that coincides with the first ideal lens. In this case,  $\hat{\mathbf{n}}' = \hat{\mathbf{e}}_z$  and  $\hat{\mathbf{n}}' \cdot \mathbf{k}' = k \cos \xi$ . With these choices, using (2.23), (2.25) and the cylindrical basis in the plane of lens L1, (2.27) becomes

$$\mathbf{E}_{\text{L}}(z = 0) = -\frac{ikE_0}{2\pi} \iint \rho d\rho d\varphi \exp\left(-\frac{\rho^2}{w_{\text{L}}^2}\right) \frac{f^{1/2}}{(\rho^2 + f^2)^{3/4}} \hat{\mathbf{e}}_1. \quad (2.28)$$

The integrals  $\int d\varphi$  along the  $\hat{\mathbf{e}}_y$  and  $\hat{\mathbf{e}}_z$  components of  $\hat{\mathbf{e}}_1$  (see (2.22)) give zero, as expected from symmetry argument: the polarization at the focus is the same as the one of the input field. The integral  $\int d\varphi$  along this component gives  $\pi(1 + \cos \xi)$ . Using the change of variable  $t = \rho^2/w_{\text{L}}^2 + 1/u^2$  with  $u = w_{\text{L}}/f$ , called the focusing strength, the expression of the field at the focus is

$$\mathbf{E}_{\text{L}}(z = 0) = -i \frac{kw_{\text{L}}E_0}{2} h(u) \hat{\mathbf{e}}_x, \quad (2.29)$$

where  $h(u)$  is a function whose expression is

$$h(u) = \frac{1}{2u} e^{1/u^2} \left[ \sqrt{u} \Gamma\left(\frac{1}{4}; \frac{1}{u^2}\right) + \frac{1}{\sqrt{u}} \Gamma\left(-\frac{1}{4}; \frac{1}{u^2}\right) \right], \quad (2.30)$$

and where  $\Gamma(a; b)$  is the incomplete Gamma function given by

$$\Gamma(a; b) = \int_b^{\infty} e^{-t} t^{a-1} dt.$$

Equation (2.29) and the derivation steps presented here are extracted from [Tey et al., 2009].

**Field scattered by the dielectric sphere** We have calculated the expression of the field, in the strong focusing regime, at the position of our small dielectric sphere. This field induces a dipole  $\mathbf{d}$  proportional to the excitation field  $\mathbf{d} = \epsilon_0 \alpha_c(\omega) \mathbf{E}_L(z=0)$  that in turns emits a field which expression, in the far field limit, is given by

$$\mathbf{E}_{\text{sc}}(\mathbf{r}, \omega) \approx -\frac{k^2}{4\pi\epsilon_0} \frac{e^{ikr}}{r} \hat{\mathbf{u}} \times (\hat{\mathbf{u}} \times \mathbf{d}). \quad (2.31)$$

With our notations, the field scattered by the small dielectric particle is explicitly

$$\mathbf{E}_{\text{sc}}(\mathbf{r}, \omega) = \frac{k^2}{4\pi} \alpha_c(\omega) E_L(z=0) \frac{e^{ikr}}{r} (\hat{\mathbf{e}}_x - \cos \theta \hat{\mathbf{u}}), \quad (2.32)$$

where  $\theta$  is the angle between the  $x$  axis and the direction of radiation.

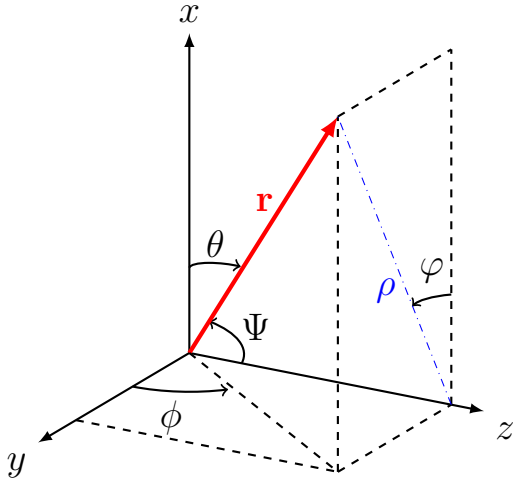


**Figure 2.6.:** 3D coordinate system and angles definitions. The dielectric particle is located at the origin.

by

$$\mathbf{E}_L(\rho, \varphi, z = +f) = -i \frac{E_0}{\sqrt{\cos \Psi}} \exp\left(+ik\sqrt{\rho^2 + f^2}\right) \exp(-\rho^2/w_L^2) \hat{\mathbf{e}}_2, \quad (2.33)$$

where  $\Psi$  denotes the angle between the  $z$  axis and a point in the plane of the second lens. It is then equal to the angle  $\xi$  introduced in (2.21). Nonetheless, the local polarization vector  $\hat{\mathbf{e}}_2$  is not perfectly equal to  $\hat{\mathbf{e}}_1$  because the field after the focus is diverging and not converging. Therefore, the expression of  $\hat{\mathbf{e}}_2$  is

$$\hat{\mathbf{e}}_2 = (\cos \Psi \cos \varphi \hat{\mathbf{e}}_\rho - \sin \Psi \cos \varphi \hat{\mathbf{e}}_z) - \sin \varphi \hat{\mathbf{e}}_\varphi. \quad (2.34)$$

**Overlap between the scattered field and the laser field** Now we have all the required quantities to derive a functional form for our transfer function. With the notations of this section, (2.16) is

$$S(\omega) = 1 + \frac{\int_{L2} \mathbf{E}_{\text{sc}}(\rho, \varphi, \omega) \cdot \mathbf{E}_{\text{L}}^*(\rho, \varphi, z = +f) \cos \Psi \rho \, d\rho \, d\varphi}{\int_{L2} |\mathbf{E}_{\text{L}}(\rho, \varphi, z = +f)|^2 \cos \Psi \rho \, d\rho \, d\varphi}, \quad (2.35)$$

where  $\cos \Psi$  accounts for the projection of the fiber mode onto the integration plane  $L2$ . Let us consider the numerator of the second term in the right hand side of equation (2.35) and denote this integral  $\mathcal{I}$ . Because the local polarization vector  $\hat{\mathbf{e}}_2$  is orthogonal to the direction of radiation  $\mathbf{r}$ , only its component along  $\hat{\mathbf{e}}_x$ , which is equal to  $\cos \Psi \cos^2 \varphi + \sin^2 \varphi$ , is integrated. Choosing a phase convention such that the laser field at the position  $z = 0$  is real, integral  $\mathcal{I}$  can be written as

$$\begin{aligned} \mathcal{I} = i \frac{k^3 \alpha_c(\omega)}{4\pi} \frac{w_{\text{L}}}{2} E_0^2 h(u) \left\{ \int_{L2} \rho \, d\rho \, d\varphi \frac{f^{3/2}}{(\rho^2 + f^2)^{5/4}} \exp\left(-\frac{\rho^2}{w_{\text{L}}^2}\right) \cos^2 \varphi \right. \\ \left. + \int_{L2} \rho \, d\rho \, d\varphi \frac{f^{1/2}}{(\rho^2 + f^2)^{3/4}} \exp\left(-\frac{\rho^2}{w_{\text{L}}^2}\right) \sin^2 \varphi \right\}. \end{aligned} \quad (2.36)$$

We find in the curly brackets of expression (2.36) the same integral encountered in (2.28). Therefore, it is equal to  $\pi w_{\text{L}} h(u)$  and  $\mathcal{I}$  is equal to

$$\mathcal{I} = i \frac{k^3 \alpha_c(\omega)}{4\pi} \frac{\pi w_{\text{L}}^2}{2} E_0^2 h^2(u). \quad (2.37)$$

**Coherent transfer functional form** The denominator in (2.35) being equal to  $\frac{1}{2} \pi w_{\text{L}}^2 E_0^2$ , the transfer function of our dielectric sphere is given by

$$S(\omega) = 1 + i \frac{k^3 \alpha_c(\omega)}{4\pi} h^2(u). \quad (2.38)$$

Finally, by replacing the expression of the polarizability of our small dielectric particle with the one of a dipole resonant at  $\omega_c$  with a width  $\Gamma_c$  (see (2.1)), the coherent transfer function can be cast into a Lorentzian form

$$S(\omega) = 1 - \frac{A}{1 - 2i \frac{\omega - \omega_c}{\Gamma_c}}, \quad (2.39)$$

where  $A = \frac{3}{2} h^2(u)$ . The coefficient  $A$  is related to the scattering ratio  $R_{\text{sc}}$  introduced in [Tey et al., 2009] through the relation  $R_{\text{sc}}(u) = 3h^2(u)$ .

**Comments on the functional form** As with the incoherent field measured in subsection 2.2.1, the experimental data are well reproduced by Lorentzian functions. This observation seems to give confidence about the functional form derived in the previous

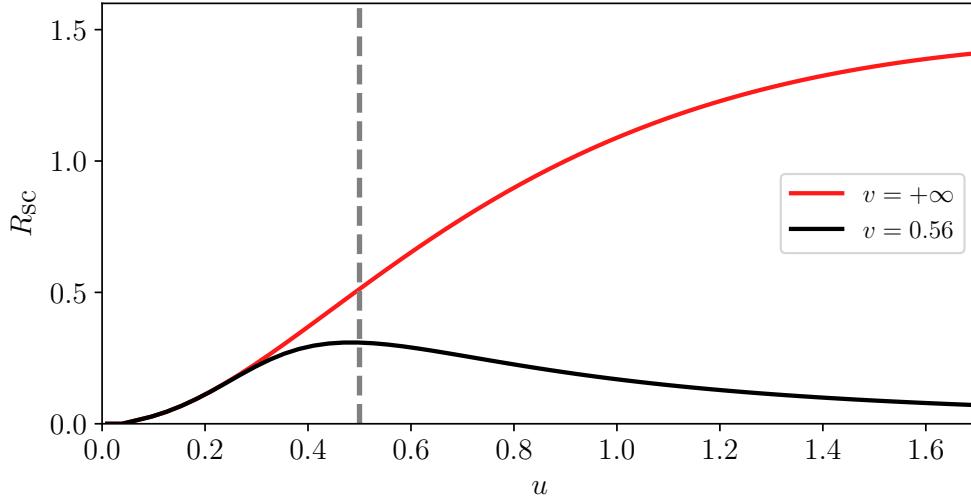


**Figure 2.7.:** Simulation of the scattering ratio for both an infinite lens  $R_{\text{sc}}^{\infty}$  (red solid line) and a finite size lens  $R_{\text{sc}}^{r_0}$  with  $v = 0.56$  (black solid line). The dashed gray vertical line corresponds to the focusing strength value in our experiment  $u = 0.5$ . In this case,  $R_{\text{sc}}^{\infty} \approx 0.52$  but  $R_{\text{sc}}^{r_0}$  is only 0.31 (42% relative difference).

paragraph, although the assumption on the cloud size is not fulfilled. However, the values given by our functional expression does not provide the same feeling. For instance, let us consider the simple case of a single atom located at the focus of the first lens. In our experiment, the input waist of our probe beam  $w_L$  is almost equal to the radius of the aspheric lens (with  $f = 8$  mm and  $NA = 0.5$ ). Then the focusing strength is equal to  $u = 0.5$ , which gives a *transmission* at resonance (see Figure 2.7)

$$|S(\omega)|^2 = |1 - A|^2 = \left| 1 - \frac{R_{\text{sc}}}{2} \right|^2 \approx 0.56.$$

The obtained value is well below the actual transmission measured (see Figure 2.4). A better estimation of the transfer function value at resonance can be provided considering the finite size of our lens. The truncated scattering ratio  $R_{\text{sc}}^{r_0}$ , with  $r_0 = 4.5$  mm the radius of our lens, is given by the formula

$$R_{\text{sc}}^{r_0} = \frac{3}{4u^3} e^{2/u^2} \left\{ \left[ u\Gamma\left(\frac{1}{4}; \frac{1}{u^2}\right) + \Gamma\left(-\frac{1}{4}; \frac{1}{u^2}\right) \right] - \left[ u\Gamma\left(\frac{1}{4}; \frac{1+v^2}{u^2}\right) + \Gamma\left(-\frac{1}{4}; \frac{1+v^2}{u^2}\right) \right] \right\}^2, \quad (2.40)$$

with  $v = r_0/f$  the truncation ratio. (2.40) is simply a reformulation of equation (45) from [Tey et al., 2009]. Figure 2.7 represents both the scattering ratio  $R_{\text{sc}} = R_{\text{sc}}^{r_0=\infty}$  and the truncated scattering ratio  $R_{\text{sc}}^{r_0}$  versus the focusing strength. As one can notice, the

two functions behave similarly when the focusing strength is below  $\sim 0.25$ . However, the difference is not negligible for focusing strength above this value. In our present case,  $u = 0.5$ , the value of the coherent transfer function at resonance is given by

$$|S(\omega)|^2 = \left| 1 - \frac{R_{\text{sc}}^{r_0}}{2} \right|^2 \approx 0.71. \quad (2.41)$$

Although the last estimation is closer to experimental measurement, it is still unable to reproduce quantitatively our data, even in the single atom case.

**Others approaches** Several theoretical models have been tested in order to explain the experimental data. The first one is the Friedberg, Hartmann and Manassah (FHM) perturbative theory ([Friedberg et al., 1973], [Manassah, 2012]). Their theory derives expressions for a collective decay rate and a collective shift for various geometries of an atomic ensemble of two-level atoms. Similarly to the simple case of two atoms in interaction presented in section 2.1, the collective shift and rate are the real and imaginary parts of the average dipole-dipole interactions. For the case of an ellipsoidal cloud with Gaussian density distribution matching the one in the experiment, the predictions differs significantly from the measured values (see [Jennewein et al., 2016]), even though the group included the Rubidium internal structure. To do so, they only considered the  $\pi$  transitions from  $(5S_{1/2}, F = 2)$  to  $(5P_{3/2}, F' = 3)$  and assumed equally populated Zeeman ground states. Under these assumptions, the only effect of the internal structure on the atom is to multiply the polarizability by a factor given by

$$\frac{1}{5} \sum_{m_F} |C_{F=2, m_F \rightarrow F'=3, m_F}|^2 = \frac{1}{5} \left( \frac{1}{3} + \frac{8}{15} + \frac{3}{5} + \frac{8}{15} + \frac{1}{3} \right) = \frac{7}{15},$$

where  $C_{F=2, m_F \rightarrow F'=3, m_F}$  are the Clebsch-Gordan coefficient associated with the transitions of interest and are listed in Figure 2.8. The lack of agreement seems to indicate that the perturbative approach is not appropriate for a dense atomic system.

Then, to go beyond the FHM perturbative treatment, the Lorentz local field theory has been applied, adapted for a dense cigar-shaped cloud. In this approach, replacing the cloud by a Gaussian continuous density distribution  $n$ , the local susceptibility is calculated using the Lorentz-Lorenz formula [Jackson, 1999]

$$\chi = \frac{n\alpha(\omega)}{1 - \frac{n\alpha(\omega)}{3}},$$

with  $\alpha(\omega)$  the polarizability of a single atom, which includes the internal atomic structure of Rubidium as described before

$$\alpha(\omega) = \frac{7}{15} \times \frac{\frac{6i\pi}{k^3}}{1 - \frac{2i\Delta}{\Gamma}}. \quad (2.42)$$

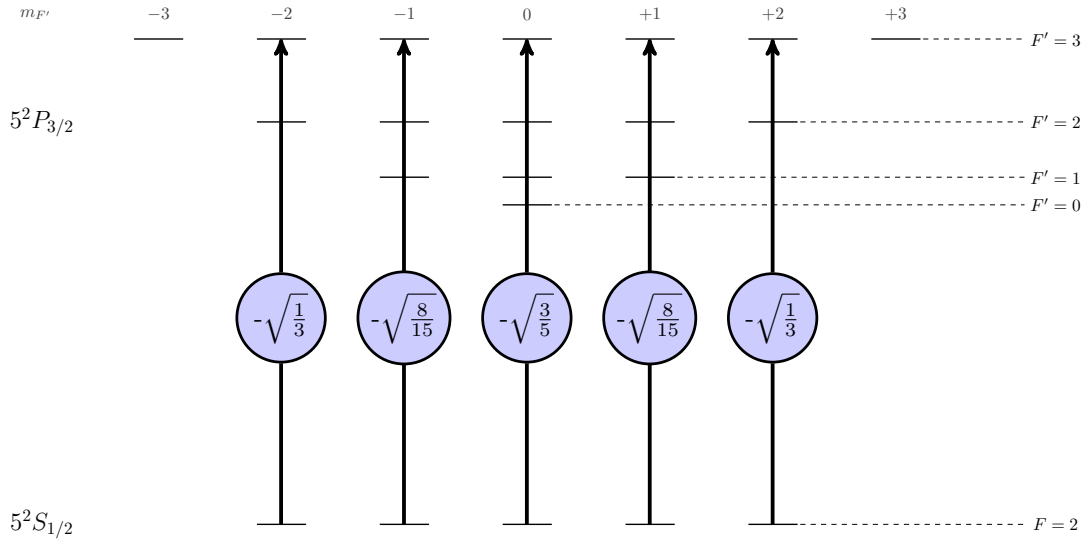


**Figure 2.8.:** Clebsch Gordan coefficients associated with  $\pi$  transition from  $(5S_{1/2}, F = 2)$  manifold to  $(5P_{3/2}, F' = 3)$  manifold. Note that the coefficients displayed here differ from the one in Appendix B. The different normalization condition has been taken into account in the simulations.

After defining a local permittivity  $\epsilon = 1 + \chi$ , Mondher Besbes, research engineer at Laboratoire Charles Fabry, used a finite element program to calculate the electric field scattered in the far field by the cloud and finally to compute the transfer function  $\mathcal{S}(\omega)$ . The mean-field response predicted by the Lorentz-Lorenz formula deviates from the data as the number of atoms increases, featuring in particular a double structure as well as a large asymmetry.

The last model that has been used to describe the data is a microscopic model where the atoms are considered as pointlike dipoles, their polarizability being given by (2.42), randomly positioned according to the Gaussian spatial distribution of the cloud. In this model, each atom is driven by the Gaussian probe beam and the field scattered by all the other atoms, leading to a set of coupled dipoles equation. The model has been described in section 2.1. The results of these simulations is depicted in Figure 2.4. As one can see, the agreement is only qualitative and tends to become inappropriate as the number of atoms increases.

### 2.2.3 Conclusion

The previous experimental results obtained in the group and summarized above, measuring either the incoherent scattering or the coherent scattering, have not lead to a quantitative agreement with theory. The coherent scattering measurement has been

compared to various models and none of them were satisfactory, not even the coupled-dipoles model which is a discrete description of the system. The possible explanations could be that one, or several, of the assumptions used to describe the system are wrong. The first two possible candidates to explain the discrepancy are:

1. the internal structure of the atoms that is not accurately taken into account. Indeed, the polarizability has simply been changed to (2.42) but it does not include optical pumping nor Raman processes. Not only that but we also assumed equal populations in each Zeeman ground levels, which may be inaccurate.
2. the residual motion of the atoms in the cloud. In all the simulations that were performed, the atomic distribution has been assumed to be frozen. However, the sample temperature being on the order of  $\sim 100 \mu\text{K}$ , the atoms are moving. This residual motion could introduce a dephasing that would minimize the dipole-dipole interactions effects, thus explaining why we always measure smaller effects than the one that theories predict.

These two points will be addressed with a new experiment that we performed at the very beginning of my thesis. They are described in more details in the next sections of this chapter.

## 2.3 TRANSMISSION THROUGH A DENSE CLOUD OF COLD TWO-LEVELS ATOMS

In this section, we describe the solution we implemented on the experiment to address the first issue mentioned at the end of the previous section. We explain how we reduced the complex internal structure of the atoms to just two levels and present the experimental results obtained in this configuration.

### 2.3.1 Polarization of the sample: towards two-level atoms

In direct connection with the previous works of the group, either experimentally or theoretically ([Pellegrino et al., 2014], [Jennewein et al., 2016], [Jenkins et al., 2016]), the biggest step made in order to address the remaining discrepancies between the experimental data and the theory of the coupled-dipoles model has been to *polarize* the sample to get rid of the internal structure of Rubidium. The atoms in the trap being initially prepared in a statistical mixture of Zeeman states  $m_F = 0, \pm 1$  of the  $F = 1$  hyperfine ground state manifold, the sample is polarized in  $|g\rangle = |5S_{1/2}, F = 2, m_F = 2\rangle$  by sending a combination of pumping and repumping light, both  $\sigma_+$  polarized with respect to the quantization axis set by a magnetic field of  $\approx 5 \text{ G}$  (see Figure 2.9). We then lift the degeneracy of the Zeeman structure even more by increasing the magnetic field to 314 G within 10 ms.

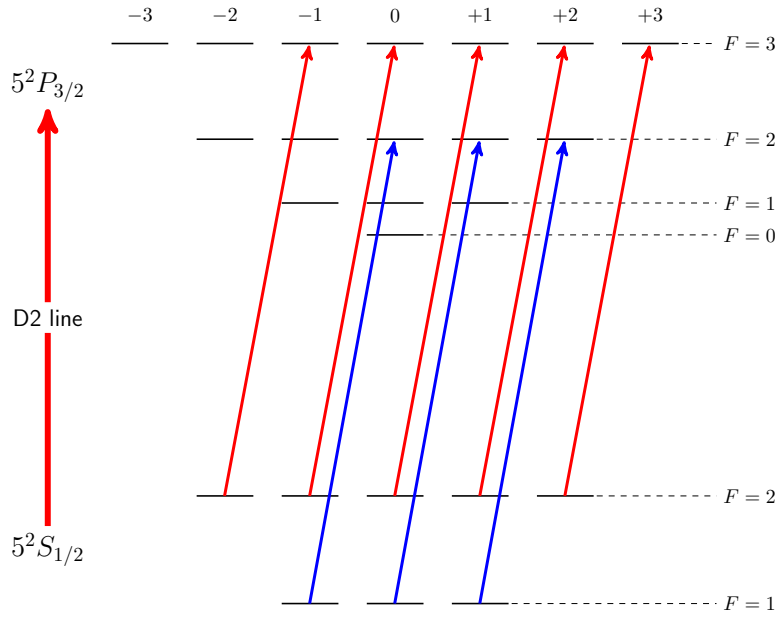


**Figure 2.9.:** Hyperfine level structure of the D2 line of  $^{87}\text{Rb}$ . The  $\sigma^+$  pumping and repumping beams are driving transitions represented in red and blue respectively.

### Choice of the value of $\mathbf{B}$ field

The specific value of the  $\mathbf{B}$  field at which we operate the experiment is not of crucial importance *per se*, but is governed by two considerations that are listed below.

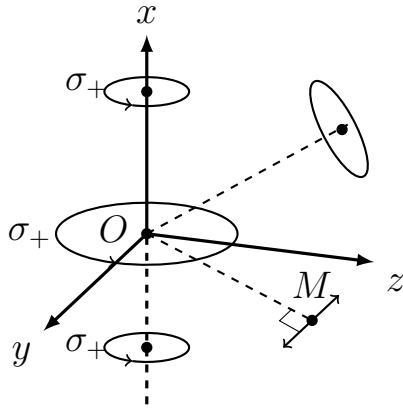


**Figure 2.10.:** Radiation from a  $\sigma_+$  rotating dipole located at the origin. The light emitted along  $x$  is  $\sigma_+$  polarized; it is linearly polarized in the  $yOz$  plane and elliptically polarized in any other direction. The figure is a reproduction of (2A.3) from [Grynberg et al., 2010].

- The first consideration concerns the probe light that is sent toward the sample. As we want a two level structure, we send a probe light that address the closed transition  $|g\rangle \rightarrow |e\rangle = |5P_{3/2}, F' = 3, m_{F'} = 3\rangle$ . We do not want to drive any other transition, therefore the closest  $\sigma_+$  transition has to be detuned by several linewidth  $\Gamma = 2\pi \times 6$  MHz. Doing so, the populations remaining in other  $m_F$  states are spectators.
- The second consideration comes from the dipole-dipole interactions itself. We do not want the field scattered by an atom of the sample at any position, thus of any polarization (see Figure 2.10), to be able to drive another transition than the one from  $|g\rangle$  to  $|e\rangle$ .

## Interaction with a static magnetic field

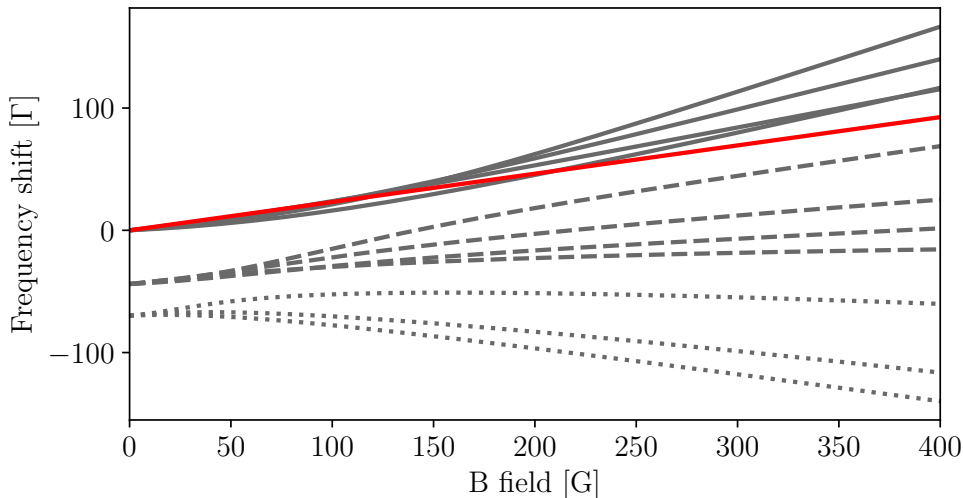


**Figure 2.11.:** Energy shift in units of the natural linewidth  $\Gamma$  of the  $\sigma^+$  transitions of the D2-line of  $^{87}\text{Rb}$  versus B field. The upper solid lines represent transitions from  $(5S_{1/2}, F = 2)$  to  $(5P_{3/2}, F' = 3)$ , the middle dashed lines represent the ones from  $(5S_{1/2}, F = 2)$  to  $(5P_{3/2}, F' = 2)$ , and the bottom dotted lines the  $(5S_{1/2}, F = 2)$  to  $(5P_{3/2}, F' = 1)$  transitions. The transition highlighted in red is the one from  $|5S_{1/2}, F = 2, m_F = 2\rangle$  to  $|5P_{3/2}, F' = 3, m_F = 3\rangle$ .

In the absence of magnetic field, the sublevels of each hyperfine level  $F$  are degenerate. However, when a magnetic field is applied, this degeneracy is lifted, according to the Hamiltonian

$$H_B = \frac{\mu_B}{\hbar}(g_S S_z + g_L L_z + g_I I_z)B_z, \quad (2.43)$$

if we choose the quantization axis  $z$  along the direction of the  $\mathbf{B}$  field. Here,  $g_S$ ,  $g_L$  and  $g_I$  are the electron spin, electron orbital and nuclear  $g$ -factors that account for various modifications to the corresponding magnetic dipole moments [Steck, 2015].

The hyperfine structure Hamiltonian, up to the electric quadrupole term, has the following form [Steck, 2015]

$$H_{\text{hfs}} = A_{\text{hfs}}\mathbf{I} \cdot \mathbf{J} + B_{\text{hfs}} \frac{3(\mathbf{I} \cdot \mathbf{J})^2 + \frac{3}{2}(\mathbf{I} \cdot \mathbf{J}) - I(I+1)J(J+1)}{2I(2I-1)J(2J-1)}, \quad (2.44)$$

where  $\mathbf{J}$  is the total electron angular momentum, sum of the orbital angular momentum  $\mathbf{L}$  and the spin angular momentum  $\mathbf{S}$ , and  $\mathbf{I}$  is the total nuclear angular momentum.  $A_{\text{hfs}}$  is the magnetic dipole constant and  $B_{\text{hfs}}$  is the electric quadrupole constant.

The full Hamiltonian that we want to compute the eigenvalues from is the sum of (2.43) and (2.44). We have then computed the energy shift of all the  $\sigma^+$  transitions

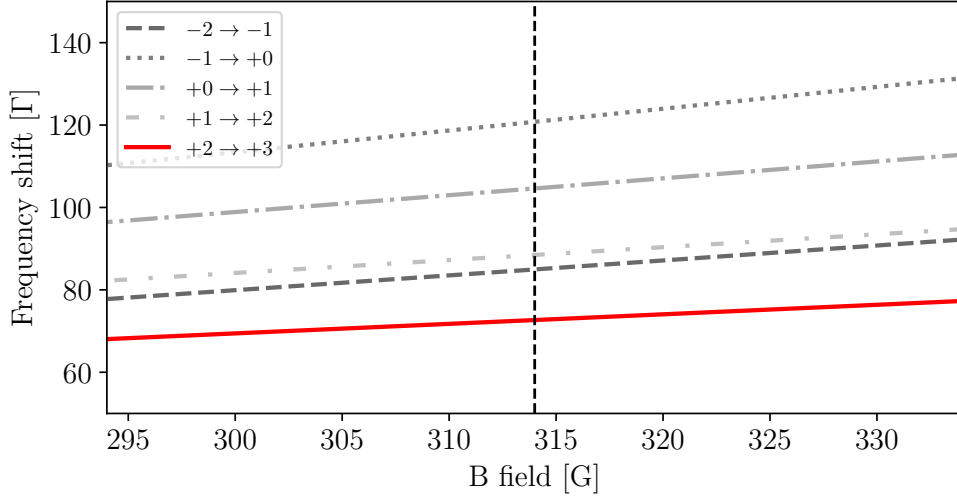


**Figure 2.12.:** Energy shift in units of the natural linewidth  $\Gamma$  of the  $\sigma^+$  transitions of the D2-line of  $^{87}\text{Rb}$  versus B field. The transitions displayed are the ones from the  $(5S_{1/2}, F = 2)$  manifold to the  $(5P_{3/2}, F' = 3)$  manifold. The vertical dashed line corresponds to the B field value applied in our experiment. The closest transition from the closed one addressed in our experiment (red line) is the one from  $|5S_{1/2}, F = 2, m_F = -2\rangle$  to  $|5P_{3/2}, F' = 3, m_F = -1\rangle$  (dashed line) and is detuned by more than  $12 \Gamma$ .

on the D2-line of Rubidium 87, as depicted on Figure 2.11, because to address the 2-level sample one has to use a closed transition to avoid any depolarization of the sample during the experiment. Here, we chose the  $\sigma^+$  transition from  $|g\rangle = |5S_{1/2}, F = 2, m_F = 2\rangle$  to  $|e\rangle = |5P_{3/2}, F' = 3, m_{F'} = 3\rangle$ . Note that one can also decide to use the  $\sigma^-$  transition from  $|5S_{1/2}, F = 2, m_F = -2\rangle$  to  $|5P_{3/2}, F' = 3, m_{F'} = -3\rangle$ .

If we zoom onto the specific value of our  $\mathbf{B}$  field, see Figure 2.12, one notices that the closest  $\sigma^+$  transition from the one we are interested in is detuned by more than  $12 \Gamma$ , thus fulfilling the first criterion that our probe light will not address any other transition than the closed one. To convince ourselves with this fact, one can compute the Rabi frequency  $\Omega$  of an atom in the cloud illuminated by the field scattered by another one. The dipole field scattered in the far-field limit and at resonance can be approximated by

$$E_{sc} \approx \frac{k^3}{4\pi} \alpha(\omega = \omega_0) E_L \frac{e^{ikr}}{kr} = \frac{3i}{2} E_L \frac{e^{ikr}}{kr}.$$

Assuming  $kr \sim 1$ , which corresponds to a density  $n \sim 5 \cdot 10^{14} \text{ at.cm}^{-3}$ , and introducing the saturation intensity  $I_{\text{sat}} = \frac{c\epsilon_0 \hbar^2 \Gamma^2}{4d^2}$ , we get

$$|\Omega|^2 = \frac{d^2 |E_{sc}|^2}{\hbar^2} = \frac{9}{8} \frac{I}{I_{\text{sat}}} \Gamma^2,$$

and finally, for  $I/I_{\text{sat}} \sim 0.01$

$$\Omega \sim \frac{\Gamma}{10} \ll 12\Gamma.$$

The Rabi frequency between two atoms in the cloud separated by a typical distance of  $\lambda/2\pi$  is thus unable to drive another transition than the closed one.

We have also computed the frequency shifts of all the other transitions, whatever the polarization, to find that the dipole-dipole interactions would have to shift the energy by about  $36 \Gamma$  for an atom in  $|5S_{1/2}, F = 2, m_F = 2\rangle$  to be able to address another transition than the closed one. Finally, with our value of B-field, the two previous criteria are satisfied.

### 2.3.2 Experimental sequence

The experiment sequence is very similar to the one presented in subsection 2.2.2. We recall it here for clarity and to emphasize the differences. Once the sample is loaded from the MOT, it is polarized with the combination of pumping and repumping beams both  $\sigma^+$  polarized with respect to the quantization axis set by the B-field. Starting from randomly populated Zeeman ground states, the pumping was able to load as much as 80% of the atoms in the state  $|g\rangle = |5S_{1/2}, F = 2, m_F = 2\rangle$  while the temperature remained almost unaffected. To probe our sample, we are sending a laser beam focused by the second aspherical lens, in confocal configuration with respect to the one that has been used to focus the dipole trap beam. The probe at the position of the atoms as a waist at  $1/e^2$  of  $1.20 \pm 0.05 \mu\text{m}$ . The probe is linearly polarized, perpendicular to the magnetic field, thus only the  $\sigma^+$  component of the probe light is driving the transition from  $|g\rangle$  to  $|e\rangle = |5P_{3/2}, F' = 3, m_{F'} = 3\rangle$ , and its intensity is kept low, around  $0.01 I_{\text{sat}}$  where  $I_{\text{sat}} = 1.65 \text{ mW.cm}^{-2}$  is the saturation intensity. The transmitted part of the probe field as well as the field scattered by the atom is collected by the aspherical lens and coupled to a single-mode fiber connected to an avalanche photodiode (APD). Doing so, we measure the overlap of the transmitted field  $\mathbf{E}(\mathbf{r}, t)$  with the mode of the fiber. The detection being time-resolved, we have access to the dynamic of the scattering. When the trapping beam is off, we send a square pulse of 300 ns to probe the cloud, then we switch on the trapping beam again to recapture the atoms. This probe-and-recapture sequence is repeated 1000 times with the same cloud. The experiment is repeated with 200 different samples.

As explained before, the field scattered by the atoms in the forward direction, the one corresponding to the propagation of the probe light, is dominated by its *coherent* part at low intensity. Then the field that we measure is the integration over the lens area of the overlap of the coherent field emitted by the cloud with the mode of the fiber. Defining a steady-state regime in the optical response gives access to the  $|S(\omega)|^2$

quantity presented in section 2.1.2. Typical temporal signal recorded by the APD are presented in Figure 2.13 (a), (b) and (c).

### 2.3.3 Experimental results

The details on the experimental sequence in the previous section as the results presented in this section are extracted from [Jennewein et al., 2018].

#### Temporal measurement

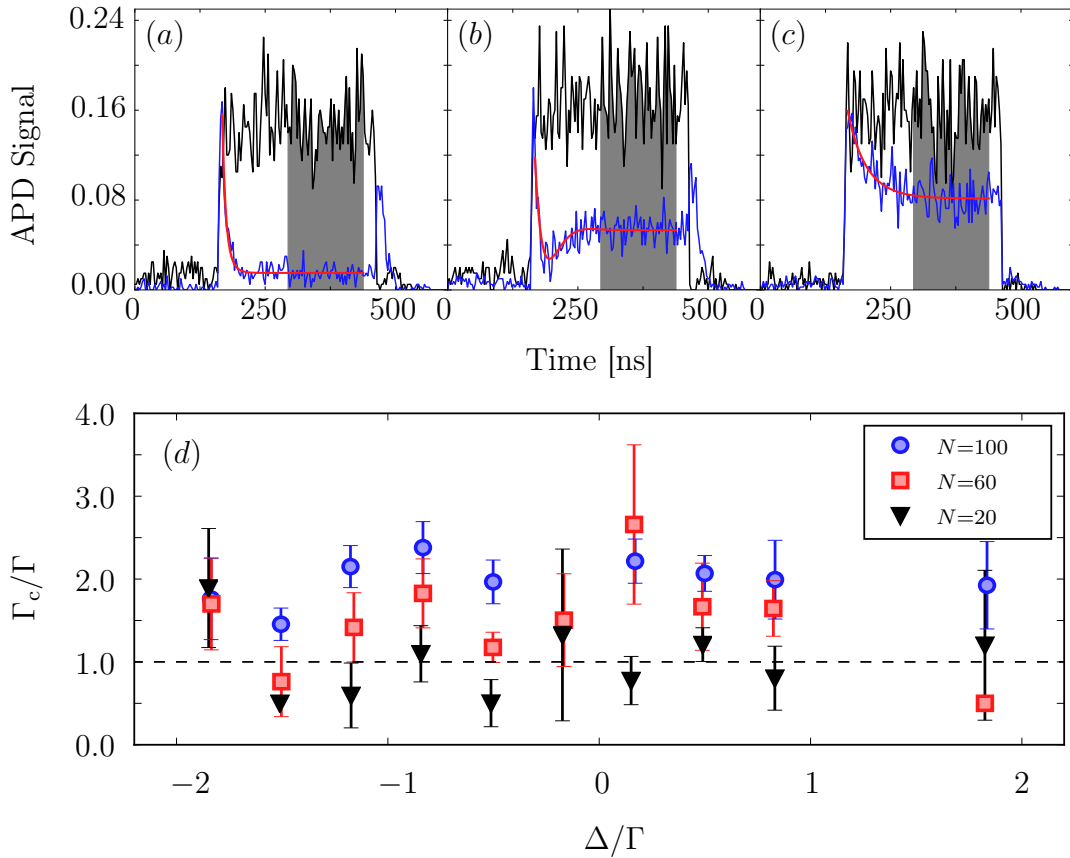


**Figure 2.13.:** Examples of temporal responses of the cloud measured by the APD. The solid black lines correspond to the signal obtained in the absence of atoms, the blue solid ones in the presence of atoms. The red lines are fits from (2.45). (a):  $N = 100$ ,  $\Delta = -0.14\Gamma$ , (b):  $N = 100$ ,  $\Delta = -1.15\Gamma$ , (c):  $N = 20$ ,  $\Delta = -0.12\Gamma$ . The time bin of the detection is 1.5 ns. The gray shaded region corresponds to our definition of the steady-state regime. (d): Decay rate  $\Gamma_c$  deduced from the fit of the temporal responses, as a function of the detuning  $\Delta$  for various atom numbers. Errors bars are given by the fitting procedure.

Here, we are reproducing the coherent scattering measurement but this time having a sample of cold *two*-level atoms. A minor difference being that previously the dipoles were linearly polarized whereas here, due to the direction of the B field and the polarization direction of the probe laser, the atomic dipoles are circularly polarized. This difference will be taken into account in the simulations of the next section.

Figure 2.13 (a), (b), and (c) show typical temporal signals recorded by our APD. The blue and black solid lines correspond respectively to the signal obtained with and without atoms, the later being used for normalization purpose. Each signal is the accumulation of 1000 release-probe-recapture using the same atomic cloud and repeated with typically 200 different clouds. The temporal signal obtained in presence of atoms are first fitted with a phenomenological function

$$|\mathcal{S}(t)|^2 = A \left| 1 - \frac{B}{1 + 2i\frac{\Delta - \Delta_c}{\Gamma_c}} \left( 1 - \exp \left( -i(\Delta - \Delta_c)t - \frac{\Gamma_c}{2}t \right) \right) \right|^2, \quad (2.45)$$

with  $A$ ,  $B$ ,  $\Delta_c$  and  $\Gamma_c$  as free parameters. This phenomenological fitting function contains the functional form (2.39) derived in subsection 2.2.2 but also includes the temporal part which corresponds to the transient regime of the system. Note that (2.45) implicitly assumes that the laser excites only one eigenmode of the system, defined by  $\Delta_c$  and  $\Gamma_c$ . The goal here is to emphasize any collective effect that can occur in the cloud and that would modify the typical response time  $1/\Gamma_c$  of the system. Figure 2.13 (d) gives the results of this fitting procedure: we are plotting the collective radiative decay rate  $\Gamma_c$  as a function of the detuning  $\Delta$  of the probe laser, for three different atoms numbers.  $\Gamma_c$  increases with the number of atoms  $N$  and is notably above  $\Gamma$ , the radiative decay rate of a single atom, when  $N > 20$ . We thus have a clear signature of the presence of collective effects in the cloud. More precisely, as  $\Gamma_c > \Gamma$ , it seems that the laser field mainly couples to super-radiant states involving a few atoms only (see [Schilder et al., 2016]). The temporal fitting enables also to define the steady-state regime, represented as a gray area in Figure 2.13.

### Steady-state regime

Figure 2.14 presents the experimental data corresponding to the measurement of the coherent transfer function of a cloud of cold two-level Rubidium atoms in the steady-state regime. The values obtained for each detuning and atom number corresponds to the ratio of the temporal signal in presence of atoms and in absence of atoms (gray filled area of Figure 2.13).

In order to compare this set of data with the multi-level case of unpolarized samples presented in subsection 2.2.2, we fit the data by a Lorentzian profile. This approach,

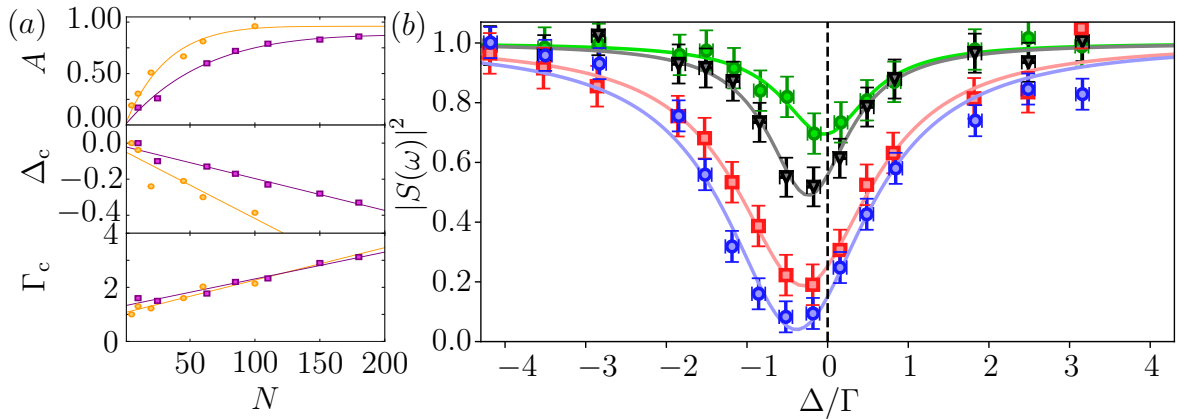


**Figure 2.14.:** Experimental measurement of the coherent transfer function of a cloud of two-level atoms and comparison with the fitting parameters obtained in the multi-level case. (a): Fitting parameters ( $A$ : amplitude,  $\Delta_c$ : shift,  $\Gamma_c$ : width) extracted from the Lorentzian fits of the coherent transfer function for various atoms numbers. The yellow points correspond to the two-level case described in this section. The purple points correspond to the multi-level case described in subsection 2.2.2 and are shown for comparison. (b): Experimental measurement of  $|S(\omega)|^2$  as a function of detuning for different atoms numbers: 10 (green circles), 20 (dark triangles), 60 (red squares) and 100 (blue circles). Horizontal error bars are set to 0.5 MHz, which is approximately  $\Gamma/10$  and corresponds to the lock precision of our probe. Vertical error bars are set equal to twice the biggest standard deviation uncertainty obtained. The solid lines are Lorentzian fits (functional form of  $|S(\omega)|^2$  derived in subsection 2.2.2).

although phenomenological, allow us to extract a line shift, a line width and an amplitude. The extracted parameters feature the same behavior with the atom number as in the multilevel case, i.e., a shift and a broadening of the line that increase with  $N$ , and a saturation of the amplitude (see Figure 2.14 (a)). Interestingly, the slope of the shift is about two times larger for the two-level atom case and the saturation of the amplitude occurs at lower  $N$ , thus suggesting that the internal atomic structure plays a role in the scattering.

## Conclusion

The measurement of the coherent optical response of a cloud of dense cold two-level atoms is the first measurement performed in a dense regime with such a clean system configuration. This measurement, and the comparison with the one performed onto an unpolarized sample, validate that the internal structure of the atoms plays a role in the scattering of light. Proofs are provided by the shift  $\Delta_c$  that increases more rapidly with two-level atoms than with multi-level ones and by the saturation of amplitude  $A$  that occurs at lower atom number  $N$ . The experimental spectra are, as in the multi-level case, well reproduced by Lorentzian function. We will now compare these data with

theory, to see if a better agreement with coupled-dipoles simulations is obtained.

## 2.4 COMPARISON BETWEEN THEORY AND EXPERIMENT

### 2.4.1 The coupled-dipoles model

The coupled-dipoles equations have already been presented. This section only purpose is to adapt the general equations derived in section 2.1 to our experimental conditions: an ensemble of  $N$   $\sigma^+$ -polarized, two-level atoms driven by a Gaussian laser field with a linear polarization perpendicular to the quantization axis set by the magnetic field.

The  $\sigma^+$ -polarized dipole  $\mathbf{d}_j$  of atoms  $j$  is given by  $\mathbf{d}_j = d_j \hat{\mathbf{e}}_+$ , with  $\hat{\mathbf{e}}_+ = -(\hat{\mathbf{e}}_y + i\hat{\mathbf{e}}_z)/\sqrt{2}$ .  $\hat{\mathbf{e}}_x$  is the unit vector along the quantization axis. The laser field used to probe the atoms is polarized along the  $y$  axis. Therefore, we have  $\mathbf{E}_L \cdot \hat{\mathbf{e}}_+^* = -E_L/\sqrt{2}$ . Consequently, (2.5) becomes

$$\left(i\Delta - \frac{\Gamma}{2}\right) d_j = +i \frac{3\pi\epsilon_0\Gamma}{k^3} \frac{\mathbf{E}_L}{\sqrt{2}} + i \sum_{l \neq j}^N \frac{V_{jl}}{\hbar} d_l, \quad (2.46)$$

where the dipole-dipole interaction term  $V_{jl}$ , which general expression is given by (2.3), in the particular case of  $\sigma_+$ -polarized dipoles becomes

$$V_{jl} = -\frac{3}{8} \frac{\hbar\Gamma}{(kR_{jl})^3} e^{ikR_{jl}} [(1 - 3\cos^2\theta_{jl})(1 - ikR_{jl}) + (1 + \cos^2\theta_{jl})(kR_{jl})^2], \quad (2.47)$$

$\theta_{jl}$  being the angle between  $\mathbf{R}_{jl}$  and the quantization axis  $\hat{\mathbf{e}}_x$ .

The simulations that are performed in this chapter follow a stochastic approach. The set of coupled equations is first solved for a given realization of the spatial distribution of the atoms in the cloud, then the scattered electric field  $\mathbf{E}_{sc}$  is calculated in the far-field. We then can calculate the overlap between the scattered field and the excitation beam in the plane of the aspherical lens, used to both trap and image the atoms in our experiment, to form the coherent optical response.

The purpose of the following sections is to investigate the modification of the coherent response of the cloud, using the coupled-dipoles model, to assess whether the remaining discrepancy could be explained by

1. a wrong estimation of the number of atoms in the cloud,
2. a bias in our measurement of the temperature of the cloud,
3. a bias in our estimation of the volume occupied by the atoms of the cloud.

## As a function of the number of atoms

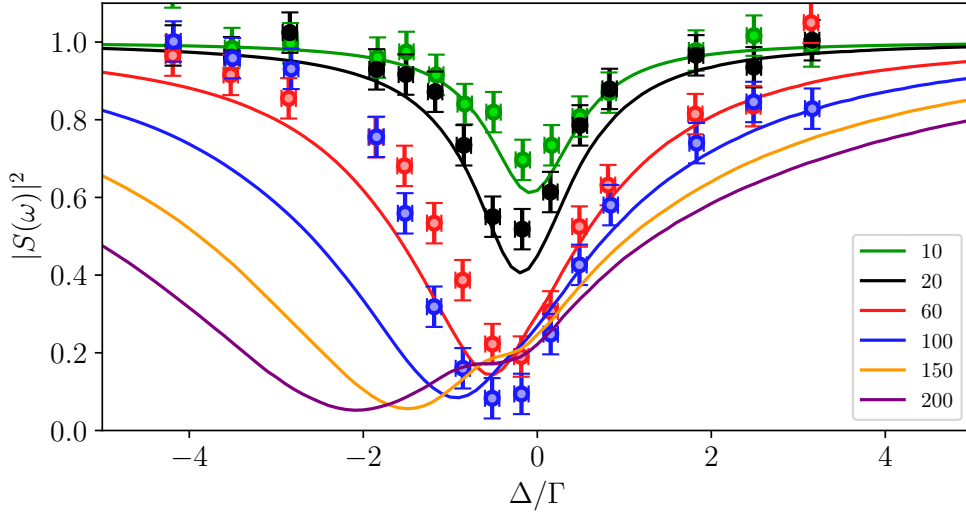


**Figure 2.15.:** Simulation of  $|S(\omega)|^2$  as a function of the number of atoms  $N$  in the trap (solid lines). Trap waist is  $1.2 \mu\text{m}$ , trap depth is  $1.0 \text{ mK}$ , saturation parameter of the probe is set to  $0.01$  and temperature of the cloud is set to  $150 \mu\text{K}$ . The points corresponds to the experimental measurements, with the same error bars as in Figure 2.14.

The relevant parameters of the coupled-dipoles model are the number of atoms  $N$  in the cloud and the density  $n$ , or more precisely the quantity  $n\lambda^3$  where  $\lambda = \lambda/2\pi$  is the reduced wavelength of the atomic transition. When this last quantity is close to 1, the strength of the dipole-dipole interaction becomes comparable to the strength of the coupling with the electromagnetic vacuum modes: an atom will as likely couple to the vacuum mode of the electromagnetic field as to a neighboring atom through a dipole-dipole interaction. Figure 2.15 represents the quantity  $|S(\omega)|^2$  as a function of the number of atoms in the cloud. I performed the simulation for a temperature of the cloud of  $150 \mu\text{K}$ , a trap depth of  $1.0 \text{ mK}$  (trapping beam assumed to be Gaussian with a waist equal to  $1.2 \mu\text{m}$ ) and a saturation parameter of the probe light  $s = 0.01$  (probing beam assumed to be Gaussian with the same waist as the trapping beam). As one can see, when the number of atom increases, the line shifts towards the red of the transition ( $\Delta < 0$ ), the width increases and the amplitude saturates. For a very large number of atoms,  $N > 100$ , a double peak structure begins to appear. In our experiment, we manage to measure the quantity up to 100 atoms. This corresponds to  $n\lambda^3 \approx 0.17$ . The data points reproduce the general features qualitatively but not quantitatively for high atom numbers. The estimation of the number of atoms in our experiment is extracted from the fluorescence signal obtained after a time of flight to ensure an independent response of the atoms. The precision of this estimation is limited by the shot noise on the camera used to collect the fluorescence of the atoms in the cloud. The number of atoms is then equal to  $N \pm \sqrt{N}$ . Based on this argument, a

wrong estimation of the number of atoms in the cloud cannot explained the difference between the experimental points and the theoretical curves. Moreover, because our data coincide with the simulations at low atom number, a bias in the estimation of  $N$  would therefore minimize the agreement at these small numbers of atoms.

As a function of the temperature of the cloud

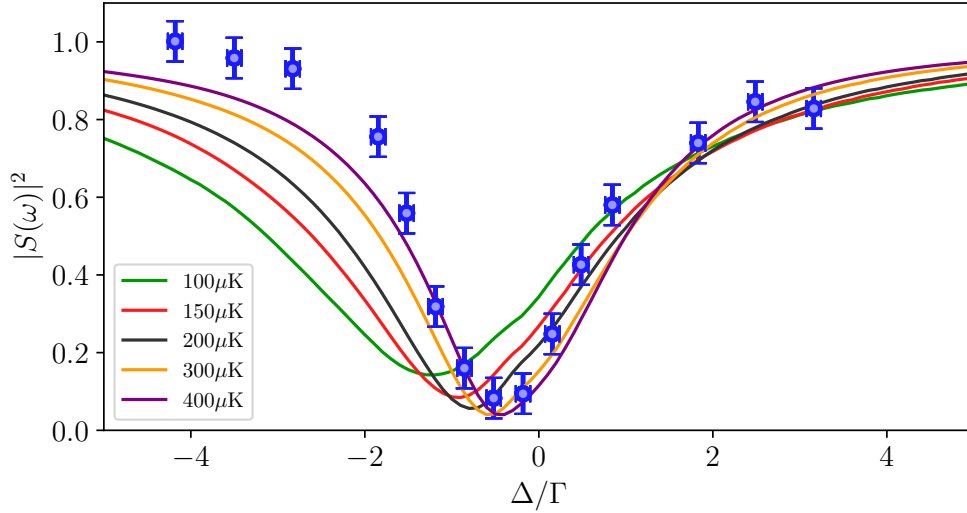


**Figure 2.16.:** Simulation of  $|S(\omega)|^2$  as a function of temperature for  $N = 100$  atoms. The trap waist and trap depth are fixed here to  $1.2 \mu\text{m}$  and  $1 \text{mK}$  respectively. Experimental data points (blue circles) are displayed for comparison.

In our desire to address the remaining discrepancies between the coupled-dipoles theory and the measurements, let us consider the same simulation as before, restricted ourselves to the case of  $N = 100$  atoms, and changing the temperature of the atoms in the cloud. We have decided to run the simulations with  $N = 100$  because the vicious effect that could have been omitted would be more pronounced when the number of atoms is high. The results are depicted in Figure 2.16. The conclusion is quite obvious: as the temperature increases, the volume occupied by the atoms increases and thus minimizes the density. As the density is decreasing, the dipole-dipole interactions strength also decreases and consequently the symmetry of the line-shaped is restored. The red-side of the line is removed and added to the blue part. The minimum of the line is shifted towards the right. All the features of the dipole-dipole interactions are minimized by an increase of temperature, because the effective density is reduced. The precision on the temperature estimation of the cloud is around 15%. Therefore, a temperature that will be off by this uncertainty will still not explained the discrepancies between experimental data and theory.

## As a function of the trap volume

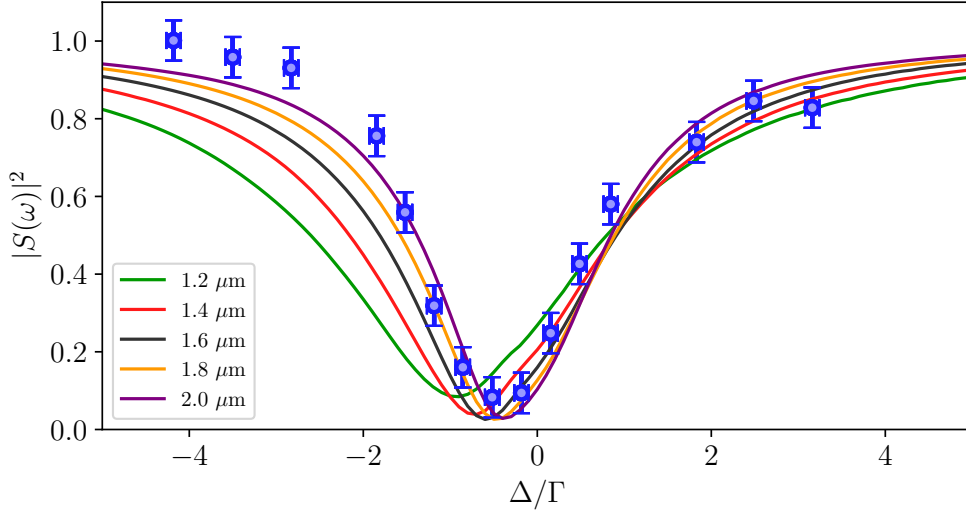


**Figure 2.17.:** Simulation of  $|S(\omega)|^2$  as a function of the waist of the trapping beam for  $N = 100$  atoms. The trap depth is fixed to 1 mK and temperature to 150  $\mu\text{K}$ . Data points (blue circles) are shown for comparison.

The investigation of the influence of the trap volume in the line shaped of the  $|S(\omega)|^2$  quantity leads to the same conclusion as the one of the influence of the temperature. As in Figure 2.16, Figure 2.17 displays a reduction in the red side of the line that is added to the blue side. The reason behind it is that a bigger trap volume reduces the effective density of the cloud the same way an increase of temperature would do. The difference between this two phenomenon relies in the dynamic of the interaction because atoms with a higher temperature moves faster. The dynamic of the interaction is not taken into account in the simulations as we compute only the steady state of a given atomic distribution. From the steady-state point of view, the two parameters seem identical. The agreement with experimental measurements gets better when the waist of the trapping beam gets close to 2.0  $\mu\text{m}$ . Nonetheless, according to [Sortais et al., 2007], our trapping beam waist is equal to  $1.20 \pm 0.05 \mu\text{m}$ . The uncertainty on this value has been estimated from the measurement of the oscillation frequency of a single atom in the dipole trap. Differences cannot be attributed to an underestimated value of the trapping beam waist as the relative precision of this measurement is not compatible with a waist of 2.0  $\mu\text{m}$ . Besides, it would not explain the agreement at low atom numbers.

In principle, the temperature  $T$  of the cloud and the volume occupied by the atoms are related in thermal equilibrium. However, it could be that thermal equilibrium is not fulfilled when the number of atoms increases. Note that because coupled-dipoles simulations agree with the experimental data at low atom number, we are looking for an effect that would vary with the number of atoms.

## Conclusion

Other simulations have been performed in order to understand the only qualitative agreement between theory and experiment, notably studying the effect of a misalignment of the probe beam with respect to the cloud, both transversally and longitudinally (see [Jennewein, 2017]). A longitudinal displacement of the focus of the probe with respect to the cloud location would introduce an asymmetry in the line shape. However, this asymmetry would be independent on the number of atoms and would be unable to explain the remaining discrepancies. The same conclusion arises for a transverse displacement of the probe which would only introduce a reduction of contrast.

To conclude, the internal structure of the atoms is not able, by itself, to reconcile experiment with the couple-dipoles theory. In this section, we investigated the influence of various parameters on the prediction of the coupled-dipoles model to determine whether it could be compatible with our measurement. So far, none of the numerical studies has been able to explain the discrepancies. Even if the modification of the parameters could restore an agreement with theory when the number of atoms, thus the density, is high, it degrades the agreement at low atom number.

### 2.4.2 Coupled-dipoles model with atomic motion

In a last attempt to address the remaining discrepancies between the theoretical models and the experimental data, we investigated the influence of motion of the atoms on the optical response of the cloud.

#### Including motion into the coupled-dipoles model

We have simulated the coupled-dipoles model (see (2.5) from subsection 2.4.1), keeping the time derivative of the atomic coherences. We assigned a position  $\mathbf{r}_j$  to each atom  $j$  according to a Gaussian distribution with widths given by the characteristics of the Gaussian trapping beam and the temperature of the cloud (c.f. (1.14)). We also assigned to each atom an initial velocity  $\mathbf{v}_j$  according to Maxwell-Boltzmann distribution given by

$$f(v) = \left( \frac{m}{2\pi k_B T} \right)^{1/2} \exp \left( -\frac{mv^2}{2k_B T} \right),$$

where  $m$  is the mass of Rubidium,  $k_B$  is the Boltzmann constant,  $T$  the temperature of the cloud and  $v$  the speed of the atom along any of the three directions of the Cartesian space. The simulation is then performed during  $t = 300$  ns and for each time step  $dt$ , the new positions of the atoms is calculated using ballistic motion

$$\mathbf{r}_j(t + dt) = \mathbf{r}_j(t) + \mathbf{v}_j dt.$$

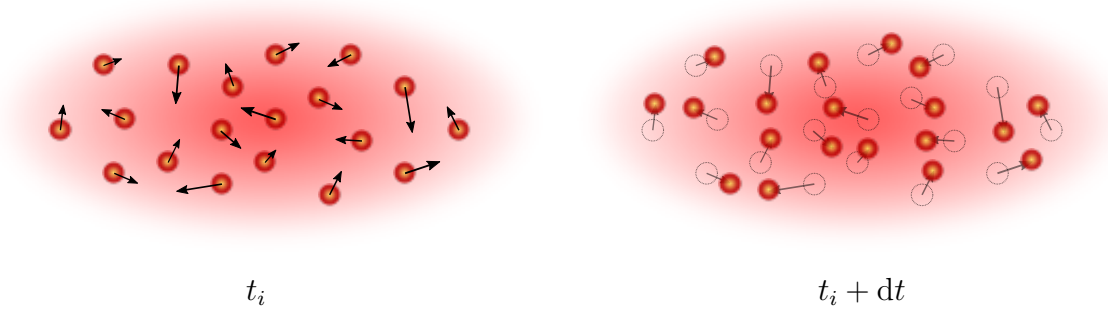


**Figure 2.18.:** Sketch of principle to explain simulations. At each time step  $t_i$ , each atom  $j$  has a specific position  $\mathbf{r}_j(t_i)$ . The interference between the laser field and the field scattered by each atom is computed knowing the interaction matrix  $V_{jl}(\mathbf{r}_j(t_i), \mathbf{r}_l(t_i))$  between atom  $j$  and atom  $l$ . In the next time step, the positions of each atom are modified based on their previous positions and their respective velocities:  $\mathbf{r}_j(t_i + dt) = \mathbf{r}_j(t_i) + \mathbf{v}_j dt$ . The velocity of each atom is assigned according to Maxwell-Boltzmann distribution and is assumed to be constant during the experiment. Doing so, we neglect the forces between atoms.

At each time step, the interaction between atoms is computed as if the atoms were frozen in that specific configuration. Let us write explicitly the time-dependent coupled-dipoles model starting from the equation on the atomic coherence  $\rho_{eg}$  (complex conjugate of (C.8))

$$\begin{aligned} \frac{d\rho_{eg}^j}{dt} = & + i \frac{\Omega_L^*}{2} \exp(+ikz_j(t)) - \left( \frac{\Gamma}{2} - i\Delta \right) \rho_{eg}^j(t) \\ & + \frac{3}{8} i\Gamma \sum_{l \neq j} \rho_{eg}^l(t) f^*(R_{jl}(t), \theta_{jl}(t)) \exp(+ikR_{jl}(t)) \end{aligned} \quad (2.48)$$

where the  $*$  sign denotes the complex conjugate and where we have omitted the retarded times, thus considering instantaneous interactions.  $R_{jl}(t) = |\mathbf{r}_j(t) - \mathbf{r}_l(t)|$  is the distance between atom  $j$  and atom  $l$  at time  $t$ , and  $\theta_{jl}(t)$  is the angle between  $R_{jl}(t)$  and the quantization axis. Both quantity depend on  $t$ , as explicitly written in the previous equation, but we will omit this dependence in the following for clarity. The  $f^*$  function is defined by

$$f^*(R, \theta) = \frac{1 + \cos^2 \theta}{kR} + (1 - 3 \cos^2 \theta) \frac{1 - ikR}{(kR)^3}, \quad (2.49)$$

and the Rabi frequency  $\Omega_L^*$  by

$$\Omega_L^* = \frac{d(\mathbf{E}_L \cdot \hat{\mathbf{e}}_+^*) \exp(-ikz)}{\hbar} = -\frac{d E_L}{\hbar \sqrt{2}} \exp(-ikz). \quad (2.50)$$

Using the fact that the classical dipole amplitude  $d_j$  of atom  $j$  is related to the atomic coherence  $\rho_{eg}^j$  by the relation  $d_j = 2d\rho_{eg}^j$ , where  $d$  is the dipole matrix element, one can

obtain the following equation

$$\begin{aligned} \dot{d}_j(t) = & - \left( \frac{\Gamma}{2} - i\Delta \right) d_j(t) - i \frac{d^2 E_L(R_j)}{\hbar \sqrt{2}} \\ & + i \sum_{l \neq j} d_l(t) \times \frac{3}{8} \Gamma f^*(R_{jl}, \theta_{jl}) \exp(ikR_{jl}), \end{aligned} \quad (2.51)$$

where the upper dot denotes the temporal derivative. Using the relation  $\hbar\Gamma = \frac{d^2 k^3}{3\pi\epsilon_0}$ , the previous equation can be rewritten as

$$\dot{d}_j(t) = - \left( \frac{\Gamma}{2} - i\Delta \right) d_j(t) - i \frac{3\pi\epsilon_0\Gamma}{k^3} \frac{E_L(R_j)}{\sqrt{2}} - i \sum_{l \neq j} \frac{V_{jl}(t)}{\hbar} d_l(t), \quad (2.52)$$

where  $V_{jl}$  is the dipole-dipole interaction potential given by (2.47). Note that because the positions of the dipoles now depend on time, so does  $V_{jl}$ . Equation (2.52) is just an ordinary first order differential equation. Associated with the initial condition that all dipoles amplitudes are null at  $t = 0$ , it becomes an initial value problem that can be solved numerically.

### Simulation procedure

We remind here the several steps of the simulations performed in this section.

1. assigning to each atom an initial position and a velocity, constant throughout the simulation procedure,
2. displacement of all the atoms based on their respective positions and velocities (ballistic motion, no forces between atoms),
3. compute the atomic dipoles and store them,
4. steps 2 and 3 are repeated until the final time defined by the user is reached.

The result of the simulation gives the amplitude of each dipole at each time step. We then calculated the total field emitted by the cloud, the interference between the excitation beam and the field scattered by all the dipoles in the far-field, that we are summing for a duration that we define as the steady-state regime. The procedure is completely similar to the one described in subsection 2.4.1 besides the fact that the simulations are now time-resolved and take into account the motion of the atoms. To be more precise, the motion of the atoms is consider here in a stochastic manner. Each atom is moving in straight lines from its initial position, according to its random initial and constant velocity. No force between atoms nor collisions is included in this model. A quick numerical application can convince ourselves that motion will not likely lead

to collisions in the cloud. Taking the highest density that we measure in our cloud,  $n \approx 10^{14}$  at.cm<sup>-3</sup>, the mean distance between atoms is of the order of  $1/n^{\frac{1}{3}} \sim 200$  nm. For a typical temperature of the cloud of 150  $\mu$ K, the mean velocity of the atoms from a Maxwell-Boltzmann distribution is around 12 cm.s<sup>-1</sup>. Then, during the 300 ns probe pulse duration, the displacement of the atoms is, on average, around 36 nm, which is small compared to the average distance between dipoles.

### Simulations results

The results of our simulations indicates that, for our temperatures, the motion of the atoms is completely negligible. In fact, if we take  $\lambda$ , the transition wavelength, as the unit of distance, and  $1/\Gamma$  as the unit of time,  $\Gamma$  being the natural linewidth of Rubidium, the velocity of our atoms is on the order of  $v = 0.004 \lambda\Gamma$  for  $T = 150 \mu$ K. The output of the simulations for this velocity is superimposed with the one obtained at 0 speed, which is the same as the one obtained in Figure 2.15 where we have removed the time-derivative and set the atoms at a fixed location. In order to see the impact of the motion, we have artificially increased the velocity of the atoms by a factor 10,  $v = 0.04 \lambda\Gamma$ , while keeping the Gaussian widths spatial distribution consistent with a temperature of  $T = 150 \mu$ K. The result of this simulation is depicted in Figure 2.19. The motion of the atoms reduces the red part of the spectrum to put it back into the blue side, thus restoring partially the symmetry of the line. However, the effect is seen for typical velocity of the atoms that are inconsistent with experimental measurement of the temperature of the cloud. In fact, an increase by a factor 10 on the velocity corresponds to an increase of a factor 100 on the temperature, which will be then equal to 15 mK, incompatible with our experimental conditions. Although the effect of motion seems to bring the theoretical line shape closer to experimental data points, it cannot explain the discrepancies between our measurements and the theory for our experimental parameters.

As pointed out in [Weiss et al., 2019], collective effects in atomic clouds seem to be robust against thermal decoherence. In [Kuraptsev and Sokolov, 2019], they claim that the displacement of the atoms results in the suppression of the impact of sub-radiant collective states, that would lead to a modification in the way the cloud of atoms scatters light. However, they also stated that the velocity of the atoms has practically no effect on the dynamics of the system at small times, the sub-radiant modes being long-lived states.

### Conclusion

As a conclusion, we still cannot reproduce the experimental measurement when including the motion of the atoms in the cloud. Another(s) ingredient(s) is still underestimated in its ability to modify the coherent response of our cloud. However, we want

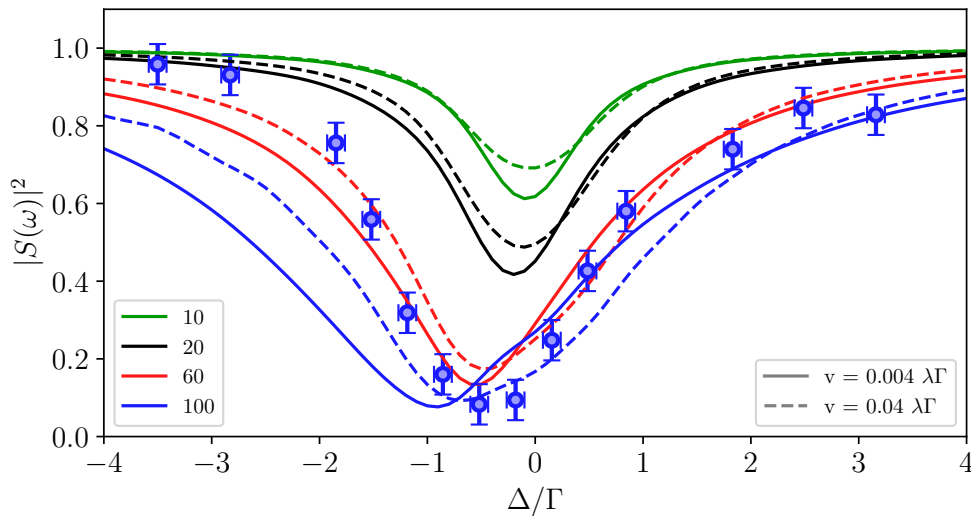


**Figure 2.19.:** Influence of motion in the optical response of a cloud of  $N = \{10, 20, 60, 100\}$  atoms. The solid line corresponds to simulation with a mean velocity of  $0.004 \lambda \Gamma$ , consistent with a Maxwell-Boltzmann distribution with a temperature of  $T = 150 \mu\text{K}$ . The dashed line corresponds to the same simulation where the velocity of the atoms has been increased to  $0.04 \lambda \Gamma$ . The blue circles correspond to experimental data obtained with  $N = 100$  and are shown for comparison.

to emphasize once again that the measurement presented here is the first one that has been able to determine that the internal structure of the atoms is not enough to explain the discrepancy between our data and the theory.

### 2.4.3 A new model to tackle the high intensity regime

We will take the opportunity of this section to present the main derivation steps of the multi-mode Maxwell-Bloch model that has been developed by our collaborators in order to address the high intensity regime of the driving field. Although our data lie under the low intensity approximation, we show here that the Maxwell-Bloch equations coincide with the coupled-dipole model at low intensity, but have the potentiality to be compared with experiment when the low intensity assumption is no longer valid. We will derive the model in the low intensity case, showing that it reproduce the coupled-dipole model. The high-intensity regime, where the coupled-dipoles model is expected to fail, is left to a possible future experiment in this regime.

#### Maxwell-Bloch equations in the low intensity regime

The model presented here has been developed by our collaborator Pierre Pillet. It is a generalization of the Maxwell-Bloch treatment of the propagation of light in a

medium consisting of  $N$  two-level atoms to the multimode case to account for the diffraction by the microscopic cloud. The derivations of the equations, starting from the master equation ruling the time-dependent density operator  $\rho(t)$  of the atomic ensemble are detailed in Appendix C. Here, we will just remind the main assumptions as the final equations of this model that govern the evolution of the atomic coherences and populations of each atom in the presence of a driving field and of dipole-dipole interactions.

1. The first assumption consists in performing a continuous medium approximation: the average coherence  $\rho_{ge}(\mathbf{r}, t)$ , population  $\rho_{ee}(\mathbf{r}, t)$ , and the slowly varying coherent field amplitude  $\Omega_+(\mathbf{r}, t) = d \langle \mathbf{E}^*(\mathbf{r}, t) \cdot \hat{\mathbf{e}}_+ \rangle \exp(ikz)/\hbar$  propagating through the atomic sample are introduced ( $d$  being the transition dipole and the unit vector  $\hat{\mathbf{e}}_+$  defines the  $\sigma_+$  polarization).
2. The second assumption is considering the quasi-one dimensional shape of our cloud. This last assumption enables to demonstrate that  $\Omega_+(\mathbf{r}, t)$  fulfills a paraxial equation.
3. Finally, diffraction is included by decomposing the coherent field onto the Laguerre-Gauss basis.

In the low intensity regime, we obtain a set of equations coupling the slowly varying averaged coherence  $\tilde{\rho}_{ge}(z, t) = \rho_{ge}(z, t) \exp(ikz)$  and the  $\Omega_+^{(q)}(z, t)$  component of the coherent field

$$\begin{cases} \frac{\partial \tilde{\rho}_{ge}}{\partial t} = - \left( \frac{\Gamma}{2} + i\Delta \right) \tilde{\rho}_{ge}(z, t) - \frac{i}{2} \sqrt{\frac{\pi w^2}{2}} \frac{1}{2\pi\sigma_r^2} \sum_{p=0}^{\infty} f_p(z) \Omega_+^{(p)}(z, t), \\ \frac{\partial \Omega_+^{(q)}}{\partial z} + \frac{1}{c} \frac{\partial \Omega_+^{(q)}}{\partial t} = -i \sqrt{\frac{2}{\pi w^2}} \frac{3\pi}{2k^2} \Gamma n f_q^*(z) \exp\left(-\frac{z^2}{2\sigma_z^2}\right) \tilde{\rho}_{ge}(z, t), \end{cases} \quad (2.53)$$

with the initial conditions  $\Omega_+(r, z = -\infty, t) = \Omega_L(r, z = -\infty, t)$ ,  $\Omega_L$  denoting the laser field. We have introduced the function  $f_p(z)$  which are overlap integrals defined as

$$f_p(z) = \int_0^{\infty} \exp\left(-\frac{r^2}{2\sigma_r^2}\right) \text{LG}_p(r, z) 2\pi r \, dr, \quad (2.54)$$

with  $\text{LG}_p$  the Laguerre-Gauss mode of order  $p$ .

### Connection with the experimental measurement

We link the set of coupled equations valid in the low intensity regime to the measured quantity on the experiment by noticing that the fibered avalanche photodiode measures the projection of the total field  $\Omega_+(r, z, t)$  at the position of the lens onto the Gaussian mode of the single-mode fiber. The avalanche photodiode therefore measures  $\left| \Omega_+^{(0)}(z, t) \right|^2$ , with  $z$  a distance that we take in practice equal to  $10\sigma_z$ .

### Steady-state solution

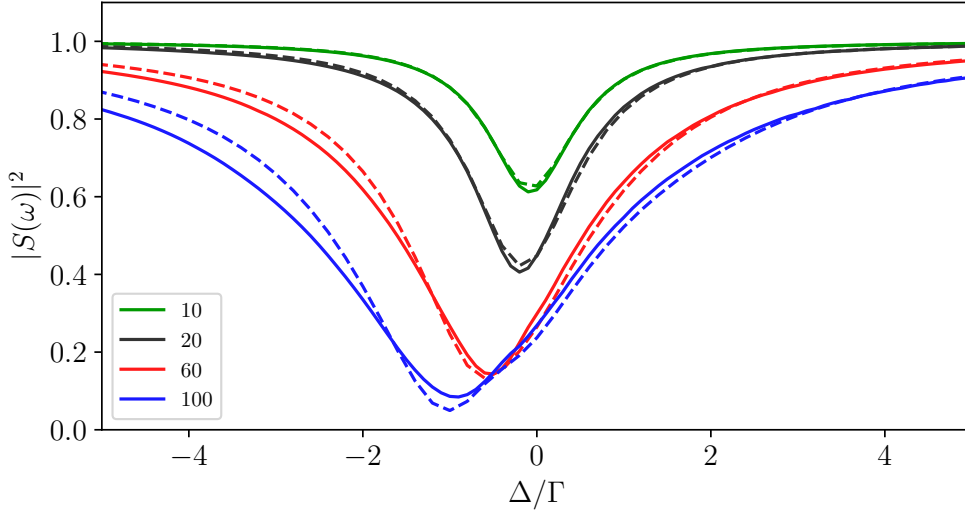


**Figure 2.20.:** Comparison of Maxwell-Bloch simulations described in this section (dashed lines) with the coupled-dipoles model (solid lines) for different atoms number  $N$  from 10 to 100. The steady-state solutions of Maxwell-Bloch equations have been obtained by decomposing the coherent field onto the 10 first Laguerre-Gauss modes. For both models, the size of the cloud is the one estimated from thermal equilibrium: Gaussian trap of  $1.2 \mu\text{m}$  waist, trap depth of  $1.0 \text{ mK}$  at  $\lambda_{\text{trap}} = 940 \text{ nm}$ ; temperature of the atoms equal to  $150 \mu\text{K}$ . The waist of the near-resonant probe beam addressing the D2 line closed transition is set to  $1.2 \mu\text{m}$ .

Finally, the steady-state response is solution of the following equation, obtained by setting the time derivative in (2.53) equal to 0

$$\frac{d\Omega_+^{(q)}}{dz} = -\frac{3\Gamma n}{4(k\sigma_r)^2} \frac{f_q^*(z)}{\Gamma + 2i\Delta} \exp\left(-\frac{z^2}{2\sigma_z^2}\right) \sum_{p=0}^{\infty} f_p(z) \Omega_+^{(p)}(z). \quad (2.55)$$

Equation (2.55) is therefore a continuous version of the coupled-dipole equations. Figure 2.20 displays the results of the simulations obtained with the procedure described here and the standard coupled-dipoles model. The results of the Maxwell-Bloch simulations feature the same behaviors as the ones of the coupled-dipoles simulations, at least up to 100 atoms, the two being even superimposed for low atom numbers indicating that the Maxwell-Bloch treatment seems legitimate here. With this new approach, the number of equations to solve does not depend on the number of atoms  $N$  but only on the number of Laguerre-Gauss modes involved. In practice, it seems that 5 to 10 modes are enough. This framework, beyond having the capability to be extended to the case of strong driving regime (see next section), is less demanding computationally than microscopic models when the number of atoms increases.

### Maxwell-Bloch equations in the high intensity regime

For the sake of completeness, we give here without derivation the set of equations of the model in the strong driving limit

$$\left\{ \begin{array}{l} \frac{\partial \rho_{ge}}{\partial t} = -\left(\frac{\Gamma}{2} + i\Delta\right) \rho_{ge}(z, t) - i\frac{\Omega(z, t)}{2} \exp(-ikz)[1 - 2\rho_{ee}(z, t)], \\ \frac{\partial \rho_{ee}}{\partial t} = -\Gamma\rho_{ee}(z, t) + \frac{i}{2}[\Omega^*(z, t) \exp(ikz)\rho_{ge}(z, t) - \Omega(z, t) \exp(-ikz)\rho_{eg}(z, t)], \\ \frac{\partial \Omega_+^{(q)}}{\partial z} + \frac{1}{c} \frac{\partial \Omega_+^{(q)}}{\partial t} = -i\sqrt{\frac{2}{\pi w^2}} \frac{3\pi}{2k^2} \Gamma n f_q^*(z) \exp\left(-\frac{z^2}{2\sigma_z^2}\right) \tilde{\rho}_{ge}(z, t), \end{array} \right. \quad (2.56)$$

with  $\Omega(z, t)$  the Rabi frequency defined by

$$\Omega(z, t) = \sqrt{\frac{\pi w^2}{2}} \frac{1}{2\pi\sigma_r^2} \sum_{p=0}^{\infty} f_p(z) \Omega_+^{(p)}(z, t). \quad (2.57)$$

Note that the equation for the field is identical to the one in the low intensity case.

The same approximations as for the low intensity regime are performed. We emphasize nonetheless that, in contrast with the low intensity regime, while performing the continuous approximation, correlations between the coherences and the populations of different atoms have to be neglected:  $\langle \rho_{ge}^l \rho_{ge}^j \rangle \approx \langle \rho_{ge}^l \rangle \langle \rho_{ge}^j \rangle$ , and  $\langle \rho_{ge}^l \rho_{ee}^j \rangle \approx \langle \rho_{ge}^l \rangle \langle \rho_{ee}^j \rangle$ , with  $\langle \cdot \rangle$  the configuration average resulting from the continuous approximation.

The steady-state regime in the strong intensity case is governed by the following equation

$$\frac{d\Omega_+^{(q)}}{dz} = -\frac{3\Gamma n}{4(k\sigma_r)^2} \frac{f_q^*(z)}{\Gamma + 2i\Delta} \exp\left(-\frac{z^2}{2\sigma_z^2}\right) \sum_{p=0}^{\infty} f_p(z) \Omega_+^{(p)}(z) \frac{\Gamma^2 + 4\Delta^2}{\Gamma^2 + 4\Delta^2 + 2|\Omega(z, t)|^2}. \quad (2.58)$$

One can recover (2.55) from (2.58) when the driving intensity is small ( $\Omega_0 \ll \Gamma$  hence  $|\Omega(z, t)| \ll \Gamma$ ). Solutions of this equation, with  $N$  equal to 100 atoms and for various saturation parameters, are displayed in Figure 2.21. We note that as  $s$  gets above unity, the amplitude and the shift of the line are drastically suppressed. It would be interesting to measure the coherent response of cold two-level atoms in the strong intensity regime to compare with the predictions of the Maxwell-Bloch model presented here. The comparison should not be too hard as the signature of the strong intensity regime is strongly visible when  $s$  is above a few units.

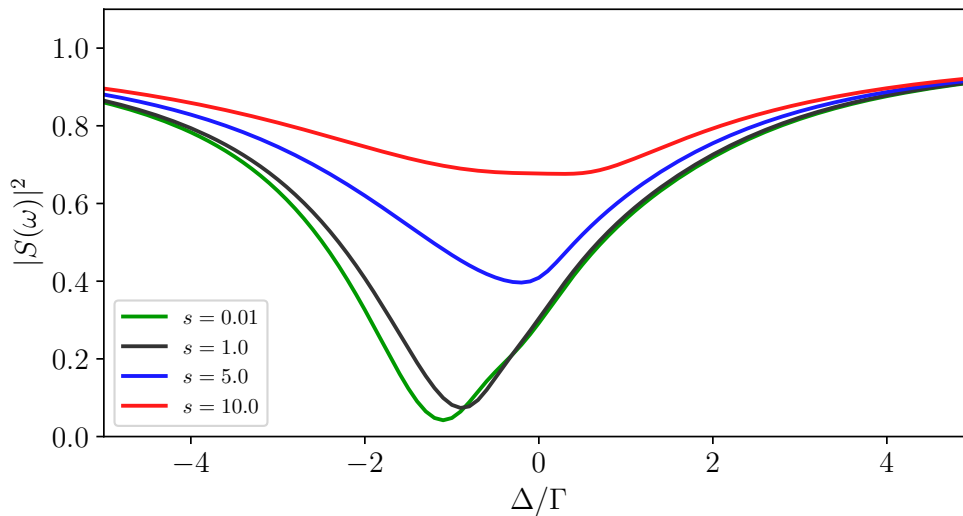


**Figure 2.21.:** Maxwell-Bloch simulations in steady-state regime. The curves represented here are the solutions of (2.58) with  $N = 100$  atoms and for various saturation parameters  $s = [0.01, 1, 5, 10]$ . The equation being able to handle to high intensity regime, we are not restricted to small values of  $s$ .

## 2.5 CONCLUSION

In this chapter, after having presented the latest experimental results obtained in our experiment, explicitly the coherent transfer function of a dense cloud of  $N$  two-level atoms probed close to resonance, we have simulated the theoretical response using a discrete coupled-dipoles models. We have tried to explain the remaining discrepancies by changing the experimental parameters on the simulations, and we have even tried to include motion, in an empirical manner, in order to obtain a better agreement. Despite all these efforts, no quantitative agreement between theory and experiment has been obtained. The two possible guilty candidates introduced at the end of section 2.3, which were the internal structure of Rubidium and the residual motion of the atoms in the cloud, do not seem to explain the discrepancies between theory and our experimental measurements.

We have to question others assumptions in our experimental approach that could be inappropriate. One possible explanation is a wrong estimation of our density. Indeed, the cloud size being smaller than the diffraction limit, we only have an undirect access to the volume occupied by the atoms in the cloud, and it is given under the assumption that the volume is an *independent* quantity. The volume calculation being related to the temperature of the cloud, we have checked experimentally that the temperature does not depend on the number of atoms in the cloud, at least over our range of atoms (from 1 to  $\sim 200$ ). But, it could be that our estimation of the volume is nonetheless wrong. An over-estimation of the density would have important impacts on the predictions of

our theoretical models: a smaller density leads to a more symmetrical coherent transfer function, featuring a smaller shift and a smaller broadening. Because we always measured less pronounced effects on our measurements compared to theoretical predictions, this point would have to be investigated for completion of our works.

This chapter has also been the opportunity to introduce and derive a new model developed by our collaborators in order to address the high intensity regime. Based on Maxwell-Bloch equations and using a continuous medium approximation, we have checked that it was consistent with the coupled-dipoles regime for weak-driving field. Although no reliable measurement has been performed in the high-intensity regime, we have now a theoretical model for a regime where the coupled-dipoles is expected to fail and that is less computational demanding compared to a discrete model.

# CHAPTER 3

## A NEW APPARATUS TO STUDY DIPOLE-DIPOLE INTERACTIONS

---

### Contents

---

<b>3.1. Design of the new apparatus</b>	<b>69</b>
3.1.1. New vacuum chamber	69
3.1.2. MOT coils	70
3.1.3. Microwave antenna	74
3.1.4. Vacuum	74
3.1.5. Other modifications	74
Computer Control	74
New CCD camera	75
<b>3.2. Alignment of the aspheric lenses</b>	<b>76</b>
3.2.1. Relevant optical quantities	76
3.2.2. The aspheric lenses	78
Choice of a given conjugation	78
Alignment procedure	81
Understanding the distribution of intensity	84
<b>3.3. Characterization of performance</b>	<b>86</b>
3.3.1. Single atom regime	87
3.3.2. Trapping frequencies	88
Aspheric lens A	88
Aspheric lens B	92
3.3.3. Lifetime measurement	93
<b>3.4. Limitation of the performance - The viewports and the spherical aberration</b>	<b>95</b>

<b>3.5. The future tools . . . . .</b>	<b>98</b>
3.5.1. Optical tweezer of variable size . . . . .	99
3.5.2. Accordion lattice . . . . .	101

---

Being unable to obtain a satisfactory agreement between theoretical models and our experimental measurements, and in order to keep investigating the influence of dipole interactions induced by resonant light in cold atomic ensembles, we have decided to upgrade the experiment to add new functionalities. The new experiment was designed with two main criteria in mind:

- allowing more flexibility on the shaping and the observation of our dense cloud of atoms. For that matter, we decided to include a second high resolution optical axis, at  $90^\circ$  from the previous one. The two axes, together, allow for the simultaneous observation of the fluorescence light emitted by the atoms (*incoherent* response) and the transmission through the cloud (*coherent* part). They also enables the shaping of the cloud into a slab for instance.
- solving experimental problems present, at different level, on all the setups of the group using high numerical aperture (NA) lenses. Two of those experimental problems being:
  - a painful alignment of the MOT. The MOT beams being small and some beams being not orthogonal to some others, owing to the small working distance  $\sim 5.7$  mm of the previous high NA aspheric lens, the displacement of the MOT to overlap with the dipole trap was not an easy task (too many coupled parameters).
  - lots of scattered light inside the chamber. This stray light, mainly due to the scattering of MOT beams onto the aspheric lens holder, is collecting by the imaging system and makes it harder to find atomic signal for instance.

We have thus decided that the new apparatus will be based on new high NA lens with larger working distance. The larger working distance will increase the available space between the two lenses of the same axis, hence limiting the scattered light on the lens holder and enabling larger MOT beams at  $90^\circ$  from each others. These high NA lenses with larger working distances did not exist when the previous setup was mounted in 2005-2006. Beyond solving the two mentioned experimental problems, the new lenses would also enable to address the question of dipole-dipole interactions in new configurations.

This chapter is organized in five parts. The first one is dedicated to the design of the new apparatus. The second part concerns the details of the challenging alignment of two crossed high resolution axes of aspheric lenses. To our knowledge, this alignment has been done only in one other group, with a different alignment procedure, almost simultaneously ([Bruno et al., 2019]). The third part of the chapter is devoted to the

characterization of the optical performance of the new apparatus. The limitations are discussed in the fourth part. Finally, the last part is an overview of the future tools that are currently implemented or will be implemented.

### 3.1 DESIGN OF THE NEW APPARATUS

The implementation of two high resolution axes, composed of high numerical aperture aspheric lenses in an almost confocal configuration, implied a modification of the vacuum chamber to provide all the optical access needed for our experiment. Beside the lens holder that has to be put in vacuum, we have also included the MOT coils and a microwave antenna inside the vacuum chamber, in contrast with the previous version of the experiment.

#### 3.1.1 New vacuum chamber

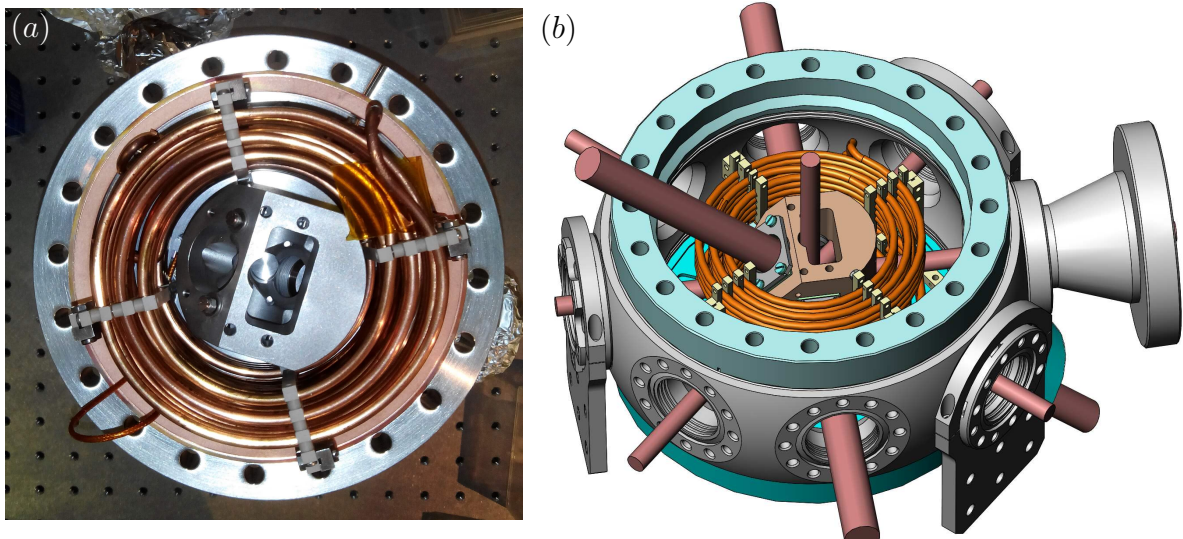


**Figure 3.1.:** (a): Picture of the vacuum chamber from the top. The lens holder is visible in the middle of the MOT coils that are fixed on the bottom part of the vacuum chamber. (b): Solidworks drawing of the vacuum chamber. We see the lens holder in the middle of the MOT coils. The MOT beams, the Zeeman beam and the two high resolution axes beams are also materialized.

The vacuum chamber is manufactured by Kimball physics (diameter 20.2 cm, CF160). The arrangement of the lens holder, the MOT coils and the microwave antenna has been designed by Florence Nogrette, research engineer at Laboratoire Charles Fabry. The main characteristic of this chamber is the second axis of aspheric lenses, whose direction is out of the plane parallel to the optical table. Indeed, because of space constraint (6

MOT beams, a Zeeman beam to slow down the atoms and one axis of two confocal aspheric lenses), all the standard optical accesses were used. The solution that has been implemented to enable another optical access for our second axis of aspheric lenses was to bring it out of the plane parallel to the optical table. It is materialized by the beam at  $45^\circ$  from the plane parallel to the optical table in Figure 3.1 (b). The optical access to this second high resolution axis is enabled by a tube that pops out of the vacuum chamber and which has motivated the name of this second generation of the experiment, *Cyclopix*, as it kind of remind the only eye of the cyclops.

### 3.1.2 MOT coils

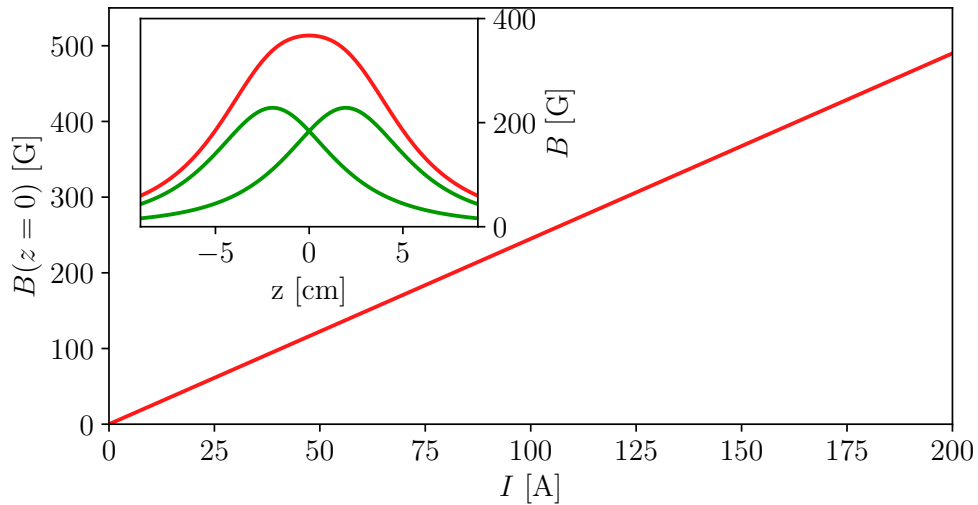


**Figure 3.2.:** Simulated  $B$  field produced by the MOT coils at the middle of the chamber (position of the cloud) versus current applied. Inset shows the field produced along the  $z$  direction for a current of 160 A. In green, the field produced by each coil; in red the sum of these two fields, with a maximum around 380 G.

The MOT coils have been designed such that they would be able to create an homogeneous magnetic field of approximately 500 Gauss with 200 A (see Figure 3.2). This homogeneous field is required if one wants to isolate a two-level structure inside the Rubidium atomic hyperfine states as the one presented in section 2.3 (the closed transition being separated from any other transition by  $12\Gamma$ ). Running such a current through the coils, even in pulsed mode, would induce some heating of the coils. Here, we address the question of the heating of the coils. By how much do the MOT coils temperature increases for a given current? And, more importantly, because of the black body radiation of the MOT coils, by how much does the lens holder temperature increases? This last question is of crucial importance as a heating will induce a dilatation of the materials and consequently a defocusing of the aspheric lenses.

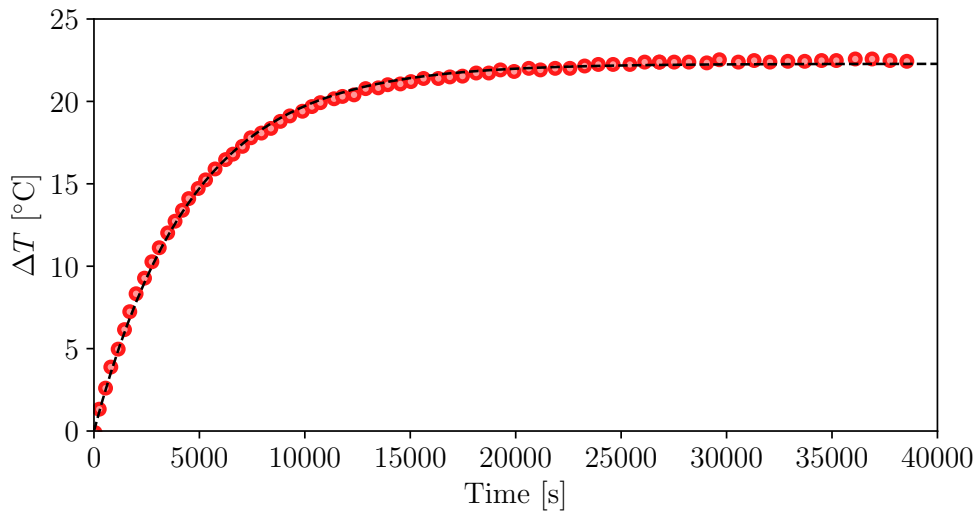


**Figure 3.3.:** Measurement of the heating of the MOT coils versus time for an applied current  $I = 12$  A. The black dashed line is an exponential fit of the data.

The MOT coils are made of 12 turns (4 layers of 3 concentric circles) of copper wire. To minimize as much as possible the resistance of the coils (but considering space constraints inside the chamber), we have chosen a wire of diameter  $2a = 4$  mm. Doing so, the resistance of each coils is  $R = 5.5$  m $\Omega$ . We applied a steady state current  $I = 12$  A, which corresponds to a power dissipated by the coil below 1 W, and measured the increase of voltage over the coil. Indeed, as the temperature increases, the resistance increases and so does the voltage, which are related through the relation

$$\frac{\Delta V}{V} = \frac{\Delta R}{R} = \alpha \Delta T, \quad (3.1)$$

where  $\alpha$  is known as the temperature coefficient of resistance and is equal to 0.0038 K $^{-1}$  for copper around 20°C. The measurement of the increase of temperature of the coil versus time is shown in Figure 3.3.

We have fitted the data with the function  $f(t) = \Delta T_{\infty}(1 - \exp(-t/\tau))$  and extracted the increase of temperature at infinite times  $\Delta T_{\infty} = 22.3$  K and a time constant  $\tau = 4621$  s (1 hour and 17 minutes). We understand and exploit those values with a simple model based on Stefan-Boltzmann law considering the coils behave as black bodies. In the stationary regime, the electrical power per unit of surface  $P_{\text{surface}}$  is dissipated as thermal radiation, hence related to the temperature increase through the following relation

$$P_{\text{surface}} = \frac{RI^2}{S_{\text{lateral}}} = \varepsilon\sigma[(T_0 + \Delta T_{\infty})^4 - T_0^4], \quad (3.2)$$

with  $R$  the resistance of the copper,  $\varepsilon$  the emissivity of our coils,  $\sigma = 5.67 \cdot 10^{-8}$  W.m $^{-2}$ .K $^{-4}$  the Stefan-Boltzmann constant and  $T_0$  the initial temperature of the coils assumed to

be the one of the surrounding. We neglect here the thermal contact with the coils flange holder. One can simplify (3.2) considering that  $\Delta T_\infty \ll T_0$  (which is the case here because  $\Delta T_\infty \sim 20$  K and  $T_0 = 300$  K)

$$RI^2 = \varepsilon\sigma S_{\text{lateral}} \times 4T_0^3 \Delta T_\infty, \quad (3.3)$$

where  $S_{\text{lateral}} = 2\pi aL$  is the lateral surface of the coil,  $L$  being the length of the wire. Finally, using the fact that  $R = \rho \frac{L}{S_\perp}$ , with  $\rho = 1.68 \cdot 10^{-8} \Omega \cdot \text{m}$  the resistivity of copper at room temperature and  $S_\perp = \pi a^2$  the transverse section of the wire, one can obtain

$$\Delta T_\infty = \frac{\rho I^2}{8\pi^2 a^3 \varepsilon \sigma T_0^3}. \quad (3.4)$$

Plugging the value of  $\Delta T_\infty$  inside the previous, we get an estimation of the emissivity of our coil:  $\varepsilon \approx 0.11$ .

The emissivity value can be confirmed using the transient regime of the curve. Assuming that the time constant  $\tau$  follows the relation

$$RI^2\tau = mC_m\Delta T_\infty, \quad (3.5)$$

with  $m$  the mass of the coil and  $C_m$  the heat capacity which is equal to  $385 \text{ J} \cdot \text{kg}^{-1} \cdot \text{K}^{-1}$  for copper. Replacing (3.4) into (3.5), and using  $m = \rho_m \pi a^2 L$  with  $\rho_m = 8.96 \text{ g} \cdot \text{cm}^{-3}$  the volumetric mass density of copper, one can get

$$\tau = \frac{\rho_m C_m a}{8\varepsilon\sigma T_0^3}. \quad (3.6)$$

When using the value of  $\tau$  extracted from the fit, we calculated the value of emissivity and obtain  $\varepsilon \approx 0.12$ , very close to the one obtained with (3.4).

We now have at our disposal a relation to predict the temperature of the coils versus time for any current  $I$

$$T_{\text{coils}} = T_0 + \Delta T_\infty (1 - \exp(-t/\tau)), \quad (3.7)$$

with  $\Delta T_\infty$  and  $\tau$  respectively given by (3.4) and (3.6). Concerned about the heating of the lens holder placed in the middle of the coils, because it could induce a variation of the relative distance between the aspheric lenses hence defocusing our image in the camera, we have measured its increase of temperature (see Figure 3.4). Note that to measure directly the temperature of the lens holder, the measurement has not been performed in vacuum. We have found an increase of temperature of  $\sim 5$  K in  $\sim 7$  hours. Similarly to the previous study, we have reproduced the data using a simple model. Assuming that the lens holder, with a heat capacity  $C$  and emissivity  $\varepsilon_h$ , is heated up

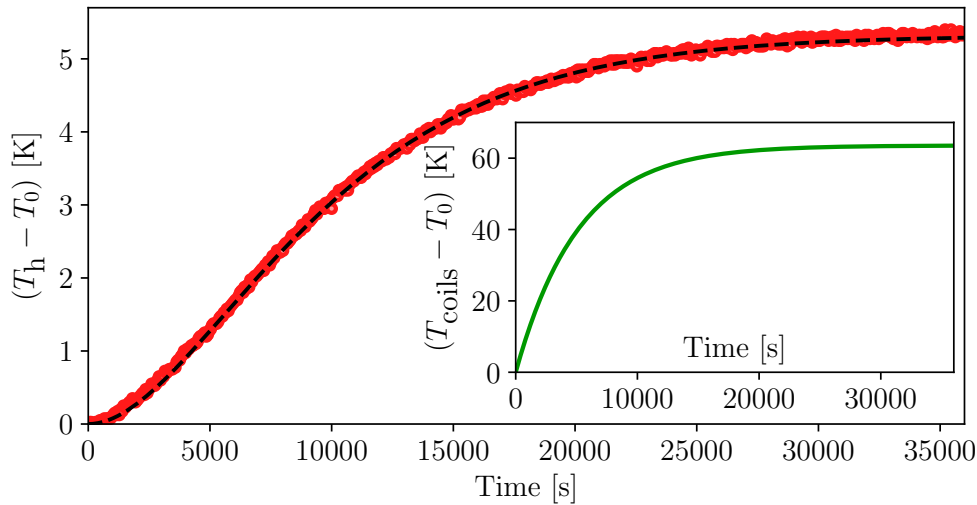


**Figure 3.4.:** Measurement of the heating of the lens holder versus time for an applied current in the coils of  $I = 20$  A. The black dashed line is a numerical simulation of the temperature when solving (3.8) with  $R = 8.5$  K.W $^{-1}$  and  $\varepsilon_{\text{holder}} = 0.14$ . Inset shows the simulated temperature of the coils versus time for  $I = 20$  A according to (3.7).

by the coils and is connected to the vacuum chamber at  $T_0$  through a thermal resistance  $R$ , its temperature  $T_h$  is a solution to the following equation

$$C \frac{dT_h}{dt} = -\frac{1}{R}(T_h - T_0) + \varepsilon_h \sigma S_{\text{lat}} [T_{\text{coils}}^4 - T_h^4], \quad (3.8)$$

with  $S_{\text{lat}} = 9 \cdot 10^3$  mm $^2$  the lateral surface of the lens holder. The value of the heat capacity is given by  $m_h \times C_m \approx 520$  J.K $^{-1}$  ( $m_h \approx 1.35$  kg). Solving (3.8) with  $R = 8.5$  K.W $^{-1}$  and  $\varepsilon_h = 0.14$  reproduces the data very well (see black dashed line in Figure 3.4). Note that to solve this equation, we have simplified  $T_h^4 \sim T_0^4$  in the black body radiation term in (3.8). However, we did not perform the approximation  $\Delta T_\infty \ll T_0$ .  $\Delta T_\infty$  being  $\sim 60$  K (see inset of Figure 3.4), the approximation  $T_{\text{coils}}^4 \sim T_0^4 + 4T_0^3 \Delta T_\infty$  would have resulted in an error of 13% when  $t \rightarrow \infty$ , and consequently an overestimation of  $R$  and  $\varepsilon_h$  of the same amount.

In conclusion, the lens holder is heating up by the MOT coils. If we consider the linear thermal expansion coefficient of stainless steel  $\alpha_L \approx 14 \cdot 10^{-6}$  K $^{-1}$ , an increase of 5 K would introduce a shift of the position of the lens of 7  $\mu\text{m}$ . Such a defocus can be not too hardly compensating on the experiment but it would require first to reach a steady state and according to the measurement, this can take as long as 7 hours. Note that the final temperature of the lens holder, and then defocus introduced on the camera, depend on the current applied in the coils. However, the power dissipated by the coils being related to the RMS value of  $I$ , running the coils at 200 A with a duty cycle of 1% would induce the same heating.

In order to not induce a defocusing of our imaging system, we have built a new pair of coils that are placed outside of the vacuum chamber and which purpose is to generate the homogeneous B field. These coils, 20.5 cm of mean diameter, are made with 19 spires of a 4 mm side square wire. The wire benefits from an empty inner part, a 2 mm diameter hole, that enables to cool down the coils by making water flow through it.

### 3.1.3 Microwave antenna

The new vacuum chamber benefits also from a microwave antenna. This antenna is made of a single coaxial wire (part number:380-SMA-MX-500, sold by allecra<sup>®</sup>) with a connector at only one of its ends. The SMA male connector enables to connect it from the outside of the vacuum chamber (feedthrough), while the other end (without connector) is placed inside the lens holder to serve as an antenna. Note, however, that no attempt has been made to adapt its impedance. The company guarantees that the cable is compatible with ultra-high vacuum below the  $10^{-10}$  mbar level. The idea behind using this cable is to be able to address the ground state hyperfine splitting of the atoms with less power than a microwave antenna would require if placed outside the vacuum chamber.

### 3.1.4 Vacuum

In contrast with the previous version of the apparatus, there are now many parts inside vacuum: the MOT coils, the lens holder, the four aspheric lenses, a microwave antenna and all the screws and connectors needed to maintain everything. This was a source of concern for the quality of the vacuum that we could reach, because of outgassing. Nonetheless, we have decided to keep the same ion pump. After several baking procedure and the use of a titanium sublimation pump, we reached a pressure of  $5 \times 10^{-11}$  mbar, measured at the gauge. The level of pressure is comparable to the one that the group had with the previous version of the apparatus. A more precise measurement of the vacuum pressure will be established with a single atom in subsection 3.3.3.

### 3.1.5 Other modifications

#### Computer Control

The computer control of the experiment has also been entirely modified. With respect to the previous one described in [Jennewein, 2017], the three National Instruments cards (the digital card NI-6534, the analog card NI-6713 and the counting card NI-6601) used in our experiment are now implemented in the same computer and a unique Python software, whose graphical interface has been designed by our co-worker from the other project in the group, Vincent Lienhard, and which has been adapted to the need of

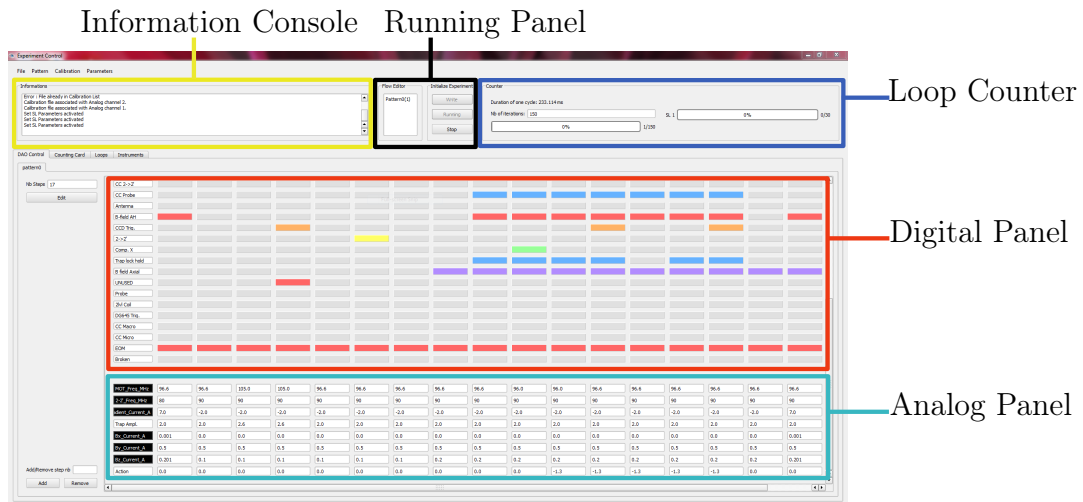


**Figure 3.5.:** Screenshot of the Python program used to control the experiment. The Digital and Analog panels set the sequence that will be written on the NI cards. The Loop counter keeps track of the number of repetition of the experiment (loops) as well as on the modification of experimental parameters (super-loops). The Running panel starts and stops the sequence, if needed. The Information Console is displaying information that may be useful for the user.

our experiment, controls these three cards. The principle of operation is similar to the one implemented and described in [Jennwein, 2017]. The only difference, besides the programming language, is that no communication protocol is needed. Before, the various cards were installed in different computers. The implementation of the sequence was done in each computer to specify to each card, with their associated software, what they were supposed to do and a communication, through local network to which all computers were connected, was needed to make the cards work together on the same sequence. Now, the cards being inside the same computer, the synchronization between the tasks implemented in each card is automatic. No need to set up a synchronization link between the different computers that hold the cards as before. The computer is sufficiently powerful to hold the three cards and run a unique 3-in-1 software to control the experiment. Another Python software, previously used by our co-workers and adapted to our needs, on a second computer, is controlling the camera. A third computer is used to analyze the data.

### New CCD camera

With respect to the previous setup, this new version benefits also from a new electron-multiplying CCD camera (EMCCD), an Andor iXon<sup>®</sup>. This camera can work in amplification mode to be sensible to the single photon level and has a quantum efficiency close to 80% at our wavelength of interest. Thus, we will manage to obtain the same

signal to noise ratio as with the previous imaging system but with less repetitions. The previous imaging system was composed of a intensifier in front of the camera that enabled to have a high sensitivity but was also responsible of a drop of the quantum efficiency to the 10% level.

## 3.2 ALIGNMENT OF THE ASPHERIC LENSES

As for the previous apparatus that has been partially described in section 1.2 and entirely presented in [Fuhrmanek, 2011], the new apparatus is composed of aspheric lenses to highly focus the trapping beam and create small dipole traps. The major difference is that this new device is not composed of only one axis of two aspheric lenses in an almost confocal configuration but of two axes of aspheric lenses orthogonal to each other. The second axis will allow to have a direct access to the measurement of the longitudinal dimension of the cloud, that was so far deduced from its transverse dimension. As will be detailed later, it will also allow to compress the cloud with laser beams [Ville et al., 2017] and thus increase its density. The first part of this section is dedicated to the definition of some relevant optical quantities. The second part is dedicated to the procedure we have used to perform the challenging alignment of our four aspheric lenses.

### 3.2.1 Relevant optical quantities

Before going into the details of the alignment procedure for the aspheric lenses, it could be useful to remind some of the optical quantities that will be used in the following sections.

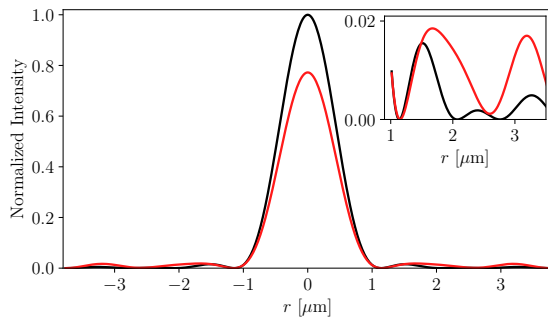


**Figure 3.6.:** Simulated intensity profile at the focus of a lens: with  $0.07\lambda$  of third order spherical aberration (red) and without aberration (black). The inset shows the profile in the wings.

Spherical aberrations can be seen, in the case of a lens, as a modification of the focal length depending on the distance of the incident ray with respect to the optical axis. In other terms, all the incident rays of light will not cross the optical axis at the same point after being focused by the lens. This results in a spread of the focus, therefore a smaller peak intensity at the focal point. From the atomic physics point of view, one will thus need more laser power to achieve the same trap depth and the same oscillations frequencies of the atoms in the trap. Aspheric lenses have been designed to overcome spherical aberrations. Beyond being vacuum compatible, they are also easier to

align and less expensive than microscope objectives. Aberrations have to be considered as soon as one wants to use an optical system out of axis and/or on axis but on large fraction of its aperture. In this respect, the relevant parameter is the numerical aperture,  $NA$ , defined as

$$NA = n \sin \alpha',$$

where  $n$  is the index of refraction of the medium in which the lens is working and  $\alpha'$  is the half-angle of the cone of light entering the lens. We will consider in the following that  $n = 1$ , unless stated differently. Another useful quantity is the working f-number  $N$ , defined as

$$N = \frac{f'}{\phi},$$

where  $f'$  is the focal length of the lens and  $\phi$  the diameter of its entrance pupil. If the aplanetic lens is working in an infinite-to-focus conjugation, we link the two previously defined parameters with the relation  $NA = 1/2N$ . An optical system, even if composed of only one element, is said to be aberration-free if its point spread function (PSF) corresponds to an Airy disk. The Airy disk is also the diffraction pattern obtained when a plane wave is going through a circular aperture. The intensity distribution, at the focal plane of the lens, is given by

$$I_{\text{stig}}(r) = I_0 \left( \frac{2J_1\left(\frac{\pi r}{\lambda N}\right)}{\frac{\pi r}{\lambda N}} \right)^2, \quad (3.9)$$

where  $J_1$  is the Bessel function of the first kind of first order,  $r$  is the radial distance from the optical axis and  $\lambda$  is the wavelength of the light. In the presence of aberrations, the point spread function of the lens is modified. When aberrations are not too important, the distribution of intensity looks like an Airy disk but the maximum of intensity is reduced, the lost intensity being redistributed in the wings of the profile, as depicted in Figure 3.6. The ratio between the maximum intensity at the focus point of the lens  $I_{\text{aberr}}$  and the maximum theoretical intensity  $I_{\text{stig}}$  which would be obtained if the lens were perfectly stigmatic (i.e., free of aberrations) is a first manner to define the optical performance of the system: it is called the Strehl Ratio and is denoted  $S$ . This ratio is related to the deformation of the wavefront [Born and Wolf, 2003]

$$S(\lambda) = \frac{I_{\text{aberr}}}{I_{\text{stig}}} \approx 1 - \frac{4\pi^2\sigma_{\Delta}^2}{\lambda^2}. \quad (3.10)$$

Here,  $\sigma_{\Delta}$  denotes the root-mean-square standard deviation of the actual wavefront with respect to the ideal one, and  $\lambda$  is the wavelength of the light. A criterion, often used by opticians to estimate the quality of an optical system, is  $S \geq 0.80$ , which turns out to be equivalent to  $\sigma_{\Delta} \leq \lambda/14$  (Marechal criterion).

A second quantity which is used to define the quality of an optical system is the Modulation Transfer Function, MTF, defined as the module of the Fourier Transform of

the PSF. This quantity indicates how much of the object's contrast is reproduced in the image as a function of the spatial frequency  $f$ . Using Fourier Transform properties, the MTF can be expressed as the auto-correlation of the entrance pupil. In the case of an aberration-free optical system with circular and homogeneous aperture, the MTF has an analytic expression given by

$$\text{MTF}(f) = \frac{2}{\pi} \left( \arccos \left( \frac{f}{f_c} \right) - \frac{f}{f_c} \sqrt{1 - \left( \frac{f}{f_c} \right)^2} \right), \quad (3.11)$$

where  $f_c = \frac{1}{\lambda N}$  is the cut-off frequency. This quantity can also be used to estimate the Strehl Ratio of an optical system. It is the ratio of the integral of the  $\text{MTF}_{\text{aberr}}$  in presence of aberrations to the integral of the MTF of an ideal optical system

$$S = \frac{\iint \text{MTF}_{\text{aberr}}(\mathbf{f}) d^2 f}{\iint \text{MTF}(\mathbf{f}) d^2 f}. \quad (3.12)$$

(3.12) is the quantity that we have used when we were trying to determine the best alignment for each aspheric lens.

### 3.2.2 The aspheric lenses

The aspheric lenses chosen for the new version of the apparatus are designed and manufactured by Asphericon<sup>®</sup>. The part number of those lenses is AHL25-20-S-U. Their diameter  $\phi$  is 25.0 mm (reduced to 20.0 mm to fit in the lens holder apertures) and their effective focal length  $f'$  is equal to 20.0 mm. They are diffraction limited up to a numerical aperture of 0.54 (0.45 after reduction of their diameter). Those lenses have a bigger diameter than the previous ones because of space constraints: the four lenses needed to look at the same point of space, not touching each other, and allowing the MOT beams to intersect at this particular point. To enable bigger MOT beams with respect to the previous experiment, the aspheric lenses have been cut on the edges. Although they have a bigger diameter compared to previous ones, they have the same numerical aperture (NA), thus enabling to obtain the same spot size at the focus of the lens as before. Those lenses are made of S-LAH64 material which has a refractive index  $n$  close to 1.78 for our relevant wavelengths.

#### Choice of a given conjugation

We have performed simulations using an optical design software, OSLO, to obtain the best focus positions for our two wavelengths of interest:  $\lambda = 780$  nm, the D2 line transition wavelength of Rubidium 87, and  $\lambda_{\text{trap}} = 940$  nm, the trapping beam wavelength used in our experiment. Because of the high refractive index of the lens, the

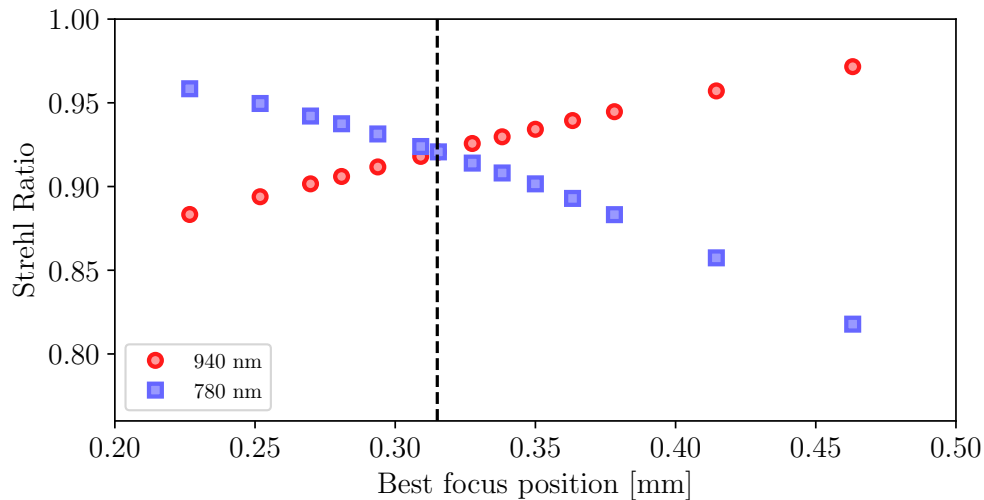


**Figure 3.7.:** Numerical simulation of the Strehl ratio at 940 nm (red circles) and 780 nm (blue squares) performed with OSLO. The best focus position is given with respect to a position that is 15.714 mm from the last surface of the lens. The Strehl Ratio at 940 nm is given in the best focus of the lens where the atoms will be trapped and the Strehl Ratio at 780 nm is given at the best position of the camera that will image the atoms trapped.

best performance for the trapping beam at  $\lambda_{\text{trap}}$ , in a collimated configuration, did not corresponds to the best performance for the imaging at  $\lambda$ . We have then decided to choose a trade-off configuration where the optical performance of the aspheric lens is similar for the two wavelengths. The criterion that we have chosen to determine the best configuration of our lenses is the Strehl ratio  $S$  and, as it can be seen in (3.10), it depends on  $\lambda$ . The result of this simulation is depicted in Figure 3.7. To be more specific, the simulation is performed as follows:

- find the best focus at 940 nm for different conjugation, i.e., for different positions of a fictitious point source emitting a spherical wave at 940 nm that will be focused by the aspheric lens (the atoms will be trapped where the intensity is maximum, i.e., where the Strehl ratio is maximum);
- knowing the position of the atoms, find the best position of the camera to image their fluorescence emission.

Doing so we have, for a given position of the atoms, the Strehl Ratio at this location for the 940 nm trapping beam and the Strehl ratio at the best position of the camera to image them at 780 nm. We found that for a position of 0.315 mm, the Strehl Ratio seen by the atoms at 940 nm and the one corresponding to the fluorescence image at 780 nm on the camera is the same, about 0.93 (see Figure 3.7). This position of the atoms dictates the position of the fictitious 940 nm point source  $d_{0,940}$  and the position of the camera  $d_{0,780}$  with respect to the first surface of the lens that, in vacuum, are the

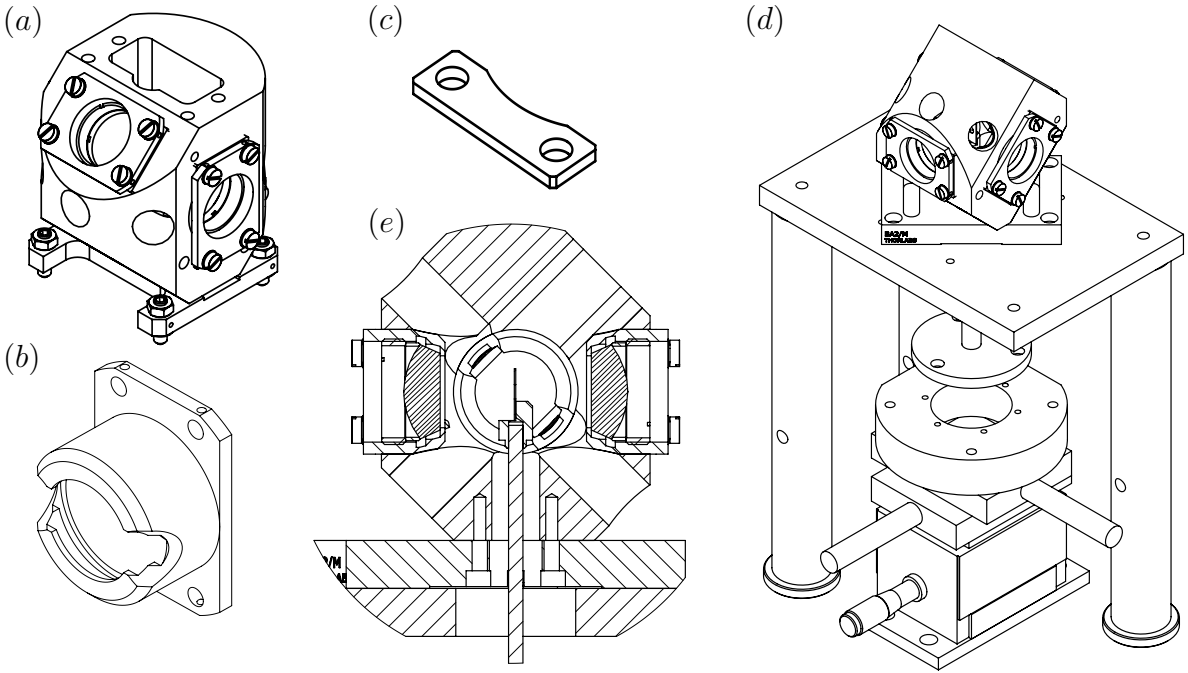


**Figure 3.8.:** Solidworks drawings of the element used for the alignment procedure of the aspheric lenses. This work has been performed by F. Nogrette. (a): Lens holder. The barrels (b) that hold the aspheric lenses are inserted inside the lens holder and separated from it with spacers made of glass (c). (d): Drawing of the apparatus used to align the aspheric lenses. The lens holder is tilted such that both high resolution axes are contained in a plane parallel to the optical table. Below it, a XYZ translation stage can displace a pinhole placed at the top of rod and that have been inserted inside the lens holder through one of its aperture (e).

following

$$\begin{aligned}d_{0,940} &= 2127 \text{ mm}, \\d_{0,780} &= 1264 \text{ mm}.\end{aligned}$$

Because the alignment procedure will be performed in air and not in vacuum, we have performed the same simulations but taking into account the modification of the index of refraction of air  $n_{\text{air}} \approx 1.0003$  compared to the one of vacuum. We found that the best focus is now at 0.369 mm. This position corresponds to the following distances in air

$$\begin{aligned}d_{940} &= 1747 \text{ mm}, \\d_{780} &= 1119 \text{ mm}.\end{aligned}$$

This conjugation is our target. We will explain in the next section how we tried to obtain this configuration for each one of the four lenses.

## Alignment procedure

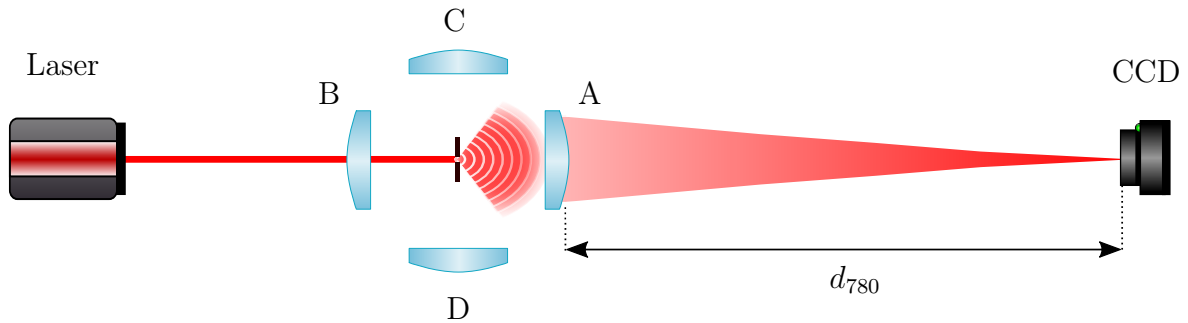


**Figure 3.9.:** Sketch of the alignment setup. A CCD camera is placed at a fixed position  $d_{780}$  while we shine a 780 nm laser beam onto a pinhole that acts like a point source for the aspheric lens A. By moving the pinhole with respect to lens A, we optimize the Strehl Ratio on the camera and we have access to the best focus of this lens.

Once the conjugation has been chosen, we have to align the four lenses. This is an experimental challenge. Indeed, we need to intersect two optical axis in space with a precision better than  $10 \mu\text{m}$  (a precision better than the field of view of our aspheric lenses). For that purpose, we have elaborated a procedure that we now describe.

Our four lenses are held in a piece of metal where two axes have been defined by the most accurate mechanical precision achievable. The general tolerances requirements, for all the parts in the vacuum chamber, were  $\pm 0.1 \text{ mm}$  for position and  $\pm 0.1^\circ$  for angle. Some parts benefit from better precision. Then, the only degree of freedom that we have to get a confocal configuration is the distance between the lenses of the same axis. To do so, we change the thickness of a piece of glass (Figure 3.8 (c)) that is placed between the piece of metal (Figure 3.8 (a)) and the barrel (Figure 3.8 (b)) that holds the lens: it acts as a spacer. We have a precision of  $1 \mu\text{m}$  on the thickness of the piece of glass. To perform the alignment of the four lenses (denoted A,B,C and D as in Figure 3.9), we put a pinhole of diameter  $1 \pm 0.5 \mu\text{m}$  inside the lens holder (Figure 3.8 (e)). This pinhole, mounted on a rotational stage as well as on a XYZ differential translation stage (Figure 3.8 (d)), is used to simulate the fluorescence of the atoms.

By sending 780 nm light on the pinhole from the back, it will act as a point source. The asphere will focus the light emitted by the pinhole that is recorded on a camera (PCO Pixelfly 12bit resolution). The camera is set at a distance  $d_{780}$  from the aspheric lens (see Figure 3.9). We first have to check that the spherical wave that it emits will cover the full aperture of the lens. To do so, an iris diaphragm has been placed just after the lens and we have measured the size of the Point Spread Function (PSF) on the camera with respect to the aperture diameter of the iris. In practice, we fit the image obtained on the camera by an Airy function and we extract its radius. We know that

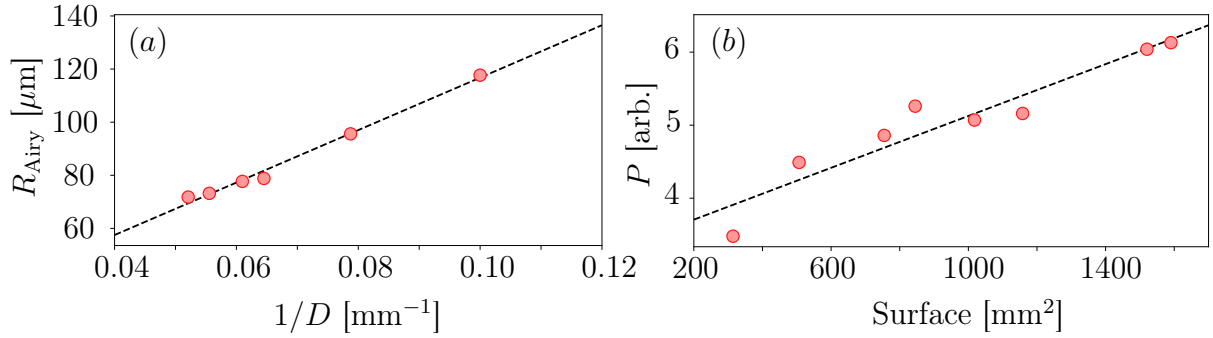


**Figure 3.10.:** (a): Size of the Airy radius fitting the Point Spread Function on the CCD camera versus the inverse of the aperture diameter. (b): Transmitted power through the iris with respect to its aperture. The power is computed by integrating the signal on the CCD camera, the background signal being removed. The transmitted flux is supposed to scale linearly with the surface of the aperture. Here, we obtain a correlation coefficient of 0.948, mainly due to the fact that the measurement of the aperture of the iris is not very accurate (uncertainty of the order of 0.05 mm).

the Airy pattern radius on the camera is given by the relation

$$\phi_{\text{Airy}} = \frac{2.44\lambda d_{780}}{D}, \quad (3.13)$$

where  $D$  is the diameter of the iris placed close to the lens. The results of this study are depicted in Figure 3.10 (a). We fit the data with a linear function and we extract the slope  $\alpha$  of the fit. We obtained  $\alpha = 988 \pm 49 \mu\text{m}\cdot\text{mm}$  which is in very good agreement with the theoretical slope  $\alpha_{\text{theo}} = 1.22\lambda d_{780} = 1024 \mu\text{m}\cdot\text{mm}$ . The conclusion is that on the full range of aperture (from 10 mm to 19.2 mm) the Airy pattern radius follows the law in one over the diameter of the aperture, so the pinhole diffraction pattern effectively covers the full aperture of the lens. To be more specific, the distance that we have taken into account to compute the theoretical slope is the distance between the camera and the iris, which is not perfectly superimposed with the lens. Another test that we performed, which is complementary to the previous one, is to measure the power  $P$  transmitted through the iris as a function of its aperture. As one can see in Figure 3.10 (b), the transmitted power scales linearly over the full range of the iris aperture, showing once again that the pinhole diffraction pattern cover the full lens aperture.

When we have the pinhole at a distance so that the size of the PSF on the camera is minimum, we know that we are in the targeted configuration. We then displace the pinhole in the transverse plane of this position to minimize the coma on the camera. Doing so, the pinhole is on the optical axis of the lens, at the proper distance from its first surface. The position of the pinhole for our first lens is our reference point. By keeping track of this position we have access to the best focus of each lens with respect

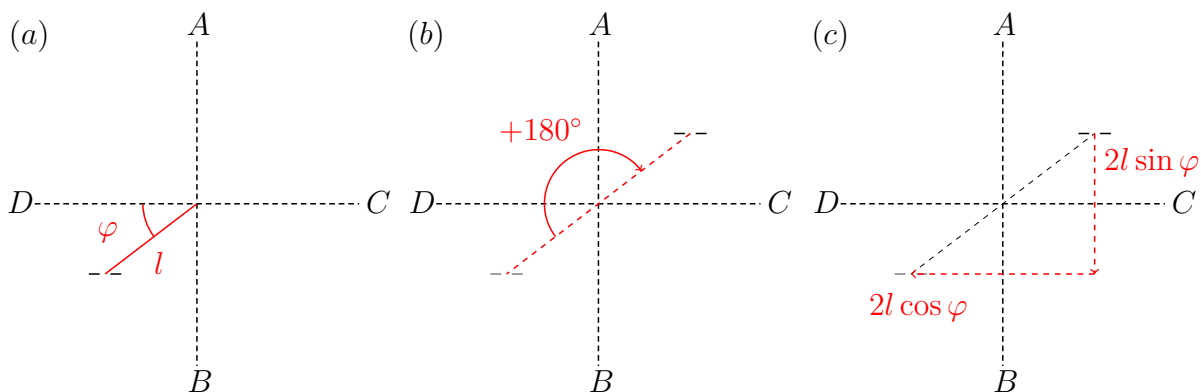


**Figure 3.11.:** Estimation of the eccentricity of the pinhole. Assuming that the pinhole image through lens  $A$  appears on the camera, and denoting  $l$  its radial distance from the axis of rotation,  $\varphi$  its angle with respect to the axis defined by lens  $D$  and  $C$  (a). We perform a rotation of  $180^\circ$  (b). The pinhole does not appear anymore on the camera. To recover its image on the camera, we have put it back to its original position, thus translating it by  $2l \sin \varphi$  long axis ( $AB$ ) and by  $2l \cos \varphi$  along axis ( $CD$ ) (c).

to this first position. But one needs to be able to replace the pinhole exactly at the same position after a rotation of the whole structure. This is achievable by knowing precisely the eccentricity of the pinhole with respect to the rotation axis. To measure this quantity, we have performed a simple test: we locate the position of the image of the pinhole on the camera, then we rotate the pinhole by  $180^\circ$  and we measure the displacement that we have to perform to obtain the position of the image of the pinhole back to its initial position. The result of this study is

$$\begin{cases} l &= 103.5 \pm 4.4 \mu\text{m} \\ \varphi &= 19.2^\circ \pm 1.4^\circ \end{cases} \quad (3.14)$$

where  $l$  is the eccentricity of the pinhole position with respect to the rotation axis and  $\varphi$  is the phase which is given with respect to the plane orthogonal to the  $AB$  axis and that contains the rotation axis (see Figure 3.11). The uncertainties are given with one standard deviation.

To summarize, the alignment procedure, although it has to be performed with a lot of caution, is quite simple. We start with lens  $A$ . The pinhole is placed in the conjugate plane of the camera, which is fixed. Then we translate the pinhole in this plane to bring it on the optical axis of the lens (i.e., we maximize the Strehl Ratio). We note this position and we study another lens. We rotate the pinhole so that it faces another lens and, knowing precisely its eccentricity, we translate it to bring it back to its initial position. We performed this procedure with each lens and, by keeping track of the pinhole position, we obtained a mapping of the best focus of each lens with respect to each other. For instance, Figure 3.12 shows the PSF obtained on the camera for lens  $C$  for dif-

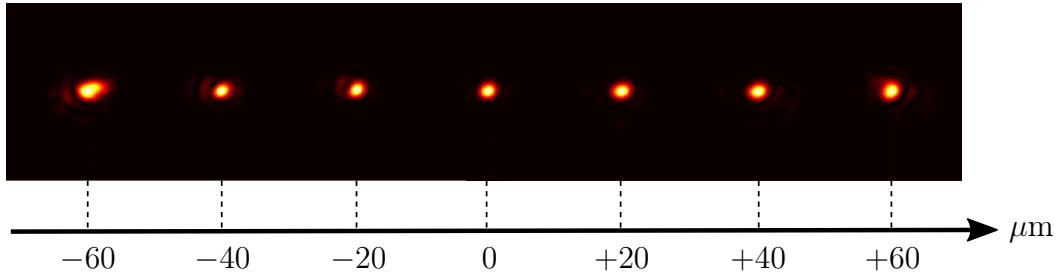


**Figure 3.12.:** PSF obtained on the camera for different position of the pinhole along the AB axis. The displacement are given with respect to the best position which is defined as the one with the highest Strehl Ratio, i.e., the one minimizing aberrations.

ferent position of the pinhole along the AB direction in the conjugate plane of the camera.

Now that we have a complete mapping of all the best focus for each lens, we know the thickness of the piece of glass we have to choose to bring all these best foci closer. Of course, if the optical axes of the lenses of the same axis (A and B or C and D) were the same, then this procedure would have perfect solution. Because the optical axes are not perfectly superimposed, after this procedure there remains a residual offset between all these best positions. That is due to the fact that the only degree of freedom that we have is the longitudinal translation of the lens along the axis defined by the mechanical construction of the lens holder. After this alignment procedure, and the modification of the thickness of the piece of glass taken into account, we obtain a configuration where all the best positions of each lens are as close as we can get them. Finally, we rely on the study mentioned in section 3.2.2 to obtain the same configuration with the lens holder in vacuum: the thickness of each piece of glass is reduced by  $54 \mu\text{m}$ .

### Understanding the distribution of intensity

In this section, we discuss the criterion used to determine what was the best position of the pinhole in the conjugate plane of the camera for each lens. To remind briefly what was said in the previous section, we shone  $780 \text{ nm}$  light, through the first lens, on a pinhole that acts like a point source for the second lens. We imaged the light that is focused by the second lens on the camera and then computed the Strehl Ratio associated with this picture (based on the definition given by (3.12)). The position of the pinhole that leads to the best Strehl Ratio on the camera is defined as the best focus of the lens. Whatever the definition used to compute the Strehl Ratio, we need to compare it to the expression of an ideal, aberration-free, optical system. The analytic expression of the relevant quantities are given for a circular aperture illuminated by a point source. However, we used a Thorlabs pinhole of diameter  $\phi = 1.0 \pm 0.5 \mu\text{m}$ ,

which is of the same order of magnitude as the wavelength of the light used for the alignment. It means that diffraction theory is not necessarily valid in this configuration and a precise description would require full electromagnetic field calculation. Here, we will investigate the modification of the intensity distribution, using diffraction theory, when the pinhole size is not small compared to the wavelength of interest. Comparing these simulations with the experimental spot sizes obtained on the camera, we will see if we find a size of the pinhole compatible with the specifications of the manufacturer.

Let us consider a point source located at  $A$ , on axis and at a distance  $z$  from a lens free of aberration, which is spatially limited by a circular aperture pupil  $p$ . Using Fraunhofer diffraction theory, the *incoherent* point spread function  $\text{PSF}_{\text{incoh}}$  in the conjugated plane of  $A$ , on axis and at a distance  $z'$  from the lens, is proportional to the modulus square of the Fourier Transform of the pupil

$$\text{PSF}_{\text{incoh}}(x', y') \propto |\text{FT}[p]|^2_{\left(\frac{x'}{\lambda z'}, \frac{y'}{\lambda z'}\right)}, \quad (3.15)$$

where  $x'$  and  $y'$  are the Cartesian coordinates in the conjugated plane of the object, and  $\lambda$  is the wavelength of the light. Using polar coordinates, the Fourier Transform is a Bessel function of first kind of first order  $J_1$

$$\text{PSF}_{\text{incoh}} \propto \left( \frac{2J_1\left(\frac{\pi r \phi_{\text{PE}}}{\lambda z'}\right)}{\frac{\pi r \phi_{\text{PE}}}{\lambda z'}} \right)^2, \quad (3.16)$$

where  $r$  is the radial coordinate in the conjugated plane of object  $A$  and  $\phi_{\text{PE}}$  is the aperture diameter. In the *incoherent* framework, the distribution of intensity in the image plane of the lens is given by the following convolution product

$$I_{\text{incoh}}(x', y') = \iint I_{\text{image}}(x'_0, y'_0) \text{PSF}_{\text{incoh}}(x' - x'_0, y' - y'_0) dx'_0 dy'_0, \quad (3.17)$$

where  $\text{PSF}_{\text{incoh}}$  is given, for a circular aperture, by (3.16), and  $I_{\text{image}}$  is the *perfect* distribution of intensity of the geometric image of the object, i.e., when no diffraction or aberration effects are considered. This distribution of intensity is related to the one of the object  $I_{\text{object}}$  through the magnification of the lens  $\gamma$ . Then, (3.17) can be rewritten

$$I_{\text{incoh}}(x', y') = \iint I_{\text{object}}\left(\frac{x'_0}{\gamma}, \frac{y'_0}{\gamma}\right) \text{PSF}_{\text{incoh}}(x' - x'_0, y' - y'_0) dx'_0 dy'_0, \quad (3.18)$$

Here, we consider the distribution of intensity in the image plane when the size of the object, the pinhole with a diameter  $\phi$ , is not small compared to the wavelength. In fact, let us recall that the manufacturer is providing a diameter  $\phi = 1.0 \pm 0.5 \mu\text{m}$  and the wavelength used for this procedure is  $\lambda = 780 \text{ nm}$ . We have computed (3.18) for our system with different sizes of the pinhole. The results of this simulation is depicted

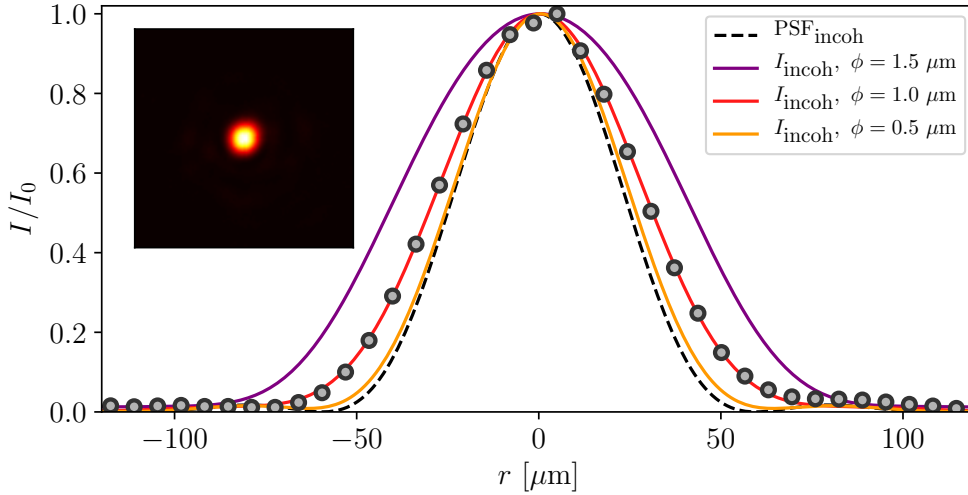


**Figure 3.13.:** Normalized distribution of intensity in the image plane of our aspheric lens when a pinhole of diameter  $\phi$  is used as the object. Calculations have been performed for three different sizes of the pinhole. The incoherent PSF (dashed dark line) is displayed for comparison. The gray dots are associated with the inset picture, obtained for the best configuration of lens C.

in Figure 3.13. One can see that when the pinhole size is smaller than the wavelength used, the distribution of intensity can be assumed to be equal to the Point Spread Function. As soon as this condition is no longer fulfilled, the convolution results in a spread of the distribution of intensity and an apodization of the secondary ring of the Airy pattern. Although the incoherent framework used here is questionable since we used a coherent source, our measured spot size on the CCD camera, see Figure 3.13, is in very good agreement with the simulated incoherent response obtained with a pinhole of size  $\phi = 1.0 \mu\text{m}$ .

### 3.3 CHARACTERIZATION OF PERFORMANCE

Before trying to reproduce previous results, such as the coherent transmission of resonant light through a dense cloud of two-level atoms, we have to characterize the performance of our new optical system. Knowing precisely its performances would result in a better confidence on our experimental results and can give a better intuition on what could possibly explain a potential disparity with theoretical predictions. An atom in a single dipole trap is a good probe to characterize our experimental setup. The single atom loading as been first shown in 2002 ([Schlosser et al., 2001]). Their fluorescence imaging is widely used in experiments ([Kuhr et al., 2001], [Nelson et al., 2007], [Bücker et al., 2009a]). It can be used to extract information about the residual background pressure in the vacuum chamber, or to measure the trapping frequencies to infer the trap characteristics lengths

for instance. In this section, we will summarize the characterization tests performed on the new apparatus.

### 3.3.1 Single atom regime

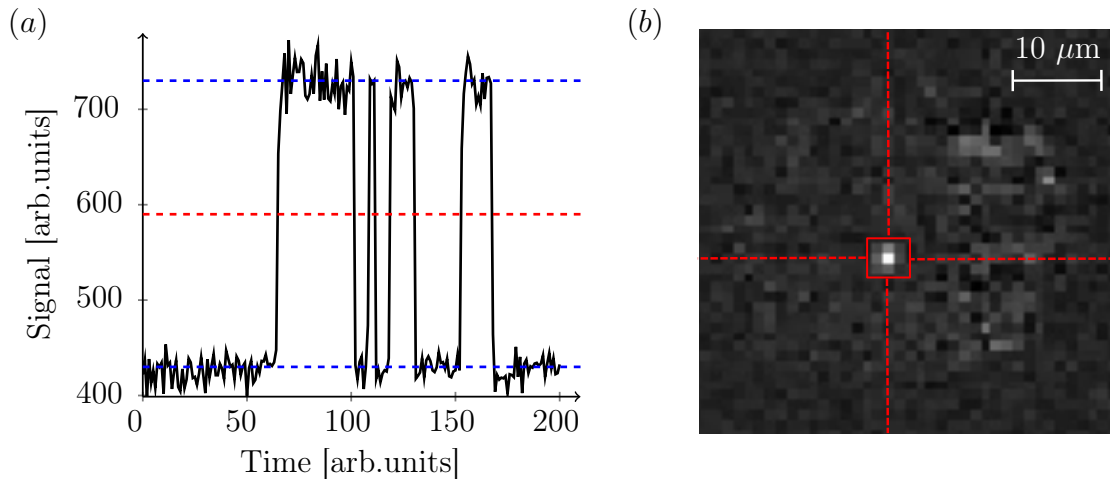


**Figure 3.14.:** (a): Temporal signal recorded by the camera. The signal is characteristic of the single atom regime: the fluorescence level of the pixel of interest is alternating between two values, the upper one corresponding to exactly 1 atom in the trap, and the lower one corresponding to no atom in the trap (dashed blue lines). The red dashed line is our threshold value to determine if an atom is present in the trap or not. (b): Picture taken by the camera. The exposure time is 50 ms. A background subtraction has been operated. We see a single pixel illuminated at the center of the image corresponding to the scattered light emitted by an atom in the dipole trap and collected by the imaging system. Each pixel ( $16 \times 16 \mu\text{m}^2$ ) corresponds to  $\sim 1 \mu\text{m}$  in the plane of the atoms.

An optical dipole trap can be filled with many atoms. The number of atoms in the trap is determined by the waist of the trapping beam, its power, as well as by various loading and collisions processes. Indeed, the interaction of light with the atoms that is responsible for the trapping being a conservative force, we only capture atoms with an energy smaller than the trap depth  $U_{\text{dip}}$ . Thanks to the MOT beams, a dissipative force is applied to the atoms that will lose their energy and will eventually stay trapped. In the trap, collisions can occur. First between atoms and residual background gases in the vacuum chamber. Second, between atoms themselves, mediated by the cooling light or not. These collisions processes are limiting the number of atoms in the trap. In order to obtain the maximum number of atoms in the trap, the experimentalist has to play with all the possible experimental parameters, as the MOT beams detuning for instance.

The single atom regime is a particular regime where the loading rate is almost compensated by the light-assisted collision in the trap. As soon as a second atom enters

the trap, they form a molecule. The absorption of quasi-resonant light is expelling both atoms from the trap, thus resulting in either 1 or 0 atom in the trap. This regime is characterized by a *step*-signal alternating between two values as depicted in Figure 3.14 (a). All the characterization tests summarized here have been performed in this regime.

### 3.3.2 Trapping frequencies

This section is divided into two parts. The first part concerns the trapping frequencies measurement of the aspheric lens A (one of the two aspheric lens of the main high resolution axis). For this lens, we have estimated the waist of our trapping beam with two independent methods. The obtained values were not consistent with the theoretical predictions. We have then decided to measure the trapping frequencies with another aspheric lens (B). The second part of this section is dedicated to it.

#### Aspheric lens A

There exists several standard protocols to determine the oscillations frequencies of an atom in the optical dipole trap, some of them are partially explained in subsection 1.3.1. More detailed explanation can be found in [Bourgain, 2014], [Béguin, 2013] or [Fuhrmanek, 2011] for instance. To measure the oscillation frequencies of a single atom in the optical dipole trap, we have used two independent techniques described in chapter 1: the parametric heating and the trap depth measurement.

**Parametric heating** By modulating the trap power at twice the oscillation frequency of the atom, in a given direction, we will transfer some energy to the atom so that, after some time, it will have enough energy to leave the trap. If we modulate at a frequency that is not resonant with an oscillation mode, the atom energy remains unperturbed and the atom stays in the trap. Measuring the survival probability as a function of the modulation frequency enables us to have access to both the longitudinal, or axial, frequency  $\omega_a$ , and the transverse, or radial, one  $\omega_r$ . The results of this measurement are depicted in Figure 3.15. In principle, one also has to measure the trap depth seen by an atom to be able to compute the oscillation frequency. Here, assuming that the trap distribution follows perfectly the one of a Gaussian beam, we get rid of the trap depth parameter by forming the ratio of the two oscillations frequencies

$$\left(\frac{\omega_r}{\omega_a}\right)^2 = 2 \left(\frac{z_R}{w_0}\right)^2 = \frac{2\pi^2 w_0^2}{\lambda^2}, \quad (3.19)$$

where we have used the definition  $z_R = \pi w_0^2 / \lambda$ . For a trap wavelength of 940 nm, this measurement gives a waist of the trapping potential equal to  $w_0 = 2.06 \pm 0.08 \mu\text{m}$ . This

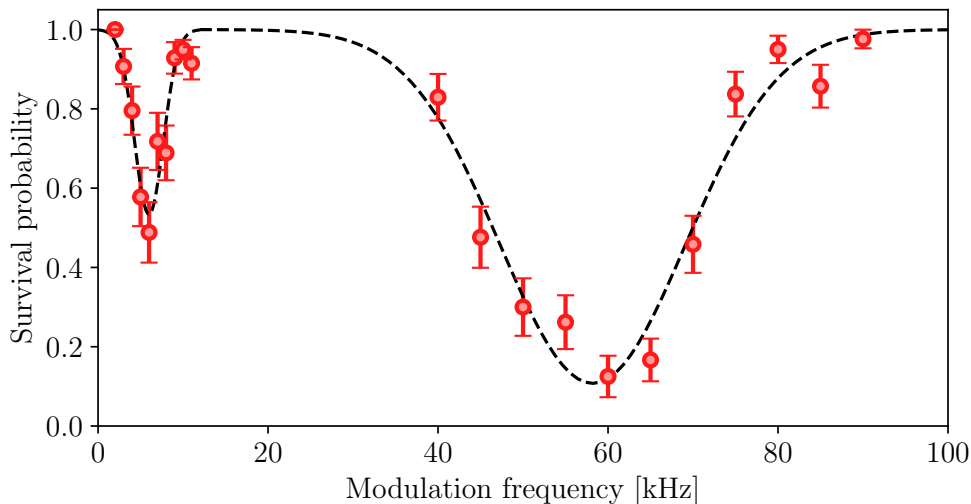


**Figure 3.15.:** Parametric heating measurement for aspheric lens A. Data points are fitted by Gaussian curve to extract the resonant frequencies for both the longitudinal and radial directions. For the axial direction, the fit gives a frequency  $2\omega_a = 6.0 \pm 0.2$  kHz; for the radial direction, the fit gives  $2\omega_r = 58 \pm 0.8$  kHz. The axial resonance being narrower, the trap power is modulated for longer times, typically  $\sim 100$  ms (compared to a few milliseconds for the radial one).

value of the waist is puzzling because it is inconsistent with the theoretical value of  $w_{0,theo} = 1.2 \mu\text{m}$  at the wavelength of the trap.

**Monopole excitation** To confirm the previous estimation of the waist, we have also measured the radial oscillation frequency using a different technique: the monopole excitation (technique based on [Engler et al., 2000] and explained in subsection 1.3.1). A typical experimental sequence is the following (see Figure 3.16 (a)):

1. start the experiment when a single atom enter the trap,
2. lower the trap depth and switch it off for typically  $5 \mu\text{s}$ . The goal of this first off-time is to synchronize the position of the different atoms in the trap. The experiment being repeated with different atoms to build a survival probability, we want each of them to start at the same position in the trap. The switch off time is chosen such that an atom at the bottom of the trap, hence with the highest velocity, will be at the edge of the trap after this time. An atom initially at the edge of the trap will stay there during the off-time as its velocity is almost zero.
3. switch on the trap for a time  $\Delta t_{\text{osc}}$ . During this time the atom will oscillate freely in the trap.
4. the trap light is switched off again, for typically  $10 \mu\text{s}$ . The atom can be at different position at the beginning of this last step, depending on the value of  $\Delta t_{\text{osc}}$ .

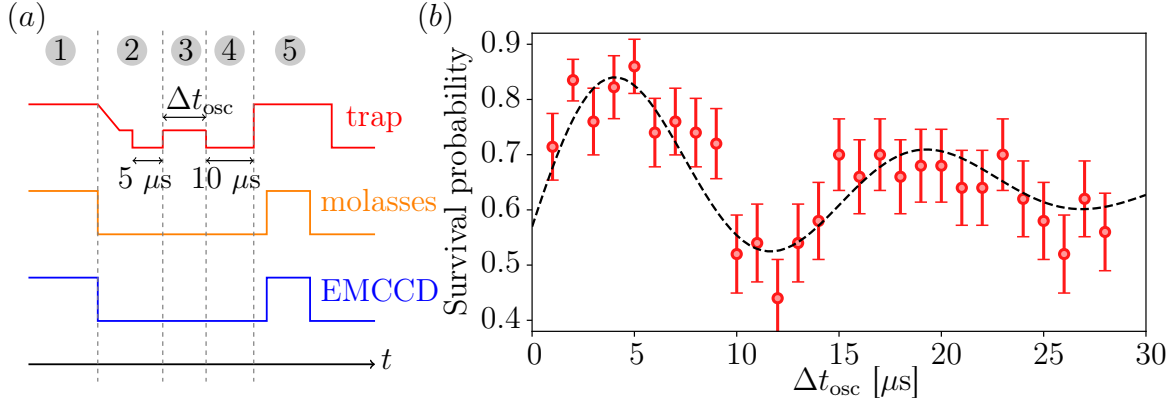


**Figure 3.16.:** (a): Chronogram of the experimental sequence. (b): Monopole excitation measurement for aspheric lens A. The black dashed line is a fit of the data with a damped sine function. From the fit, we extract  $2\omega_r = 65.6 \pm 3.2$  kHz.

5. finally, at the end of the  $10 \mu\text{s}$ , the trap is switch on again and we checked if the atom has been recaptured or not.

The sequence enables to reconstruct the recapture probability as a function of  $\Delta t_{\text{osc}}$  which should oscillates at twice the radial oscillation frequency of the trap. Because the atom is not exactly at the same position at the beginning of each sequence, the sine behavior is damped. The result of this measurement is depicted in Figure 3.16 (b). We have fitted the data with the function  $B + A \exp(-t/\tau) \sin(2\omega_r t + \phi)$  and extracted the radial oscillation frequency  $2\omega_r = 65.6 \pm 3.2$  kHz. This value has been obtained with the same trap depth as the one for the parametric heating measurement. This two measurements, performed in the same experimental conditions, provides almost the same values which gives us some confidence about our measurement.

**Trap depth measurement** The second measurement performed to confirm the waist value obtained with the parametric heating was a trap depth measurement. For this, we measure the detuning that we need to apply to a near resonant,  $\sigma_+$ -polarized probe beam addressing the transition from  $|g\rangle = |5S_{1/2}, F = 2, m_F = +2\rangle$  to  $|e\rangle = |5P_{3/2}, F = 3, m_F = +3\rangle$  for expelling an atom from the dipole trap. More precisely, for each trap depth  $U_{\text{dip}}$ , or equivalently each power of the trap beam  $P_{\text{trap}}$ , we measured a survival probability spectrum, as for instance the one shown in Figure 3.17 (a). The minimum of this spectrum corresponds to the probe frequency which is resonant with the atom. Comparing this frequency with the natural resonant frequency of the atom (in free-space, no trap), we have access to the trap depth seen by the atom with this specific power of the trapping beam. Note that this is only true because our probe will address the specific transition from  $|g\rangle$  to  $|e\rangle$  and because our trap has a polarization  $\pi$ . Doing so, state  $|e\rangle$  is not shifted and  $|g\rangle$  is shifted by exactly  $U_{\text{dip}}$ . For another trap polarization, the exact shift of the two level involved has to be considered. For Gaussian

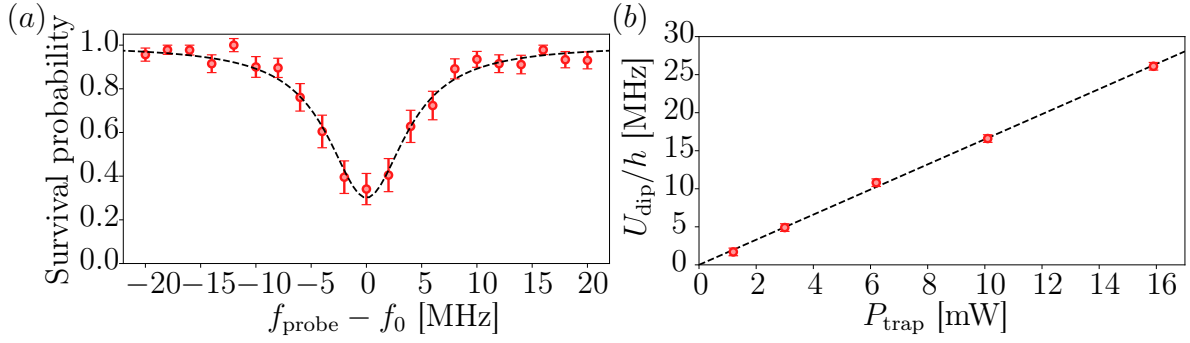


**Figure 3.17.:** (a): Survival probability spectrum as a function of the probe frequency. The spectrum has been taken for a particular trap depth. The frequency of the probe is displayed with respect to the resonant frequency  $f_0$  in this particular configuration. (b): Trap depth as a function of the power in the trap. Each data point corresponds to a specific spectrum as the one shown in (a). The black dashed line is a linear regression of the data and provides a slope of  $1.65 \pm 0.02 \text{ MHz.mW}^{-1}$ .

beams, the trap depth  $U_{\text{dip}}$  is related to the power of the beam  $P$  through the relation (c.f. (1.8))

$$U_{\text{dip}} = \frac{\hbar\Gamma^2}{8} \frac{2P}{\pi w^2 I_{\text{sat}}} \left( \frac{1}{3\Delta_1^-} - \frac{1}{3\Delta_1^+} + \frac{2}{3\Delta_2^-} - \frac{2}{3\Delta_2^+} \right) = \alpha P, \quad (3.20)$$

with  $\alpha$  a proportionality constant. Figure 3.17 (b) corresponds to this calibration measurement. The linear fit of the data gives a slope equal to  $1.65 \pm 0.02 \text{ MHz.mW}^{-1}$ . For the parametric heating measurement as for the excitation of the monopole, the power of the trapping beam was 5.6 mW. This power corresponds to  $U_{\text{dip}} \simeq h \times 9.2 \text{ MHz} \simeq k_B \times 440 \text{ } \mu\text{K}$ . Using (1.13) and the value of the radial oscillation frequency measured with parametric heating (monopole excitation), we estimated a waist of the beam equal to  $w_0 = 2.2 \text{ } \mu\text{m}$  ( $2.0 \text{ } \mu\text{m}$ ).

However, we found a surprising fact. The theoretical slope can be calculated for every waist of the the trapping beam (see (3.20)). Reversing the relation and using our measured value of the slope, we obtained a corresponding waist of  $1.24 \text{ } \mu\text{m}$ . This value is really close to the theoretical prediction but inconsistent with the two previous estimations of the waist. It could be because of the failure of the Gaussian description of the beam, or maybe something went wrong when measuring the oscillations frequencies. If we consider a waist of  $2.0 \text{ } \mu\text{m}$ , assuming that the Gaussian beam description is accurate, the slope should be equal to  $0.63 \text{ MHz.mW}^{-1}$  instead of  $1.65 \text{ MHz.mW}^{-1}$ , which is not compatible with the measurement uncertainty.

**Conclusion** The estimated value of the waist are almost similar with two independent methods and is not compatible with the theoretical prediction of a diffraction limited

optical system. The trap depth slope alone seems to indicate a compatible waist with the optimal one but is inconsistent with the two others estimation. Something is still not fully understood for our system. After some investigation, we found that the dichroic mirror used to separate the fluorescence light emitted by the atoms and the trap light was introducing some astigmatism. However, changing its position on the optical setup (where the trap beam was smaller and then less aberrations were introduced) did not improved the estimated value of the waist. At this stage, two options were available:

1. buying a higher quality dichroic mirror,
2. using the opposite aspheric lens B to send the trapping beam. The fluorescence light will be collected by aspheric lens A and separated from the trap with the same dichroic mirror but at least the trap light seen by the atoms will not be distorted by the dichroic mirror.

We have opted for the second option, and the associated measurement is presented in the next section.

### Aspheric lens B

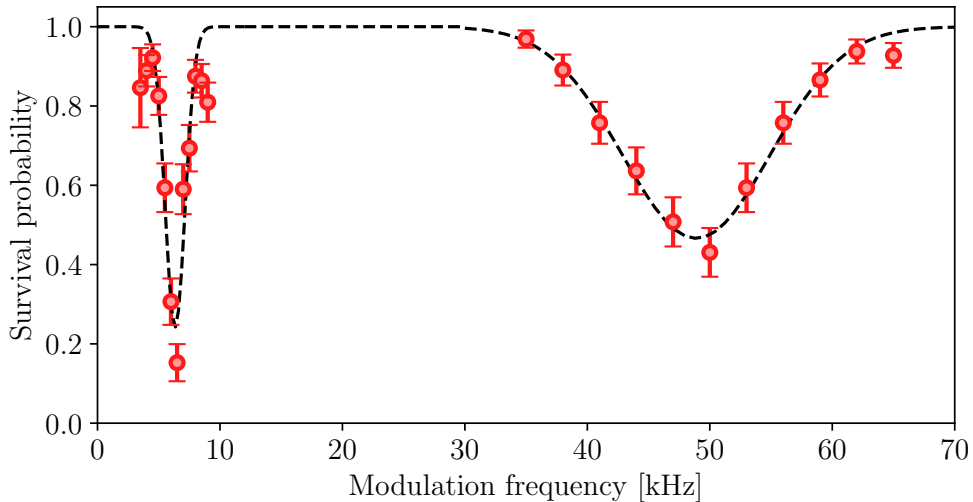


**Figure 3.18.:** Parametric heating measurement. Data points are fitted by Gaussian curve to extract the resonant frequencies for both the longitudinal and radial directions. For the axial direction, the fit gives a frequency  $2\omega_a = 6.3 \pm 0.2$  kHz; for the radial direction, the fit gives  $2\omega_r = 49 \pm 2$  kHz.

**Parametric heating** The same measurement has been performed with aspheric lens B and it has resulted in an estimated value of the waist of  $w_0 = 1.64 \pm 0.05$   $\mu\text{m}$ . Once again this measurement has been confirmed with a trap depth measurement (not

presented here). Although the difference with the theoretical value is smaller for this lens, the result is still incompatible with the optimal performance.

**Conclusion** Whether the dichroic mirror was introducing aberrations is debatable. However, both aspheric lenses from the main high resolution optical axis seems to have degraded performances. The difference between the estimated values of the waist and the theoretical one can be attributed to two different factors, if one assumes that both aspheric lenses are diffraction limited.

1. The first one is the failure of the Gaussian beam approach. Indeed, a clipped Gaussian beam is not perfectly a Gaussian beam. However, the previous experimental setup, similar in its features to this new one, provided a value of the waist that was consistent with the theoretical one.
2. The second factor is aberrations. After a long investigation, the remaining optical element that has not been tested was the viewport. In fact, if our trapping beam before the chamber is aberration-free, sent on the axis of the aspheric lens that is supposed to be diffraction limited, then the only optical element in between is the viewport of the vacuum chamber. Being present with both lens, it could introduce some spherical aberrations that have degraded our beam, whatever our effort to prevent that. This last point is addressed in section 3.4.

### 3.3.3 Lifetime measurement

The lifetime of an atom in the trap is an important quantity. The longer an atom can stay in trap, in absence of resonant light, the longer the experimental sequence can be. Several loss mechanisms can induced a loss of an atom in the trap, in order of importance: trap power and frequencies fluctuations, trap laser light absorption and background collisions. The first cited mechanism can be neglected as the trap power fluctuation is kept very low (a few percent), with no frequencies components oscillating at any multiple of the trapping frequencies. Concerning the second mechanism, we estimated the scattering rate  $R$  of an atom in the dipole trap, which is given by

$$R = \frac{\Gamma^3 I_{\text{trap}}}{8 I_{\text{sat}}} \left| \frac{1}{3\Delta_1^2} + \frac{2}{3\Delta_2^2} \right|, \quad (3.21)$$

where  $\Delta_1$  and  $\Delta_2$  are respectively the detunings of the trap laser frequency with respect to the D1 and D2 line of  $^{87}\text{Rb}$ , and  $I_{\text{trap}} = \frac{2P}{\pi w^2}$  is the trap intensity, assumed to be Gaussian, at the position of the atoms, with  $P$  the power of the trap light and  $w$  its waist. Assuming a waist of  $w = 1.6 \mu\text{m}$ , a power  $P = 30 \text{ mW}$  and a trapping wavelength of 940 nm, we obtain a theoretical value of  $R \approx 20$  photons/s. If we further assume that a photon absorption and emission process leads to a heating of  $2E_r$ , with  $E_r = 362 \text{ nK}$  the recoil energy of a photon, the associated heating rate is  $\alpha = 2E_r R \approx 14 \mu\text{K/s}$ . Because

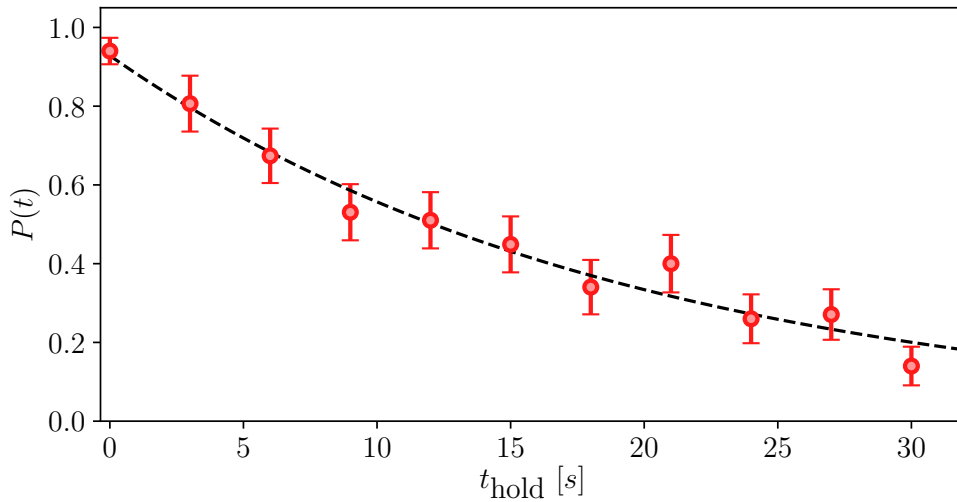


**Figure 3.19.:** Lifetime measurement. The data points correspond to the probability that an atom is still in the trap after a time  $t_{\text{hold}}$ . The black dashed line is an exponential fit that gives a lifetime of  $19.6 \pm 1.3$  s.

the trap depth is of the order of  $U/k_B \approx 1.6$  mK for this particular measurement, the associated lifetime would be on the order of  $U/\alpha \approx 114$  s. Therefore, losses due to heating can be confidently neglected.

To measure the lifetime of the atom in the trap, the experimental sequence is quite simple. Starting from a molasses, when an atom enters the dipole trap, we switch off the cooling beams but the dipole trap is still on. After a time  $t_{\text{hold}}$ , we switch on again the cooling beams to see if the atoms is still in the trap or not. Repeating the experiment for various holding times gives access to the lifetime probability. The experimental results of this measurement is depicted in Figure 3.19. An exponential decay fit of the data provides a lifetime  $\tau = 19.6 \pm 1.3$  s. The inverse of the lifetime gives the loss rate  $\gamma_{\text{exp}} = 51 \pm 8 \cdot 10^{-3} \text{s}^{-1}$ .

To confirm that the lifetime obtained is compatible with the measured pressure, we computed the background gas density of  $\text{H}_2$  associated with our experimental loss rate. Indeed, at this low pressure, we assume that the background gas is mainly  $\text{H}_2$ . Knowing the scattering cross section between Rb and  $\text{H}_2$ ,  $\sigma = 295 \text{\AA}^2$  ([Bali et al., 1999]), one can calculate a theoretical loss rate  $\gamma/n_{\text{H}_2} = 4.9 \cdot 10^{-9} \text{cm}^3 \cdot \text{s}^{-1}$  where  $n_{\text{H}_2}$  is the density of the  $\text{H}_2$  background gas. Relating the experimental measurement with the theoretical value enables us, by using ideal gas law at room temperature  $T = 300$  K, to estimate the background gas pressure  $P_{\text{background}} = 4.3 \cdot 10^{-10}$  mbar. This value is a factor 10 higher the value displayed by the vacuum gauge. The considerable difference can be attributed to several factors.

1. First of all, the gauge (Pfeiffer Vacuum Cold Cathode Gauge) is not really precise at pressure below  $10^{-10}$  mbar.
2. Second, we have neglected losses due to collisions with other Rubidium atoms that can be present in the vacuum chamber or can come from the atomic beam that we used to load the MOT.

However, a typical lifetime of 20 s is enough for our type of measurement, where the typical sequence duration is on the order of 1 s.

### 3.4 LIMITATION OF THE PERFORMANCE - THE VIEWPORTS AND THE SPHERICAL ABERRATION

The optical characterization of this new apparatus was not entirely satisfying as the waist of the trapping beam,  $w = 1.64 \mu\text{m}$  using aspheric lens B, inferred from the measurement of the oscillation frequencies in the trap, is bigger than the predicted value  $w_{\text{theo}} = 1.2 \mu\text{m}$ . As stated at the end of subsection 3.3.2, the introduction of spherical aberrations by the viewports could be the reason of this mismatch. It is important to be able to determine if this candidate is the real culprit because spherical aberration can considerably modify the intensity distribution of the trap. Thus, the assumption that the trapping beam behaves as a Gaussian one may be inaccurate. The comparison with theory may also be impacted as the initial spatial distribution of the atoms in the cloud may not be the one expected from a perfect Gaussian beam. Moreover, if the trap beam is less focused than expected, the maximum density achievable in the cloud can be lower than what we expect.

The optical quality of our viewports are not the highest one of the market. If it was not a problem previously when using beams of diameter equals to 9.0 mm, the new apparatus is now using beams of diameter equals to 19.2 mm. The goal of this section is to estimate, with simulation, the amount of spherical aberration that the viewport would have to introduce in order to be able to reproduce the experimental measurement presented in subsection 3.3.2.

As the beam goes through optical elements, it can accumulate optical aberrations that will modify its intensity distribution. Because our aspheric lenses are diffraction limited up to  $\text{NA}=0.45$ , and all the others optical elements of the trapping setup are mirrors and lenses used near their optical axis with small angles and a small beam diameter, thus minimizing aberrations, the last element that can induce strong modifications of the intensity distribution of our trapping beam is the viewport on the vacuum chamber. Assuming the alignment is done carefully, the most obvious kind of aberrations that

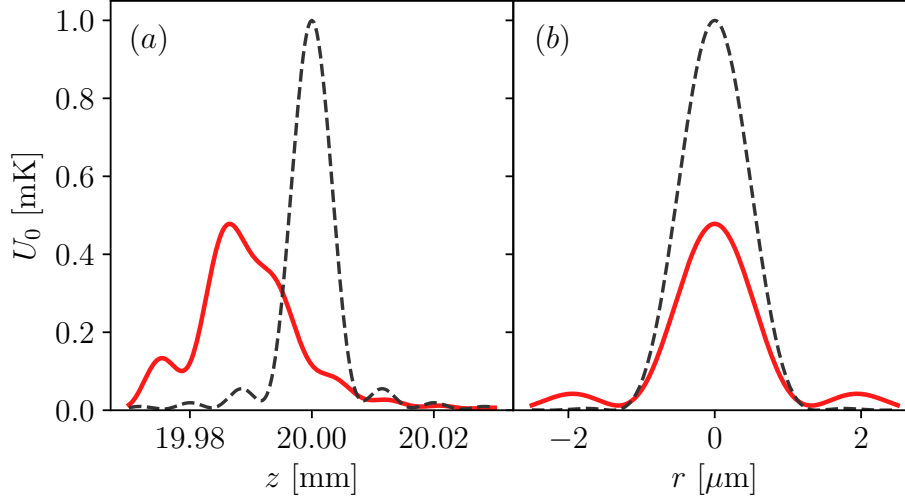


**Figure 3.20.:** Intensity distribution at the focus of the aspheric lens. (a): Axial intensity distribution of a clipped and focused Gaussian beam. The simulation is performed in absence of primary spherical aberration (dashed black line) and with spherical aberration  $kS_1 = -11.7$  (red solid line). (b): Radial intensity distribution of a clipped and focused Gaussian beam at the position where the axial intensity is maximum. Once again, the simulation is performed with (red solid line) and without (dashed black line) spherical aberration.

the viewport can introduce is a spherical aberration. Spherical aberrations are found in optical systems manufactured with spherical surfaces. Light rays at the edges of this surface are more (or less) refracted/reflected than light rays close to the optical axis, thus limiting the maximum resolution achievable. Here, following [Pu and Zhang, 1998], we consider the propagation of a Gaussian beam with spherical aberrations after it has been focused by the high numerical aperture aspheric lens. The spherical aberration is not introduced by the lens in our analysis but by the viewport. However it is a phase factor that arises as if it was introduced by the lens. The spherical aberration at the position of the lens is expressed as

$$\phi_{\text{SA}} = Sr^4, \quad (3.22)$$

where  $r$  is the radial coordinate and  $S$  the amplitude coefficient of the spherical aberration. To use the same notations as in [Pu and Zhang, 1998], we introduce the dimensionless variable  $t = r/a$  where  $a$  is the radius of the aperture limiting the aspheric lens. We also define a new spherical aberration coefficient  $S_1 = Sw^4$  such that the aberration function becomes

$$\phi_{\text{SA}} = S_1 \frac{a^4}{w^4} t^4. \quad (3.23)$$

The field at the focal plane of the lens is then given by

$$U(u', v') = -\frac{2\pi i a^2 A_0}{\lambda f'} \left(1 - \frac{u'}{2N_a}\right) \times \int_0^1 J_0(v't) \exp \left[ -\left(\frac{a}{w}\right)^2 t^2 + ikS_1 \left(\frac{a}{w}\right)^4 t^4 - \frac{iu't^2}{2} \right] t dt, \quad (3.24)$$

where  $N_a = a^2/\lambda f'$  is the Fresnel number of the lens viewed from the geometrical focus,  $J_0$  is a Bessel function of first kind and zero order and  $A_0$  is the amplitude of the Gaussian field expressed by  $E_0 = A_0 \exp(-r^2/w^2)$ . The dimensionless optical parameters  $u'$  and  $v'$  are given by

$$u' = 2\pi N_a \frac{z - f'}{z}, \quad v' = 2\pi N_a \frac{r f'}{a z}. \quad (3.25)$$

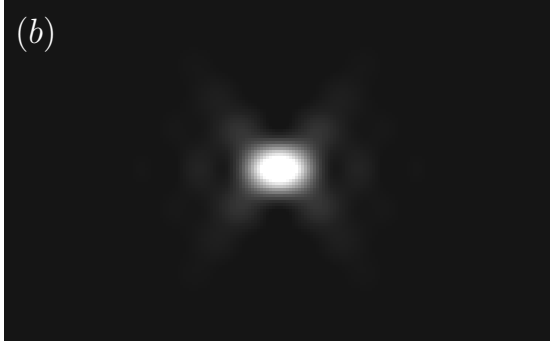
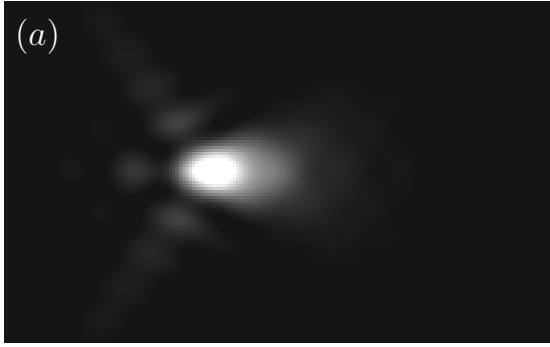


**Figure 3.21.:** Simulated Gaussian beam propagation near the focus of the aspheric lens. (a): with spherical aberration ( $kS_1 = -8$ ); (b): without spherical aberration.

The intensity is the modulus squared of (3.24) and can be evaluated at any position near the focus. In Figure 3.20, we simulate the distribution of intensity of a Gaussian beam focused by our aspheric lens without spherical aberration ( $kS_1 = 0$ , black dashed lines) and with spherical aberration ( $kS_1 = -11.7$ , red solid line). The waist of the incoming beam is set equals to the aperture radius of our aspheric lens. As one can see, besides the fact that spherical aberrations reduce the maximum intensity at the focus of the lens, it does not change drastically the radial distribution of intensity (Figure 3.20 (b)): rings appears around the central peak but the width of the central peak remains almost equal to the one in absence of spherical aberration. However, the axial distribution of intensity is heavily modified (Figure 3.20 (a)). The focus spot is shifted towards the lens and the distribution of intensity is no longer symmetric with respect to the maximum. This is the main difference that we wanted to point out. The radial distribution of the field may remain nearly Gaussian in presence of spherical aberration,

but this is absolutely not the case of its axial distribution. Thus, assuming a perfect Gaussian beam distribution and computing the ratio of the oscillations frequencies of the atom in the trap may give a bigger waist than the theoretical one. In the

present case, we have fitted the intensity distribution in both cases with an harmonic function to extract the oscillations frequencies that an atom should see in the trap. Then, we have computed the ratio of these quantities to obtain the corresponding waist, as if no spherical aberration were present. The ratio of the oscillations frequencies is given by the square root of (3.19)

$$\frac{\omega_r}{\omega_a} = \sqrt{2} \frac{\pi w_0}{\lambda}. \quad (3.26)$$

The simulation, performed with  $kS_1 = -11.7$  (SA) and  $kS_1 = 0$  (noSA), gives

$$\begin{aligned} \left(\frac{\omega_r}{\omega_a}\right)_{\text{SA}} &\approx 7.70, \\ \left(\frac{\omega_r}{\omega_a}\right)_{\text{noSA}} &\approx 5.67. \end{aligned}$$

We have thus a 36% modification of the ratio of the oscillations frequencies in presence of this amplitude of spherical aberration. Given that the theoretical waist at the focus of the lens that one should obtain, for an input waist equal to the radius of the aspheric lens, is  $w_{\text{noSA}} = 1.20 \mu\text{m}$ , the corresponding waist  $w_{\text{SA}}$  obtained with this amount of spherical aberration is

$$w_{\text{SA}} = 1.63 \mu\text{m}. \quad (3.27)$$

The value obtained with this simulation is really close to the one measured  $w = 1.64 \mu\text{m}$ . This study indicates the amount of spherical aberrations that the viewport needs to introduce to explain the discrepancy between the theoretical waist and the measured one. However, other tests have to be performed in order to confirm that the viewport is the only culprit. No interferometric measurement has been performed on the viewports themselves because they were already placed on the vacuum chamber and we would have to break the vacuum in order to do them. Without this complementary test, nothing confirms that the amount of spherical aberration set in this simulation is consistent with the one introduced by the viewport. It seems that it corresponds to an extreme spherical aberration as the trap depth drops by a factor 2 (see Figure 3.20). It can also be that the viewport introduce some spherical aberration that distorts the distribution of intensity of the beam but another(s) element(s) on our optical setup is responsible for the rest of the modification, by introducing some spherical aberration and/or another kind of aberration. Although we carefully checked every step of our optical setup and the good behavior of each one of the optical elements used, no other possible explanation has been found.

### 3.5 THE FUTURE TOOLS

In this last section, we will give an overview of the tools that have been implemented, or have been planned to be implemented in our new apparatus.

### 3.5.1 Optical tweezer of variable size

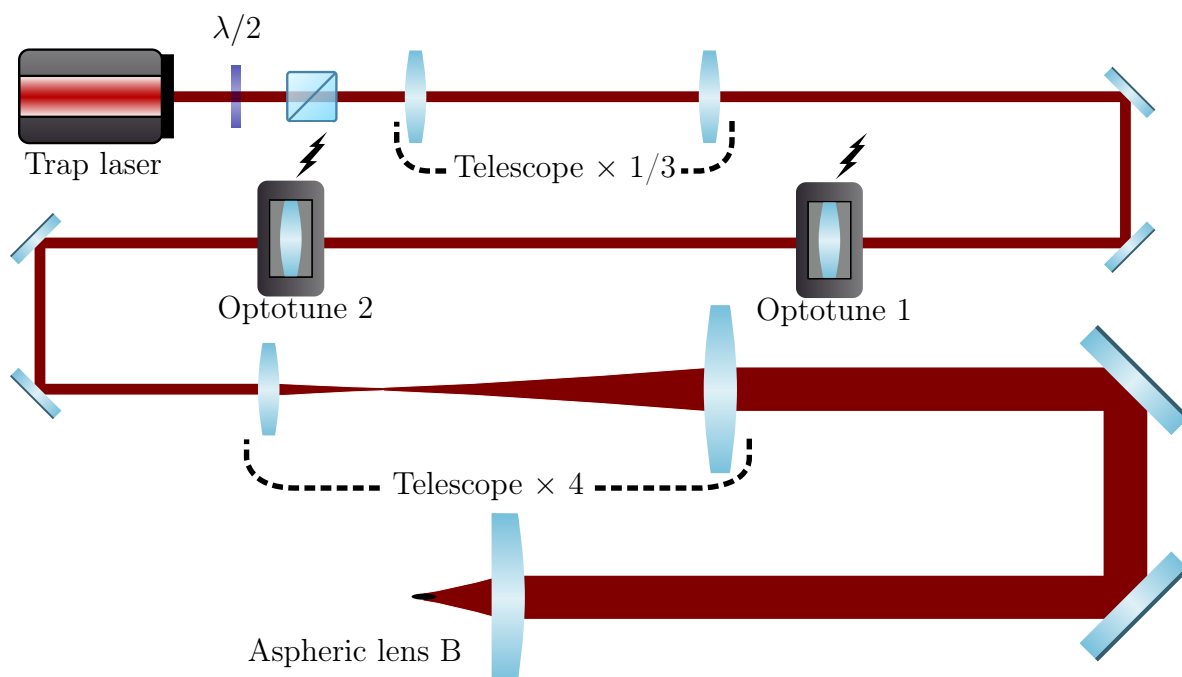


**Figure 3.22.:** Sketch of the optical setup implementing an optical tweezer of variable size. A 940 nm laser beam linearly polarized goes first through a  $\times 1/3$  telescope to reduce its size and limit the amount of aberrations eventually introduced by the Optotunes. Then, the beam goes from the telescope of variable magnification ratio depending on the current applied to each one of the tunable lens. Their relative distance on the experiment as their limiting currents enable to choose the magnification ratio between 1.1 and  $\sim 3.4$ . After that, the beam goes through a  $\times 4$  telescope in order to be able to cover the full aperture of the aspheric lens when the magnification ratio of the opto-telescope is at its maximum value.

The first tool that has been implemented is an optical tweezer of variable size. This could be a very powerful tool for the loading of atoms. Previously, we were loading a micro-trap of waist  $1.2 \mu\text{m}$  from a bigger trap, called macro-trap, with a waist of  $4 \mu\text{m}$ . Approximately 10% of the atoms in the macro-trap were transferred, resulting in about 200 atoms in the micro-trap. Using a single trap, initially big, and then adiabatically compressing it could lead to a large increase in the number of atoms ultimately loaded in the trap, thus increasing the density and allowing us to observe stronger dipole-dipole interactions. For that purpose, we used tunable focal length lenses manufactured by Optotune. Those tunable lenses are polymer lenses whose shape is adjusted by applying a current. The focal length is accordingly modified to the desired value within milliseconds. Using two of these lenses (EL-10-30 Series) in an afocal telescope configuration, we can vary the size of the output beam, that in turn modifies the size of the beam at the focus of the aspheric lens (see Figure 3.22).

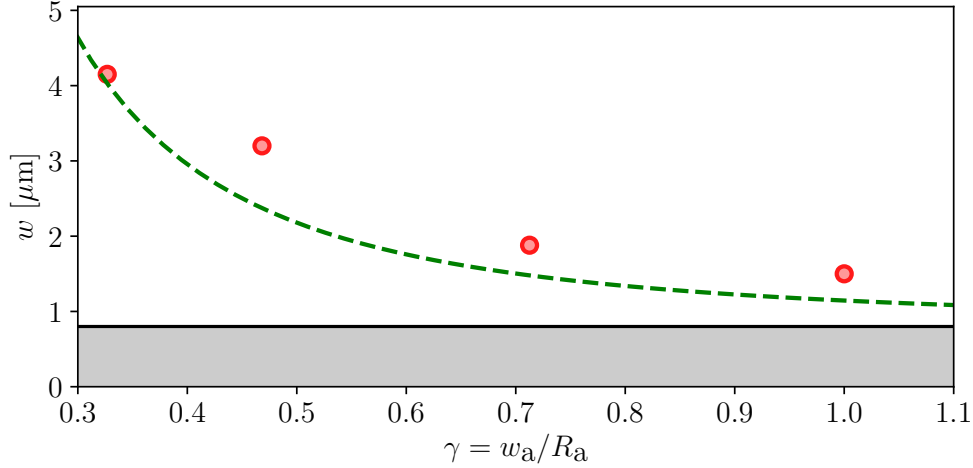


**Figure 3.23.:** Waist seen by the atoms as a function of the clipping ratio  $\gamma$  of the input beam. The waist of the input beam at the position of the aspheric lens  $w_a$  is modified by the magnification ratio of the telescope formed by two Optotune lenses. The dashed green line corresponds to theoretical simulations of the minimum waist obtained for a focused Gaussian beam which is clipped by an aperture. The dark solid line corresponds to the minimum waist achievable given the size of the lens. It is obtained when  $w_a \rightarrow \infty$ .

Figure 3.23 displays the waist seen by the atoms at the focal point after the aspheric lens versus the clipping ratio of the input beam  $\gamma$  defined as

$$\gamma = \frac{w_a}{R_a},$$

where  $w_a$  is the waist of the input beam at the position of the aspheric lens and  $R_a = 9.6$  mm is the radius of the aperture, i.e., the radius of the lens holder clipping the beam. To perform this measurement, we send a  $\approx 1$  mm waist beam onto a  $\times 1/3$  *standard* telescope to limit the aberrations introduced by the Optotune lenses. The beam goes through the telescope formed by the Optotune lenses. Due to their relative distance and their maximum voltage specifications, the modification of the magnification of this telescope is bounded between 1 and 3.5 approximately. Then the beam goes through another *standard* telescope of magnification 4 in order to be able to cover the full aperture of the lens, which is 19.2 mm. The waist of the beam  $w_a$  at the position of the aspheric lens inside the chamber is estimated from its waist at a given position before the chamber. To determine the waist at the focus of the aspheric lens, the trap depth seen by the atoms for various power of the beam is measured. Assuming that the input beam follows a Gaussian distribution, we rewrite the expression of the trap depth as

$$U_{\text{dip}} = \frac{\alpha}{w^2} \times P,$$

where  $w$  is the waist of the beam,  $P = \frac{1}{2}\pi w^2 I$  its power and  $\alpha$  a constant factor that can be computed. The trap depth is linear with the power of the beam. By measuring it for various powers, as was done in subsection 3.3.2, we extract a slope which is related to the waist of the beam.

In Figure 3.23, the theoretical waist that we should obtain at the focus of the lens is also represented. The theory is extracted from [Gillen et al., 2010]. In fact, when the Gaussian distribution is clipped by an aperture, the distribution of the beam is no longer Gaussian. When the waist of the input beam is large with respect to the aperture,  $\gamma \gg 1$ , we consider the distribution of intensity at the aperture as uniform and we recover the maximum optical resolution of our optical system. This limit is represented by the horizontal dark line in Figure 3.23: it is the size at  $1/e^2$  of the Airy pattern which is close to 800 nm. In contrario, when  $\gamma \ll 1$ , the distribution of the beam is almost purely Gaussian. One can see that for  $\gamma = 0.33$ , the waist measured is equal to the one predicted, but as soon as  $\gamma$  is above 0.4, the measured value is always bigger than the one predicted. Once again, different kind of aberrations can be responsible for this difference. The tool is nonetheless promising as it could be used to increase the density of the cloud and maybe to perform evaporation in the trap.

### 3.5.2 Accordion lattice

A future tool that we would like to implement on the experiment is an accordion lattice. The name as well as the principle are extracted from [Ville et al., 2017]. Using two small beams with adjustable distance between them, incident on one of the aspheric lenses of the second axis (the one at  $45^\circ$ ), would result in interference fringes. As shown in Figure 3.24, the two beams that overlap after the aspheric lens are created by two polarization beamsplitter cubes (PBS). The distance between them is directly related to the distance of the incoming beam with respect to the edge of the PBS. This distance is adjusted thanks to an acousto-optic deflector combined with a telescope that translates the deflection angle into a transverse displacement. The interfringe  $i$  at the focus of the lens is given by the relation

$$i = \frac{\lambda}{2 \sin(\theta/2)}, \quad (3.28)$$

where  $\lambda$  is the wavelength of the trap laser. (3.28) can be written in terms of the distance between the beams and the focal length  $f'$  of the aspheric lens

$$i = \frac{\lambda}{2d} \sqrt{f'^2 + d^2}. \quad (3.29)$$

If we initially set the distance between the two beams such that the full cloud is located inside a single fringe, we can increase the distance between the beams such that the cloud stays inside the single fringe but get compressed. This tool could be useful to

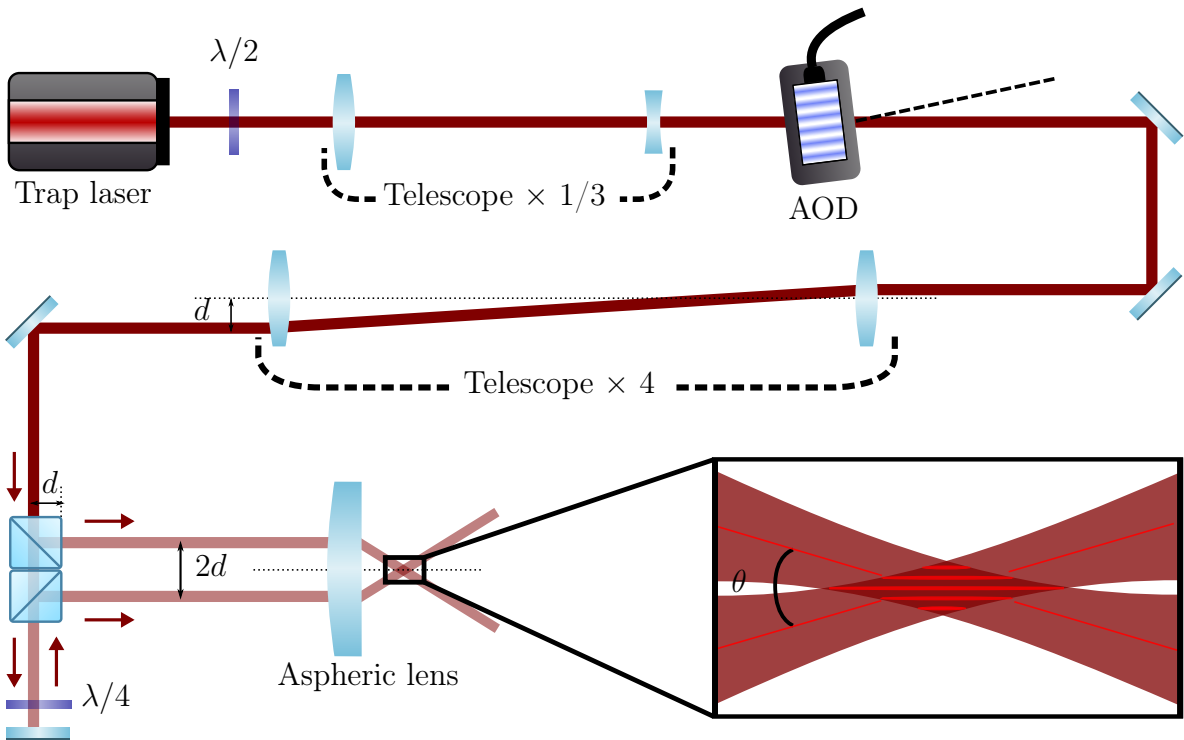


**Figure 3.24.:** Sketch of principle of the accordion setup. The beam diameter of the trap laser is first reduced before going into an acousto-optic deflector (AOD). The deflection of the beam is converted in a transverse displacement thanks to a second telescope. After that, the beam is divided in two thanks to two polarization beamsplitter cubes (PBS). We adjust the polarization of the incoming beam with the half-wave plate just after the laser such that half the power is reflected by the first PBS. The part transmitted by the first cube is also transmitted by the second. After being reflected by a mirror, hence passing twice into a quarter-wave plate, the beam is totally reflected by the second PBS. The two beams, transversally separated by a distance  $2d$ , are focused by the aspheric lens. Their overlap gives rise to fringes into which the atoms can be loaded.

increase the density in the cloud, as well as to modify the aspect ratio of the cloud to see if it has an influence on the way it scatters light.

# CHAPTER 4

## TOWARDS LIGHT SCATTERING BY 1D CHAIN OF ATOMS

---

### Contents

---

<b>4.1. Light scattering in a 1D chain . . . . .</b>	<b>104</b>
4.1.1. Growth of the excitation probability along the chain . . . . .	106
General case: $a \neq j\frac{\lambda}{2}, j \in \mathbb{N}$ . . . . .	107
Special case: $a = j\frac{\lambda}{2}, j \in \mathbb{N}$ . . . . .	109
4.1.2. Robustness of the system with experimental imperfections . . . . .	110
Perfect system . . . . .	112
With defects . . . . .	113
With disorder . . . . .	114
With disorder and defects . . . . .	116
4.1.3. Investigation of the effect of the temperature . . . . .	117
4.1.4. Investigation of the effect of a Gaussian beam in the excitation probability . . . . .	117
4.1.5. Conclusion . . . . .	118
<b>4.2. Super Imaging of the 1D chain of atoms . . . . .</b>	<b>119</b>
4.2.1. Creation of the picture . . . . .	119
4.2.2. Algorithm . . . . .	121
4.2.3. Performance evaluation of the algorithm . . . . .	123
4.2.4. Conclusion . . . . .	124

---

We have seen that, even though dipole-dipole interactions in atomic ensemble seem to be known theoretically, it is very hard to obtain a satisfying agreement with experimental data in the dense regime. The explanation for this lack of agreement could come from some of the hypothesis of the theoretical framework that are not fulfilled in experiments,

as for instance thermal equilibrium. This would imply a wrong estimation of the volume occupied by the atoms in the trap and consequently a wrong estimation of the strength of the dipole-dipole interactions. The cloud size being smaller than our optical resolution, this point is hard to verify.

In order to keep investigating the dipole-dipole interactions in dense ensembles, I have devoted part of my PhD work to the construction of the new version of the apparatus (see chapter 3). The new version has been designed to solve some experimental problems, for instance having the molasses beams at  $90^\circ$  from each others in order to facilitate the alignment of the MOT, but mostly to integrate a second axis of high optical resolution, orthogonal to the first one. The combination of these two axes opens the field of study of the dipole-dipole interactions in new kind of geometries, for instance 1D and 2D systems. Moreover, structuring the atomic distribution could help, the effect of the interactions being enhanced by interference between the scattered field as presented in [Bettles et al., 2016b], [Shahmoon et al., 2017b]. Here, we take a first step in this direction to look at new opportunities offered by this structuration.

The first part of this chapter is dedicated to the study of the influence of dipole-dipole interactions in 1D systems. More specifically, we will study theoretically the scattering of light along a 1D chain of atoms and its robustness towards experimental imperfections. Based on the work of [Sutherland and Robicheaux, 2016], we show that the propagation of an excitation along a 1D chain of interacted atoms is maintained in presence of disorder and defects in the system. A nonexhaustive list of works related to this subject is: [Munro et al., 2018], [Iakoupov et al., 2016], [Bettles et al., 2015b] and [Bettles et al., 2016a]. Using one of our high resolution optical axis to create the 1D chain, by reflecting the trap light, we used the second axis to observe the position of the excited atoms. We would therefore be able to compare theoretical predictions of the dipole-dipole interactions with experimental data in a different configuration: an ordered 1D chain randomly filled with atoms.

The second part of the chapter, in direct connection with the first part, concerns the development of an algorithm that tries to recover the positions of the atoms in the 1D chain based on their fluorescence image taken at  $90^\circ$  from the trapping axis. The idea was to see in which range of parameters it would have been possible to extract, with a high fidelity, the initial configuration of atoms in the 1D chain and comparing that to our experimental parameters.

## 4.1 LIGHT SCATTERING IN A 1D CHAIN

The Cyclopix experiment has the ability to trap the atoms along one direction and to observe the system with a high NA lens placed under vacuum at  $90^\circ$  from the trapping

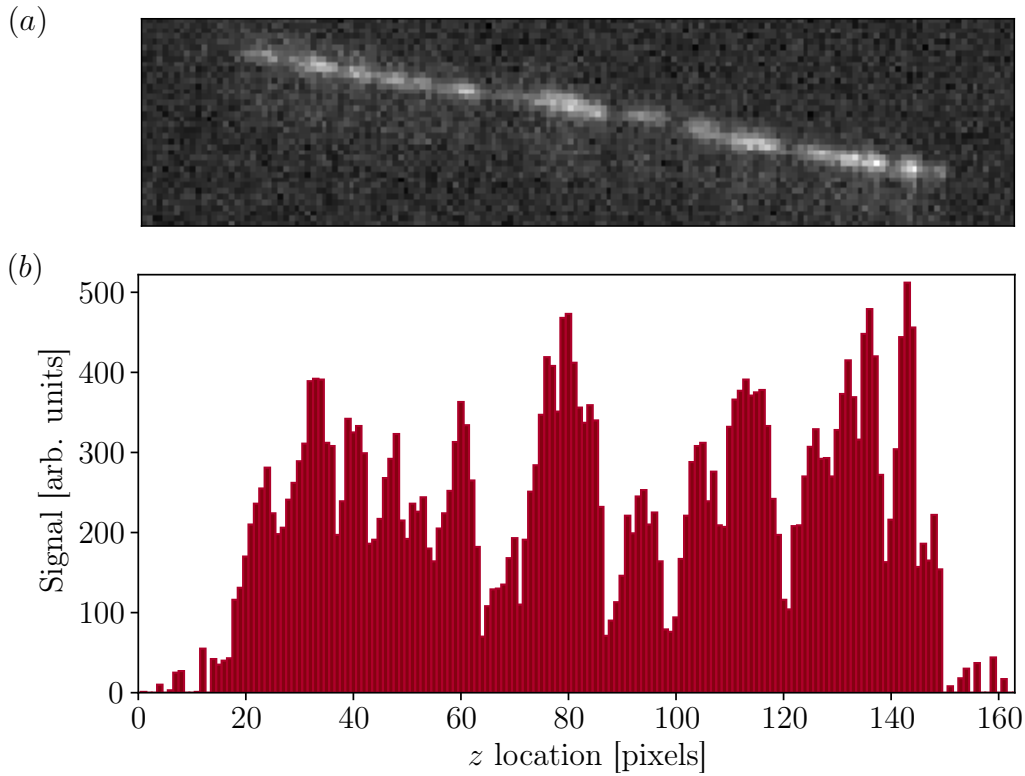


**Figure 4.1.:** (a): Experimental observation of a 1D chain of  $\sim 100$  atoms observed with the aspheric lens at  $90^\circ$  from the trapping axis. Exposure time of the camera is set to 50 ms and the signal to noise ratio (SNR) is  $\sim 1.5$ . The fluorescence of the atoms is induced by the MOT beams. The background has been subtracted. (b): Trace orthogonal to the trapping axis.

axis. We can then excite the system along the trapping axis and collect the fluorescence of each atom along the other axis to be able to determine where the excited atoms are located. But the side fluorescence is strongly suppressed in comparison with the forward scattering. However, our system has been able to image such a system: Figure 4.1 (a) is an example of a picture of the 1D chain taken from the side. The fluorescence of the atoms has been induced by the MOT beams and has been collected on our CCD camera during 50 ms. A background subtraction has been applied. Figure 4.1 (b) is a trace of the picture orthogonal to the trapping axis of the chain ( $z$  axis). We have then the opportunity to measure experimentally collective effects in 1D chain of atoms. Let us first derive the expression of these collective effects and then see if they survive the experimental imperfections.

The physical system studied here is a 1D chain of atoms aligned along the  $z$  axis, each atom being separated from another by a constant lattice spacing  $a$  (see Figure 4.2). We consider the steady state of such a system when illuminating by a plane wave shined along the axis of the chain and polarized along the  $x$  axis. One can show that for values

of the lattice spacing not equal to a multiple of half the wavelength of the transition, the probability of excitation along the chain increases or decreases depending on the sign of the detuning of the laser field. In contrast, when the lattice spacing  $a = j\frac{\lambda}{2}$ , where  $j$  is an integer, the probability of excitation is symmetrical with respect to the middle of the chain.



**Figure 4.2.:** Sketch of the physical system under study. Atoms are represented by red balls, located on an array of lattice constant  $a$ , and illuminated from the left by a monochromatic, linearly-polarized laser field.

### 4.1.1 Growth of the excitation probability along the chain

For a weak laser, a collection of two-level atoms polarized in the  $x$  direction can be treated as coupled damped harmonic oscillators. Following the notation of the authors in [Sutherland and Robicheaux, 2016]

$$\dot{b}_n(t) = \left( i\Delta - \frac{\Gamma}{2} \right) b_n(t) - i\frac{d}{\hbar} E_L(\mathbf{r}_n) - \frac{\Gamma}{2} \sum_{m \neq n} G(\mathbf{r}_m - \mathbf{r}_n) b_m(t), \quad (4.1)$$

where  $b_n = d_n/d$ , with  $d_n$  is the notation used in chapter 2, represents the normalized polarization amplitude of atom  $n$ ,  $d$  is the electric dipole matrix element,  $E_L(\mathbf{r}_n) = E_0 e^{ikr_n}$  is the laser field at atom  $n$ ,  $\Delta$  is the detuning,  $\Gamma$  is the single atom decay rate, and  $G(\mathbf{r})$  is the field propagator

$$G(\mathbf{r}) = \frac{3e^{ikr}}{2i} \left\{ [3|\hat{\mathbf{r}} \cdot \hat{\mathbf{e}}_x|^2 - 1] \left[ \frac{1}{(kr)^3} - \frac{i}{(kr)^2} \right] + [1 - |\hat{\mathbf{r}} \cdot \hat{\mathbf{e}}_x|^2] \frac{1}{kr} \right\}. \quad (4.2)$$

In our system, because  $\hat{\mathbf{r}} = \hat{\mathbf{e}}_z$ , the expression of the field propagator (4.2) simplifies to

$$G(\mathbf{r}) = \frac{3e^{ikr}}{2i} \left[ \frac{1}{kr} + \frac{i}{(kr)^2} - \frac{1}{(kr)^3} \right]. \quad (4.3)$$

With our apparatus, we retroreflect the optical tweezer to create a 1D array of traps separated by a distance  $\lambda_{\text{trap}}/2$ . Depending on the wavelength of the trap laser  $\lambda_{\text{trap}}$ , two different cases are considered.

**General case:  $a \neq j\frac{\lambda}{2}$ ,  $j \in \mathbb{N}$**

We first consider the case  $a \neq j\frac{\lambda}{2}$ , where  $j$  is an integer and  $\lambda$  is the transition wavelength. To try to understand the increase or the decrease of the excitation probability along the chain, the main hypothesis made by the authors is to consider that the forward scattering is the main contribution of the dipole-dipole interaction. Doing so, the atom  $n$  will see the contribution of the laser field and the field emitted by the  $n-1$  atoms before him (in the  $-\mathbf{k}$  direction). To confirm this fact, let us rewrite (4.1) in steady-state with the change of variable  $b_n = \frac{2id}{\hbar\Gamma} E_n$

$$0 = (2i\delta - 1)E_n - E_L(\mathbf{r}_n) - \sum_{m \neq n} G(\mathbf{r}_m - \mathbf{r}_n)E_m. \quad (4.4)$$

In this equation,  $\delta = \Delta/\Gamma$  is the reduced detuning and  $E_n$  the field scattered by atom  $n$ . It is related to the normalized dipole amplitude  $b_n$  through the relation  $b_n = \epsilon_0 \alpha \frac{E_n}{d}$ , with  $\alpha = \frac{6i\pi}{k^3}$  the on resonance polarizability of the atoms, hence the change of variable. Using the fact that the atoms are located at specific values  $r_n = na$ , the field propagator (4.3) is

$$G(\mathbf{r}_m - \mathbf{r}_n) = \frac{3e^{ika|m-n|}}{2ika|m-n|} \left[ 1 + \frac{i}{ka|m-n|} - \frac{1}{(ka|m-n|)^2} \right] = \frac{3e^{ika|m-n|}}{2ika|m-n|} f_{m-n}, \quad (4.5)$$

and (4.4) becomes

$$(2i\delta - 1)E_n - \sum_{m \neq n} \frac{3e^{ika|m-n|}}{2ika|m-n|} f_{m-n} E_m = E_0 e^{ikna}. \quad (4.6)$$

Assuming that  $ka \gg 1$ , one can solve perturbatively in the interaction and would get the zeroth order scattered field

$$E_n^{(0)} = \frac{E_0 e^{ikna}}{2i\delta - 1}, \quad (4.7)$$

and the first order

$$E_n^{(1)} = \frac{E_0 e^{ikna}}{2i\delta - 1} + \sum_{m \neq n} \frac{3e^{ika|m-n|}}{2ika|m-n|} f_{m-n} \frac{E_0 e^{ikma}}{2i\delta - 1}. \quad (4.8)$$

Factorizing a global  $e^{ikna}$  factor and splitting the sum into two parts finally leads to

$$E_n^{(1)} = \frac{E_0 e^{ikna}}{2i\delta - 1} \left\{ 1 + \frac{3}{2i(2i\delta - 1)} \left[ \underbrace{\sum_{m < n} \frac{f_{m-n}}{ka(n-m)}}_{\text{forward scattering}} + \underbrace{\sum_{m > n} \frac{f_{m-n}}{ka(m-n)} e^{2ika(m-n)}}_{\text{backward scattering}} \right] \right\}. \quad (4.9)$$

With equation (4.9), we see that the forward scattering, which means the field radiated by the previous atoms, has no varying phase factor. So the various field add constructively, even at long range. This somehow lifts the condition  $1/kl > 1$  to see collective effects. On the other hand, the backward scattering is suppressed at long range because of the phase factor, hence the assumption made by the authors in [Sutherland and Robicheaux, 2016].

To obtain an intuition of how the excitation probability of atom  $n$  varies with the detuning, we start again from (4.9), forgetting backward scattering contribution

$$E_n^{(1)} \approx \frac{E_0 e^{ikna}}{2i\delta - 1} \left\{ 1 + \frac{3}{2i(2i\delta - 1)} \sum_{m < n} \frac{f_{m-n}}{ka(n-m)} \right\}. \quad (4.10)$$

The probability of excitation corresponds to the modulus square of the dipole amplitude  $b_n$ , which is itself proportional to the modulus square of the emitted field. There, one gets, assuming  $f_{m-n} = 1$  for simplicity

$$\begin{aligned} |E_n^{(1)}|^2 &= \frac{|E_0|^2}{1 + 4\delta^2} \left| 1 + \frac{3}{2i(2i\delta - 1)} \sum_{m < n} \frac{1}{ka(n-m)} \right|^2, \\ &= \frac{|E_0|^2}{1 + 4\delta^2} \left\{ \left( 1 - \frac{3}{2} \frac{2\delta}{1 + 4\delta^2} \sum_{m < n} \frac{1}{ka(n-m)} \right)^2 + \left( \frac{3}{2} \frac{1}{1 + 4\delta^2} \sum_{m < n} \frac{1}{ka(n-m)} \right)^2 \right\}, \end{aligned}$$

which gives, to lowest order in  $\frac{1}{ka}$ ,

$$\approx \frac{|E_0|^2}{1 + 4\delta^2} \left\{ 1 - \frac{6\delta}{1 + 4\delta^2} \sum_{m < n} \frac{1}{ka(n-m)} \right\}.$$

Finally, using the relation  $|b_n|^2 = \frac{4d^2}{\hbar^2 \Gamma^2} |E_n|^2$  and the notation  $p = m - n$ , the probability of excitation of atom  $n$  is

$$\mathcal{P}_n = \frac{(dE_0/\hbar)^2}{\Delta^2 + \Gamma^2/4} \left\{ 1 - \frac{3\Gamma\Delta}{2ka(\Delta^2 + \Gamma^2/4)} \sum_{p=1}^{n-1} \frac{1}{p} \right\}. \quad (4.11)$$

Equation (4.11) is the same as (15) from [Sutherland and Robicheaux, 2016]. In the article, the authors gave the main features of the phenomenon:

- the probability increases along the chain when  $\Delta < 0$ , while it decreases when  $\Delta > 0$ ;
- Although this expression is only accurate in the limit  $ka \gg 1$ , the behavior is still qualitatively reproduced in the regime  $ka \sim 1$ ;

- one should be careful when entering the regime  $a < \lambda/2$  as the behavior of the system is dominated by subradiant modes for some values of  $\Delta$ . But outside of a given range of detunings, the distribution is still logarithmic;
- when  $a = j\frac{\lambda}{2}$ , the previous expression is not appropriate (see next section).

**Special case:  $a = j\frac{\lambda}{2}$ ,  $j \in \mathbb{N}$**

In this section we consider the case where the lattice spacing is equal to a multiple of half the wavelength of the atomic transition. In that case, it seems that the contribution of the atoms being placed in the  $\mathbf{k}$  direction cannot be neglected anymore. In order to convince ourselves, let us start over from (4.9), with  $p = |m - n|$  and  $f_{m-n} = 1$  for simplicity

$$E_n^{(1)} = \frac{E_0 e^{ikna}}{2i\delta - 1} \left\{ 1 + \frac{3}{2i(2i\delta - 1)} \frac{1}{ka} \left[ \sum_{p=1}^{n-1} \frac{1}{p} + \sum_{p=1}^{N-n} \frac{1}{p} e^{2ipka} \right] \right\}. \quad (4.12)$$

In the previous case,  $a \neq j\frac{\lambda}{2}$ , we neglected the backward scattering because of the phase factor that destroyed the field at long range. However, here, the phase factor of the backward scattering is also equal to 1:  $e^{2ip \times \frac{2\pi}{\lambda} \times j\frac{\lambda}{2}} = e^{2i\pi \times jp} = 1$ . Therefore, backward scattering cannot be neglected anymore. The probability of excitation of atom  $n$  is then given by, to first order in  $1/ka$

$$\mathcal{P}_n = \frac{(dE_0/\hbar)^2}{\Delta^2 + \Gamma^2/4} \left\{ 1 - \frac{3\Gamma\Delta}{2j\pi(\Delta^2 + \Gamma^2/4)} \left[ \sum_{p=1}^{n-1} \frac{1}{p} + \sum_{p=1}^{N-n} \frac{1}{p} \right] \right\}. \quad (4.13)$$

To know which atom has the highest excitation probability, for  $\Delta < 0$ , we consider the following factor

$$A_n = \sum_{p=1}^{n-1} \frac{1}{p} + \sum_{p=1}^{N-n} \frac{1}{p}. \quad (4.14)$$

We are looking for which  $n$ ,  $A_n$  is maximum. Considering the case  $n - 1 < N - n$  (atom  $n$  is located in the first half of the 1D chain),  $A_n$  becomes

$$A_n = 2 \sum_{p=1}^{n-1} \frac{1}{p} + \sum_{p=n}^{N-n} \frac{1}{p}. \quad (4.15)$$

In (4.15), the first sum is associated with small values of  $p$ , which are the ones with the largest contribution. We thus understand that the second sum, the one associated with the highest values of  $p$ , hence the smallest contribution, has to be canceled to maximize  $A_n$ . Indeed, the number of elements in  $A_n$  is constant ( $N$  atoms, thus  $N - 1$  terms).

The ones that are removed from the second sum are then put back into the first one, increasing the value of  $A_n$ . From this we deduced that

$$\begin{aligned} \frac{dA_n}{dn} = 0 &\iff \sum_{p=n}^{N-n} \frac{1}{p} = 0, \\ &\iff \begin{cases} n = \frac{N}{2} \text{ if } N \text{ is even,} \\ n = \frac{N}{2} \pm 1 \text{ if } N \text{ is odd.} \end{cases} \end{aligned}$$

The probability of excitation is then maximum (minimum) for negative (positive) detuning at the middle of the chain. One can also show that the amplitude of dipoles are symmetric with respect to the middle of the 1D chain, hence the relation

$$b_1 = b_N, \quad b_2 = b_{N-1}, \quad \dots$$

This results is consistent with the one presented in [Sutherland and Robicieux, 2016].

### 4.1.2 Robustness of the system with experimental imperfections

In this section, we address questions related to the experimental demonstration of the previous phenomenon. In fact, (4.10) encourages us to think that the increase of scattered field along the chain (general case) is robust again both a random loading of the 1D chain and a position noise of the atoms present in the chain.

**Random loading** Assuming  $f_p = 1$  for simplicity, the random loading of each lattice site  $p$  in the 1D chain is described by a random variable  $\epsilon_p$ , which is either 1 or 0. Averaged over many realizations, the sum in (4.10) becomes

$$\left\langle \sum_p \frac{\epsilon_p}{pka} \right\rangle = \sum_p \frac{\langle \epsilon_p \rangle}{pka} = \frac{1}{2} \sum_p \frac{1}{pka}. \quad (4.16)$$

The random loading of the chain does not change the behavior of the system, it only reduces the interactions by a factor 2.

**On-axis disorder** To consider the noise in the atoms positions along the chain axis, we introduce a random centered variable  $\delta z_p$  so that the position of atom  $p$  is given by  $pa + \delta z_p$ . In this case, still assuming  $f_p = 1$  and  $\delta z_p \ll a$ , the sum in (4.10) becomes

$$\left\langle \sum_p \frac{1}{pka + k\delta z_p} \right\rangle \approx \sum_p \frac{1}{pka} - \sum_p \frac{1}{pka} \frac{\langle \delta z_p \rangle}{pa} = \sum_p \frac{1}{pka}. \quad (4.17)$$

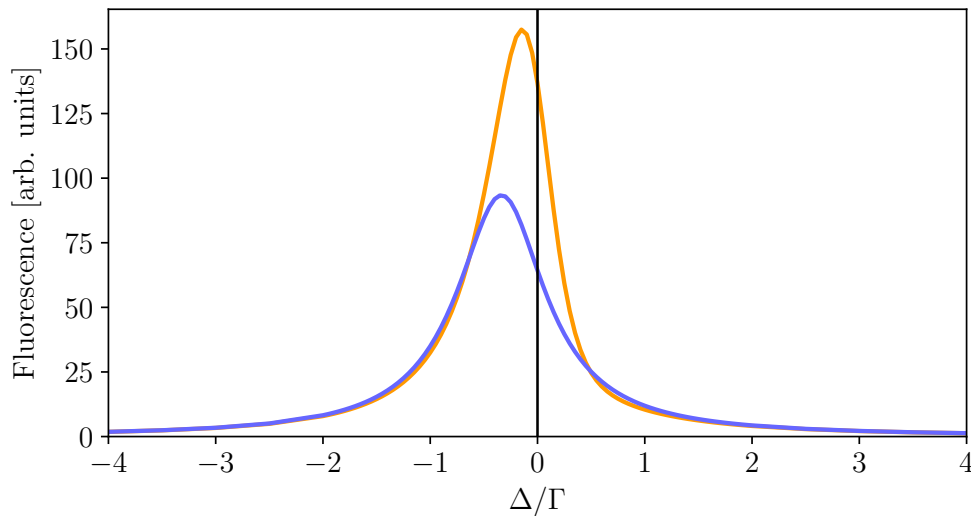


**Figure 4.3.:** Total fluorescence emitted by a 1D chain of 100 atoms (50% filling fraction is considered here). The blue solid line is the spectrum obtained from the general solution of (4.6), the orange solid line is the one associated with the perturbative treatment (see equations (4.7) and (4.9)).

The increase of scattered field amplitude along the chain is then robust to on-axis position noise.

Everything seems to indicate that the physical system under study here is robust against physical imperfections. Note however that these conclusions are based on the derivation of (4.10) that relies on various assumptions. If it gives a picture of what is going on, it can fail to reproduce the exact behavior of the system. For instance, it fails quite badly to reproduce the fluorescence spectrum of atoms for small detunings as depicted in Figure 4.3. Therefore, we decided to perform simulations to confirm that the collective effects survives the experimental imperfections. We will first consider a 1D chain of 8 lattice sites, randomly filled with 0 or 1 atoms. Then we will consider the same physical system but add some noise in the transverse and in the longitudinal positions of each atoms, to take into account the non zero temperature of the atoms on a real experiment.

To simulate the behavior of the system, we choose to run Monte-Carlo Wave simulations [Mølmer et al., 1993], restricting ourselves to the single excitation basis. Doing so, the results should not differ from the regular steady-state solution of the system when this steady-state behavior is rapidly reached. However, some steady-state solutions requires a long transient time, an important information that is not provided by the regular calculation. Monte-Carlo Wave simulations being time resolved, we have access to the actual behavior of the system for the specific times during which we simulate

our experiment. For very long transient time, the behavior of the system can be very different from the steady-state one and we would then know that we are in such a case.

In all this section

- the lattice spacing  $a$  is taken equal to half the wavelength of the trapping laser:  $a = 940/2 = 470 \text{ nm} = 0.6\lambda$  with  $\lambda$  the transition wavelength of the D2 line of  $^{87}\text{Rb}$ ;
- the Monte-Carlo Wave Function simulation, based on a Python package provided by Nikola Šibalić<sup>1</sup>, has been run for  $12 \times \frac{1}{\Gamma} \approx 312 \text{ ns}$  and is repeated typically 120 times;
- the probabilities of excitation are all normalized, if not specified, to the single atom excitation probability case.

### Perfect system

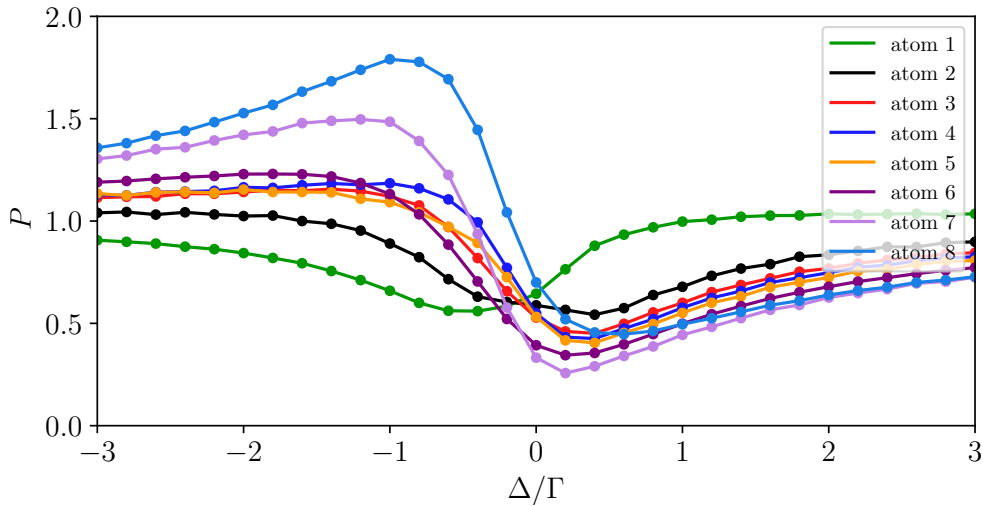


**Figure 4.4.:** Probability of excitation  $P$  of each atom of the 1D chain versus detuning  $\Delta$ , in units of the natural linewidth  $\Gamma$ . The simulation is repeated 20 times here.

First, let's see how much difference in the excitation probability one should expect between the beginning and the end of a perfect (fully filled, no noise) 1D chain of 8 atoms. For a perfect system, the growth of the excitation along the chain is clearly visible, even for a small chain of only 8 atoms. For instance, if you consider a detuning

---

<sup>1</sup>Nikola Šibalić, *DoDo: A Python library for calculating dynamics and optical response of Dense Optical Dipoles*, to be published.

of the probe laser of  $-1\Gamma$ , you see that the probability of excitation of the last atoms is almost 3 times bigger than the one of the first atom (see Figure 4.4). The excitation probabilities of atoms located in the middle of the chain (atom 3 to 6) are very similar and then difficult to distinguish. Determining if the excitation is at the beginning of the chain (atom 1 and 2) or at the end (atom 7 and 8) is completely feasible, as those are spatially separated by typically  $3\lambda$ , which is bigger than the optical resolution of our imaging system.

### With defects

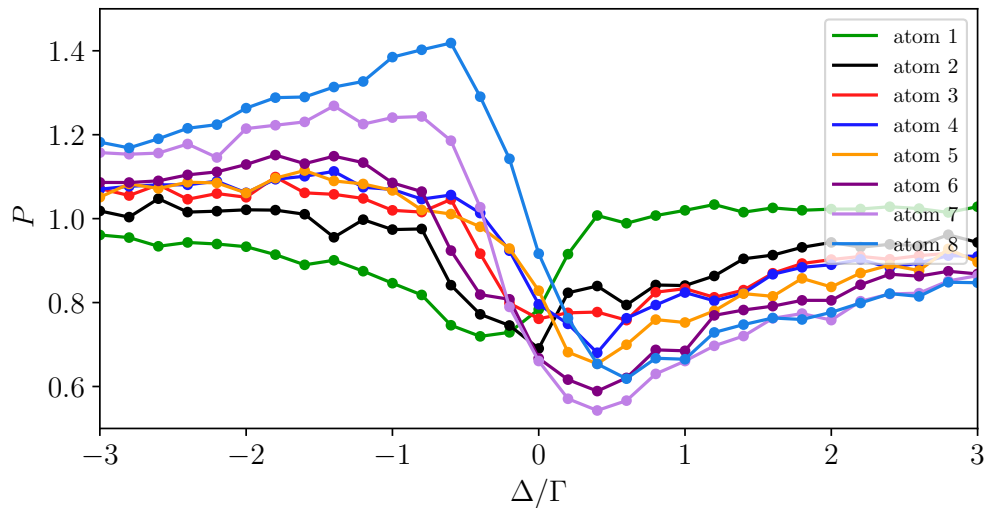


**Figure 4.5.:** Probability of excitation of each atom of the 1D chain versus detuning with 50% filling probability. The simulation is repeated 100 times for each detunings.

In this section, we consider the case of the 1D chain previously introduced with each site having 50% probability to be filled with an atom. The idea is to reproduce the behavior of the system on our experiment: each lattice site is either filled with an atom or empty. Moreover, the loading is not deterministic. The simulation is then repeated to average on the atomic configurations. For the moment, no disorder is introduced in the position of the atoms. Once again, the excitation is localized at the end of the chain for negative detunings and at the beginning of the chain for positive detunings but it is less contrasted. For instance, if we consider the  $-1\Gamma$  detuning case, we see that the last atom is 1.6 times more likely to be excited than the first one (see Figure 4.5). It is almost two times less than the perfect 1D chain but it is still visible experimentally.

### With disorder

To observe the effect of disorder only, and not a combination of several effects, we took a 1D chain of 8 atoms perfectly loaded, but introducing a bit of noise in the position of each atom. The simulation is repeated 100 times to average on the relative distances between atoms.

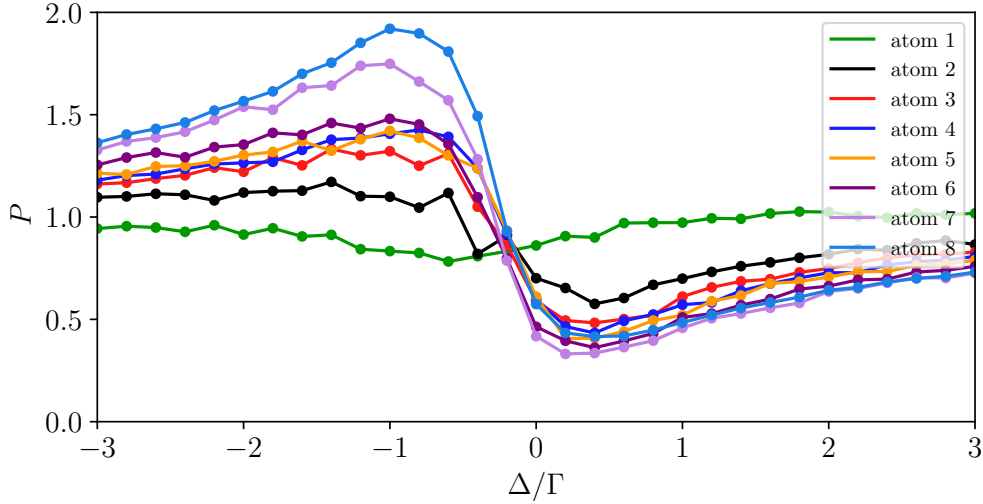


**Figure 4.6.:** Probability of excitation of each atom of the 1D chain versus detuning with  $0.06\lambda$  disorder in the  $z$ -direction. No defect in the filling of the 1D chain is included here. The simulation is repeated 100 times for each detuning.

**Longitudinal disorder** We proceed step by step to be able to point out the main experimental limitation that could eventually destroy the observation of the phenomenon that we want to demonstrate. Let us consider first the noise in the longitudinal direction (the one of the 1D chain). The 1D array is created by the interference of two contra-propagative Gaussian beams. Assuming that each beam is accurately represented by a plane wave and has the same intensity, the intensity along the  $z$ -direction is given by

$$I(z) = 4I_0 \sin^2 \left( \frac{2\pi z}{\lambda_{\text{trap}}} \right), \quad (4.18)$$

where  $\lambda_{\text{trap}}$  is the wavelength of the laser used to create the traps. To get the spatial extension of the harmonic oscillator along the  $z$ -direction, we are developing the intensity profile around one of its maxima

$$I(z) \sim 4I_0 \left( \frac{2\pi z}{\lambda_{\text{trap}}} \right)^2. \quad (4.19)$$

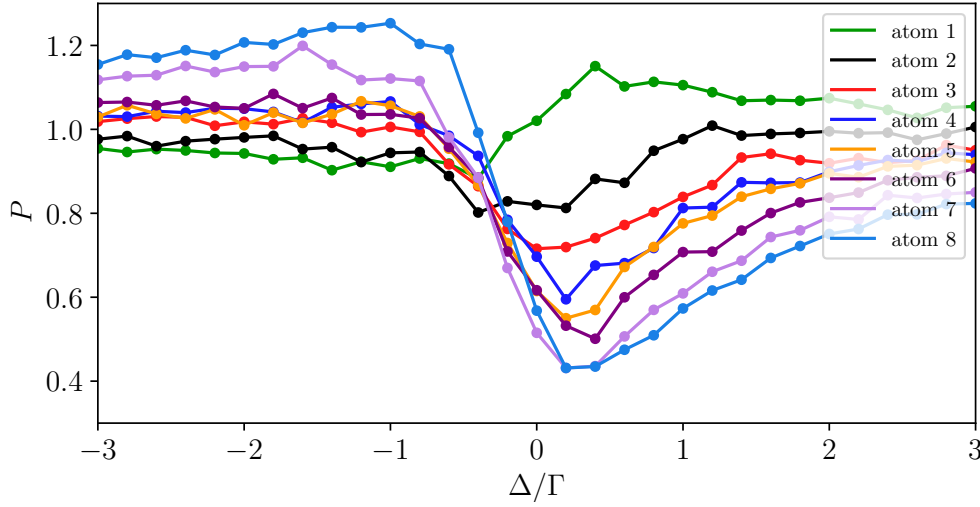


**Figure 4.7.:** Probability of excitation of each atom of the 1D chain versus detuning with  $0.06\lambda$  disorder in the  $z$ -direction and  $0.3\lambda$  disorder in the transverse direction. No defect in the filling of the 1D chain is included here. The simulation is repeated 100 times for each detunings.

The trapping potential follows the distribution of intensity given by (4.19), then

$$\frac{1}{2}m\omega_z^2 z^2 = \frac{16\pi^2 U_0}{\lambda_{\text{trap}}^2} z^2, \quad (4.20)$$

with  $\omega_z$  the longitudinal frequency of the harmonic oscillator,  $U_0$  the trapping potential,  $m$  the mass of  $^{87}\text{Rb}$ . The spatial extension of the wave-function of an harmonic oscillator in its ground state is given by

$$\frac{1}{2}m\omega_z^2 \Delta z^2 = \frac{1}{2}k_B T, \quad (4.21)$$

with  $\Delta z$  the width of the wave-function,  $k_B$  the Boltzmann constant and  $T$  the temperature. Replacing (4.20) in (4.21), one can get an estimation of the position noise in the longitudinal direction

$$\Delta z = \frac{\lambda_{\text{trap}}}{4\pi} \sqrt{\frac{k_B T}{2U_0}}. \quad (4.22)$$

For a trap depth  $U_0$  of 1 mK and a temperature of the atoms around  $100 \mu\text{K}$ , the longitudinal noise is  $\Delta z \approx 0.02\lambda$ . We have run the simulation with a disorder in the  $z$ -direction of three times this value,  $0.06\lambda$ , to take into account a possible heating of the atoms during the probe time (see Figure 4.6). This is not completely negligible as the separation between two atoms in our case is  $a = 0.6\lambda$ , so it represents 10% of  $a$ .

**Transverse and longitudinal disorder** Because the longitudinal disorder does not seem to prevent us from seeing the phenomenon on the experiment, we will keep it equal

to  $0.06\lambda$  and we will add the transverse disorder on a fully loaded 1D chain of 8 atoms. To estimate the transverse disorder on our system, we will consider that the transverse trapping in each lattice site is the one given by a Gaussian beam of waist at  $1/e^2$  equal to  $w_0$ . Using the same kind of procedure as the one used for longitudinal disorder, one gets

$$\Delta r = \frac{w_0}{2} \sqrt{\frac{k_B T}{U_0}}. \quad (4.23)$$

For a waist of  $1.6 \mu\text{m}$ , a trap depth of 1 mK and a typical temperature of the atoms of  $100 \mu\text{K}$ , the transverse extension is  $\Delta r \approx 0.30\lambda$ . This is roughly half the lattice spacing  $a$  that can increase the distance between two following atoms by up to 40%.

In contrast with Figure 4.6, Figure 4.7 shows that the transverse disorder is reducing the growth of excitation along the 1D chain. This can be attributed to the fact that the transverse disorder introduces a phase factor in the forward scattering field that will minimize the constructive interference. Even if the angle between the propagation of the field between two atoms and the trapping axis remains small, the confinement being less tight in the transverse direction compared to the on-axis one could explain why the reduce of the collective effects seems more pronounced for transverse disorder.

#### With disorder and defects

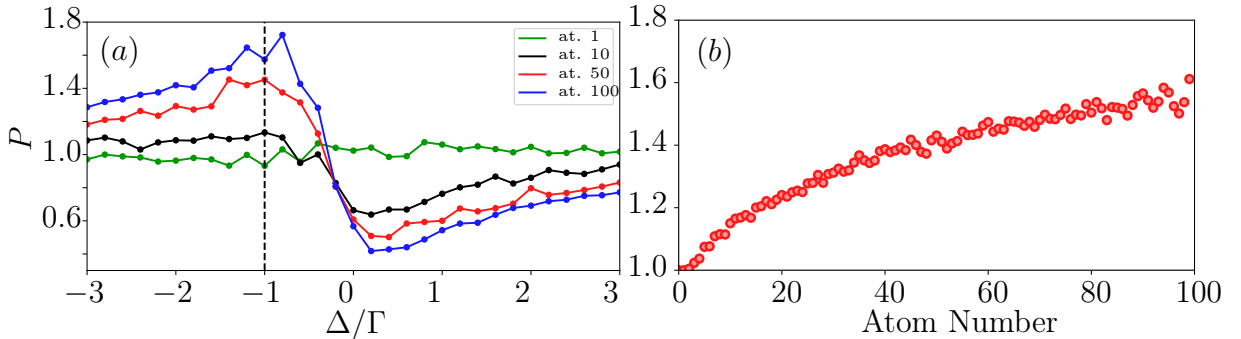


**Figure 4.8.:** (a): Probability of excitation of each atom of the 1D chain versus detuning with  $0.06\lambda$  disorder in the  $z$ -direction and  $0.3\lambda$  disorder in the transverse direction. 50% filling fraction is included here. The simulation is repeated 50 times for each detunings. (b): Probability of excitation of each atom along a 1D chain of 100 atoms with  $\Delta = -1.0\Gamma$ . Same filling fraction and disorder as in (a). The simulations performed here are solutions of (4.6), averaged over 1000 different configurations.

Now we consider the most imperfect system: a 1D chain of 8 atoms with disorder in their respective positions and with a filling fraction of 50% of each lattice site. Figure 4.8 (a) is very similar to Figure 4.7. Doing more repetition is enough to forget

about the defects in the filling of the 1D chain. In Figure 4.8 (b), we simulated the probability of excitation along a 1D chain of 100 lattice sites for a detuning of  $-1.0\Gamma$ . The simulation corresponds to the solution of the set of coupled equations (4.4) and repeated 1000 times. The results are in very good agreement with the one presented in [Sutherland and Robicheaux, 2016], although we included here the filling fraction of 50% and disorder on the position of the atoms due to their temperature.

### 4.1.3 Investigation of the effect of the temperature

In this section, we consider a chain of 15 atoms with 50% filling fraction and disorder along all directions calculated from various temperature of the atoms. We simulated the response system for various detunings of interest, thus representing the spatial localization of the excitation along the chain. Seeing that the last atom, or more specifically the few last atoms, are more likely to be excited for negative detuning is feasible, even for a decent range of atom temperatures (see Figure 4.9).

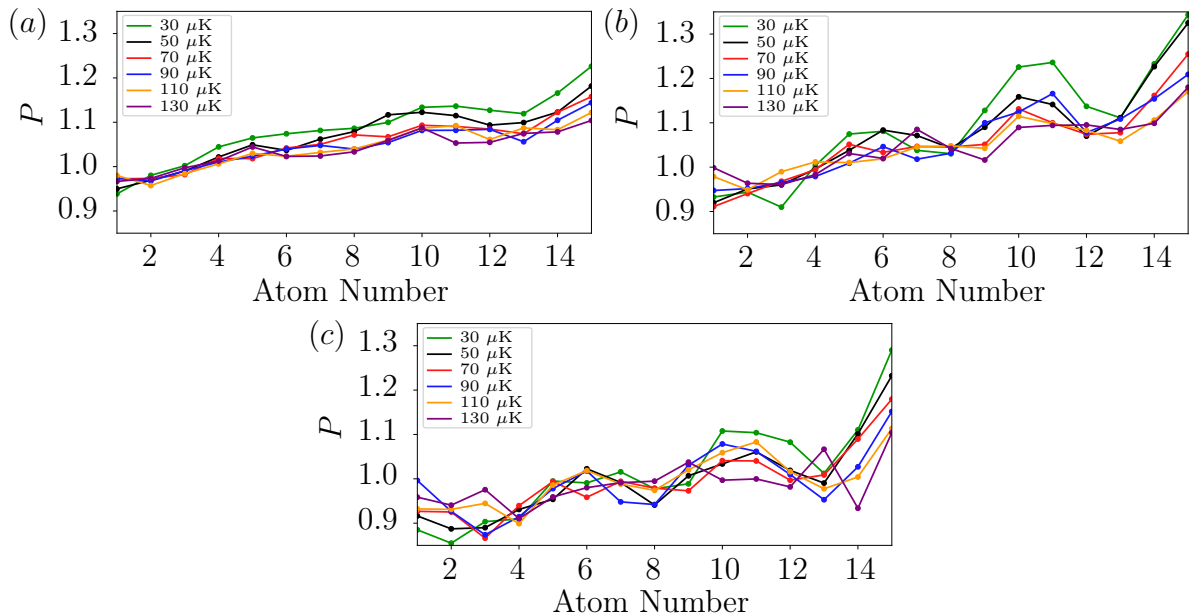


**Figure 4.9.:** Excitation probability of a 1D chain of 15 atoms with 50% filling fraction and in presence of disorder estimated from temperature for various detunings:  $\Delta = -2.5\Gamma$  (a),  $\Delta = -1.0\Gamma$  (b) and  $\Delta = -0.5\Gamma$  (c).

### 4.1.4 Investigation of the effect of a Gaussian beam in the excitation probability

Considering the fact that the transverse disorder is the main effect that tends to destroy the growth of excitation along the chain, one might be concerned about the fact that

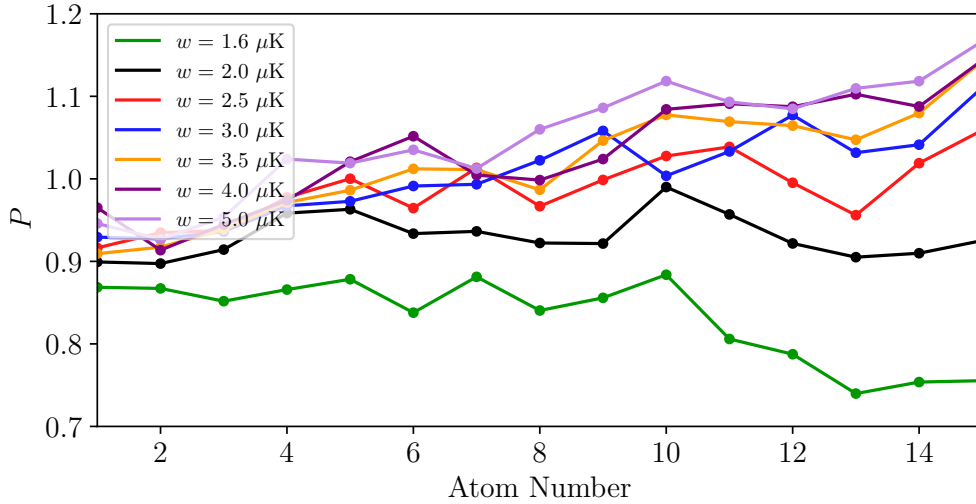


**Figure 4.10.:** Probability of excitation along a 1D chain of 15 atoms, for a detuning of  $-1.0\Gamma$ , a temperature of  $100 \mu\text{K}$  and a Gaussian excitation beam of waist  $w$ .

a Gaussian beam, with a none-infinite radius of curvature, can destroy the effect even more. Indeed, an atom slightly outside of the center of the beam will not see exactly the same phase as one located on its axis. Let us check to which point a Gaussian profile of the excitation beam can decrease the excitation probability along the chain. To do that, we will consider a 1D chain of 15 atoms, with a temperature of  $100 \mu\text{K}$ , and a detuning  $\Delta = -1.0\Gamma$ . We simulated the response of the system for various waists of the excitation beam, having in mind that when the waist tend to infinity, we should recover the results obtained with the plane wave as the excitation beam. For a waist of the excitation beam above  $2.5 \mu\text{m}$ , the effect of the Gaussian beam can be neglected and the results obtained in the case of the plane wave are still valid. But we can experimentally demonstrate that for a tightly focused Gaussian beam (with a waist below  $2.5 \mu\text{m}$ ), in presence of disorder, the growth of excitation is destroyed. More surprisingly, it seems that the effect discussed here is reversed.

### 4.1.5 Conclusion

The localization of the excitation, which seems to survive the imperfections of the physical system, is still subjected to the fact that the imaging system has a sufficient resolution to define if it is the beginning or the end of the 1D chain which is excited, and to the fact that the atoms emit enough photons to be detected. There is no need to adjudicate on the second point, as we managed to observe the fluorescence emitted by the atoms of the 1D chain (see Figure 4.1 (a)). As for first point, it can be easily solved by creating a longer 1D chain, as the one presented in Figure 4.1 (a).

## 4.2 SUPER IMAGING OF THE 1D CHAIN OF ATOMS

After having confirm with simulations that the growth of an excitation along a 1D chain of atoms is robust against both filling defects and disorder, we wanted to address the imaging of the chain of atoms in our experiment. As explained, our apparatus will allow us to create a 1D chain and trap around 100 atoms ( $\simeq 200$  lattice sites) using the first axis. The second high resolution optical axis can collect the fluorescence image of this chain. But because the lattice spacing between two neighbor atoms ( $a = \lambda_{\text{trap}}/2 = 470$  nm) is smaller than our resolution (around  $1.5 \mu\text{m}$ ), we cannot know, with direct measurement, the position of each atoms. It would be useful, nonetheless, to be able to know as precisely as possible the configuration of atoms in the chain for each experiment. We would therefore be able, ideally with a single shot, to post process our data for particular configuration for instance.

People have reported sub-diffraction imaging reconstruction in various fields: in biology ([Lubeck and Long, 2012], [Eng et al., 2019]) and in atomic physics ([Bücker et al., 2009b], [Sherson et al., 2010]) for instance; and with various methods, including the use of machine learning and neural networks ([Zhu et al., 2018], [Floyd, 1991]). Image analysis is powerful and can allow sub-diffraction imaging if the signal to noise ratio (SNR) is high enough. To investigate the possibility to implement such a tool on our experiment, we simulated typical pictures that can be obtained on our EMCCD (knowing the initial random configuration of atoms in the chain). Then, we studied the success rate of an algorithm in reconstructing the initial atomic configuration from the given picture and for various SNR.

### 4.2.1 Creation of the picture

The creation of the picture has to reproduce an experimental one with the highest fidelity possible to be able to have a good estimation of the performance of the algorithm in recovering the initial atomic distribution on real images. Here, based on the detailed work presented in [Alberti et al., 2016], we present the several steps to simulate the images.

1. Creation of the perfect picture (Figure 4.11 (a))
  - We start from a randomly filled 1D array, each site of the chain having a probability  $1/2$  to be filled by an atom.
  - We also consider the finite temperature of the atoms ( $\simeq 40 \mu\text{K}$ ) and the trapping potential characteristics to introduce some noise in their position with respect to the absolute location of the lattice site.

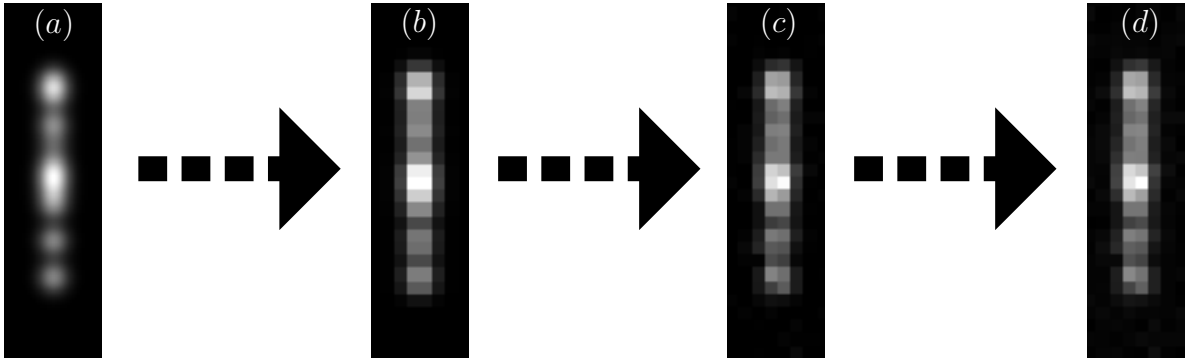


**Figure 4.11.:** Presentation of the picture at different stage of its creation. (a): Perfect image with 18 atoms (37 lattice sites). (b): Binned picture. Pixel size corresponds to  $1 \mu\text{m}$ . (c): Binned picture with shot noise. (d): Final picture. The read-out-noise of the camera is added to the previous picture.

- Then, we convolve this almost 1D atomic distribution with the PSF of our imaging system. For simplicity here, the PSF of a single atom is considered to be a 2D Gaussian function with a waist of  $1.6 \mu\text{m}$ .
2. The next step is a binning of the previous perfect image to simulate the integration of the fluorescence signal on our CCD camera (Figure 4.11 (b)). The pixel size is chosen equal to  $1 \mu\text{m}$ , as in our experiment. To be accurate, the *perfect* image being created by a computer, it is discretized by nature. But it corresponds to a pixel size of typically  $\sim 100 \text{ nm}$ , sufficiently small compared to the size of the pixel use in the binning procedure to be considered as *perfect*.
  3. Then we are adding shot noise on the obtained picture (Figure 4.11 (c)). Each pixel value is modified by an amount randomly chosen from a Poisson distribution with a parameter that depends on the initial value of that pixel. For example, if the pixel value was  $N$  (photons, counts,...), we replace this value by another one randomly chosen from the probability distribution

$$P(X = k) = \frac{\lambda^k \exp(-\lambda)}{k!}, \quad (4.24)$$

with  $\lambda = N$ .

4. Finally, we are adding the read-out-noise of the camera and some background noise to reproduce the experimental pictures (Figure 4.11 (d)). This value depends on the parameters of the camera, but seems to be equal to a few photons per pixel for a large range of working parameters.

For each picture we created, we save the initial atomic distribution. This initial distribution will be compared to the one obtained by the algorithm to evaluate its performances.

### 4.2.2 Algorithm

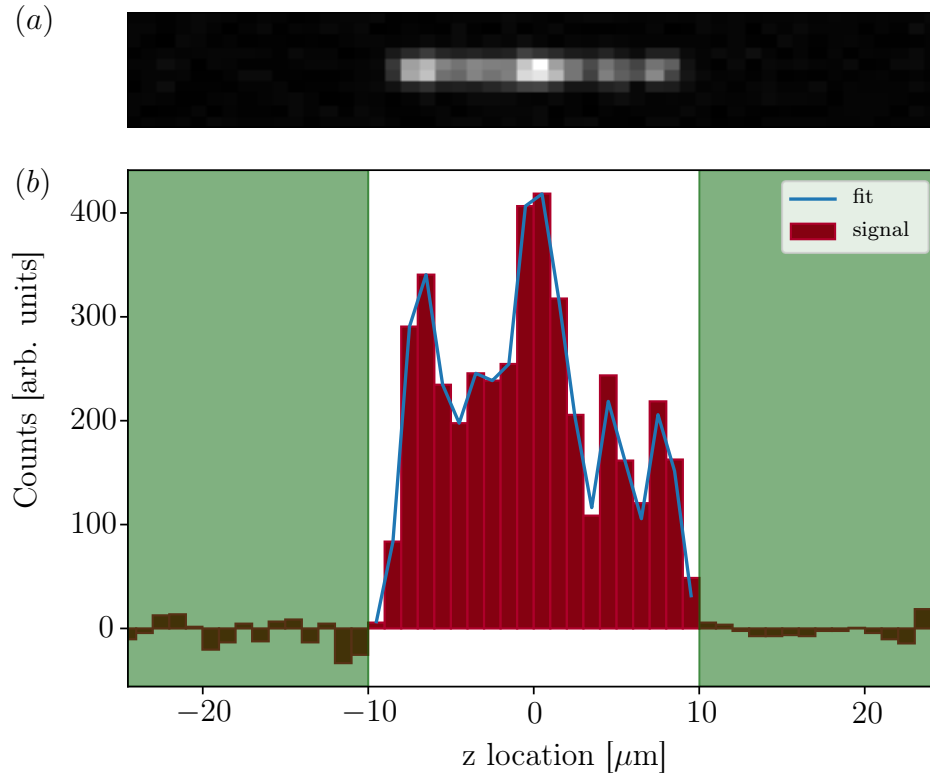


**Figure 4.12.:** Output of the fitting algorithm. (a): Initial picture with 18 atoms (37 lattice sites). (b): Trace of the picture along the direction of the chain  $z$ . The green stripes delimit the ROI into which the algorithm is performing the fitting procedure. The result of the fit is represented with the continuous blue line. It correspond to the optimal reproduction of the signal associated with the reconstructed position of the atoms in the chain.

The fitting procedure is done in several steps that are described in this section.

First of all, the algorithm subtracts the background. The subtracted value is defined by averaging the pixels values in region of the picture where no atoms are present.

After the background subtraction, the algorithm is defining a region of interest (ROI) within which the atoms are located. Because the chain is a 1D system and fitting a 1D function would require less computational time, the algorithm is also tracing along the direction of the chain.

Then, the algorithm tries to determine the number of atoms present in the chains by summing the contribution of each pixel within the ROI. To estimate the number of atoms, the algorithm needs that the user provides some single atom pictures under the

same experimental conditions. The more pictures are provided, the better the algorithm will be able to determine the number of atoms in others pictures. This step is crucial as if the estimation is wrong, he won't be able to reproduce the initial atomic configuration. Note that we have included a feature that requests the algorithm to perform the fitting procedure with two different atom numbers if it is difficult to choose between  $n$  and  $n + 1$ . For instance, let us say that the ratio of the counts of the pixels in the picture and the counts obtained with a single atom is giving  $n + \varepsilon$ , where  $n$  is an integer and  $\varepsilon$  a real number corresponding to the fractional part of the ratio. If  $\varepsilon \ll 1$  ( $\varepsilon \simeq 1$ ) then the algorithm will fit the picture with  $n$  ( $n + 1$ ) atoms. But if  $\varepsilon \simeq 1/2$ , the algorithm will first try to fit the picture with  $n$  atoms, then with  $n + 1$  atoms. For both cases, it will estimate the error between its fit and the picture and will choose which value is more appropriate.

After these steps, the fitting procedure occurs. The algorithm that we used is a basin-hopping algorithm: it is a stochastic algorithm which attempts to find the global minimum of a smooth scalar function of one or several variables ([Wales, 2003], [Wales and Doye, 1997], [Wales and Scheraga, 1999]). The algorithm is iterative, each cycle being composed of three steps:

1. random perturbation of the coordinates,
2. local minimization,
3. accept or reject the new coordinates based on the function value.

This type of algorithm has been designed to reproduce the natural process of energy minimization of clusters of atoms and is thus perfectly appropriate for our problem. Note that, once again, the fitting procedure relies on the single atom pictures provided by the user. Indeed, from the fit of each single atom picture, the algorithm has extracted an average signal per atom in order to determine the number of atoms in other pictures, but it has also estimated the width and the amplitude of the fluorescence PSF of a single atom. Knowing precisely those parameters is highly related to the success rate of the algorithm as it will try to reproduce the picture by summing single atom response. The algorithm is allowed to slightly vary the amplitude of the fluorescence image of each atom to tackle the shot noise still present in the trace of the picture.

At this stage, the algorithm provides the positions of the atom it has found that best reproduce the signal, as represented in Figure 4.12 (b). However, the location of the atoms are not always exactly at the lattice sites locations. Even though a condition implemented in the basinhopping algorithm prevent it from choosing the position of two atoms closer than a fraction of the lattice spacing  $a/2$ , we still have to assign each position variable to a real lattice site location. To do so, we perform an assignment procedure which is the following:

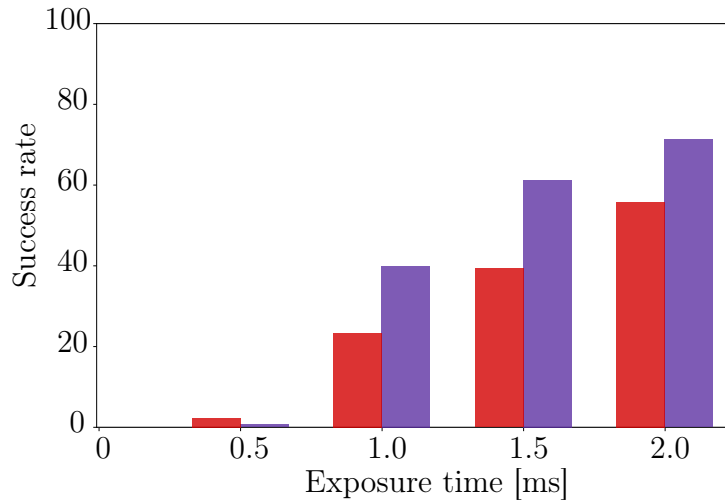


**Figure 4.13.:** Success rate obtained on the same set of pictures by the algorithm with the correction procedure presented in the text (purple bars) and without this correction procedure (red bars).

- the assignment of an atom in a given lattice site is based on proximity.
- if another atom would have been assigned to this lattice site in absence of the first one, then this atom is assign to the second closest available lattice site.

Finally, we run a last basic optimization. From the reconstructed positions of atoms, we are modifying the position of each atom, one at a time, by one lattice site. We compute the error between this new configuration and the initial picture. If the computed error is smaller than the previous one, the configuration is updated to this new one. This optimization runs until all the atoms have been moved. This last optimization step has been the result of our investigation in order to improve the performance of the algorithm. This correction part definitely increases the success rate of the fitting procedure, up to 20% in the best cases as depicted in Figure 4.13.

### 4.2.3 Performance evaluation of the algorithm

To evaluate the performance of the algorithm, we provide a set of pictures (typically 100 different pictures) for which we now the lattice sites filled with an atom. The algorithm tries to reconstruct the atomic distribution. The output of the algorithm is compared with the initial configuration for all the picture, giving us an estimation of the performance of the algorithm.

The success rate of the algorithm, for a pixel resolution of  $1.0 \mu\text{m}$ , is represented in Figure 4.14 as a function of the exposure time. As one can see, the success rate of the algorithm increases with the exposure time. Indeed, the higher the exposure time,

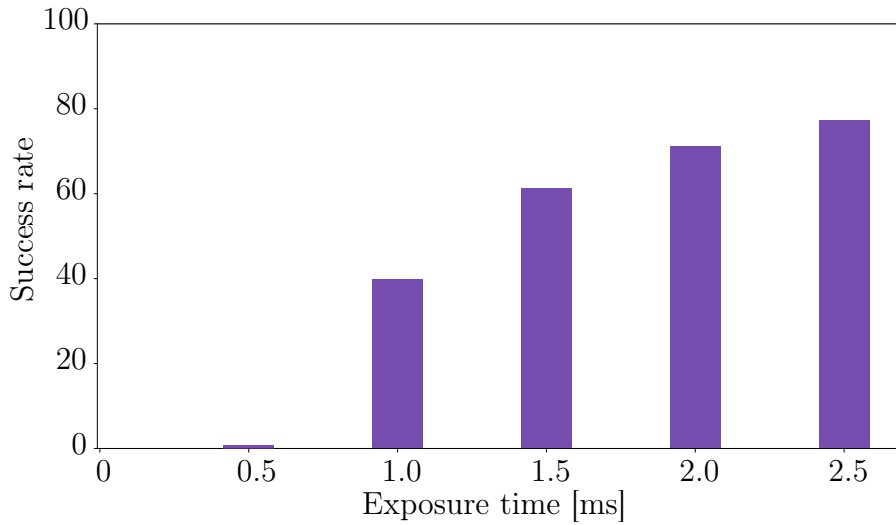


**Figure 4.14.:** Success rate obtained with our algorithm for a pixel resolution of  $1.0 \mu\text{m}$ . As the exposure time increases, the signal to noise ratio does the same and the fitting procedure becomes more successful.

the higher the SNR. It is then easier for the algorithm to find precisely the location of atoms in the lattice site. One can understand this fact thinking about the opposite case: as the exposure time decreases, the signal is smaller and smaller so that at some point it gets hidden in the various sources of noise of the picture.

We have also tested the algorithm with a different value of the pixel resolution, for instance with  $0.5 \mu\text{m}$ . Needless to explain that as the fluorescence signal of each atoms is spread over more pixels, a higher exposure time is required to reach the same SNR value as the one with a pixel resolution of  $1 \mu\text{m}$ . However, it seems that the algorithm does not reach a better performance than the one obtained with the pixel resolution set to  $1 \mu\text{m}$ .

#### 4.2.4 Conclusion

The general feeling about this study is that it is very difficult to obtain a high success rate (above 90%) when the pixel resolution is above or of the same magnitude as the width of PSF of our imaging system. In principle, as demonstrated in [Alberti et al., 2016], [Bücker et al., 2009b] or [Sherson et al., 2010], a higher success rate can be obtained by increasing the magnification ratio of our imaging system. However, this approach would require a longer exposure time to collect more signal, consequently increasing the possibility to loose atoms and/or add new ones in the initial configuration, thus rendering any post processing of data useless as the initial picture would not corresponds to the configuration of atoms during the experimental sequence.

The tool is available for further analysis and can be upgraded easily. We also would like to point out that new ways of solving this type of problem, super-resolution imaging, are available today. In fact, huge progress has been made in the field of neural networks, particularly in the field of image reconstruction, mostly in biology and medical research. But those tools are definitely relevant for our approach of the problem. Neural networks can be trained with a lot of experimental pictures and then we would rely on its learning to determine the atomic configuration on any other pictures for which the atomic distribution is unknown. It could be interesting for example to compare the performance of a neural network based approach with the one of our standard fitting algorithm.



# CONCLUSION

---

In this thesis, we have summarized the results obtained in our group concerning the scattering of light by a dense sample of cold atoms. The *incoherent* part of the scattering [Pellegrino et al., 2014] has first been measured, leading to the observation that the results were different from the ones obtained in the case of hot vapours [Keaveney et al., 2012]. This surprising difference motivated the measurement of the *coherent* part of the scattering [Jennewein et al., 2016], to perform a direct comparison with mean-field models that were used in the group of Charles Adams and only relevant for the *coherent* part of the scattered field. This measurement did not lead to a quantitative agreement nonetheless. To confirm this result, a microscopic theoretical description has also been applied but it did not provide a better agreement. At this stage, many questions remained unanswered. As the theoretical description is always an idealization of physical systems plagued with technical imperfections, we wanted to address them in order to better understand our results and maybe to recover a more satisfying agreement with theory.

The first one that we wanted to remove is the internal structure of atoms. Even if they were supposed to be taken into account in the models used to compare our data with, forgotten and eventually unknown effects can still occur. We thus created a sample of cold *two-level* atoms by applying a large homogeneous magnetic field to lift the degeneracy of the Zeeman internal structure of the atoms. The measurement performed in this regime [Jennewein et al., 2018] yielded a satisfying agreement with theory at least at low atom number but not at high atom number. We concluded that the internal structure of atoms does in fact play a role in the way atoms scatter light, but it is not, alone, enough to explain the discrepancies observed between our measurements and the theoretical predictions. We have then investigated the influence of a variation of several quantities relevant for the dipole-dipole interactions, such as the number of atoms in the trap, the temperature of the atoms or the volume they occupy. Indeed, the cloud size being smaller than our optical resolution, we have to rely on the thermodynamic equilibrium hypothesis to infer it from the measurement of the temperature. This hypothesis is hard to check experimentally, but we have shown that it would have to be drastically modified in order to explain the remaining discrepancies. We have also address the role of atomic motion in the cloud. All the simulations performed so far were assuming a frozen atomic distribution. However, due to their temperature, atoms are moving during the probe time. Typically, for temperature on the order of  $100 \mu\text{K}$ , they move by  $30 \text{ nm}$  during the

300 ns of probe duration, even though it is small compared to the mean inter-particle distance, which for our highest measured density is around 200 nm. We have shown that atomic motion does play a role on the coherent scattering line shaped but for velocities at least a factor 10 above the one estimated. The motion was introduced empirically in the simulation, each atoms having a ballistic motion with a specific direction and a specific velocity according to Maxwell-Boltzmann distribution. Doing so, the motion is taken into account classically and no force induced by dipole-dipole interaction is considered between atoms. Nonetheless, these results coincide with the works of [Weiss et al., 2019] and [Kuraptsev and Sokolov, 2019] which state that the collective emission of light by a dense ensemble of cold atoms is robust against thermal decoherence, at least for our probe duration. We have also presented a new model, derived by Pierre Pillet. This model, based on optical Bloch equations, reproduces the coupled-dipoles simulations at low saturation intensity, but has the advantage to not be limited to the weak driving limit. A first measurement of the coherent transmission through a dense cloud of cold two-level atoms has been performed with  $s \approx 1$  and  $s \approx 8$  (see [Jennewein, 2017], appendix E), but further tests are needed in order to allow for a comparison with this model.

The major part of my PhD work was dedicated to the modification and characterization of the new generation of the experimental apparatus. The goal was to solve some experimental imperfections of the previous version and, mostly, open the road for new kind of measurements configurations. The new generation, with the one built at ICFO in the group of M. W. Mitchell and presented in [Bruno et al., 2019], are the only ones that are endowed with two crossed high resolution optical axes. We elaborated an alignment procedure, detailed in chapter 3. Then, I have characterized the performance of the aspheric lenses using a single atom at the bottom of an optical dipole trap. Although the results obtained did not match perfectly the optimal performance expected, we have tried to understand them in terms of the spherical aberration that could be introduced by the viewports. The simulations I have performed seemed to indicate that the viewports introduce a large amount of spherical aberration in order to degrade the optical performance of our lenses to the measured values. Although it is not impossible, it does not seem totally convincing. Further tests have to be done, on the viewports directly for instance, in order to understand why our optical performance are degraded. Nonetheless, the apparatus has been able to trap atoms on one axis and observe them with the second axis, which is already a success.

Finally, the last chapter of this manuscript investigates the robustness of the propagation of an excitation along a 1D chain of atoms with respect to physical imperfections. To do so, we have added physical imperfections to a 1D chain of atoms to determine if the results presented in the work of [Sutherland and Robicieux, 2016] were still valid in a real experiment. We added noise in the positions of the atoms and the random filling of each lattice site. We have shown that within our experimental parameters,

---

the propagation of excitation survives the physical imperfections. It logically calls for a future experiment to demonstrate this effect. In a very last study, I have tried to elaborate an algorithm to extract the positions of the atoms along the 1D chain based on their fluorescence image. In direct connection with the previous work of this chapter, the tool, if successful, would have enabled to post process our data for every given atomic configuration in the 1D chain. With our experimental parameters, the tool is not successful enough. However, it can be upgraded using more sophisticated techniques and maybe integrated on the experiment.

The influence of dipole-dipole interactions in dense samples has still some remaining features that are not fully understood. In this manuscript, we have tried to gather as much as possible the different measurements, theories and interpretations performed in our group to draw the clearest picture obtained so far. Not having solved all the problems related to the questions, we have nonetheless dig deeper into the field and try to see where is (are) the critical point(s) that prevent us from obtaining a satisfactory agreement between theory and data. We have not found it yet, but the list gets shorter. New experiments have to be performed in order to find the underlying assumption that is apparently not fulfilled in our experiments, and in others, that would restore a good agreement between dipole-dipole interactions predictions in dense ensembles and our results. The group wants also to investigate effects of dipole-dipole interactions in ordered samples. We have seen, theoretically, one of this effect on a 1D chain of atoms. The new apparatus has the potentiality to measure the collective effects on these types of systems. It could also, in a near future, investigate the effects of these interactions on 2D systems. Theoretical works have demonstrated that, depending on the lattice spacing, 2D arrays of atoms can interact strongly with light and eventually reflect totally the incoming beam ([Bettles et al., 2016b], [Shahmoon et al., 2017b]). It could be an experimental demonstration of the construction of light-matter interface based on dipole-dipole interactions which our apparatus would be able to achieve. Finally, it would also be interesting to investigate quantum correlations in these type of systems.

In a nutshell, having a proper understanding of dipole-dipole interactions in dense regime would be a huge success. It would allow to further investigate the influence of dipole-dipole interactions in the quantum regime with confidence. The apparatus presented in this manuscript is waiting to perform new experiments and I truly hope that it will be associated with wonderful results in the future.



# APPENDIX A

## ELECTRIC FIELD PRODUCED BY A DIPOLE

---

This appendix gives a detailed derivation of the electric field produced by a dipole. Its expression is introduced in chapter 2 and used in all the numerical simulations of the chapter. The derivation done here will start from Maxwell's equations

$$\nabla \cdot \mathbf{E} = \rho/\epsilon_0 \quad (\text{A.1}) \quad \nabla \cdot \mathbf{B} = 0 \quad (\text{A.3})$$

$$\nabla \times \mathbf{E} = -\frac{\partial \mathbf{B}}{\partial t} \quad (\text{A.2}) \quad \nabla \times \mathbf{B} = \mu_0 \mathbf{j} + \frac{1}{c^2} \frac{\partial \mathbf{E}}{\partial t} \quad (\text{A.4})$$

Applying the rotational operator to (A.2) and substituting the temporal derivative of (A.4) into it, one gets an equation which relates the electric field to its sources

$$\begin{aligned} \nabla \times (\nabla \times \mathbf{E}) &= \nabla(\nabla \cdot \mathbf{E}) - \nabla^2 \mathbf{E} \\ &= -\frac{\partial}{\partial t}(\nabla \times \mathbf{B}) \\ &= -\mu_0 \frac{\partial \mathbf{j}}{\partial t} - \frac{1}{c^2} \frac{\partial^2 \mathbf{E}}{\partial t^2} \end{aligned}$$

and finally

$$\left( \nabla^2 - \frac{1}{c^2} \frac{\partial^2}{\partial t^2} \right) \mathbf{E} = \frac{1}{\epsilon_0} \nabla \rho + \mu_0 \frac{\partial \mathbf{j}}{\partial t}. \quad (\text{A.5})$$

The exact same procedure can be applied to the magnetic field, leading to

$$\left( \nabla^2 - \frac{1}{c^2} \frac{\partial^2}{\partial t^2} \right) \mathbf{B} = -\mu_0 \nabla \times \mathbf{j}. \quad (\text{A.6})$$

At this point, in most textbooks, authors usually introduce the vector potential  $\mathbf{A}$  and the scalar potential  $\varphi$ . These variables lead to two new equations, one of them having the advantage to be a scalar equation. In fact, (A.3) is telling us that the  $\mathbf{B}$  is equal to a purely rotational field, up to a gradient of some function, that we call  $\mathbf{A}$

$$\mathbf{B} = \nabla \times \mathbf{A}. \quad (\text{A.7})$$

By inserting (A.7) into (A.2), we get

$$\nabla \times \left( \mathbf{E} + \frac{\partial \mathbf{A}}{\partial t} \right) = 0.$$

This non-rotational field is then of the form of a gradient of a function, that we call the scalar potential  $\varphi$

$$\mathbf{E} = -\nabla\varphi - \frac{\partial \mathbf{A}}{\partial t}, \quad (\text{A.8})$$

the negative sign in front of the gradient being a convention.

The electric field and magnetic field are completely defined by Maxwell's equations, but the scalar and vector potential, through the definition that have been made, are not uniquely defined. We can still defined the divergence of the vector potential to be whatever we want: this is called a gauge choice. Here we will use the Lorenz gauge

$$\nabla \cdot \mathbf{A}_L + \frac{1}{c^2} \frac{\partial \varphi_L}{\partial t} = 0, \quad (\text{A.9})$$

the capital letter L being here to remind the reader that the Lorenz gauge choice has been made. Within this gauge condition, the equation on the vector potential  $\mathbf{A}_L$  is obtained by replacing (A.8) and (A.7) into (A.4)

$$\left( \nabla^2 - \frac{1}{c^2} \frac{\partial^2}{\partial t^2} \right) \mathbf{A}_L = -\mu_0 \mathbf{j}. \quad (\text{A.10})$$

Similarly, we can derive the equation for the scalar potential  $\varphi_L$  by replacing (A.8) into (A.1)

$$\left( \nabla^2 - \frac{1}{c^2} \frac{\partial^2}{\partial t^2} \right) \varphi_L = -\frac{\rho}{\epsilon_0}. \quad (\text{A.11})$$

The solution of either (A.10) or (A.11) can be determined in solving the Green function  $G(\mathbf{r}, t)$  of the following equation

$$\left( \nabla^2 - \frac{1}{c^2} \frac{\partial^2}{\partial t^2} \right) G(\mathbf{r}, t) = -\delta(\mathbf{r})\delta(t), \quad (\text{A.12})$$

and then convolving this general solution to the source term in (A.10) or (A.11). The resolution of (A.12) done here will use distribution theory. First of all, we rewrite (A.12) in the Fourier domain

$$(-k^2 + k_0^2)G(\mathbf{k}, \omega) = -1, \quad (\text{A.13})$$

with  $k_0 = \omega/c$  and  $G(\mathbf{k}, \omega)$  the Fourier transform of  $G(\mathbf{r}, t)$  defined by

$$G(\mathbf{k}, \omega) = \int_{-\infty}^{+\infty} G(\mathbf{r}, \omega) e^{-i\mathbf{k}\cdot\mathbf{r}} d^3\mathbf{r} = \int_{-\infty}^{+\infty} \int_{-\infty}^{+\infty} G(\mathbf{r}, t) e^{-i(\mathbf{k}\cdot\mathbf{r} + \omega t)} d^3\mathbf{r} dt.$$

According to distribution theory, the solution of (A.13) is

$$G(\mathbf{k}, \omega) = \text{P.V.} \left[ \frac{1}{k^2 - k_0^2} \right] + C\delta(k - k_0) + C'\delta(k + k_0), \quad (\text{A.14})$$

where  $C$  and  $C'$  are integration constant and  $\text{P.V.}f$  denotes the principal value of  $f$  defined. Assuming  $f$  has only one discontinuity in  $a$ , the principal value is defined, for every test function  $\phi$ , by

$$\text{P.V.}f = \text{P.V.} \int f(x)\phi(x) dx = \lim_{\epsilon \rightarrow a} \left[ \int_{-\infty}^{\epsilon^-} f(x)\phi(x) dx + \int_{\epsilon^+}^{+\infty} f(x)\phi(x) dx \right].$$

Taking the inverse Fourier transform of (A.14) with respect to the wavevector components and assuming that the Green function only depends on the modulus of  $\mathbf{k}$ , we get

$$G(\mathbf{r}, \omega) = \frac{1}{2\pi r} \text{Im} \left[ \underbrace{\text{P.V.} \int_0^{+\infty} \frac{k}{k^2 - k_0^2} e^{ikr} dk}_{I_1} + C \underbrace{\int_0^{+\infty} k\delta(k - k_0) e^{ikr} dk}_{I_2} + C' \underbrace{\int_0^{+\infty} k\delta(k + k_0) e^{ikr} dk}_{I_3} \right]. \quad (\text{A.15})$$

We can evaluate the contribution of the first integral, denoted  $I_1$  in (A.15), in the complex plane. Choosing a closed half-circle in the upper-half of the complex plane, the Residue theorem enables to write

$$\begin{aligned} I_1 &= \frac{1}{2} \times \text{P.V.} \int_{-\infty}^{+\infty} \frac{k}{k^2 - k_0^2} e^{ikr} dk \\ &= \frac{1}{2} \times \left( i\pi \frac{k_0 e^{ik_0 r}}{2k_0} + i\pi \frac{k_0 e^{-ik_0 r}}{2k_0} \right) \\ &= \frac{i\pi}{2} \cos(k_0 r). \end{aligned} \quad (\text{A.16})$$

The two others integrals are straightforward

$$I_2 = k_0 e^{ik_0 r}, \quad (\text{A.17})$$

and  $I_3 = 0$  because  $-k_0$  does not belong to the domain of integration. Finally, using (A.16), (A.17) into (A.15), one gets

$$G(\mathbf{r}, \omega) = \frac{1}{4\pi r} \cos(k_0 r) + \frac{Ck_0}{2\pi^2 r} \sin(k_0 r).. \quad (\text{A.18})$$

(A.18) can be recast into the form

$$G(\mathbf{r}, \omega) = A \frac{e^{ik_0 r}}{r} + B \frac{e^{-ik_0 r}}{r}, \quad (\text{A.19})$$

with

$$\begin{aligned} A &= \frac{1}{8\pi} + \frac{Ck_0}{4i\pi^2} \\ B &= \frac{1}{8\pi} - \frac{Ck_0}{4i\pi^2}. \end{aligned}$$

Sommerfeld radiation condition dictates that  $B = 0$ , therefore  $C = i\pi/2k_0$  and

$$G(\mathbf{r}, \omega) = \frac{e^{ik_0 r}}{4\pi r}. \quad (\text{A.20})$$

The final step consists in taking the inverse Fourier transform of (A.20) with respect to the pulsation components and one would obtain

$$G(\mathbf{r}, t) = \frac{1}{4\pi r} \delta\left(t - \frac{r}{c}\right). \quad (\text{A.21})$$

Now that we have the expression of the Green tensor, we can write the expression of the scalar potential and the vectorial potential by convolving it with the source terms

$$\varphi_L = \frac{1}{4\pi\epsilon_0} \int \frac{\rho\left(\mathbf{r}', t - \frac{|\mathbf{r}-\mathbf{r}'|}{c}\right)}{|\mathbf{r}-\mathbf{r}'|} d^3\mathbf{r}', \quad (\text{A.22})$$

$$\mathbf{A}_L = \frac{\mu_0}{4\pi} \int \frac{\mathbf{j}\left(\mathbf{r}', t - \frac{|\mathbf{r}-\mathbf{r}'|}{c}\right)}{|\mathbf{r}-\mathbf{r}'|} d^3\mathbf{r}'. \quad (\text{A.23})$$

(A.22) and (A.23) are general expressions of the scalar potential and vector potential associated with Maxwell's equations in the Lorenz gauge. In the following, we will derive the expression of these two quantities for a single dipole located at the origin.

The charge density  $\rho$  associated with a dipole can be written as

$$\begin{aligned} \rho(\mathbf{r}, t) &= -\mathbf{p}(t) \cdot \nabla \delta(\mathbf{r}), \\ &= -\nabla \cdot (\mathbf{p}(t) \delta(\mathbf{r})), \end{aligned} \quad (\text{A.24})$$

with  $\mathbf{p}(t)$  the dipole moment. To go from the first line to the second one, we have used the vectorial relation  $\nabla \cdot (f\mathbf{U}) = f\nabla \cdot \mathbf{U} + \mathbf{U} \cdot \nabla f$ . Using the charge conservation associated with (A.24), we obtain the current density of a dipole

$$\mathbf{j}(\mathbf{r}, t) = \dot{\mathbf{p}}(t) \delta(\mathbf{r}). \quad (\text{A.25})$$

Replacing (A.25) into (A.23) gives

$$\mathbf{A}_L(\mathbf{r}, t) = \frac{\mu_0}{4\pi} \frac{\dot{\mathbf{p}}(t - r/c)}{r}. \quad (\text{A.26})$$

Replacing (A.26) into (A.7) gives the magnetic field produced by a single dipole

$$\mathbf{B}(\mathbf{r}, t) = -\frac{\mu_0}{4\pi} \mathbf{r} \times \left[ \frac{\ddot{\mathbf{p}}(t - r/c)}{cr^2} + \frac{\dot{\mathbf{p}}(t - r/c)}{r^3} \right], \quad (\text{A.27})$$

where we have used the relation  $\nabla \times (f\mathbf{U}) = f\nabla \times \mathbf{U} + \nabla f \times \mathbf{U}$ . To obtain the expression of the electric field produced by a dipole, we also need the expression of the scalar potential  $\varphi_L$ , which is explicitly

$$\varphi_L(\mathbf{r}, t) = -\frac{1}{4\pi\epsilon_0} \int_{-\infty}^{+\infty} d^3\mathbf{r}' \frac{\mathbf{p}\left(t - \frac{|\mathbf{r}-\mathbf{r}'|}{c}\right)}{|\mathbf{r}-\mathbf{r}'|} \cdot \nabla_{\mathbf{r}'} \delta(\mathbf{r}'). \quad (\text{A.28})$$

(A.28) can be integrated by parts and it would leads to

$$\begin{aligned} \varphi_L(\mathbf{r}, t) &= \frac{1}{4\pi\epsilon_0} \int_{-\infty}^{+\infty} d^3\mathbf{r}' \nabla_{\mathbf{r}'} \cdot \left[ \frac{\mathbf{p}\left(t - \frac{|\mathbf{r}-\mathbf{r}'|}{c}\right)}{|\mathbf{r}-\mathbf{r}'|} \right] \delta(\mathbf{r}') \\ &= \frac{1}{4\pi\epsilon_0} \nabla_{\mathbf{r}'} \cdot \left[ \frac{\mathbf{p}\left(t - \frac{|\mathbf{r}-\mathbf{r}'|}{c}\right)}{|\mathbf{r}-\mathbf{r}'|} \right]_{\mathbf{r}'=0} \\ &= \frac{1}{4\pi\epsilon_0} \left[ \frac{1}{|\mathbf{r}-\mathbf{r}'|} \nabla_{\mathbf{r}'} \cdot \mathbf{p}\left(t - \frac{|\mathbf{r}-\mathbf{r}'|}{c}\right) + \mathbf{p}\left(t - \frac{|\mathbf{r}-\mathbf{r}'|}{c}\right) \cdot \nabla_{\mathbf{r}'} \frac{1}{|\mathbf{r}-\mathbf{r}'|} \right]_{\mathbf{r}'=0} \\ &= \frac{1}{4\pi\epsilon_0} \left[ \frac{1}{|\mathbf{r}-\mathbf{r}'|} \dot{\mathbf{p}}\left(t - \frac{|\mathbf{r}-\mathbf{r}'|}{c}\right) \cdot \frac{1}{c} \frac{\mathbf{r}-\mathbf{r}'}{|\mathbf{r}-\mathbf{r}'|} + \mathbf{p}\left(t - \frac{|\mathbf{r}-\mathbf{r}'|}{c}\right) \cdot \frac{\mathbf{r}-\mathbf{r}'}{|\mathbf{r}-\mathbf{r}'|^3} \right]_{\mathbf{r}'=0} \\ &= \frac{1}{4\pi\epsilon_0} \left[ \frac{\dot{\mathbf{p}}(t - r/c) \cdot \mathbf{r}}{cr^2} + \frac{\mathbf{p}(t - r/c) \cdot \mathbf{r}}{r^3} \right] \end{aligned} \quad (\text{A.29})$$

To obtain the expression of the electric field produced by the dipole, we have to insert (A.29) and (A.26) into (A.8)

$$\begin{aligned} \mathbf{E}(\mathbf{r}, t) &= -\frac{1}{4\pi\epsilon_0} \left[ \frac{1}{cr^2} \nabla(\dot{\mathbf{p}}(t - r/c) \cdot \mathbf{r}) + \frac{\dot{\mathbf{p}}(t - r/c) \cdot \mathbf{r}}{c} \nabla\left(\frac{1}{r^2}\right) + \frac{1}{r^3} \nabla(\mathbf{p}(t - r/c) \cdot \mathbf{r}) \right. \\ &\quad \left. + \mathbf{p}(t - r/c) \cdot \mathbf{r} \nabla\left(\frac{1}{r^3}\right) \right] - \frac{\mu_0}{4\pi} \frac{\ddot{\mathbf{p}}(t - r/c)}{r}. \end{aligned}$$

In the next steps, we will omit the dependency in  $t - r/c$  for clarity.

$$\mathbf{E}(\mathbf{r}, t) = -\frac{1}{4\pi\epsilon_0} \left[ \frac{\dot{\mathbf{p}}}{cr^2} - \frac{(\mathbf{r} \cdot \ddot{\mathbf{p}})\mathbf{r}}{c^2 r^3} - \frac{2(\mathbf{r} \cdot \dot{\mathbf{p}})\mathbf{r}}{cr^4} + \frac{\mathbf{p}}{r^3} - \frac{(\mathbf{r} \cdot \dot{\mathbf{p}})\mathbf{r}}{cr^4} - \frac{3(\mathbf{r} \cdot \mathbf{p})\mathbf{r}}{r^5} \right] - \frac{\mu_0}{4\pi} \frac{\ddot{\mathbf{p}}}{r},$$

and using the relation  $\epsilon_0\mu_0c^2 = 1$ , we get

$$= -\frac{1}{4\pi\epsilon_0} \left[ \frac{\dot{\mathbf{p}}}{cr^2} - \frac{(\mathbf{r} \cdot \ddot{\mathbf{p}})\mathbf{r}}{c^2r^3} - \frac{3(\mathbf{r} \cdot \dot{\mathbf{p}})\mathbf{r}}{cr^4} + \frac{\mathbf{p}}{r^3} - \frac{3(\mathbf{r} \cdot \mathbf{p})\mathbf{r}}{r^5} + \frac{\ddot{\mathbf{p}}}{r} \right].$$

If we note  $\mathbf{r} = r\hat{\mathbf{u}}$  and  $\mathbf{p}(t - r/c) = p e^{-i\omega(t-r/c)} \hat{\mathbf{e}}$ , then the expression of the electric field becomes

$$\begin{aligned} \mathbf{E}(\mathbf{r}, t) &= -\frac{p e^{-i\omega(t-r/c)}}{4\pi\epsilon_0} \left\{ -\frac{i\omega}{cr^2} \hat{\mathbf{e}} + \frac{\omega^2}{c^2r} (\hat{\mathbf{u}} \cdot \hat{\mathbf{e}}) \hat{\mathbf{u}} + \frac{3i\omega}{cr^2} (\hat{\mathbf{u}} \cdot \hat{\mathbf{e}}) \hat{\mathbf{u}} + \frac{1}{r^3} \hat{\mathbf{e}} - \frac{3}{r^3} (\hat{\mathbf{u}} \cdot \hat{\mathbf{e}}) \hat{\mathbf{u}} - \frac{\omega^2}{c^2r} \hat{\mathbf{e}} \right\} \\ &= \frac{p e^{-i\omega(t-r/c)}}{4\pi\epsilon_0 r^3} \left\{ [3(\hat{\mathbf{u}} \cdot \hat{\mathbf{e}}) \hat{\mathbf{u}} - \hat{\mathbf{e}}](1 - ikr) + [\hat{\mathbf{e}} - (\hat{\mathbf{u}} \cdot \hat{\mathbf{e}}) \hat{\mathbf{u}}](kr)^2 \right\} \end{aligned} \quad (\text{A.30})$$

Using the vector triple product, (A.30) is sometimes written under the following form

$$\mathbf{E}(\mathbf{r}, t) = \frac{p e^{-i\omega(t-r/c)}}{4\pi\epsilon_0 r^3} \left\{ [3(\hat{\mathbf{u}} \cdot \hat{\mathbf{e}}) \hat{\mathbf{u}} - \hat{\mathbf{e}}](1 - ikr) + [(\hat{\mathbf{u}} \times \hat{\mathbf{e}}) \times \hat{\mathbf{u}}](kr)^2 \right\}. \quad (\text{A.31})$$

# APPENDIX B

## CLEBSH-GORDAN COEFFICIENTS OF $^{87}\text{Rb}$ D1 & D2 LINE - $\pi$ TRANSITIONS

---

Clebsch-Gordan coefficients associated with  $\pi$  transitions on the D1 and D2 line of  $^{87}\text{Rb}$  and used in the derivation of the light shift induced by a laser beam on the ground states levels (section 1.1.1). The coefficients are given with the normalization convention chosen in [Steck, 2015].

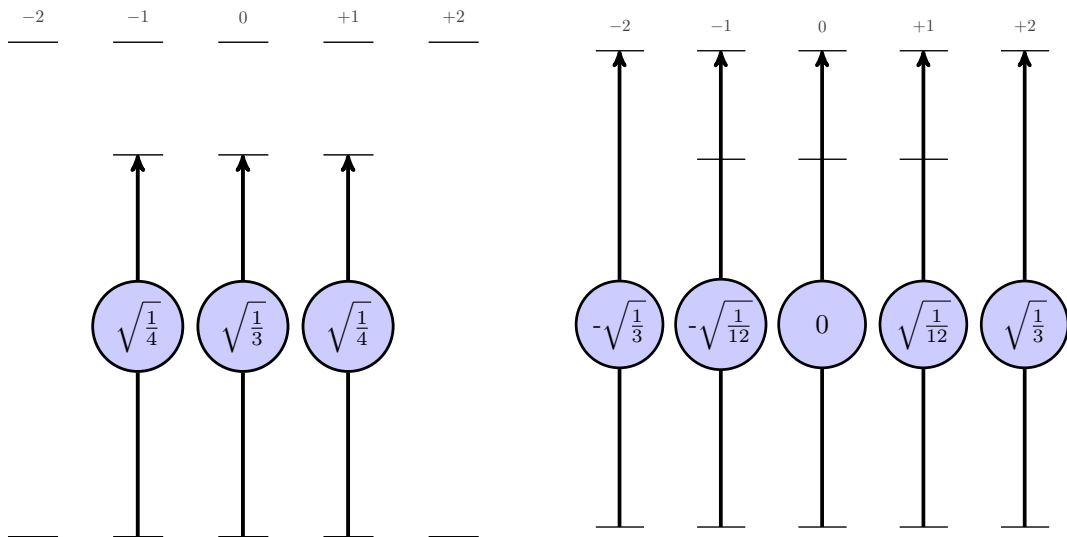


**Figure B.1.:** Clebsch-Gordan coefficients for  $\pi$  transition on the D1 line. The bottom hyperfine states correspond to the  $(5S_{1/2}, F = 2)$  manifold, and the upper states represent the  $(5P_{1/2}, F' = 1)$  and  $(5P_{1/2}, F' = 2)$  manifolds.

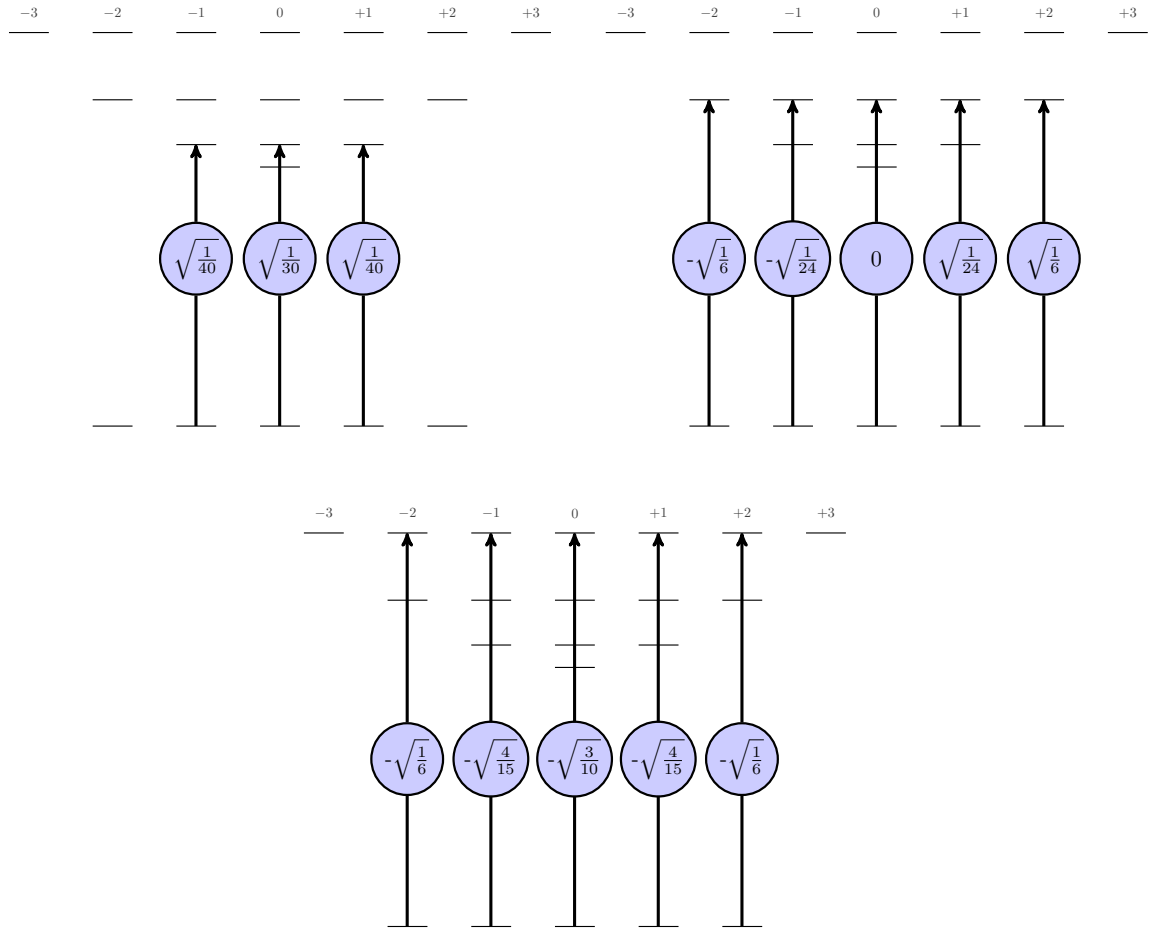


**Figure B.2.:** Clebsh-Gordan coefficients for  $\pi$  transition on the D2 line. The bottom hyperfine states correspond to the  $(5S_{1/2}, F = 2)$  manifold, and the upper hyperfine states represent the  $(5P_{3/2}, F' = 0)$ ,  $(5P_{3/2}, F' = 1)$ ,  $(5P_{3/2}, F' = 2)$  and  $(5P_{3/2}, F' = 3)$  (from bottom to top) manifolds.

## MAXWELL-BLOCH EQUATIONS FOR COHERENT LIGHT SCATTERING

---

Here, we derived the model developed by P. Pillet to explain the coherent light scattering by a cloud of two-level atoms. The model is compared with experimental data, in the low saturation limit, in chapter 2.

The model starts from the master equation ruling the density operator  $\rho(t)$  describing a collection of  $N$  two-level atoms with ground and excited states  $|g\rangle$  and  $|e\rangle$  respectively (transition frequency  $\omega_0$ ) in interaction with the modes of the vacuum field. In interaction representation this equation reads, in the absence of driving field

$$\begin{aligned}
 \frac{d\rho(t)}{dt} = & -\frac{\Gamma}{2} \sum_{j=1}^N \{r_j^+ r_j^-, \rho(t)\} - 2r_j^- \rho(t) r_j^+ \\
 & - \frac{3\Gamma}{8} \sum_{l \neq j} \left( r_j^+ r_j^- \rho\left(t - \frac{R_{jl}}{c}\right) - r_l^- \rho\left(t - \frac{R_{jl}}{c}\right) r_j^+ \right) \\
 & \quad \times \left( -i \frac{1 + \cos^2 \theta_{jl}}{kR_{jl}} - (1 - 3 \cos^2 \theta_{jl}) \frac{kR_{jl} + i}{(kR_{jl})^3} \right) \exp(ikR_{jl}) \\
 & + \frac{3\Gamma}{8} \sum_{l \neq j} \left( r_j^- r_j^+ \rho\left(t - \frac{R_{jl}}{c}\right) - r_l^+ \rho\left(t - \frac{R_{jl}}{c}\right) r_j^- \right) \\
 & \quad \times \left( i \frac{1 + \cos^2 \theta_{jl}}{kR_{jl}} - (1 - 3 \cos^2 \theta_{jl}) \frac{kR_{jl} - i}{(kR_{jl})^3} \right) \exp(-ikR_{jl}). \quad (C.1)
 \end{aligned}$$

Here,  $\{.,.\}$  is the anticommutator of two operators,  $\Gamma$  is the decay rate of state  $|e\rangle$  and  $k = \omega_0/c$ . The atoms  $j$  and  $l$  are located at positions  $\mathbf{R}_j$  and  $\mathbf{R}_l$  respectively, the inter-particle distance being  $R_{jl} = |\mathbf{R}_{jl}| = |\mathbf{R}_j - \mathbf{R}_l|$ , and  $\theta_{jl}$  is the angle between vector  $\mathbf{R}_{jl}$  and the quantization axis  $\hat{\mathbf{e}}_x$ . The atomic dipoles are circularly polarized in the  $yz$  plane. Finally, the raising and lowering operators  $r_j^\pm$  for atom  $j$  are defined as

$$r_j^+ = |e\rangle_j \langle g|_j \qquad r_j^- = |g\rangle_j \langle e|_j$$

The equations are established by choosing the quantization axis along the direction of the applied magnetic field. When deriving (C.1), the Born approximation has been made: only one spontaneous emission event is supposed to occur during the characteristic evolution time of the system  $\approx 1/(N\Gamma)$ . However, the usual Markov approximation has not been made, thus the presence of the retarded time  $t - R_{jl}/c$  in the equation. One may think this point is not crucial but it will lead to a simpler form of the final equation.

The density operator of atom  $j$  is obtained by tracing over the  $l \neq j$  atoms. Using the notation  $\rho^j(t) = \text{Tr}_{l \neq j}[\rho(t)]$ , we obtain

$$\begin{aligned} \frac{d\rho^j(t)}{dt} = & -\frac{\Gamma}{2}([r_j^+ r_j^-, \rho^j(t)] - 2r_j^- \rho^j(t) r_j^+) \\ & + i\frac{3\Gamma}{8} \sum_{l \neq j} \left[ \rho_{eg}^l(t - \frac{R_{jl}}{c}) r_j^+, \rho^j(t - \frac{R_{jl}}{c}) \right] \\ & \quad \times \left( \frac{1 + \cos^2 \theta_{jl}}{kR_{jl}} + (1 - 3\cos^2 \theta_{jl}) \frac{1 - ikR_{jl}}{(kR_{jl})^3} \right) \exp(ikR_{jl}) \\ & + i\frac{3\Gamma}{8} \sum_{l \neq j} \left[ \rho_{ge}^l(t - \frac{R_{jl}}{c}) r_j^-, \rho^j(t - \frac{R_{jl}}{c}) \right] \\ & \quad \times \left( \frac{1 + \cos^2 \theta_{jl}}{kR_{jl}} - (1 - 3\cos^2 \theta_{jl}) \frac{1 + ikR_{jl}}{(kR_{jl})^3} \right) \exp(-ikR_{jl}), \quad (\text{C.2}) \end{aligned}$$

where  $[\cdot, \cdot]$  the commutator of two operators.

We now add the laser driving field  $\mathbf{E}_L = E_L(\mathbf{r})\hat{\mathbf{e}}_y$  propagating in the direction  $\hat{\mathbf{e}}_z$  with vector  $k_L = 2\pi/\lambda$ . One should keep in mind that  $k_L$  is different from  $k = \omega_0/c$ , but as we operate close to an atomic transition, we will use in the following  $k_L = k$ . The laser beam is described here with a Gaussian spatial profile,

$$E_L(r, z) = E_0 \frac{w_0}{w(z)} \exp\left(\frac{-r^2}{w(z)^2}\right) \exp\left(ikz + ik\frac{r^2}{2R(z)} - i\arctan(z/z_R)\right). \quad (\text{C.3})$$

Here, we have chosen the opposite phase convention compared to (1.10). Equation (C.3) can be rewritten as follows

$$E_L = E_0 \frac{1}{1 + iz/z_R} \exp\left(\frac{i}{2} \frac{kr^2}{z - iz_R}\right) \exp(ikz). \quad (\text{C.4})$$

We also defined the Rabi frequency associated to the slow-varying envelope of the laser amplitude by  $\Omega_L^* = d(\mathbf{E}_L \cdot \hat{\mathbf{e}}_+^*) \exp(-ikz)/\hbar$

$$\Omega_L = \Omega_0 \frac{iz_R}{z + iz_R} \exp\left(-\frac{i}{2} \frac{kr^2}{z + iz_R}\right), \quad (\text{C.5})$$

with  $\hat{\mathbf{e}}_+ = -(\hat{\mathbf{e}}_y + i\hat{\mathbf{e}}_z)/\sqrt{2}$  and  $\Omega_0 = -dE_0/\hbar$ . We then obtain the equation relating the coherence  $\rho_{ge}^j$  of atom  $j$  and the ground and excited populations,  $\rho_{gg}^j(t)$  and  $\rho_{ee}^j(t)$

$$\begin{aligned} \frac{d\rho_{ge}^j(t)}{dt} = & -\left(\frac{\Gamma}{2} + i\Delta\right) \rho_{ge}^j(t) + i\frac{\Omega_L(r_j, z_j)}{2} e^{-ikz_j} \left( \rho_{ee}^j(t - \frac{R_{jl}}{c}) - \rho_{gg}^j(t - \frac{R_{jl}}{c}) \right) \\ & + \frac{3}{8}i\Gamma \sum_{l \neq j} \rho_{ge}^l(t - \frac{R_{jl}}{c}) \left[ \rho_{ee}^j(t - \frac{R_{jl}}{c}) - \rho_{gg}^l(t - \frac{R_{jl}}{c}) \right] \\ & \times \left[ \frac{1 + \cos^2 \theta_{jl}}{kR_{jl}} + (1 - 3\cos^2 \theta_{jl}) \frac{1 + ikR_{jl}}{(kR_{jl})^3} \right] \exp(-ikR_{jl}). \end{aligned} \quad (\text{C.6})$$

Similarly, the equation on the excited state population is

$$\begin{aligned} \frac{d\rho_{ee}^j(t)}{dt} = & -\Gamma \rho_{ee}^j(t) + \frac{3\Gamma}{8}i\Gamma \sum_{l \neq j} \rho_{eg}^l(t - \frac{R_{jl}}{c}) \rho_{ge}^j(t - \frac{R_{jl}}{c}) \\ & \times \left[ \frac{1 + \cos^2 \theta_{jl}}{kR_{jl}} + (1 - 3\cos^2 \theta_{jl}) \frac{1 - ikR_{jl}}{(kR_{jl})^3} \right] \exp(ikR_{jl}) \\ & - \frac{3}{8}i\Gamma \sum_{l \neq j} \rho_{ge}^l(t - \frac{R_{jl}}{c}) \rho_{eg}^j(t - \frac{R_{jl}}{c}) \\ & \times \left[ \frac{1 + \cos^2 \theta_{jl}}{kR_{jl}} + (1 - 3\cos^2 \theta_{jl}) \frac{1 + ikR_{jl}}{(kR_{jl})^3} \right] \exp(-ikR_{jl}) \\ & + i\frac{\Omega_L^*(r_j, z_j)}{2} \exp(ikz_j) \rho_{ge}^j(t) - i\frac{\Omega_L(r_j, z_j)}{2} \exp(-ikz_j) \rho_{eg}^j(t). \end{aligned} \quad (\text{C.7})$$

Let's now restrict ourselves to the weak driving field limit, hence assuming  $\rho_{ee}^j \approx 0$  and  $\rho_{gg}^j \approx 1$ . The model derived here remains valid in the high intensity regime if the evolution of the atomic population is considered. Our goal here is to derive a simple form of the previous equations in order to validate its results by comparing them with the coupled-dipole model, only valid in the weak driving limit. Under this assumption, (C.6) becomes

$$\begin{aligned} \frac{d\rho_{ge}^j(t)}{dt} = & -i\frac{\Omega_L(r_j, z_j)}{2} \exp(-ikz_j) - \left(\frac{\Gamma}{2} + i\Delta\right) \rho_{ge}^j(t) \\ & - \frac{3}{8}i\Gamma \sum_{l \neq j} \rho_{ge}^l(t - \frac{R_{jl}}{c}) f(R_{jl}, \theta_{jl}) \exp(-ikR_{jl}), \end{aligned} \quad (\text{C.8})$$

where we have introduced the function

$$f(R, \theta) = \frac{1 + \cos^2 \theta}{kR} + (1 - 3\cos^2 \theta) \frac{1 + ikR}{(kR)^3}. \quad (\text{C.9})$$

The coherence  $\rho_{eg}^j(t)$  being related to the complex amplitude of the atomic dipole  $j$ , (C.8) in steady-state is identical to the coupled-dipole one derived from classical electrodynamics (see Figure 2.20). Let us now introduced the equations for the electromagnetic

field. The total field at the location of atom  $j$  is the superposition of the laser field and the field emitted by all the other atoms. Expressed in terms of the slow-varying Rabi frequency defined by  $\Omega^* = d(\mathbf{E} \cdot \hat{\mathbf{e}}_+) \exp(-ikz)/\hbar$ , the field driving the  $\sigma_+$ -polarized dipoles is given by

$$\Omega(\mathbf{R}_j, t) = \Omega_L(r_j, z_j) + \frac{3\Gamma}{8} \exp(ikz_j) \sum_{l \neq j} \rho_{ge}^l(t - \frac{R_{jl}}{c}) \exp(-ikR_{jl}) f(R_{jl}, \theta_{jl}). \quad (\text{C.10})$$

This expression, valid for any amplitude of the laser field, can be decomposed into its propagating ( $\Omega_+$ , direction  $\mathbf{k}_L$ ) and counter-propagating ( $\Omega_-$ , direction  $-\mathbf{k}_L$ ) parts

$$\Omega_+(\mathbf{R}_j, t) = \Omega_L(r_j, z_j) + \frac{3\Gamma}{4} \exp(ikz_j) \sum_{l < j} \rho_{ge}^l(t - \frac{R_{jl}}{c}) \exp(-ikR_{jl}) f(R_{jl}, \theta_{jl}), \quad (\text{C.11})$$

$$\Omega_-(\mathbf{R}_j, t) = \frac{3\Gamma}{4} \exp(ikz_j) \sum_{l > j} \rho_{ge}^l(t - \frac{R_{jl}}{c}) \exp(-ikR_{jl}) f(R_{jl}, \theta_{jl}). \quad (\text{C.12})$$

With these notations, (C.8) becomes

$$\frac{d\rho_{ge}^j(t)}{dt} = -\left(\frac{\Gamma}{2} + i\Delta\right) \rho_{ge}^j(t) - \frac{i}{2} (\Omega_+(r_j, z_j, t) + \Omega_-(r_j, z_j, t)) \exp(-ikz_j). \quad (\text{C.13})$$

We have checked numerically that for our experimental parameters, the counter-propagating part of the field is negligible, therefore we will use, in the following,  $\Omega(\mathbf{R}_j, t) \approx \Omega_+(\mathbf{R}_j, t)$ .

The next step, in the derivation of this model, consists in a *continuous media approximation*, i.e. we calculate the configuration average of both  $\rho_{ge}^j$  and  $\Omega_+(\mathbf{R}_j, t)$ . In other terms, we calculate the coherent part of the electromagnetic field

$$\langle \Omega_+^*(\mathbf{R}_j, t) \rangle = d \langle (\mathbf{E}(\mathbf{R}_j, t) \cdot \hat{\mathbf{e}}_+) \exp(-ikz_j) \rangle / \hbar. \quad (\text{C.14})$$

This approximation is consistent with the fact that in our experiment we measure the field propagating in the forward direction, dominated by the coherent part in the low-intensity limit. Doing so, we neglect the fluctuations of the electromagnetic field around its mean value. In order to keep the notations and the equations simple, we will forget in the following the brackets of the configuration average, and we will replace the coherence  $\rho_{ge}^j$  operator by a continuous function  $\rho_{ge}(r, z, t)$ . We will also assume, based on the parameters of our experiments, that the coherence function does not depend on the radial coordinate:  $\rho_{ge}(r, z, t) \approx \rho_{ge}(z, t)$ . This is equivalent of considering that our system is one-dimensional. This assumption is needed in order to show that the coherent field  $\Omega_+(r, z, t)$  fulfills a paraxial equation. It can be derived following several steps. First, we introduce the radial average  $\bar{\Omega}_+(z, t)$  of the coherent field

$$\bar{\Omega}_+(z, t) = \frac{1}{2\pi\sigma_r^2} \int_0^\infty \Omega_+(r, z, t) \exp\left(-\frac{r^2}{2\sigma_r^2}\right) 2\pi r dr. \quad (\text{C.15})$$

We then replace the sums by integrals involving the spatial distribution of the cloud (with peak density  $n$ ), which is assumed to be Gaussian with  $\sigma_r$  and  $\sigma_z$  the widths at  $1/e^2$  in the radial and longitudinal directions respectively,

$$\begin{aligned}\bar{\Omega}_+(z, t) &= \frac{1}{2\pi\sigma_r^2} \int_0^\infty \Omega_L(r, z) \exp\left(-\frac{r^2}{2\sigma_r^2}\right) 2\pi r dr \\ &\quad + \frac{n}{2\pi\sigma_r^2} \frac{3\Gamma}{4} \exp(ikz) \int dx dy \exp\left(-\frac{r^2}{2\sigma_r^2}\right) \\ &\quad \times \int_{-\infty}^z dz' \int dx' dy' f(R', \theta') \rho_{ge}(z', t - \frac{R'}{c}) \\ &\quad \times \exp(-ikR') \exp\left(-\frac{x'^2 + y'^2}{2\sigma_r^2} - \frac{z'^2}{2\sigma_z^2}\right).\end{aligned}\quad (\text{C.16})$$

Here,  $r = \sqrt{x^2 + y^2}$  and  $R' = \sqrt{(x - x')^2 + (y - y')^2 + (z - z')^2}$ . Introducing the relative coordinates  $X = x - x'$ ,  $Y = y - y'$  and  $Z = z - z'$ , and using expression (C.5), we obtain

$$\begin{aligned}\bar{\Omega}_+(z, t) &= \frac{z_R}{z_R - iz + k\sigma_r^2} \Omega_0 \\ &\quad + \frac{3\Gamma n}{8} \exp(ikz) \int_{-\infty}^z dz' \rho_{ge}(z', t - \frac{Z}{c}) J(Z) \exp\left(-\frac{z'^2}{2\sigma_r^2}\right),\end{aligned}\quad (\text{C.17})$$

with  $J(Z)$  a kernel function

$$J(Z) = \int dX dY f(R', \theta') \exp\left(-\frac{X^2 + Y^2}{4\sigma_r^2} - ikR'\right),\quad (\text{C.18})$$

where  $R' = \sqrt{X^2 + Y^2 + Z^2}$ . One can find, after some calculation, an analytic expression for this function

$$J(z) = \frac{J_1(z)}{2} \left(3 + \frac{1}{2k^2\sigma_r^2} + \frac{k^2 z^2}{4k^4\sigma_r^4}\right) + \frac{i\pi}{k^2} \left(1 + i\frac{z}{2k\sigma_r^2}\right) \exp(-ikz),\quad (\text{C.19})$$

where

$$\begin{aligned}J_1(z) &= \int_0^\infty \exp\left(-\frac{r^2}{4\sigma_r^2}\right) \frac{\exp(-ik\sqrt{r^2 + z^2})}{k\sqrt{r^2 + z^2}} 2\pi r dr \\ &= \frac{2\pi\sqrt{\pi}}{k} \sigma_r \exp(-k^2\sigma_r^2) \text{Erfc}\left(\frac{|z|}{2\sigma_r} + ik\sigma_r\right) \exp\left(\frac{z^2}{4\sigma_r^2}\right),\end{aligned}\quad (\text{C.20})$$

and Erfc is the complementary error function defined by

$$\text{Erfc}(x) = 1 - \text{Erf}(x) = \frac{2}{\sqrt{\pi}} \int_x^\infty e^{-t^2} dt.\quad (\text{C.21})$$

Using the asymptotic expression  $\text{Erfc}(x) \approx \frac{1}{x\sqrt{\pi}} \exp(-x^2)$  for  $|x| \gg 1$ , we get

$$J(z) \approx -\frac{2i\pi}{k^2} \frac{b}{b-iz} \exp(-ikz), \quad (\text{C.22})$$

with  $b = 2k\sigma_r^2$ . The previous approximation is valid for our experimental parameters, as  $1/kb \leq 0.1$ . The above calculation shows that the field  $\bar{\Omega}_+(z, t)$  is the radial average of the field

$$\begin{aligned} \Omega_+(r, z, t) = & \Omega_L(r, z) - i \frac{3\pi\Gamma n}{4k^2} \int_{-\infty}^z dz' \rho_{ge}(z', t - \frac{z-z'}{c}) \\ & \times \frac{2b}{b-2i(z-z')} \exp\left(-\frac{kr^2}{b-2i(z-z')}\right) \exp\left(-\frac{z'^2}{2\sigma_z^2}\right) \exp(ikz'). \end{aligned} \quad (\text{C.23})$$

With this form, one can check that the coherent field  $\Omega_+(r, z, t)$  is solution of a paraxial equation

$$\begin{aligned} \frac{\partial \Omega_+(r, z, t)}{\partial z} + \frac{1}{c} \frac{\partial \Omega_+(r, z, t)}{\partial t} - \frac{1}{2ikr} \frac{\partial}{\partial r} \left( r \frac{\partial \Omega_+(r, z, t)}{\partial r} \right) \\ = -i \frac{3\pi}{2k^2} \Gamma n \rho_{ge}(z, t) \exp\left(-\frac{kr^2}{b} - \frac{z^2}{2\sigma_z^2}\right) \exp(ikz). \end{aligned} \quad (\text{C.24})$$

Equation (C.24) is still valid in the strong driving regime. Note that to obtain this form of the equation, the retarded times have to be kept, otherwise extra terms would have appeared. The paraxial equation for the field (C.24) is coupled to the equation on the coherence

$$\frac{\partial \rho_{ge}(z, t)}{\partial t} = -\left(\frac{\Gamma}{2} + i\Delta\right) \rho_{ge}(z, t) - i \frac{\Omega_+(r, z, t)}{2} \exp(-ikz), \quad (\text{C.25})$$

with the initial conditions  $\Omega_+(r, z = -\infty, t) = \Omega_L(r, z = -\infty, t)$  and  $\rho_{ge}(z, t = 0) = 0$ . We then consider the diffraction of the light by the cloud. The diffraction transfers part of the laser light with Gaussian spatial profile to higher order Gaussian modes. Mathematically, we thus decompose the field  $\Omega_+(r, z, t)$  onto the Laguerre-Gauss modes propagating in the direction  $\mathbf{k}_L$

$$\Omega_+(r, z, t) = \sqrt{\frac{\pi z_R}{k}} \sum_{q=0}^{\infty} \Omega_+^{(q)}(z, t) \text{LG}_q(r, z). \quad (\text{C.26})$$

The expression of the Laguerre-Gauss modes are

$$\begin{aligned} \text{LG}_q(r, z) = & \sqrt{\frac{k}{\pi z_R}} \left( \frac{1 + iz/z_R}{1 - iz/z_R} \right)^q \left( \frac{1}{1 - iz/z_R} \right) \\ & \times \text{L}_q \left( \frac{kz_R r^2}{z^2 + z_R^2} \right) \exp\left(-\frac{i}{2} \frac{kr^2}{z + iz_R}\right), \end{aligned} \quad (\text{C.27})$$

with  $L_q(r)$  the Laguerre polynomial of order  $q$ . It is solution of the following second-order linear differential equation

$$xy'' + (1-x)y' + qy = 0. \quad (\text{C.28})$$

A closed form for this polynomial is given by

$$L_q(x) = \sum_{k=0}^q \binom{q}{k} \frac{(-1)^k}{k!} x^k. \quad (\text{C.29})$$

The mode  $q = 0$  describes the Gaussian mode ( $\text{TEM}_{qm} = \text{TEM}_{00}$ ) of the probe field. The cylindrical symmetry of our system allows us to restrict the solutions to the modes with  $m = 0$  only. The Laguerre polynomials satisfy the orthogonality conditions

$$\int_0^\infty LG_q(r, z) LG_p^*(r, z) 2\pi r dr = \delta_{p,q}. \quad (\text{C.30})$$

As a last step, a radial average is performed to reach a set of coupled equations that are now easy to solve numerically

$$\begin{cases} \frac{\partial \tilde{\rho}_{ge}}{\partial t} = - \left( \frac{\Gamma}{2} + i\Delta \right) \tilde{\rho}_{ge}(z, t) - i \frac{\Omega(z, t)}{2}, \\ \frac{\partial \Omega_+^{(q)}}{\partial z} + \frac{1}{c} \frac{\partial \Omega_+^{(q)}}{\partial t} = -i \sqrt{\frac{2}{\pi w^2}} \frac{3\pi}{2k^2} \Gamma n f_q^*(z) \exp\left(-\frac{z^2}{2\sigma_z^2}\right) \tilde{\rho}_{ge}(z, t), \end{cases} \quad (\text{C.31})$$

with  $\tilde{\rho}_{ge}(z, t) = \rho_{ge}(z, t) \exp(ikz)$  the slow-varying coherence and  $\Omega(z, t)$  the Rabi frequency defined by

$$\Omega(z, t) = \sqrt{\frac{\pi w^2}{2}} \frac{1}{2\pi\sigma_r^2} \sum_{p=0}^{\infty} f_p(z) \Omega_+^{(p)}(z, t), \quad (\text{C.32})$$

and where we have introduced the function  $f_p(z)$  defined as

$$f_p(z) = \int_0^\infty \exp\left(-\frac{r^2}{2\sigma_r^2}\right) LG_p(r, z) 2\pi r dr. \quad (\text{C.33})$$



# RÉSUMÉ

---

## INTRODUCTION

Bien que le problème de l'interaction entre la lumière et la matière soit étudié depuis très longtemps et que les théories qui lui sont associées permettent d'expliquer bon nombre de phénomènes physiques, celui de l'interaction dipolaire en régime dense et proche de résonance ne semble toujours pas parfaitement compris. Le nuage électronique entourant l'atome, lorsque celui-ci est soumis à une onde électromagnétique, se polarise et un dipôle apparaît. Lorsqu'un deuxième dipôle induit se trouve à proximité du premier, ils peuvent se mettre à interagir: c'est l'interaction dipolaire. Cette interaction est d'autant plus forte que les dipôles sont proches et que la longueur d'onde du champ électromagnétique est proche d'une transition atomique.

## CHAPITRE 1

Dans le premier chapitre, après un rapide rappel des concepts théoriques en lien avec l'interaction lumière-matière, je présente la manière avec laquelle nous préparons expérimentalement des nuages désordonnés constitués d'atomes froids de Rubidium 87 au foyer de lentilles asphériques de forte ouverture numérique placées sous vide. Ce premier chapitre est également l'occasion d'expliquer comment nous mesurons les différentes quantités physiques qui caractérisent ces nuages et qui seront utilisées dans le reste du manuscrit.

## CHAPITRE 2

Dans ce second chapitre, je rappelle les différentes mesures qui ont été réalisées dans le groupe d'Antoine Browaeys, au Laboratoire Charles Fabry, en lien avec la diffusion de lumière par des nuages denses d'atomes froids. Je présente ensuite la dernière mesure réalisée et à laquelle j'ai participé: la diffusion cohérente de lumière par un ensemble d'atomes à deux niveaux. On comparera les résultats obtenus aux résultats des simulations qui sont basées sur le modèle des dipôles couplés. Le modèle des dipôles couplés est un modèle microscopique dans lequel chaque atome du nuage est soumis au champ laser d'excitation et à la somme des champs rayonnés par les autres dipôles

du nuage, de sorte que tous les atomes du nuage sont couplés. Bien que l'accord entre résultats expérimentaux et théorie soit restauré lorsque le nombre d'atomes constituant le nuage est faible, le désaccord persiste lorsque celui-ci augmente. Les simulations présentées tentent donc d'expliquer ce désaccord en s'attaquant à plusieurs des hypothèses du modèle, notamment celle qui concerne l'absence de mouvement des atomes. À la fin du chapitre, on présente un nouveau modèle développé par l'un de nos collaborateurs et qui permet d'étudier de tels systèmes au-delà de la limite de faible excitation, hypothèse qui considère que les dipôles réagissent linéairement au champ d'excitation.

## CHAPITRE 3

À défaut d'obtenir un accord satisfaisant entre la théorie et l'expérience concernant les mesures expérimentales discutées au chapitre précédent, il a été décidé de modifier le dispositif expérimental. Ce troisième chapitre présente les modifications que j'ai réalisées sur l'expérience, notamment concernant l'implémentation de deux axes optiques haute résolution en configuration confocale et à  $90^\circ$  l'un de l'autre. J'insisterai sur la procédure d'alignement que nous avons mise au point ainsi que sur la caractérisation, réalisée à l'aide d'atomes uniques, des performances optiques du système. Je tente également d'expliquer pourquoi les performances optiques semblent dégradées par rapport aux performances théoriques attendues en considérant les aberrations possiblement introduites par les hublots de la chambre à vide. Pour terminer le chapitre, je présente rapidement les futurs outils prometteurs qui sont ou seront prochainement mis en place sur l'expérience afin d'avoir un plus grand contrôle sur la préparation de nos systèmes d'atomes froids.

## CHAPITRE 4

Le dernier chapitre commence par une étude théorique de la diffusion de la lumière par une chaîne d'atomes froids. Le nouveau dispositif possédant la capacité de piéger les atomes selon une direction, en réfléchissant le laser de piègeage pour former une onde stationnaire, et de collecter la lumière émise par les atomes avec le second axe, on a cherché à observer les effets des interactions dipolaires dans des systèmes ordonnés. En se basant sur [Sutherland et Robicheaux, 2016] dans lesquels les auteurs prédisent l'augmentation de la quantité de la lumière diffusée par les atomes le long de la chaîne pour des désaccords négatifs de la sonde, j'ai cherché ici à vérifier que cet effet était robuste aux imperfections expérimentales, qu'il s'agisse du chargement aléatoire des différents sites du réseau ou bien du mouvement résiduel des atomes lié à leur température non nulle. Cette étude confirme que l'effet est observable. La deuxième partie de ce chapitre est consacrée à déterminer s'il est possible, à partir d'une image de la chaîne prise par notre expérience, de reconstruire la distribution atomique, la distance entre deux sites voisins étant inférieure à la résolution du système d'imagerie. Cette étude

---

préliminaire ne permet pas de l'affirmer, compte tenu du RSB (Rapport Signal à Bruit) des images. L'algorithme pourra néanmoins être amélioré avec l'implémentation de différentes techniques de reconstruction d'images.

## CONCLUSION

Pour conclure, malgré nos efforts pour comprendre la réponse optique d'un nuage dense et désordonné d'atomes froids sondé proche de résonance, le désaccord entre les résultats expérimentaux et ceux des simulations persiste. Le nouveau dispositif expérimental que j'ai construit devrait permettre d'approfondir ces études mais également de les étendre, notamment en étudiant les effets des interactions dipolaires dans les systèmes ordonnés.



# REFERENCES

---

- [Alberti et al., 2016] Alberti, A., Robens, C., Alt, W., Brakhane, S., Karski, M., Reimann, R., Widera, A., and Meschede, D. (2016). Super-resolution microscopy of single atoms in optical lattices. *New Journal of Physics*, 18:053010. → Cited on pages 119, 124
- [Aljunid et al., 2009] Aljunid, S. A. and Tey, M. K., Chng, B., Liew, T., Maslennikov, G., Scarani, V., and Kurtsiefer, C. (2009). Phase shift of a weak coherent beam induced by a single atom. *Phys. Rev. Lett.*, 103:153601. → Cited on pages 2, 37
- [Anderson, 1972] Anderson, P. W. (1972). More is different. *Science*, 177(4047):393–396. → Cited on page 1
- [Araújo et al., 2016] Araújo, M. O., Krešić, I., Kaiser, R., and Guerin, W. (2016). Superradiance in a large and dilute cloud of cold atoms in the linear-optics regime. *Phys. Rev. Lett.*, 117:073002. → Cited on page 3
- [Bali et al., 1999] Bali, S., O’Hara, K., Gehm, M., Granade, S., and Thomas, J. (1999). Quantum-diffractive background gas collisions in atom-trap heating and loss. *Phys. Rev. A*, 60:R29. → Cited on page 94
- [Bücker et al., 2009a] Bücker, R., Perrin, A., Manz, S., Betz, T., Koller, C., Plisson, T., Rottmann, J., Schumm, T., and Schmiedmayer, J. (2009a). Single atom sensitive fluorescence imaging of ultracold quantum gases. *New Journal of Physics*, 11:103039. → Cited on page 86
- [Bücker et al., 2009b] Bücker, R., Perrin, A., Manz, S., Betz, T., Koller, C., Plisson, T., Rottmann, J., Schumm, T., and Schmiedmayer, J. (2009b). Single-particle-sensitive imaging of freely propagating ultracold atoms. *New Journal of Physics*, 11(10):103039. → Cited on pages 119, 124
- [Bender et al., 2010] Bender, H., Stehle, C., Slama, S., Kaiser, R., Piovella, N., Zimmermann, C., and Courteille, P. W. (2010). Observation of cooperative mie scattering from an ultracold atomic cloud. *Phys. Rev. A*, 82:011404. → Cited on page 2
- [Bettles et al., 2015a] Bettles, R. J., Gardiner, S. A., and Adams, C. S. (2015a). Cooperative ordering in lattices of interacting two-level dipoles. *Phys. Rev. A*, 92:063822. → Cited on page 2

- [Bettles et al., 2015b] Bettles, R. J., Gardiner, S. A., and Adams, C. S. (2015b). Cooperative ordering in lattices of interacting two-level dipoles. *Phys. Rev. A*, 92:063822. → Cited on page 104
- [Bettles et al., 2016a] Bettles, R. J., Gardiner, S. A., and Adams, C. S. (2016a). Cooperative eigenmodes and scattering in one-dimensional atomic arrays. *Phys. Rev. A*, 94:043844. → Cited on page 104
- [Bettles et al., 2016b] Bettles, R. J., Gardiner, S. A., and Adams, C. S. (2016b). Enhanced optical cross section via collective coupling of atomic dipoles in a 2d array. *Phys. Rev. Lett.*, (116):103602. → Cited on pages 104, 129
- [Béguin, 2013] Béguin, L. (2013). *Measurement of the van der Waals interaction between two Rydberg atoms*. PhD thesis, Université Paris-Sud. → Cited on pages 20, 88
- [Bienaimé et al., 2010] Bienaimé, T., Bux, S., Lucioni, E., Courteille, P. W., Piovella, N., and Kaiser, R. (2010). Observation of a cooperative radiation force in the presence of disorder. *Phys. Rev. Lett.*, 104:183602. → Cited on page 2
- [Born and Wolf, 2003] Born, M. and Wolf, E. (2003). *Principles of Optics: Electromagnetic Theory of Propagation, Interference and Diffraction of Light*. Cambridge University Press. Seventh edition. → Cited on page 77
- [Bourgain, 2014] Bourgain, R. (2014). *Diffusion de la lumière dans les nuages denses mésoscopiques d'atomes froids*. PhD thesis, Institut d'Optique Graduate School. → Cited on page 88
- [Bourgain et al., 2013] Bourgain, R., Pellegrino, J., Jennewein, S., Sortais, Y. R. P., and Browaeys, A. (2013). Direct measurement of the wigner time delay for the scattering of light by a single atom. *Opt. Lett.*, 38(11):1963–1965. → Cited on page 2
- [Bruno et al., 2019] Bruno, N., Bianchet, L. C., Prakash, V., Li, N., Alves, N., and Mitchell, M. W. (2019). Maltese cross coupling to individual cold atoms in free space. *Optics Express*, 27(21):31042. → Cited on pages 68, 128
- [Campbell et al., 2017] Campbell, S. L., Hutson, R. B., Marti, G. E., Goban, A., Darkwah Oppong, N., McNally, R. L., Sonderhouse, L., Robinson, J. M., Zhang, W., Bloom, B. J., and Ye, J. (2017). A fermi-degenerate three-dimensional optical lattice clock. *Science*, 358(6359):90–94. → Cited on page 2
- [Chabé et al., 2014] Chabé, J., Rouabah, M.-T., Bellando, L., Bienaimé, T., Piovella, N., Bachelard, R., and Kaiser, R. (2014). Coherent and incoherent multiple scattering. *Phys. Rev. A*, 89:043833. → Cited on page 2

- 
- [Chalony et al., 2011] Chalony, M., Pierrat, R., Delande, D., and Wilkowski, D. (2011). Coherent flash of light emitted by a cold atomic cloud. *Phys. Rev. A*, 84:011401. → Cited on page 2
- [Chang et al., 2004] Chang, D. E., Ye, J., and Lukin, M. D. (2004). Controlling dipole-dipole frequency shifts in a lattice-based optical atomic clock. *Phys. Rev. A*, 69:023810. → Cited on page 2
- [Cohen-Tannoudji et al., 2018] Cohen-Tannoudji, C., Diu, B., and Laloe, F. (2018). *Mécanique quantique*. EDP science, 2nd Edition. → Cited on page 26
- [Dalibard, 2013] Dalibard, J. (2013). Cours collège de france. <https://www.college-de-france.fr/site/jean-dalibard/>. → Cited on page 8
- [Darquié, 2005] Darquié, B. (2005). *Manipulation d’atomes dans des pièges dipolaires microscopiques et émission contrôlée de photons par un atome unique*. PhD thesis, Université Paris-Sud. → Cited on page 10
- [Dicke, 1954] Dicke, R. H. (1954). Coherence in spontaneous radiation processes. *Phys. Rev.*, 93:99–110. → Cited on page 33
- [Durant et al., 2007] Durant, S., Calvo-Perez, O., Vukadinovic, N., and Greffet, J.-J. (2007). Light scattering by a random distribution of particles embedded in absorbing media: full-wave monte carlo solutions of the extinction coefficient. *J. Opt. Soc. Am. A*, 24(9):2953–2962. → Cited on page 29
- [Eng et al., 2019] Eng, C.-H. L., Lawson, M., Zhu, Q., Dries, R., Koulena, N., Takei, Y., Yun, J., Cronin, C., Karp, C., Yuan, G.-C., and Cai, L. (2019). Transcriptome-scale super-resolved imaging in tissues by rna seqfish+. *Nature*, 568:235–239. → Cited on page 119
- [Engler et al., 2000] Engler, H., Weber, T., Mudrich, M., Grimm, R., and Weidemüller, M. (2000). Very long storage times and evaporative cooling of cesium atoms in a quasielectrostatic dipole trap. *Phys. Rev. A*, 62:031402. → Cited on pages 17, 89
- [Feynman et al., 1965] Feynman, R. P., Leighton, R. B., and Sands, M. (1965). *The Feynman Lectures on Physics, vol. 2: Mainly electromagnetism and matter*. Addison-Wesley. → Cited on page 3
- [Floyd, 1991] Floyd, C. E. (1991). An artificial neural network for spect image reconstruction. *IEEE Transactions on Medical Imaging*, 10(3):485–487. → Cited on page 119
- [Foot, 2005] Foot, C. J. (2005). *Atomic physics*, volume 7. Oxford University Press. → Cited on page 1

- [Friedberg et al., 1973] Friedberg, R., Hartmann, S., and Manassah, J. (1973). Frequency shift and absorption by resonant systems of two-level atoms. *Physics Reports*, 7:101. → Cited on page 43
- [Fuhrmanek, 2011] Fuhrmanek, A. (2011). *From single to many atoms in a microscopic optical dipole trap*. PhD thesis, Université Paris-Sud. → Cited on pages 13, 14, 16, 19, 76, 88
- [Gillen et al., 2010] Gillen, G. D., Seck, C. M., and Guha, S. (2010). Analytical beam propagation model for clipped focused-gaussian beams using vector diffraction theory. *Optics Express*, 18:4023. → Cited on page 101
- [Grynberg et al., 2010] Grynberg, G., Aspect, A., and Fabre, C. (2010). *Introduction to Quantum Optics - From the semi-classical approach to Quantized Light*. Cambridge University Press. Complement 2C.3. → Cited on pages 8, 46
- [Huang et al., 2010] Huang, J.-S., Kern, J., Geisler, P., Weinmann, P., Kamp, M., Forchel, A., Biagioni, P., and Hecht, B. (2010). Mode imaging and selection in strongly coupled nanoantennas. *Nano Letters*, 10(6):2105–2110. PMID: 20411912. → Cited on page 1
- [Huntemann et al., 2016] Huntemann, N., Sanner, C., Lipphardt, B., Tamm, C., and Peik, E. (2016). Single-ion atomic clock with  $3 \times 10^{-18}$  systematic uncertainty. *Phys. Rev. Lett.*, 116:063001. → Cited on page 1
- [Iakoupov et al., 2016] Iakoupov, I., Ott, J. R., Chang, D. E., and Sørensen, A. S. (2016). Dispersion relations for stationary light in one-dimensional atomic ensembles. *Phys. Rev. A*, 94:053824. → Cited on page 104
- [Jackson, 1999] Jackson, J. D. (1999). *Classical Electrodynamics*. John Wiley and Sons, third edition. → Cited on pages 26, 43
- [Javanainen et al., 1999] Javanainen, J., Ruostekoski, J., Vestergaard, B., , and Francis, M. R. (1999). One-dimensional modeling of light propagation in dense and degenerate samples. *Phys. Rev. A*, 59:649. → Cited on page 27
- [Jenkins et al., 2016] Jenkins, S., Ruostekoski, J., Javanainen, J., Jennewein, S., Bourgain, R., Pellegrino, J., Sortais, P., and Browaeys, A. (2016). Collective resonance fluorescence in small and dense atom clouds: Comparison between theory and experiment. *Phys. Rev. A*, 94:023842. → Cited on page 45
- [Jennewein, 2017] Jennewein, S. (2017). *Optical Response of dense  $^{87}\text{Rb}$  clouds*. PhD thesis, Université Paris-Sud. → Cited on pages 13, 57, 74, 75, 128

- 
- [Jennewein et al., 2016] Jennewein, S., Besbes, M., Schilder, N., Jenkins, S., Sauvan, C., Ruostekoski, J., Greffet, J.-J., Sortais, P., and Browaeys, A. (2016). Coherent scattering of near-resonant light by a dense microscopic cold atomic cloud. *Phys. Rev. Lett.*, 116:233601. → Cited on pages 4, 35, 36, 43, 45, 127
- [Jennewein et al., 2018] Jennewein, S., Brossard, L., R. P. Sortais, Y., Browaeys, A., Cheinet, P., Robert, J., and Pillet, P. (2018). Coherent scattering of near-resonant light by a dense, microscopic cloud of cold two-level atoms: Experiment versus theory. *Phys. Rev. A*, 97:053816. → Cited on pages 50, 127
- [Keaveney et al., 2012] Keaveney, J., Hughes, I. G., Sargsyan, A., Sarkisyan, D., and Adams, C. S. (2012). Maximal refraction and superluminal propagation in a gaseous nanolayer. *Phys. Rev. Lett.*, 109:233001. → Cited on pages 3, 127
- [Kuhr et al., 2001] Kuhr, S., Alt, W., Schrader, D., Müller, M., G., V., and Meschede, D. (2001). Deterministic delivery of a single atom. *Science*, 293:278. → Cited on page 86
- [Kuraptsev and Sokolov, 2019] Kuraptsev, A. and Sokolov, I. (2019). Influence of atomic motion on the collective effects in dense and cold atomic ensembles. *arXiv:1907.01029*. → Cited on pages 60, 128
- [Kwong et al., 2015] Kwong, C. C., Yang, T., Delande, D., Pierrat, R., and Wilkowski, D. (2015). Cooperative emission of a pulse train in an optically thick scattering medium. *Phys. Rev. Lett.*, 115:223601. → Cited on page 3
- [Kwong et al., 2014] Kwong, C. C., Yang, T., Pramod, M. S., Pandey, K., Delande, D., Pierrat, R., and Wilkowski, D. (2014). Cooperative emission of a coherent superflash of light. *Phys. Rev. Lett.*, 113:223601. → Cited on page 2
- [Lett et al., 1988] Lett, P., Watts, R., Westbrook, C., Phillips, W., Gould, P., and Metcalf, H. (1988). Observation of atoms laser cooled below the doppler limit. *Phys. Rev. Lett.*, 61:169. → Cited on page 17
- [Li et al., 2013] Li, Y., Evers, J., Feng, W., and Zhu, S.-Y. (2013). Spectrum of collective spontaneous emission beyond the rotating-wave approximation. *Phys. Rev. A*, 87:053837. → Cited on page 33
- [Lubeck and Long, 2012] Lubeck, E. and Long, C. (2012). Single-cell systems biology by super-resolution imaging and combinatorial labeling. *Nature methods*, 9(7):743–748. → Cited on page 119
- [Manassah, 2012] Manassah, J. (2012). Cooperative radiation from atoms in different geometries: decay rate and frequency shift. *Adv. Opt. Photon.*, 4:108–156. → Cited on page 43

- [Marti et al., 2018] Marti, G. E., Hutson, R. B., Goban, A., Campbell, S. L., Poli, N., and Ye, J. (2018). Imaging optical frequencies with 100  $\mu\text{Hz}$  precision and 1.1  $\mu\text{m}$  resolution. *Phys. Rev. Lett.*, 120:103201.  $\rightarrow$  Cited on page 2
- [Mølmer et al., 1993] Mølmer, K., Castin, Y., and Dalibard, J. (1993). Monte carlo wave-function method in quantum optics. *J. Opt. Soc. Am. B*, 10(3):524–538.  $\rightarrow$  Cited on page 111
- [Munro et al., 2018] Munro, E., Asenjo-Garcia, A., Lin, Y., Kwek, L. C., Regal, C. A., and Chang, D. E. (2018). Population mixing due to dipole-dipole interactions in a one-dimensional array of multilevel atoms. *Phys. Rev. A*, 98:033815.  $\rightarrow$  Cited on page 104
- [Nelson et al., 2007] Nelson, K., Li, X., and Weiss, D. (2007). Imaging single atoms in a three-dimensional array. *Nature Physics*, 3:556.  $\rightarrow$  Cited on page 86
- [Ozeri et al., 2005] Ozeri, R., Langer, C., Jost, J., DeMarco, B., Ben-Kish, A., Blakestad, B., Britton, J., Chiaverini, J., Itano, W. M., Hume, D., Leibfried, D., Rosenband, T., Schmidt, P., and Wineland, D. (2005). Hyperfine coherence in the presence of spontaneous photon scattering. *Phys. Rev. Lett.*, 95:030403.  $\rightarrow$  Cited on page 11
- [Pellegrino et al., 2014] Pellegrino, J., Bourgain, R., Jennewein, S., Sortais, P., Jenkins, S., Ruostekoski, J., and Browaeys, A. (2014). Observation of suppression of light scattering induced by dipole-dipole interactions in a cold-atom ensemble. *Phys. Rev. Lett.*, 113:133602.  $\rightarrow$  Cited on pages 3, 33, 34, 35, 45, 127
- [Perczel et al., 2017] Perczel, J., Borregaard, J., Chang, D. E., Pichler, H., Yelin, S. F., Zoller, P., and Lukin, M. D. (2017). Topological quantum optics in two-dimensional atomic arrays. *Phys. Rev. Lett.*, 119:023603.  $\rightarrow$  Cited on page 2
- [Peyrot et al., 2019a] Peyrot, T., Beurthe, C., Coumar, S., Roulliy, M., Perronet, K., Bonnay, P., Adams, C. S., Browaeys, A., and Sortais, Y. R. P. (2019a). Fabrication and characterization of super-polished wedged borosilicate nano-cells. *Opt. Lett.*, 44(8):1940–1943.  $\rightarrow$  Cited on page 3
- [Peyrot et al., 2019b] Peyrot, T., Sibalik, N., Sortais, Y. R. P., Browaeys, A., Sargsyan, A., Hughes, I. G., and Adams, C. S. (2019b). Measurement of the atom-surface van der waals interaction by transmission spectroscopy in a wedged nano-cell. To appear in *Physical Review A*.  $\rightarrow$  Cited on page 3
- [Peyrot et al., 2018] Peyrot, T., Sortais, Y. R. P., Browaeys, A., Sargsyan, A., Sarkisyan, D., Keaveney, J., Hughes, I. G., and Adams, C. S. (2018). Collective lamb shift of a nanoscale atomic vapor layer within a sapphire cavity. *Phys. Rev. Lett.*, 120:243401.  $\rightarrow$  Cited on page 3

- 
- [Peyrot et al., 2019c] Peyrot, T., Sortais, Y. R. P., Greffet, J.-J., Browaeys, A., Sargsyan, A., Keaveney, J., Hughes, I. G., and Adams, C. S. (2019c). Optical transmission of an atomic vapor in the mesoscopic regime. *Phys. Rev. Lett.*, 122:113401. → Cited on page 3
- [Phillips and Metcalf, 1982] Phillips, W. and Metcalf, H. (1982). Laser deceleration of an atomic beam. *Phys. Rev. Lett.*, 48:596–599. → Cited on page 15
- [Pu and Zhang, 1998] Pu, J. and Zhang, H. (1998). Intensity distribution of gaussian beams focused by a lens with spherical aberration. *Optics Communications*, 151:331–338. → Cited on page 96
- [Rashed, 1990] Rashed, R. (1990). A pioneer in anaclastics: Ibn sahl on burning mirrors and lenses. *Isis*, 81(3):464–491. → Cited on page 1
- [Roof et al., 2016] Roof, S. J., Kemp, K. J., Havey, M. D., and Sokolov, I. M. (2016). Observation of single-photon superradiance and the cooperative lamb shift in an extended sample of cold atoms. *Phys. Rev. Lett.*, 117:073003. → Cited on page 3
- [Schilder et al., 2016] Schilder, N., Sauvan, C., Hugonin, J.-P., Jennewein, S., Sortais, Y., Browaeys, A., and Greffet, J.-J. (2016). Role of polaritonic modes on light scattering from a dense cloud of atoms. *Phys. Rev. A*, 93:063835. → Cited on page 51
- [Schlosser et al., 2002] Schlosser, N., Reymond, G., and Grangier, P. (2002). Collisional blockade in microscopic optical dipole traps. *Phys. Rev. Lett.*, 89:023005. → Cited on page 20
- [Schlosser et al., 2001] Schlosser, N., Reymond, G., Protsenko, I., and Grangier, P. (2001). Subpoissonian loading of a microscopic dipole trap. *Nature*, 411:1024. → Cited on page 86
- [Scully, 2009] Scully, M. O. (2009). Collective lamb shift in single photon dicke superradiance. *Phys. Rev. Lett.*, 102:143601. → Cited on page 33
- [Shahmoon et al., 2017a] Shahmoon, E., Wild, D. S., Lukin, M. D., and Yelin, S. F. (2017a). Cooperative resonances in light scattering from two-dimensional atomic arrays. *Phys. Rev. Lett.*, 118:113601. → Cited on page 2
- [Shahmoon et al., 2017b] Shahmoon, E., Wild, D. S., Lukin, M. D., and Yelin, S. F. (2017b). Cooperative resonances in light scattering from two-dimensional atomic arrays. *Phys. Rev. Lett.*, 118:113601. → Cited on pages 104, 129
- [Sherson et al., 2010] Sherson, J. F., Weitenberg, C., Endres, M., Cheneau, M., Bloch, I., and Kuhr, S. (2010). Single-atom-resolved fluorescence imaging of an atomic mott insulator. *Nature*, 467:68–72. → Cited on pages 119, 124

- [Sortais et al., 2007] Sortais, Y., Marion, H., Tuchendler, C., Lance, A. M., Lamare, M., Fournet, P., Armellin, C., Mercier, R., Messin, G., Browaeys, A., and Grangier, P. (2007). Diffraction-limited optics for single-atom manipulation. *Phys. Rev. A*, 75:013406. → Cited on pages 3, 15, 16, 56
- [Steck, 2015] Steck, D. A. (2015). Rubidium 87 D line data. available online at <http://steck.us/alkalidata>. → Cited on pages 37, 47, 137
- [Sutherland and Robicheaux, 2016] Sutherland, R. T. and Robicheaux, F. (2016). Collective dipole-dipole interactions in an atomic array. *Phys. Rev. A*, 94:013847. → Cited on pages 5, 104, 106, 108, 110, 117, 128
- [Tey et al., 2009] Tey, M. K., Maslennikov, G., Liew, T. C. H., Aljunid, S. A., Huber, F., Chng, B., Chen, Z., Scarani, V., and Kurtsiefer, C. (2009). Interfacing light and single atoms with a lens. *New Journal of Physics*, 11:043011. → Cited on pages 37, 39, 41, 42
- [Ville et al., 2017] Ville, J. L., Bienaimé, T., Saint-Jalm, R., Corman, L., Aidelsburger, M., Chomaz, L., Kleinlein, K., Perconte, D., Nascimbène, S., Dalibard, J., and Beugnon, J. (2017). Loading and compression of a single two-dimensional bose gas in an optical accordion. *Phys. Rev. A*, 95:013632. → Cited on pages 76, 101
- [Wales, 2003] Wales, D. J. (2003). *Energy Landscapes*. Cambridge University Press. → Cited on page 122
- [Wales and Doye, 1997] Wales, D. J. and Doye, J. P. K. (1997). Global optimization by basin-hopping and the lowest energy structures of lennard-jones clusters containing up to 110 atoms. *The Journal of Physical Chemistry A*, 101(28):5111–5116. → Cited on page 122
- [Wales and Scheraga, 1999] Wales, D. J. and Scheraga, H. A. (1999). Global optimization of clusters, crystals, and biomolecules. *Science*, 285(5432):1368–1372. → Cited on page 122
- [Weiss et al., 2019] Weiss, P., Cipris, A., Araújo, M., Kaiser, R., and Guerin, W. (2019). Robustness of dicke subradiance against thermal decoherence. *Phys. Rev. A*, 100:033833. → Cited on pages 60, 128
- [Zhu et al., 2018] Zhu, B., Liu, J. Z., Cauley, S. F., Rosen, B. R., and Rosen, M. S. (2018). Image reconstruction by domain-transform manifold learning. *Nature*, 555:487–492. → Cited on page 119

**Titre :** Étude des interactions dipolaires induites par la lumière dans des ensembles d'atomes froids

**Mots clés :** atomes froids, interactions dipôle-dipôle, diffusion de la lumière, effets collectifs, super-radiance

**Résumé :** Notre équipe étudie le comportement collectif d'un gaz d'atomes en présence d'interactions de type dipôle-dipôle. Ces interactions apparaissent lorsqu'on illumine les atomes avec un laser de longueur d'onde quasi-résonant avec une transition atomique : les atomes se polarisent sous l'effet du champ laser, et les dipôles induits interagissent entre eux via le champ qu'ils rayonnent. Cette interaction est d'autant plus forte que les atomes sont proches les uns des autres, et peut perturber considérablement le comportement radiatif de l'ensemble atomique, voire empêcher l'excitation de plusieurs atomes à la fois. Par exemple, un nuage d'atomes dense peut se comporter comme une cavité sans miroirs : le laser peut exciter certains modes de rayonnement particuliers, qui rayonnent chacun avec sa fréquence et son taux de relaxation propres, différents de ceux d'un atome individuel. Certains de ces modes collectifs sont super-radiants (le nuage réémet l'excitation emmagasinée plus rapidement que ne le ferait un atome individuel), d'autres sont au contraire sub-radiants. Afin d'étudier ces phénomènes, notre équipe a construit une

expérience qui permet de piéger entre 1 et ~500 atomes froids de rubidium dans un piège laser de dimensions  $\sim 1 \mu\text{m}^3$ . Nous excitons les atomes près de la transition à 780 nm. La taille du nuage, de l'ordre de 100 nm, est proche de la longueur d'onde réduite. Enfin, l'élargissement Doppler des transitions atomiques est négligeable (atomes froids). La situation est donc quasi-idéale pour l'observation de modes de rayonnement collectifs. Nous avons observé expérimentalement les effets de ces interactions, mais l'accord avec la théorie ne semble être, jusqu'à présent, que qualitatif (malgré nos efforts pour nous soustraire de la structure interne des atomes). Nous avons donc décidé de construire une deuxième version du dispositif expérimental. Cette ambitieuse deuxième version dispose à présent de deux axes optiques haute résolution. En plus de résoudre certains problèmes expérimentaux présent dans la précédente version, elle ouvre la voie à de nouvelles expériences pour étudier les interactions dipolaires : nouveaux régimes de densité et nouvelles configurations atomiques comme les chaînes d'atomes.

**Title :** Study of light-induced dipolar interactions in cold atoms assemblies

**Keywords :** cold atoms, dipole-dipole interactions, light scattering, collective effects, superradiance

**Abstract :** Our team studies the collective behaviour of an atomic gas in the presence of dipole-dipole interactions. These interactions appear when the atoms are illuminated by a laser of wavelength  $\lambda$  that is nearly resonant with an atomic transition : the atoms are polarized by the laser field, and the induced dipoles interact with each other through the field they radiate. This interaction becomes stronger when the atoms are closer to each other, and can considerably perturb the radiative behaviour of the atomic ensemble, or even prevent the simultaneous excitation of several atoms. For instance, a dense atomic cloud can behave like an optical cavity without any mirrors : the laser can excite certain radiation modes, each with its own frequency and life time, which are different from those of an individual atom. Some of these collective modes are super-radiant (the atomic cloud re-emits the stored excitation faster than an individual atom), others are sub-radiant. To study these phenomena, our team has built an experiment that allows

the trapping of 1 up to ~500 cold rubidium atoms in a laser trap of  $\sim 1 \mu\text{m}^3$  in size. We excite the atoms close to the transition at 780nm. The size of the atomic cloud, on the order of 100 nm, is close to the reduced wavelength. Also, the Doppler broadening of the atomic transition is negligible (cold atoms). The situation is therefore nearly ideal for the observation of the collective radiation modes. We observed the effects of these interactions, but no quantitative agreement with theory has been obtained so far (despite our efforts to simplify the internal atomic structure). We have thus decided to build a second version of the experimental apparatus. This challenging second version now possesses two high resolution optical axes. Not only solving some experimental problems of the previous version, it opens the road to new kind of experiments to study dipolar interactions: new regime of densities and new kind of geometries, as 1D chain of atoms for instance.